MICRORHEOLOGY FOR PROTEIN THERAPEUTICS DEVELOPMENT

by

Lilian Lam Josephson

A dissertation submitted to the Faculty of the University of Delaware in partial fulfillment of the requirements for the degree of Doctor of Philosophy in Chemical Engineering

Fall 2016

MICRORHEOLOGY FOR PROTEIN THERAPEUTICS DEVELOPMENT

by

Lilian Lam Josephson

Approved: _____

Abraham M. Lenhoff, Ph.D.
Chair of the Department of Chemical and Biomolecular Engineering

Approved: _____

Babatunde A. Ogunnaike, Ph.D.
Dean of the College of Engineering

Approved: _____

Ann L. Ardis, Ph.D.
Senior Vice Provost for Graduate and Professional Education

I certify that I have read this dissertation and that in my opinion it meets the academic and professional standard required by the University as a dissertation for the degree of Doctor of Philosophy.

Signed: _____

Eric M. Furst, Ph.D.
Professor in charge of dissertation

I certify that I have read this dissertation and that in my opinion it meets the academic and professional standard required by the University as a dissertation for the degree of Doctor of Philosophy.

Signed: _____

Normal J. Wagner, Ph.D.
Member of dissertation committee

I certify that I have read this dissertation and that in my opinion it meets the academic and professional standard required by the University as a dissertation for the degree of Doctor of Philosophy.

Signed: _____

Abraham M. Lenhoff, Ph.D.
Member of dissertation committee

I certify that I have read this dissertation and that in my opinion it meets the academic and professional standard required by the University as a dissertation for the degree of Doctor of Philosophy.

Signed: _____

Christopher J. Roberts, Ph.D.
Member of dissertation committee

I certify that I have read this dissertation and that in my opinion it meets the academic and professional standard required by the University as a dissertation for the degree of Doctor of Philosophy.

Signed: _____

William J. Galush, Ph.D.
Member of dissertation committee

To know wisdom and instruction,
to understand words of insight,
to receive instruction in wise dealing,
in righteousness, justice, and equity;
to give prudence to the simple,
knowledge and discretion to the youth -
Let the wise hear and increase in learning,
and the one who understands obtain guidance,
to understand a proverb and a saying,
the words of the wise and their riddles.

King Solomon, *c. 970–931 BC*

ACKNOWLEDGEMENTS

The road to knowledge is never an easy path. I have many people who loved and supported me, without whom I would not have continued on this journey. I would like to first thank my mom and dad, for sacrificing their lives in the move to America for my sake, and for supporting my endeavors without question. You have shown me what it means to be hardworking with your own lives, and I am forever grateful for what you have done for me.

I would next like to thank Tyler, for the strength and hope you have instilled in me. You pulled me out of the dark pit when I was at my lowest, and you rejoice with me when I am moving forward. Your love kept me going, and I honestly couldn't have done this without you. Your brilliant mind has shown me a new world to marvel in, and science has never been more fun (and in depth). Thank you for indulging me in my Pooh obsession - life without Sweetie the Pooh (and the rest of the peeps) is unimaginable.

InterGrad and church were integral for my life in Delaware; I appreciate all the prayers and support from the small group and church families. Fellow grad students, I am honored to have shared this journey with you all; I thank Anne, Becky, Heather, Kofi, Offei, Julie, Baily, Madelyn, Katie, Elisabethe and Tyler W. for being there every week. I have made some incredible friends in my life, and I will always treasure the times we had together at Madison Drive with Abby, Yun, and Jeff. A special shout out to CG and Liz (and Owen!) for sharing your passion and music, Mary Elizabeth for "adopting" Tyler and me, Annette for the awesome cookies, and Rev. Mary for spending precious times with me. I have also spent considerable time with friends from the department. The nights of Catan games with Stephen and Jennifer rejuvenated

me in the weekends, and the chats with Jill, Kathy, and Ru in the office often eased a long day in lab.

I was fortunate enough to spend five months at Genentech in the last year of my Ph.D. The science happening there is of the highest caliber, and I was inspired to push the limits of my own research. I would like to thank Dr. Karthikan Rajagopal, Dr. Debby Chang, and Dr. Isidro Zarraga for our discussions; Dr. Sarah Gierke and Dr. Meredith Sagolla from gRED Center of Advance Light Microscopy for the facility setup; Catherine Shi for showing me around and teaching me all the tricks; and Eileen, Nate, Michelle, Kate, and Pervina for making me feel welcomed in the new workplace. I would like to specifically thank Dr. Danielle Leiske and Dr. William Galush, who have been amazing mentors to me. Because of this internship, I've met some very awesome friends in the Duboce Triangle neighborhood – thank you for the continuous support from the west coast, Josh & Shea, Ben & Simona, Kay, April, Haley, and Patty!

I would like to thank my committee. Each member has had a unique contribution to this dissertation and had helped mold the research and myself as a scientist. To my advisor, Prof. Eric M. Furst: You have always been my role model as a scholar. Your enthusiasm for science inspires me, and I am fortunate to be able to learn from you. Thank you for all the opportunities you have given me and the guidance along the way.

Last but not least, I owe it all to Jesus my God.

TABLE OF CONTENTS

Appendix

LIST OF TABLES

LIST OF FIGURES

ABSTRACT

Monoclonal antibody (mAb) protein therapeutics are a rapidly growing class of pharmaceuticals. High protein concentrations are required for long-term storage and subcutaneous administration, but these concentrations often result in significantly higher solution viscosities. Viscosity of mAb solutions is used as a development-risk screening factor during early stage development. However, proteins are scarce at this stage of development, and a formulation screen must be conducted quickly to "lock" a suitable formulation that mitigates potential viscosity issues for further clinical development. Multiple particle tracking (MPT) microrheology addresses these needs for rheological measurements of protein solutions with microliter sample volumes and rapid acquisition. In this work, the accuracy and precision of MPT methods are improved via new theoretical approaches, and MPT microrheology is implemented in a device for high-throughput characterization of mAb solution viscosities for early stage pharmaceutical development.

In passive microrheology viscosity is typically determined by the logarithmic intercept of the mean-squared displacement (MSD). This approach biases the largest lag times τ, which are also those with the poorest statistics. A new method is described that identifies an optimal lag time τ from an MPT experiment to calculate the viscosity using the Van Hove self-correlation. Particle displacement follows a Gaussian distribution, and deviations from Gaussian behavior, quantified using the excess kurtosis α_2, indicate which lag times are unsuitable for the viscosity calculation through the use of a test statistic Z_{α_2}. This method ensures that sources of error in the MPT experiment are minimized, generating the most accurate and precise measurements. Particle tracking uncertainty, or static error, has typically been measured with immobilized particles in a gel, but the imaging conditions of the gel are not identical to those

in the sample of interest. To estimate the static error ϵ under sample conditions, a new *in situ* method was developed. This method is also derived using the excess kurtosis α_2, and it enables measurement of the static error using the same data collected during the MPT experiment. The correction of the mean-squared displacement by the *in situ* method is more reliable than the gel estimation, which overcorrects for the static error. With the true MSD now accessible at short lag times, experimental artifacts can now be distinguished from phenomena in solution, even in highly viscous ($>$ 10,000 cP) solutions.

These new methods are used to characterize viscosity profiles for therapeutic protein solutions with a high-throughput microfluidic device with multiple channels for 2 μL samples on a single microscope slide. Mounted on a temperature control stage, this device executes 72 temperature-concentration dependent viscosity measurements in less than 6 hours. An Arrhenius temperature dependence has been observed for the viscosities of two humanized immunoglobulin antibodies, mAb1 and mAb2. Remarkably, the two mAbs have different concentration dependence; even though they share 98% identical sequences, mAb1 has as much as ten times the viscosity of mAb2 at 90 mg/mL at 0.9°C, underscoring the importance of such screening in early stage development.

Particle tracking microrheology also enables the first study and comparison of the viscosity profiles of bispecific mAbs (BsAb-A/B and BsAb-B/C) and their monospecific counterparts (mAb-A, mAb-B, and mAb-C). The viscosity of mAb-C is higher than that of mAb-A, and the Arrhenius mixing rule accurately predicted the mixture of (mAb-A + mAb-C) and the solution of BsAb-A/C. While mAb-A and mAb-B have similar viscosity profiles, their mixture and BsAb-A/B have significantly higher viscosity. Microstructure and protein-protein interactions are examined using light scattering and size exclusion chromatography, and possible mechanisms for the increase in viscosity are discussed.

In summary, new algorithms have been developed to increase accuracy and precision of multiple particle tracking microrheology, and a new device has been developed

for characterizing protein formulations for early stage pharmaceutical development. As part of this thesis work, multiple particle tracking microrheology has been implemented in an industrial laboratory to support early stage pharmaceutical development. With a sample size of 2 μL and with an acquisition time on the order of seconds, accurate and rapid characterization of a library of protein formulations can now be done at a fraction of the time and cost of bulk rheology.

Chapter 1

INTRODUCTION

1.1 Motivation and Goals

The focus of this thesis is to develop a small-scale rheology device to characterize the viscosity of therapeutic protein solutions during early stage pharmaceutical development, as well as to establish new methods for improving the precision and accuracy of microrheological measurements. Concentrated monoclonal antibody (mAb) protein therapeutics have been a target of drug formulations for the past decade [1]. Along with the number of mAb therapeutics coming to market, there is an increasing emphasis on delivery via subcutaneous injection to increase dose efficacy and patient compliance, which requires protein concentrations well above those encountered for traditional intravenously administered products. High protein concentrations, in the range of 100–250 mg/ml, often result in significantly higher solution viscosities [2] placing limits on the "syringibility" of a drug formulation [3, 4]. Viscosity is also important during manufacturing; it affects the pressure needed to perform membrane filtrations during purification [5].

To circumvent these potential challenges, the rheological properties of the protein solutions must be well characterized early in the drug development timeline (prior to Phase 1 clinical trials, with less than tens of human subjects) and are used as a screening criterion. Measurements must also be done with a minimal amount of material and sample preparation time, because material is scarce in early stages of development, and screening experiments must be completed quickly to push the timeline forward. These constraints make passive microrheology, in particular multiple particle tracking microrheology (MPT), an attractive technique to be developed for pharmaceutical research and development laboratories. Multiple particle tracking has become

an important method to measure the rheology of many biological soft materials; examples include the rheology of F-actin solutions [6–8], the microviscosity of genomic DNA solutions [9], the viscoelastic response of folding and unfolding of bovine serum albumin [10], nanoparticle diffusion in bovine vitreous matrix [11], the intracellular mechanics of cultured cells [12], time cure superposition of solid-liquid transitions in peptide hydrogels [13, 14], and the gel network structure and interface layer formation of β-lactoglobulin [15, 16].

Passive microrheology uses the thermal fluctuations and resulting Brownian motion trajectories of colloidal probe particles embedded in microliter-sized samples to determine rheological properties of the solution. The small sample volumes (1–10 μL) and short acquisition time (on the order of seconds) permit high-throughput microrheological characterization of biomaterials [10, 17, 18]. Moreover, video-based particle tracking microrheology requires fairly common laboratory equipment, such as a microscope, video camera, and computer, making the experiments straightforward to implement. During the course of this thesis, an instrument was set up and benchmarked in less than one week at Genentech in South San Francisco, and continues to be used.

This thesis details the design of a microfluidic device for high-throughput microrheology experiments; the 2 μL channels enable 72 temperature-concentration viscosity measurements of mAb solutions in less than 6 hours, with only mg of materials required. The techniques developed in this thesis are used to investigate the viscosity profiles of bispecific antibodies relative to their monospecific counterparts for the first time. The development of new statistical analysis of particle tracking data improves the accuracy and precision of microrheological measurements. A new *in situ* method of estimating the noise floor in a microscopy system is also introduced in this work. The noise floor measured *in situ* is more robust and accurate than the conventional approach, and requires no additional experiments.

This chapter will first provide an overview of monoclonal antibody (mAb) solutions as protein therapeutics. This is followed by a discussion of the current understanding of the factors that affect the viscosity of monoclonal antibody solutions, as

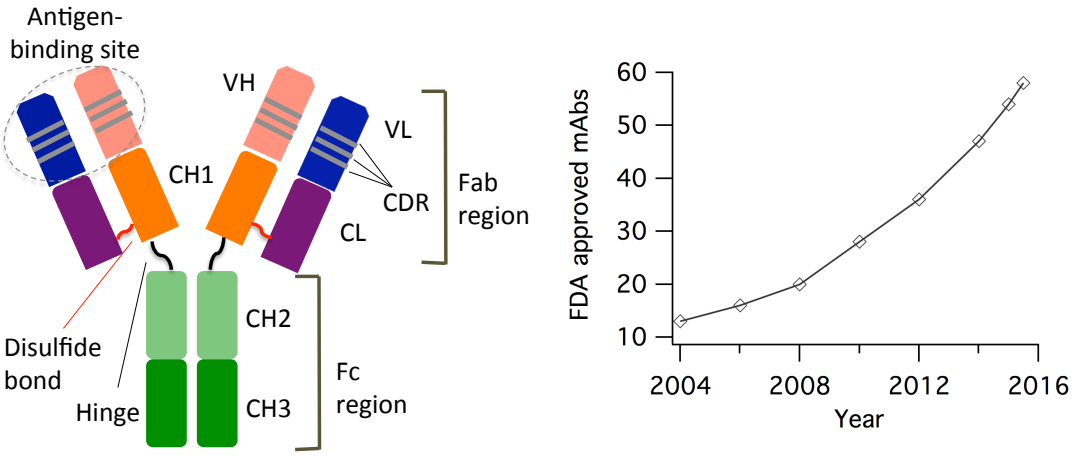

Figure 1.1: Schematic of an IgG monoclonal antibody showing key structural features (left) and the number of US FDA approved mAb therapeutics, as of July 2016 [19–21].

well as the available rheological techniques that are used in characterizing the mAbs. Next, the main principles of passive microrheology are described, in particular, its operating regime and high-throughput capabilities. Lastly, a thesis overview concludes this chapter.

1.2 Monoclonal antibody (mAb) and its development

Recombinant DNA technology has made possible protein expression in a variety of microbial, plant and mammalian systems [22]. Concentrated monoclonal antibody (mAb) protein therapeutics have been a target of drug formulations, and the development of mAbs has increased exponentially for the past decade (Fig. 1.1). [1, 19–21]. As of July 2016, there have been 58 mAbs approved in the United States, at the rate of 5–8 approvals every year, with hundreds more in clinical development. Here we provide a brief overview of the structure, synthesis and development of mAb therapeutics.

The basic structure of a monoclonal (i.e., coming from a single cell line) immunoglobulin G (IgG) antibody is shown in Fig. 1.1. The antibody consists of a variable (V) region and a constant (C) region, connected by a flexible hinge region

that imparts flexibility in mAbs. Interchain disulfide bonds link the heavy chains (H) to the light chains (L). The stem of the Y structure (Fc region) is subdivided into CH1, CH2, and CH3 regions that interact with cellular receptors, and the top of the Y structure (Fab region) contains the antigen-binding region, made up with ∼110 amino acid residues on both VH and VL regions. The variable regions contain three hypervariable sequences called complementarity determining regions (CDRs), flanked by the framework regions. The CDRs bind to a single antigen target, typically leading to fewer side effects than small molecule drugs; therein lies the advantage of using mAbs as therapeutics.

The mAb drug substance is synthesized using host cells, typically *Escherichia coli* and Chinese hamster ovary cells, that are transformed with the appropriate genetic coding for manipulation of protein generation during fermentation or cell-culture processing. The cells are centrifugally harvested, and the expressed proteins are recovered, purified, and exchanged in the preformulation buffer. Only $\sim$ 1–10 g of this scarce material is available for the rest of the early stage development (including formulation, analytical methods, toxicology, etc). The preformulation buffer is not suited for further clinical development, which can only occur after the optimized formulation has been created and "locked". The early stage formulation optimization surveys a large composition space (protein concentrations, excipients, pH, ionic strength, etc.), and the stability, solubility, and viscosity of the proteins are examined under each condition. Because of the material scarcity and the urgency in the timeline, early stage (Phase 0–1) formulation requires a rapid screening method that only uses a small sample for each biophysical property examined. The early formulation lock will continue to be optimized as the molecule advances through the clinical development stages.

1.3 Factors affecting mAb solution viscosity

The lack of extended microstructures in a stable protein solution precludes complex rheological behavior, but these materials are not mundane. The viscosity of a protein solution may be determined by molecular-scale protein-protein interactions,

and thus can be sensitive to the amino acid sequence, as well as the pH, ionic strength, and excipient species present in a formulation. The formulation composition space is rich, and potentially complex. The work of Yadav et al. [23] demonstrates the ability to tune the solution viscosity during early stage development by altering the amino acid sequence, and formulations were screened with viscosity as a parameter to achieve optimal compositions [25, 26].

1.3.1 Formulation

The development of a stable formulation requires screening of different excipients, each one serving a different, specific purpose (besides the need to lower the viscosity of the final drug product). Proteins can undergo different routes of degradation. The diversity of chemistry due to differences in the 20 common amino acids that construct a mAb leads to challenges in finding the optimal formulation that minimizes all degradation routes. In particular, degradation routes such as Asp isomerization and deamidation are dependent on the pH and ionic strength [27]. The buffer strength is typically kept low (< 50 mM) to provide enough buffering capacity for pH control, and at the same time allow the pH to change rapidly upon administration into the human body. Fig. 1.2 shows the pH dependence of the chemical degradation rate constants and viscosity of an IgG1 mAb (GNE) [27]. Degradation kinetics are optimized near pH 6.0; however, this is also when the viscosity of the solution is at the maximum.

The effect of ionic strength on the protein solution viscosity is shown in Fig. 1.3A. The addition of 200 mM salt screens the electrostatic charges on the protein surface, effectively disrupting the self-association that leads to a rise in viscosity for this molecule. Kanai et al. [28] also studied the effect of specific ions on the solution viscosity. Specific-ion effects, also known as Hofmeister effects, also impact the interactions, stability and viscosity of the proteins [28–35]. The Hofmeister series of ions describe the ability of ions from "salting out" (kosmotropes) to "salting in" (chaotropes). The series of anions (SO_4^{2-}, Cl^-, Br^-, I^-, SCN^-, from kosmotropic to chaotropic) has a strong correlation with the viscosity of the IgG1 at a constant concentration; the more chaotropic the salt, the

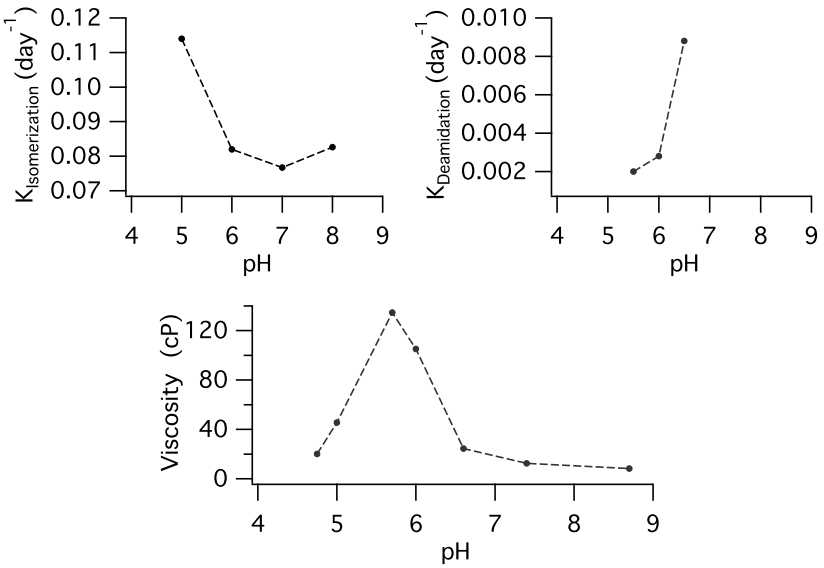

Figure 1.2: Effect of pH on protein isomerization rate, deamidation rate, and solution viscosity at 130 mg/mL an IgG1 antibody (GNE), with a pI of 7.8. Adapted from [27].

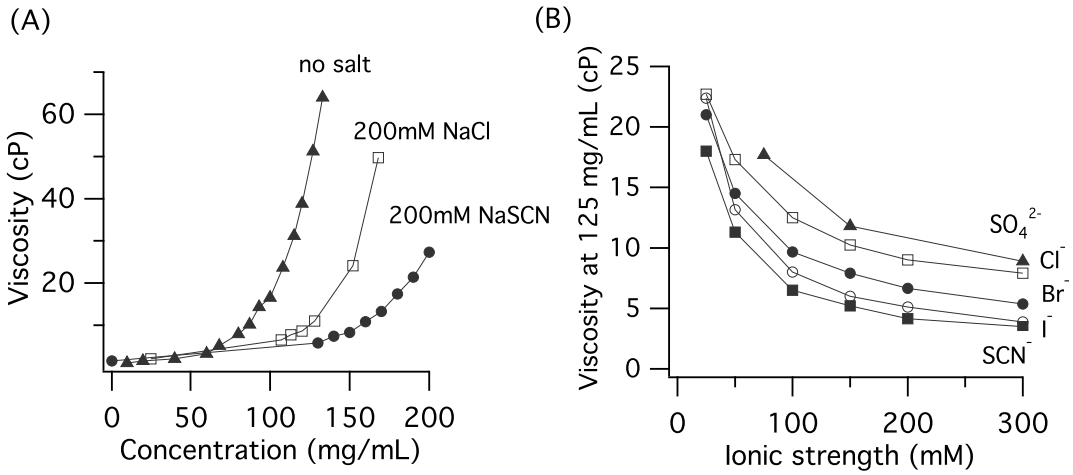

Figure 1.3: Effect of ionic strength and choice of salts on protein solution viscosity. (A) Viscosity of an IgG1 antibody (GNE) in 30 mM histidine-chloride buffer, pH 6.0. (B) Viscosity of 125 mg/mL of mAb1 as a function of ionic strength, in 30mM histidine-chloride buffer, with sodium salt made with the Hofmeister series for anions. Adapted from [28].

lower the viscosity (Fig. 1.3B). They hypothesized that chaotropic anions are breaking the self-association of the antibody, and thereby reducing viscosity. Chaotropic salts have also been observed to decrease electrostatic repulsive protein-protein interactions as well as the net charge of the protein molecule [32].

The use of salt, such as arginine hydrochloride [36], can decrease the viscosity of the protein solutions, but in some cases, salts have been found to have a detrimental effect on the stability of mAbs [33, 37]. Additional protein stabilizers such as sugar molecules are used in protein liquid formulations. Sugars stabilize the mAbs through preferential exclusion of the sugars from the protein surface, leading to preferential hydration for the protein molecules; this shifts the equilibrium away from unfolded states towards a more compact, native state mAb [38]. He et al. [26] studied the effect of 10% w/v of seven common monosaccharides and disaccharides on the viscosity of an IgG1 antibody (Amgen), formulated in 10 mM sodium acetate, pH 5.0. The viscosity of a 10% w/v sugar content (< 2 cP) should not contribute significantly to the solution viscosity in the absence of the proteins. While the sugars offer stabilization and protection to the proteins (as shown in thermal unfolding experiments), the viscosity of sugar-protein solutions is significantly higher than that observed in protein-free solutions or sugar-free protein solutions.

Surfactants are added in the formulation to minimize aggregate formation at the hydrophobic air/water interface that are generated during manufacturing or delivery (stirring, agitation, swirling, shaking, etc.). Polysorbate 20 has been found to prevent mAb aggregation and precipitation during shear [39], and at small amounts ($< 0.5\%$ w/v), surfactants do not contribute significantly to the zero-shear viscosity. However, in measuring the bulk shear viscosity, a surfactant-free antibody solution shows yielding behavior at the air/water interface, as the formation of interfacial film and clusters contribute to the measurement [40, 41]. The works of Johnston and Ewoldt [42] and Ewoldt et al. [43] provide an overview on how to circumvent experimental challenges in measuring shear rheology for protein solutions.

1.3.2 Specific interactions

Solution viscosities are also affected by both pairwise and higher-order intermolecular interactions in antibody solutions. The pairwise intermolecular interactions can be tested by measuring the osmotic second virial coefficient (B_{22}) and diffusion interaction parameter (k_D) using static and dynamic light scattering. A positive value for B_{22} or k_D indicates repulsive protein-protein interactions between two protein molecules, while a negative value indicates attractive protein-protein interactions, although k_D may be negative due to hydrodynamic effects even when B_{22} is positive. The work of Saito et al. [44], Connolly et al. [45], and Neergaard et al. [46] found that both k_D and B_{22} are proportional measures of self-intermolecular interactions, and are good indicators for viscosity of mAb solutions up to ∼200 mg/mL. These protein-protein interaction parameters suggest that reversible self-association of the antibodies plays a dominant role in concentrated protein solutions and directly affects the mAb solution viscosity (as well as aggregation propensity) [28, 47–49]. However, Binabaji et al. [50] recently reported that B_{22} fails to predict mAb solution viscosity as concentration increases beyond 200 mg/mL. Instead, the osmotic third virial coefficient B_{222} is used to predict viscosity for protein concentrations up to 300 mg/mL. This observation of higher-order cluster or structure involving three or more antibody molecules is corroborated by prior work in the literature; Lilyestrom et al. [51], Yearley et al. [52], and Godfrin et al. [53] inferred the formation of *reversible* clusters through small angle x-ray scattering and neutron spin echo, as well as the impact of microstructure formation on increasing solution viscosity of the monoclonal antibody solutions. Patapoff and Esue [39], Nicoud et al. [54] and Barnett et al. [55] noted that the *irreversible* aggregate formation also increases viscosity of concentrated protein solutions.

Even under identical formulation conditions, some proteins experience self-association or aggregation, while others do not. This behavior emerges from differences in the protein amino acid sequences, which influence the molecular conformations and protein-protein interactions. Singh et al. [56] attributes the pattern and location of charged residues in the complementarity determining region (CDR) in promoting the

dipole-dipole interactions that lead to a rise in viscosity. Replacing the charged residues in the sequence of the CDR for mAb-1 decreases the charge asymmetry in the molecule, leading to a loss of self-association and a lowered viscosity; however, the same charge mutant swap does not have the same effect on mAb-2 [23, 57].

These findings all highlight the complexity of antibody behavior, whether the protein-protein interactions that lead to increase in solution viscosity arise from electrostatic attributes (e.g. pI, dipole moments, charge distribution, net charge) or hydrophobic interactions (the tendency to repel water molecules). Because of such complexity, it is difficult to accurately predict viscosity behavior in emerging antibody molecules, rendering an experimental screen to be the most efficient way to test solution viscosity. This emphasizes the need for a small-volume rheological device for measuring concentrated antibody formulations in the early stage of development.

1.4 Rheological techniques in pharmaceutical development

The need for small volume rheology in the biopharmaceutical industry has established a fertile market for new instruments and techniques. Fig. 1.4 summarizes and compares the volume requirements of typical rheometry methods used in biopharmaceutical research. The macrorheology category is comprised of methods that measure the bulk or macroscopic response of the fluid using macroscale instruments or geometries, with its shortest length scale greater than the order of millimeters. This category includes glass capillary viscometers [2, 48], rolling ball viscometers [39], and rotational rheometers [28, 41, 45, 48, 59], with a volume range of 0.1 mL to 8 mL. While these conventional macrorheology measurements are an effective means for characterizing therapeutic protein solutions, they are hindered by the scarcity of material, especially during early development, when it is desirable to screen many candidate molecules over a wide range of conditions.

In response to the demands to miniaturize rheology experiments, several microfluidic or capillary techniques have emerged. These techniques have geometries

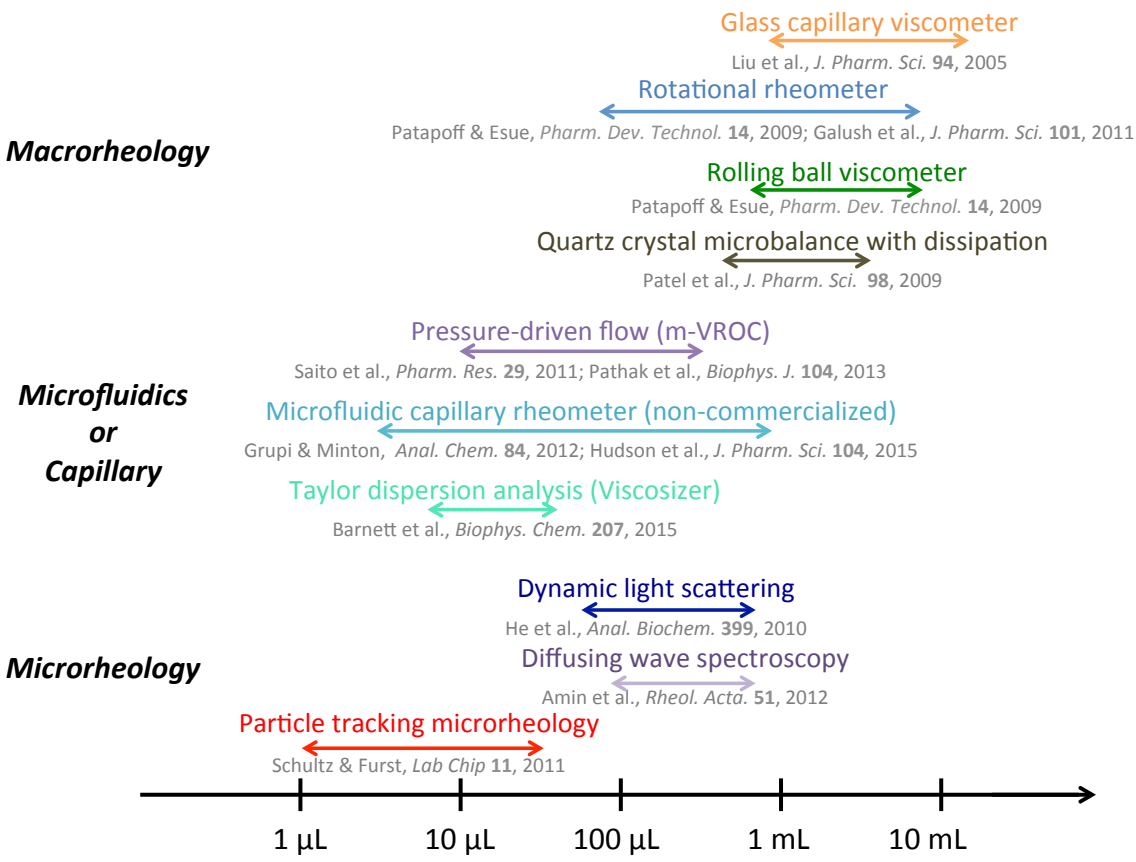

Figure 1.4: Typical sample volumes for methods used to measure mAb solution rheology. From [58].

with length scale on the order of tens to hundreds of micrometers. Commercial instruments, including Rheosense's m-VROC [60] and Malvern's Viscosizer [61], require as little as 100 μL samples to sweep a frequency range of $10^{-1} - 10^{4}$ s^{-1}. These instruments could be paired with an autosampler for automated data collection without user involvement (once all of the samples are prepared), enabling high-throughput screening experiments. Recently, Grupi and Minton [62] and Hudson et al. [63] have documented the development of a custom-built microfluidic device for mAbs with as little as 6 μL samples. Microfluidic technologies also have the advantage of automated sample preparation, generating a library of samples with varying concentrations and compositions using droplet formation junctions [17, 64–66].

Lastly, the microrheology category includes methods that embed colloidal particles (on the order of 100 nm to μm) to probe the material rheology (as is further discussed in Section 1.5). Microrheology typically uses 2–30 μL samples and has a short acquisition time per sample, on the order of 10 s. These techniques are usually lab-based and custom-made, although commercial instruments by manufacturers such as LS Instruments [67] and Formulaction [68] have been recently offered that perform light-scattering based microrheology. Existing dynamic light scattering setups have also been used to measure mAb solution viscosities [69, 70] with samples as small as 35 μL. Microscopy-based microrheology techniques use even smaller samples (on the order of 2-10 μL), and have a further advantage of relatively simple experimental setup, only requiring a light microscope and relatively high-speed video camera, which are available in many laboratories.

1.5 Microrheology

Traditional rheological measurements apply a steady stress or shear to deform the material of interest and record its response. In contrast, microrheology characterizes complex fluids by measuring the motion of embedded colloidal particles and extracting rheological properties. There are two distinct approaches in microrheology: active and passive. Active microrheology measures material response using particles

driven by an externally applied force, such as an electric field [71, 72], magnetic field [73, 74], or micro-manipulations [75–78]. These experiments are analogous to macrorheological measurements, in which an external stress is used to deform the sample, and the resulting fluid response is measured to extract information about the material. However, since the size scale of the manipulation is in the range of nm to μm, the particles in active microrheological experiments are locally deforming the material, therefore probing the local viscoelastic properties. Heilbronn [79], Freundlich [80] and Seifriz [81] pioneered the oldest implementation of active microrheology using magnetic particles in the 1920s to study the structure of gelatin and cellular protoplasm. Since then, active microrheology has found applications in studies of entangled solutions of filamentous actin [73, 82, 83], worm-like micelles [84], associating polymers [85, 86], and colloidal suspensions and gels [87, 88]. The advantage of active microrheology is its capability for measuring high viscosities and nonlinear viscoelastic responses. Optical tweezers have also been used to extract single-molecule level of information, such as bond dynamics and rupture forces in a depletion colloidal gel [78], as well as biophysical information that is unattainable in traditional biochemical assays, such as titin protein folding-unfolding transition [89], DNA dynamics [90, 91], interaction energies and forces between biological materials [92], and molecular interactions between mAb and targeted antigen [93]. However, magnetic or optical tweezers typically require elaborate or customized setups and specialized training, which may not fit the needs of a fast-paced formulation and viscosity screening lab.

In comparison, passive microrheology characterizes the linear viscoelastic response of the material through particle movement driven by inherent thermal forces. Robert Brown's observations in 1828 provided crucial ideas to the foundation of passive microrheology [94], when he observed organelles of pollen grains moving on the surface of water without any induced external force. Albert Einstein later explained this unexpected motion in terms of collisions of the microscopic particles with the surrounding water molecules. Einstein's explanation, published in 1905 [95], states that

the particles' thermal motion, now called Brownian motion, is characterized by a diffusion coefficient, D, and is related to its hydrodynamic drag force ζ (first derived by Stokes in 1850 [96]),

$$D = \frac{k_B T}{\zeta} = \frac{k_B T}{6\pi a \eta} \tag{1.1}$$

in a fluid with viscosity η. Einstein's theory was proven by Jean Perrin in 1909 [97], in the first ever recorded "multiple particle tracking" experiment, when he measured the motion of 0.4 μm particles in water and found that the mean squared displacement $\langle \Delta x^2(t) \rangle$ is directly proportional to time t. His seminal work proved indirectly the existence of atoms, and derived the mathematical link relating the thermal motion of the particles (a measurable quantity using a microscope) and the material rheological properties in which the particles are embedded by

$$\langle \Delta x^2(t) \rangle + \langle \Delta y^2(t) \rangle + \langle \Delta z^2(t) \rangle = 6Dt. \tag{1.2}$$

The displacement of particles can be detected using an optical microscope (e.g. multiple particle tracking) or by light scattering (e.g. diffusing wave spectroscopy, dynamic light scattering); the main principles behind passive microrheology are the same, differing only in the range of length and time scale and methods of data analysis.

Passive microrheology has several advantages that makes it a suitable technique to be applied in a protein formulation lab to rapidly screen viscosities. First, microrheology only requires a small volume of sample, typically between 1 and 10 μL. At such volume and length scale, rapid mass and heat transfers in capillary/microfluidic sample chambers enable high-throughput sample preparation [17, 98–100] and simultaneous temperature equilibration between multiple samples [101]. Second, microrheology has short acquisition times (on the order of minutes), and at the same time, accesses multiple decades of frequencies. A typical multiple particle tracking experiment capturing time scales from 10 μs to 10 s (or frequencies $f = 0.1 - 100$ s^{-1}) can be completed in less than 2 minutes. The short experimental time per sample facilitates rapid data acquisition in screening applications, where over 100 rheological measurements can be

completed in a single day [102]. Third, microrheology is sensitive to small changes in viscosity that might not be accessible in macrorheometry. Conventional rheology instruments monitor the torque response of the material, which places a mechanical constraint on the instrument's sensitivity to low viscosity materials for applications such as the derivation of the intrinsic viscosity. Fourth, passive microrheology can be free of air-water interfaces. Prior work has shown that in several rheometric geometries, the interfacial activity of protein solutions complicates viscosity measurements [42, 43, 103]. Surface tension also contributes to error in low torque rheometry measurements because of sensitivity to the irregularities in the surface, which may create a net torque [40, 43]. However, in fairness, microrheology introduces a solid-liquid interface; steps to minimize such surface interactions are detailed in Sec. 2.2.1.1. Last but not least, passive microrheology, in particular microscopy-based methods, only requires a microscope, a relatively high-speed camera (capable of shutter speed of > 20 frames per second), and a computer.

1.5.1 Operating limits

While passive microrheology has many advantages, it does not replace conventional rheometry, but is rather complementary. Passive microrheology enables rapid screening in early stage of formulation and excels at low viscosity applications, whereas macrorheology can access high shear rates and nonlinear rheological properties like shear-thinning. The combination of the two methods can lead to a more complete understanding of protein solution rheology. Microrheology is also limited to soft materials applications, since microrheology measures the movement of small colloidal particles in the material. Fig. 1.5 shows the operating limits of multiple particle tracking by video microscopy calculated for the commonly-used 1 μm particle.

The spatial resolution that arises from the camera setup sets the lower bound on the length scale. As will be discussed in depth in Chapter 4, the apparent mean

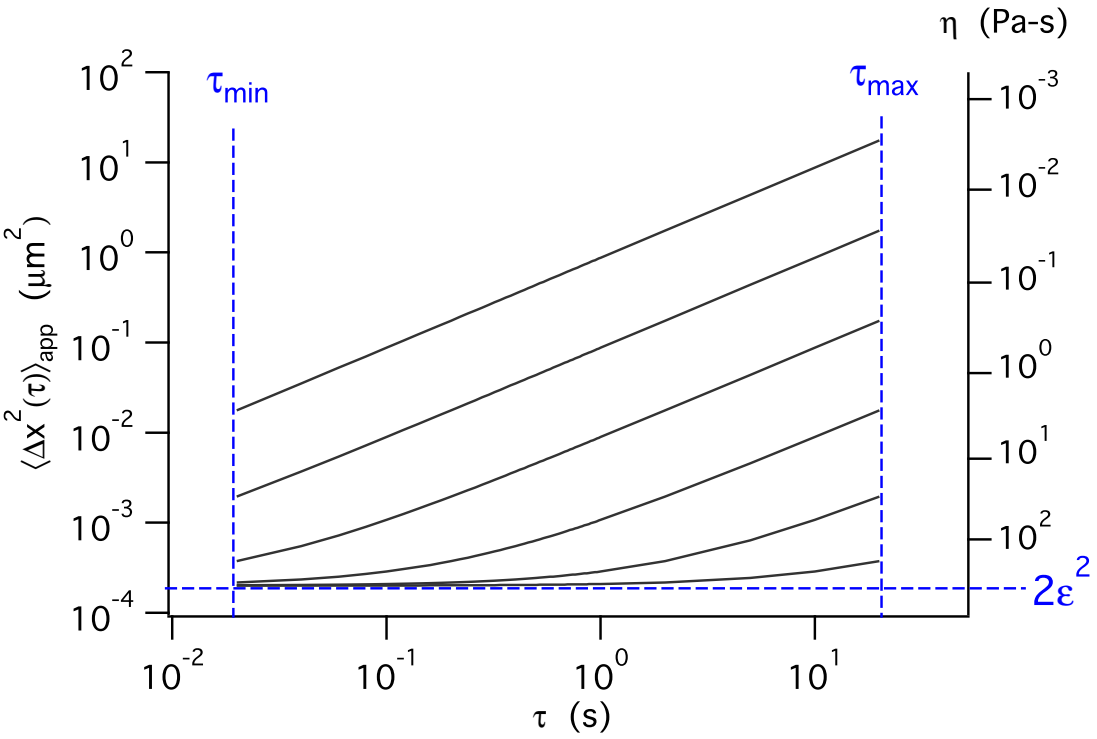

Figure 1.5: Operating regime of multiple particle tracking microrheology, calculated for a probe with diameter 2a = 1 μm.

squared displacement of the particle $\langle \Delta\hat{x}(\tau)^2 \rangle$ is

$$\langle \Delta\hat{x}^2(\tau) \rangle = \langle \Delta x^2(\tau) \rangle + 2\epsilon^2. \tag{1.3}$$

where ϵ represents the static error, or the inherent inaccuracy to track the position of a particle within a spatial resolution. Fig. 1.5 shows how ϵ affects $\langle \Delta\hat{x}^2(\tau) \rangle$; as the measured MSD approaches $2\epsilon^2$, it exhibits an apparent plateau. This spatial resolution sets the operating regime of particle tracking microrheology, limiting the maximum viscosity that can be probed, as calculated by $\eta_{\max} = kT\tau/3\pi a\epsilon^2$.

There are two bounds on the time scale, $\tau_{\min}$ and $\tau_{\max}$. The lower limit $\tau_{\min}$ is set by the frame rate f which the high speed camera in the imaging system is capable of achieving, without inducing excessive dynamic error from the exposure time σ (as discussed in Chapter 2). The frame rate f sets the lag time step τ, and is usually set between $f = 20 - 50$ frames per seconds, or $\tau_{\min} = 0.02$ – 0.05 s. The upper bound of the time scale $\tau_{\max}$ is limited by the overall acquisition time of the measurement. Theoretically, with a highly viscous Newtonian fluid, one could take a video over indefinite time (hours) to move a sufficient distance above the noise floor. However, it is infeasible to track the sample over such long times due to computer/video capability and macroscopic vibration or movement (i.e., accidental bump to the microscope table). The tracking statistics also decrease as $N \sim \tau^{-1}$ at shorter τ, and as particles move out of the focal plane, the trajectories are truncated [104]. Moreover, for samples with a time-dependent rheology (on the order of minutes), such as the material change during a hydrogelation reaction, fast acquisition times are needed to ensure the MSD approximates a stationary property on that time scale.

The operating limits can be shifted by changing the probe size, provided that this does not violate the Stokes continuum assumption (as discussed in Chapter 2). For example, Cohen and Weihs [105] measured the microrheology of Israeli honey up to 20 Pa-s using $2a = 0.2$ μm probe particles. Within these limits, the rheology of the material does not need to be known *a priori* to calculate the viscosity. Under

circumstances at which Newtonian behavior can be assumed, the static error can be accounted for and the material viscosity can still be calculated at large lag time. For potential therapeutic proteins in early development, their viscosity ranges from 1 mPa-s to at most hundreds of mPa-s, many of which behave like a Newtonian fluid at low shear rate. Thus, multiple particle tracking is well suited for viscosity measurements of protein solutions.

1.5.2 High-throughput capabilities

Breedveld and Pine [106] first proposed the use of microrheology for high-throughput screening, creating a water/salt/surfactant phase diagram by measuring a library of block copolypeptides; the samples are placed in a multi-well plate on an automated stage with automated data acquisition. He et al. [69] had a similar, automated setup for dynamic light scattering microrheology to screen formulations for protein therapeutics.

Further high-throughput microrheological experiments focused on the integration with microfluidics technology. For example, Schultz and Furst [17] measured the hydrogelation kinetics of a library of samples with a linear composition gradient generated by microfluidic T-junction. Droplet-forming microfluidic system has also been used to screen hundreds of protein crystallization conditions [107]. These nL-sized droplets can be stored on chip [65, 108], and through the incorporation of membranes [109–112], protein solutions can be concentrated and buffer-exchanged into different formulations, requiring little human interaction.

1.6 Thesis Overview

The focus of this thesis is to develop a small-scale microrheology technique via the use of microfluidics to characterize therapeutic protein solutions during early stage development, as well as to improve the precision and accuracy of microrheological measurements through the use of statistical analysis.

Chapter 2 describes the materials and methods used in the experiments, including a detailed description of multiple particle tracking and its tracking algorithm and errors, the development of a rapid fabrication for creating a microfluidics device, the design and calibration of the temperature control stage, as well as the protein characterization methods. This chapter can serve as a tutorial and guideline for setting up microrheology experiments in a lab for the first time.

Chapter 3 details the analysis of multiple particle tracking statistics using the excess kurtosis α_2 and its test statistic Z_{α_2}; this method of analysis selects the optimal lag time that maximizes the number of independent displacement observations while minimizing the tracking error, with a demonstrated precision and accuracy within 2% relative error for all the standards sample. The microrheology of two monoclonal antibodies are studied and compared to their bulk rheology. The probe particle stability and the protein stability during the particle tracking experiments for these two mAbs are also examined in detail.

Chapter 4 presents a derived mathematical model that relates the static error in particle tracking to the statistics parameter excess kurtosis α_2. Since α_2 is calculated from a particle tracking experiment (along with the usual mean squared displacement), this model presents a way to measure the particle tracking noise floor *in situ*. High concentration sucrose solutions are used in particle tracking experiments to validate the model, showing better accuracy in estimating the static error ϵ than the standard method of measuring trapped particles in a stiff gel.

Chapter 5 demonstrates the temperature-dependent viscometry of the two mAbs presented in Chapter 3 using microrheology in a high-throughput biocompatible microfluidic device. The micrometer size scale in a microfluidic device allows for rapid temperature equilibration, and only a small, local environment needs to be enclosed and controlled. The microfluidic devices are prepared using the fabrication techniques described in Chapter 2. In this chapter, the microfluidic sticker design and the choice of fabrication material are described. Sucrose solutions (55 wt%) are used as a standard

to be embedded in the microfluidic device to measure the on-chip temperature. A calibration curve is developed to back calculate the temperature based on the measured mean squared displacement of the sucrose solution using the Arrhenius equation. The Peltier temperature control setup is validated with sucrose samples from 10 wt% to 55 wt%. In a single day, 72 temperature-concentration viscosity measurements of 2 mAb solutions can be made; the microrheology experiment throughput is increased significantly due to the elimination of separate temperature equilibration in each sample, as compared to bulk rheometry.

Chapter 6 investigates the rheology of two bispecific antibodies (BsAb) and their monospecific counterparts using particle tracking microrheology; the experiments were performed in Genentech's R&D laboratory as part of the implementation of the microrheology technique. In the microrheology experiments, we discovered that while both bispecific antibodies have high viscosity ($\geq$ 30 cP above 100 mg/mL), the underlying reasons for the increase in viscosity are different. One bispecific antibody, BsAb-A/C, is the combination of a low-viscosity monospecific antibody mAb-A and a high-viscosity mAb-C. The 1:1 mixture of mAb-A and mAb-C shows that these two protein molecules do not experience cross-protein interactions that are significantly different than their self-interactions, and the viscosity profile of the (mAb-A + mAb-C) mixture, as well as their combined bispecific antibody, are adequately described by the Arrhenius mixture rule. On the other hand, the viscosity of BsAb-A/B is significantly higher than its monospecific counterparts mAb-A and mAb-B; the viscosity profile of the (mAb-A + mAb-B) mixture cannot be accounted for by the Arrhenius mixture rule, suggesting that there are stronger underlying interactions between the protein molecules. Size exclusion chromatography with a short guard column and light scattering methods are used to probe the protein-protein interactions more in depth, though in this first-pass investigation, neither protein characterization method provides definitive evidence for the mechanism behind the viscosity increase.

Chapter 7 presents a second analysis method for particle tracking microrheology via Fourier image analysis. This method, also known as Differential Dynamic

Microscopy, is applied to examine sucrose solutions and poly(ethylene oxide) solutions. The results are compared to those obtained from the real-space analysis in the particle tracking algorithm described in Chapter 2. The advantages and challenges are also compared between MPT and DDM. Finally, Chapter 8 summarizes the conclusions and discusses the outlook and future directions for this work.

REFERENCES

[1] S. R. Aggarwal. What's fueling the biotech engine 2012 to 2013. *Nature Biotechnology*, 32(1):32–39, 2014.

[2] S. Yadav, S. J. Shire, and D. S. Kalonia. Factors Affecting the Viscosity in High Concentration Solutions of Different Monoclonal Antibodies. *Journal of Pharmaceutical Sciences*, 99(12):4812–4829, 2010.

[3] V. Burckbuchler, G. Mekhloufi, A. P. Giteau, J. L. Grossiord, S. Huille, and F. Agnely. Rheological and syringeability properties of highly concentrated human polyclonal immunoglobulin solutions. *European Journal of Pharmaceutics and Biopharmaceutics*, 76(3):351–356, 2010.

[4] A. Allmendinger, S. Fischer, J. Huwyler, H.-C. Mahler, E. Schwarb, I. E. Zarraga, and R. Mueller. Rheological characterization and injection forces of concentrated protein formulations: an alternative predictive model for non-Newtonian solutions. *European journal of pharmaceutics and biopharmaceutics : official journal of Arbeitsgemeinschaft für Pharmazeutische Verfahrenstechnik e.V*, 87(2):318–328, 2014.

[5] I. D. Gulyakin, L. L. Nikolaeva, E. V. Sanarova, A. V. Lantsova, and N. A. Oborotova. Use of Membrane Filters in Production Technology for Sterile Drugs. *Pharmaceutical Chemistry Journal*, 50(1):33–37, 2016.

[6] M. L. Gardel, M. T. Valentine, J. C. Crocker, A. R. Bausch, and D. A. Weitz. Microrheology of Entangled F-Actin Solutions. *Physical Review Letters*, 91(15): 158302, 2003.

[7] M. T. Valentine, P. D. Kaplan, D. Thota, J. C. Crocker, T. Gisler, R. K. Prud'homme, M. Beck, and D. A. Weitz. Investigating the microenvironments of inhomogeneous soft materials with multiple particle tracking. *Physical Review E*, 64(6):061506, 2001.

[8] J. C. Crocker, M. T. Valentine, E. R. Weeks, T. Gisler, P. D. Kaplan, A. G. Yodh, and D. A. Weitz. Two-Point Microrheology of Inhomogeneous Soft Materials. *Physical Review Letters*, 85(4):888–891, 2000.

[9] A. Goodman, Y. Tseng, and D. Wirtz. Effect of Length, Topology, and Concentration on the Microviscosity and Microheterogeneity of DNA Solutions. *Journal of Molecular Biology*, 323(2):199–215, 2002.

[10] R. S. Tu and V. Breedveld. Microrheological detection of protein unfolding. *Physical review. E, Statistical, nonlinear, and soft matter physics*, 72(4), 2005.

[11] Q. Xu, N. J. Boylan, J. S. Suk, Y.-Y. Wang, E. A. Nance, J.-C. Yang, P. J. McDonnell, R. A. Cone, E. J. Duh, and J. Hanes. Nanoparticle diffusion in, and microrheology of, the bovine vitreous ex vivo. *Journal of Controlled Release*, 167 (1):76–84, 2013.

[12] J. C. Crocker and B. D. Hoffman. Multiple-particle tracking and two-point microrheology in cells. *Methods in cell biology*, 83:141–178, 2007.

[13] T. H. Larsen, K. M. Schultz, and E. M. Furst. Hydrogel microrheology near the liquid-solid transition. *Korea-Australia Rheology Journal*, 20(3), 2008.

[14] T. H. Larsen and E. M. Furst. Microrheology of the Liquid-Solid Transition during Gelation. *Physical Review Letters*, 100(14):146001, 2008.

[15] A. M. Corrigan and A. M. Donald. Particle tracking microrheology of gel-forming amyloid fibril networks. *The European Physical Journal E*, 28(4):457–462, 2009.

[16] G. Balakrishnan, D. Durand, and T. Nicolai. Particle Diffusion in Globular Protein Gels in Relation to the Gel Structure. *Biomacromolecules*, 12(2):450–456, 2011.

[17] K. M. Schultz and E. M. Furst. High-throughput rheology in a microfluidic device. *Lab on a Chip*, 11(22):3802–3809, 2011.

[18] K. M. Schultz and E. M. Furst. Microrheology of biomaterial hydrogelators. *Soft Matter*, 8(23):6198, 2012.

[19] D. M. Ecker, S. D. Jones, and H. L. Levine. The therapeutic monoclonal antibody market. *mAbs*, 7(1):9–14, 2014.

[20] J. M. Reichert. Antibodies to watch in 2016. *mAbs*, 8(2):197–204, 2016.

[21] Antibody Society. Therapeutic mAbs in approved or in regulatory review during Jan-June 2016, 2016. URL http://www.antibodysociety.org/wordpress/wp-content/uploads/2016/08/Therapeutic-mAbs-in-approved-or-in-regulatory-review2016.pdf.

[22] S. J. Shire. Monoclonal Antibodies: Meeting the Challenges in Manufacturing, Formulation, Delivery and Stability of Final Drug Product. Woodhead Publishing, Waltham, MA, 2015.

[23] S. Yadav, A. Sreedhara, S. Kanai, J. Liu, S. Lien, H. Lowman, D. S. Kalonia, and S. J. Shire. Establishing a Link Between Amino Acid Sequences and Self-Associating and Viscoelastic Behavior of Two Closely Related Monoclonal Antibodies. *Pharmaceutical Research*, 28(7):1750–1764, 2011.

[24] J. D. Schmit, F. He, S. Mishra, R. R. Ketchem, C. E. Woods, and B. A. Kerwin. Entanglement Model of Antibody Viscosity. *Journal of Physical Chemistry B*, 118(19):5044–5049, 2014.

[25] F. He, C. E. Woods, E. Trilisky, K. M. Bower, J. R. Litowski, B. A. Kerwin, G. W. Becker, L. O. Narhi, and V. I. Razinkov. Screening of Monoclonal Antibody Formulations Based on High-Throughput Thermostability and Viscosity Measurements: Design of Experiment and Statistical Analysis. *Journal of Pharmaceutical Sciences*, 100(4):1330–1340, 2011.

[26] F. He, C. E. Woods, J. R. Litowski, L. A. Roschen, H. S. Gadgil, V. I. Razinkov, and B. A. Kerwin. Effect of Sugar Molecules on the Viscosity of High Concentration Monoclonal Antibody Solutions. *Pharmaceutical Research*, 28(7):1552–1560, 2011.

[27] S. J. Shire. Formulation and manufacturability of biologics. *Current Opinion in Biotechnology*, 20(6):708–714, 2009.

[28] S. Kanai, J. Liu, T. W. Patapoff, and S. J. Shire. Reversible Self-Association of a Concentrated Monoclonal Antibody Solution Mediated by Fab–Fab Interaction That Impacts Solution Viscosity. *Journal of Pharmaceutical Sciences*, 97(10): 4219–4227, 2008.

[29] M. Bostrom, D. Williams, and B. W. Ninham. Special ion effects: Why the properties of lysozyme in salt solutions follow a Hofmeister series. *Biophysical Journal*, 85(2):686–694, 2003.

[30] F. W. Tavares, D. Bratko, H. W. Blanch, and J. M. Prausnitz. Ion-specific effects in the colloid-colloid or protein-protein potential of mean force: Role of salt-macroion van der waals interactions. *Journal of Physical Chemistry B*, 108 (26):9228–9235, 2004.

[31] X. Tadeo, M. Pons, and O. Millet. Influence of the hofmeister anions on protein stability as studied by thermal denaturation and chemical shift perturbation. *Biochemistry*, 46(3):917–923, 2007.

[32] P. Arosio, B. Jaquet, H. Wu, and M. Morbidelli. On the role of salt type and concentration on the stability behavior of a monoclonal antibody solution. *Biophysical Chemistry*, 168-169:19–27, 2012.

[33] J. Rubin, L. Linden, W. M. Coco, A. S. Bommarius, and S. H. Behrens. Salt-Induced Aggregation of a Monoclonal Human Immunoglobulin G1. *Journal of Pharmaceutical Sciences*, 102(2):377–386, 2013.

[34] G. V. Barnett, V. I. Razinkov, B. A. Kerwin, T. M. Laue, A. H. Woodka, P. D. Butler, T. Perevozchikova, and C. J. Roberts. Specific-Ion Effects on the Aggregation Mechanisms and Protein–Protein Interactions for Anti-streptavidin Immunoglobulin Gamma-1. *Journal of Physical Chemistry B*, 119(18):5793–5804, 2015.

[35] D. Arzensek, D. Kuzman, and R. Podgornik. Hofmeister Effects in Monoclonal Antibody Solution Interactions. *Journal of Physical Chemistry B*, 119(33):10375–10389, 2015.

[36] N. Inoue, E. Takai, T. Arakawa, and K. Shiraki. Specific Decrease in Solution Viscosity of Antibodies by Arginine for Therapeutic Formulations. *Molecular Pharmaceutics*, 11(6):1889–1896, 2014.

[37] R. M. Fesinmeyer, S. Hogan, A. Saluja, S. R. Brych, E. Kras, L. O. Narhi, D. N. Brems, and Y. R. Gokarn. Effect of Ions on Agitation- and Temperature-Induced Aggregation Reactions of Antibodies. *Pharmaceutical Research*, 26(4):903–913, 2009.

[38] S. N. Timasheff. Protein-solvent preferential interactions, protein hydration, and the modulation of biochemical reactions by solvent components. *Proceedings of the National Academy of Sciences*, 99(15):9721–9726, 2002.

[39] T. W. Patapoff and O. Esue. Polysorbate 20 prevents the precipitation of a monoclonal antibody during shear. *Pharmaceutical Development and Technology*, 14(6):659–664, 2009.

[40] V. Sharma, A. Jaishankar, Y.-C. Wang, and G. H. McKinley. Rheology of globular proteins: apparent yield stress, high shear rate viscosity and interfacial viscoelasticity of bovine serum albumin solutions. *Soft Matter*, 7(11):5150–5160, 2011.

[41] J. A. Pathak, R. R. Sologuren, and R. Narwal. Do clustering monoclonal antibody solutions really have a concentration dependence of viscosity? *Biophysical Journal*, 104(4):913–923, 2013.

[42] M. T. Johnston and R. H. Ewoldt. Precision rheometry: Surface tension effects on low-torque measurements in rotational rheometers. *Journal of Rheology*, 57 (6):1515–1532, 2013.

[43] R. H. Ewoldt, M. T. Johnston, and L. M. Caretta. Experimental challenges of shear rheology: how to avoid bad data. In S. E. Spagnolie, editor, *Complex Fluids in Biological Systems*, pages 207–244. Springer, 2015.

[44] S. Saito, J. Hasegawa, N. Kobayashi, N. Kishi, S. Uchiyama, and K. Fukui. Behavior of Monoclonal Antibodies: Relation Between the Second Virial Coefficient (B 2) at Low Concentrations and Aggregation Propensity and Viscosity at High Concentrations. *Pharmaceutical Research*, 29(2):397–410, 2011.

[45] B. D. Connolly, C. Petry, S. Yadav, B. Demeule, N. Ciaccio, J. M. R. Moore, S. J. Shire, and Y. R. Gokarn. Weak Interactions Govern the Viscosity of Concentrated Antibody Solutions: High-Throughput Analysis Using the Diffusion Interaction Parameter. *Biophysical Journal*, 103(1):69–78, 2012.

[46] M. S. Neergaard, D. S. Kalonia, H. Parshad, A. D. Nielsen, E. H. Møller, and M. van de Weert. Viscosity of high concentration protein formulations of monoclonal antibodies of the IgG1 and IgG4 subclass - prediction of viscosity through protein-protein interaction measurements. *European journal of pharmaceutical sciences : official journal of the European Federation for Pharmaceutical Sciences*, 49(3):400–410, 2013.

[47] C. G. Hall and G. N. Abraham. Size, shape, and hydration of a self-associating human IgG myeloma protein: Axial asymmetry as a contributing factor in serum hyperviscosity. *Archives of biochemistry and biophysics*, 233(2):330–337, 1984.

[48] J. Liu, M. D. H. Nguyen, J. D. Andya, and S. J. Shire. Reversible Self-Association Increases the Viscosity of a Concentrated Monoclonal Antibody in Aqueous Solution. *Journal of Pharmaceutical Sciences*, 94(9):1928–1940, 2005.

[49] A. Saluja and D. S. Kalonia. Nature and consequences of protein-protein interactions in high protein concentration solutions. *International Journal of Pharmaceutics*, 358(1-2):1–15, 2008.

[50] E. Binabaji, J. Ma, and A. L. Zydney. Intermolecular Interactions and the Viscosity of Highly Concentrated Monoclonal Antibody Solutions. *Pharmaceutical Research*, 32(9):3102–3109, 2015.

[51] W. G. Lilyestrom, S. J. Shire, and T. M. Scherer. Influence of the Cosolute Environment on IgG Solution Structure Analyzed by Small-Angle X-ray Scattering. *Journal of Physical Chemistry B*, 116(32):9611–9618, 2012.

[52] E. J. Yearley, P. D. Godfrin, T. Perevozchikova, H. Zhang, P. Falus, L. Porcar, M. Nagao, J. E. Curtis, P. Gawande, R. Taing, I. E. Zarraga, N. J. Wagner, and Y. Liu. Observation of Small Cluster Formation in Concentrated Monoclonal Antibody Solutions and Its Implications to Solution Viscosity. *Biophysical Journal*, 106(8):1763–1770, 2014.

[53] P. D. Godfrin, I. E. Zarraga, J. Zarzar, L. Porcar, P. Falus, N. J. Wagner, and Y. Liu. Effect of Hierarchical Cluster Formation on the Viscosity of Concentrated Monoclonal Antibody Formulations Studied by Neutron Scattering. *Journal of Physical Chemistry B*, 120(2):278–291, 2016.

[54] L. Nicoud, M. Lattuada, A. Yates, and M. Morbidelli. Impact of aggregate formation on the viscosity of protein solutions. *Soft Matter*, 11(27):5513–5522, 2015.

[55] G. V. Barnett, W. Qi, S. Amin, E. Neil Lewis, and C. J. Roberts. Aggregate structure, morphology and the effect of aggregation mechanisms on viscosity at elevated protein concentrations. *Biophysical Chemistry*, 207:21–29, 2015.

[56] S. N. Singh, S. Yadav, S. J. Shire, and D. S. Kalonia. Dipole-Dipole Interaction in Antibody Solutions: Correlation with Viscosity Behavior at High Concentration. *Pharmaceutical Research*, 31(9):2549–2558, 2014.

[57] S. Yadav, T. M. Laue, D. S. Kalonia, S. N. Singh, and S. J. Shire. The influence of charge distribution on self-association and viscosity behavior of monoclonal antibody solutions. *Molecular Pharmaceutics*, 9(4):791–802, 2012.

[58] L. L. Josephson, E. M. Furst, and W. J. Galush. Particle tracking microrheology of protein solutions. *Journal of Rheology*, 60(4):531–540, 2016.

[59] I. E. Zarraga, R. Taing, J. Zarzar, J. Luoma, J. Hsiung, A. Patel, and F. J. Lim. High Shear Rheology and Anisotropy in Concentrated Solutions of Monoclonal Antibodies. *Journal of Pharmaceutical Sciences*, 102(8):2538–2549, 2013.

[60] Rheosense. m-VROC viscometer. URL http://www.rheosense.com/products/viscometers/m-vroc/overview.

[61] Malvern. Viscosizer TD. URL http://www.malvern.com/en/products/product-range/viscosizer-td/.

[62] A. Grupi and A. P. Minton. Capillary Viscometer for Fully Automated Measurement of the Concentration and Shear Dependence of the Viscosity of Macromolecular Solutions. *Analytical Chemistry*, 84(24):10732–10736, 2012.

[63] S. D. Hudson, P. Sarangapani, J. A. Pathak, and K. B. Migler. A Microliter Capillary Rheometer for Characterization of Protein Solutions. *Journal of Pharmaceutical Sciences*, 104(2):678–685, 2015.

[64] Š. Selimović, Y. Jia, and S. Fraden. Measuring the nucleation rate of Lysozyme using microfluidics. *Crystal Growth and Design*, 9(4):1806–1810, 2009.

[65] H. Boukellal, Š. Selimović, Y. Jia, G. Cristobal, and S. Fraden. Simple, robust storage of drops and fluids in a microfluidic device. *Lab on a Chip*, 9(2):331–338, 2009.

[66] J.-u. Shim, G. Cristobal, D. R. Link, T. Thorsen, and S. Fraden. Using Microfluidics to Decouple Nucleation and Growth of Protein Crystals †. *Crystal Growth and Design*, 7(11):2192–2194, 2007.

[67] L. S. Instruments. Diffusing Wave Spectroscopy. URL http://www.lsinstruments.ch/technology/diffusing_wave_spectroscopy_dws/.

[68] Formulaction. Rheolaser Master. URL http://www.formulaction.com/en/microrheology/bulk-rheology.

[69] F. He, G. W. Becker, J. R. Litowski, L. O. Narhi, D. N. Brems, and V. I. Razinkov. High-throughput dynamic light scattering method for measuring viscosity of concentrated protein solutions. *Analytical Biochemistry*, 399(1):141–143, 2010.

[70] P. M. Tessier, J. Wu, and C. D. Dickinson. Emerging methods for identifying monoclonal antibodies with low propensity to self-associate during the early discovery process. *Expert opinion on drug delivery*, 11(4):461–465, 2014.

[71] M. Wang and R. J. Hill. Dynamic electric-field-induced response of charged spherical colloids in uncharged hydrogels. *Journal of Fluid Mechanics*, 640:357, 2009.

[72] L. G. Wilson and W. C. K. Poon. Small-world rheology: an introduction to probe-based active microrheology. *Physical Chemistry Chemical Physics*, 13(22): 10617–10630, 2011.

[73] F. Ziemann, J. Rädler, and E. Sackmann. Local measurements of viscoelastic moduli of entangled actin networks using an oscillating magnetic bead microrheometer. *Biophysical Journal*, 66(6):2210–2216, 1994.

[74] P. Habdas, D. Schaar, A. C. Levitt, and E. R. Weeks. Forced motion of a probe particle near the colloidal glass transition. *Europhysics Letters (EPL)*, 67(3): 477–483, 2007.

[75] M. T. Valentine, L. E. Dewalt, and H. D. Ou-Yang. Forces on a colloidal particle in a polymer solution: a study using optical tweezers. *Journal of Physics Condensed Matter*, 8(47):9477–9482, 1996.

[76] D. Velegol and F. Lanni. Cell Traction Forces on Soft Biomaterials. I. Microrheology of Type I Collagen Gels. *Biophysical Journal*, 81(3):1786–1792, 2001.

[77] M. L. Gardel, M. T. Valentine, and D. A. Weitz. Microrheology. In K. S. Breuer, editor, *Microscale diagnostic techniques*. 2005.

[78] K. A. Whitaker and E. M. Furst. Bond rupture between colloidal particles with a depletion interaction. *Journal of Rheology*, 60(3):517–529, 2016.

[79] A. Heilbronn. Eine neue methode zur bestimmung der viskosität lebender protoplasten. *Jahrb. Wiss. Bot.*, 61:284, 1922.

[80] H. Freundlich. Über die Struktur der Kolloidteilchen und über den Aufbau von Solen und Gelen. *European Journal of Inorganic Chemistry*, 61(10):2219–2233, 1928.

[81] W. Seifriz. The Structure of Protoplasm and of Inorganic Gels: An Analogy. *Journal of Experimental Biology*, 1(3):431–443, 1924.

[82] F. Amblard, A. C. Maggs, B. Yurke, A. N. Pargellis, and S. Leibler. Subdiffusion and Anomalous Local Viscoelasticity in Actin Networks. *Physical Review Letters*, 77(21):4470–4473, 1996.

[83] M. Keller, J. Schilling, and E. Sackmann. Oscillatory magnetic bead rheometer for complex fluid microrheometry. *Review of Scientific Instruments*, 72(9):3626, 2001.

[84] N. Cappallo, C. Lapointe, D. H. Reich, and R. L. Leheny. Nonlinear microrheology of wormlike micelle solutions using ferromagnetic nanowire probes. *Physical Review E*, 76(3):031505, 2007.

[85] M. T. Valentine, L. E. Dewalt, and H. D. Ou-Yang. Forces on a colloidal particle in a polymer solution: a study using optical tweezers. *Journal of Physics Condensed Matter*, 8(47):9477–9482, 1999.

[86] L. A. Hough and H. D. Ou-Yang. Viscoelasticity of aqueous telechelic poly(ethylene oxide) solutions: Relaxation and structure. *Physical Review E*, 73(3):031802, 2006.

[87] A. Meyer, A. Marshall, B. G. Bush, and E. M. Furst. Laser tweezer microrheology of a colloidal suspension. *Journal of Rheology*, 50(1):77–92, 2006.

[88] L. C. Hsiao, M. J. Solomon, K. A. Whitaker, and E. M. Furst. A model colloidal gel for coordinated measurements of force, structure, and rheology. *Journal of Rheology*, 58(5):1485–1504, 2014.

[89] M. S. Z. Kellermayer, S. B. Smith, H. L. Granzier, and C. Bustamante. Folding-Unfolding Transitions in Single Titin Molecules Characterized with Laser Tweezers. *Science*, 276(5315):1112–1116, 1997.

[90] P. Gross, G. Farge, E. J. G. Peterman, and G. J. L. Wuite. Combining Optical Tweezers, Single-Molecule Fluorescence Microscopy, and Microfluidics for Studies of DNA–Protein Interactions. In *Single Molecule Tools, Part B:Super-Resolution, Particle Tracking, Multiparameter, and Force Based Methods*, pages 427–453. Elsevier, 2010.

[91] I. Heller, G. Sitters, O. D. Broekmans, G. Farge, C. Menges, W. Wende, S. W. Hell, E. J. G. Peterman, and G. J. L. Wuite. STED nanoscopy combined with optical tweezers reveals protein dynamics on densely covered DNA. *Nature Methods*, 10(9):910–916, 2013.

[92] D. Leckband. Measuring the Forces that Control Protein Interactions. *Annual Review of Biophysics and Biomolecular Structure*, 29(1):1–26, 2000.

[93] H. D. Chen, K. K. Ge, Y. M. Li, J. G. Wu, Y. Q. Gu, H. M. Wei, and Z. G. Tian. Application of optical tweezers in the research of molecular interaction between lymphocyte function associated antigen-1 and its monoclonal antibody. *Cellular & molecular immunology*, 4(3):221–225, 2007.

[94] R. Brown. A brief account of microscopical observations made in the months of June, July and August 1827, on the particles contained in the pollen of plants; and on the general existence of active molecules in organic and inorganic bodies. *Philosophical Magazine and Annals of Philosophy*, 4(21):161–173, 1828.

[95] A. Einstein. On the movement of small particles suspended in a stationary liquid demanded by the molecular-kinetic theory of heat (Über die von der molekularkinetischen Theorie der Wärme geforderte Bewegung von in ruhenden Flüssigkeiten suspendierten Teilchen). *Annalen der Physik*, 322:549–560, 1905.

[96] G. G. Stokes. On the Effect of the Internal Friction of Fluids on the Motion of Pendulums. In *Mathematical and Physical Papers*, pages 1–10. Cambridge University Press, Cambridge, 2009.

[97] J. Perrin. Mouvement brownien et réalité moléculaire. *Ann. de Chim. et Phys.*, 1909.

[98] R. Seemann, M. Brinkmann, T. Pfohl, and S. Herminghaus. Droplet based microfluidics. *Reports on Progress in Physics*, 75(1):016601, 2012.

[99] M. F. DeLaMarre, A. Keyzer, and S. A. Shippy. Development of a Simple Droplet-Based Microfluidic Capillary Viscometer for Low-Viscosity Newtonian Fluids. *Analytical Chemistry*, 87(9):4649–4657, 2015.

[100] G. T. Vladisavljevic, I. Kobayashi, and M. Nakajima. Production of uniform droplets using membrane, microchannel and microfluidic emulsification devices. *Microfluidics and Nanofluidics*, 13(1):151–178, 2012.

[101] L. L. Josephson, W. J. Galush, and E. M. Furst. Parallel temperature-dependent microrheological measurements in a microfluidic chip. *Biomicrofluidics*, 10(4): 043503, 2016.

[102] K. M. Schultz, A. D. Baldwin, K. L. Kiick, and E. M. Furst. Measuring the modulus and reverse percolation transition of a degrading hydrogel. *ACS macro letters*, 1(6):706–708, 2012.

[103] M. M. Castellanos, J. A. Pathak, and R. H. Colby. Both protein adsorption and aggregation contribute to shear yielding and viscosity increase in protein solutions. *Soft Matter*, 10(1):122–131, 2014.

[104] T. Savin and P. S. Doyle. Statistical and sampling issues when using multiple particle tracking. *Physical review. E, Statistical, nonlinear, and soft matter physics*, 76(2):021501, 2007.

[105] I. Cohen and D. Weihs. Rheology and microrheology of natural and reduced-calorie Israeli honeys as a model for high-viscosity Newtonian liquids. *Journal of Food Engineering*, 100(2):366–371, 2010.

[106] V. Breedveld and D. J. Pine. Microrheology as a tool for high-throughput screening. *Journal of Materials Science*, 38(22):4461–4470, 2003.

[107] B. Zheng, L. S. Roach, and R. F. Ismagilov. Screening of protein crystallization conditions on a microfluidic chip using nanoliter-size droplets. *Journal of the American Chemical Society*, 125(37):11170–11171, 2003.

[108] J.-u. Shim, G. Cristobal, D. R. Link, T. Thorsen, Y. Jia, K. Piattelli, and S. Fraden. Control and measurement of the phase behavior of aqueous solutions using microfluidics. *Journal of the American Chemical Society*, 129(28): 8825–8835, 2007.

[109] S. Song, A. K. Singh, T. J. Shepodd, and B. J. Kirby. Fabrication and characterization of photopatterned polymer membranes for protein concentration and dialysis in microchips. In *Solid-State Sensor, Actuator and Microsystems Workshop*, 2004.

[110] R. S. Foote, J. Khandurina, S. C. Jacobson, and J. M. Ramsey. Preconcentration of proteins on microfluidic devices using porous silica membranes. *Analytical Chemistry*, 77(1):57–63, 2005.

[111] C. Kim, C. Ryu, L. W. Kim, S. J. Sim, and H. Chae. Microfluidic dialysis device fabrication for protein solution enrichment and its enrichment enhancement by plasma surface treatment of a membrane. *Journal of the Korean Physical Society*, 51(3):993–999, 2007.

[112] Š. Selimović, F. Gobeaux, and S. Fraden. Mapping and manipulating temperature-concentration phase diagrams using microfluidics. *Lab on a Chip*, 10(13):1696–1699, 2010.

Chapter 2

MATERIALS AND METHODS

The aim of this thesis is to develop a method for rapid characterization of therapeutic protein solutions using small volume samples at the early stages of pharmaceutical development. The protein solution viscosity is used as a screening or risk factor in developing biological therapeutics, since it is an important biophysical parameter that affects downstream development and manufacturing. To accomplish these goals, multiple particle tracking microrheology is used as the characterization technique. We further improve the technique by (1) combining microrheology and microfluidics to decrease the required sample size, and (2) using temperature control via a Peltier module to generate samples over a large range of operating conditions.

2.1 Materials

2.1.1 Microspheres

Microspheres used in microrheology experiments must be carefully prepared to ensure the colloidal particles do not aggregate or interact with the material of interest, which affects the measurements. Fluorescent polystyrene (PS) particles with or without surface functionalities, with diameters ranging from 0.2 μm to 1 μm, are purchased from reputable manufacturers, Polysciences, Inc. (Warrington, PA) or Molecular Probes (Eugene, OR). The stock solutions typically come in 2–2.5 % w/v. The probe particles are washed to remove excess fluorescent dye and possible contaminants from their synthesis and storage. The centrifugation time and speed are chosen carefully to avoid

irreversible particle aggregation during the washing steps. For spherical particles, the settling velocity can be calculated using Stokes' Law,

$$V = \frac{2Ga^2(\rho_1 - \rho_2)}{9\eta} \tag{2.1}$$

where V is the velocity (cm/s), G is the g-force (cm/s^2), ρ_1 is the density of the particle (g/cm^3), ρ_2 is the density of the suspending media (g/cm^3), η is viscosity (poise or g/cm-s), and a is the radius of the spherical particle (cm). To estimate appropriate times for centrifugation, choose a desired centrifugation force (typically between 5000 G and 20000 G), calculate the settling velocity, and compare the resultant velocity to the height of the centrifuge tube. For example, a 1.0 μm polystyrene particle placed in a microcentrifuge generating 10000 G will settle at a velocity of 2.77 x 10^{-2} cm/s; placing the microspheres in a 4 cm high tube would require a 144 s centrifuge run at the minimum. The actual time required to completely pellet the microspheres could be up to 50% longer. Such calculations are intended as guidelines to estimate centrifugation time. For all 1 μm particles at upwards of 2.5% w/v, the particles are centrifuged for 6 minutes at 5000 G as a starting point. If, upon observations, the probes have not sufficiently settled, a one-minute centrifugation run at 5000 G is added. After the centrifugation, the supernatant is discarded and the particles are re-disperse in the same volume of ultra-pure water (Milli-Q, Millipore, resistivity $\leq$ 18.2 M Ω cm). These washing procedures are repeated at least three times for each batch of particles taken out of the manufacturer's stock solutions. In the last washing step, the particles are re-dispersed in 4–5 fold less water to concentrate up the microspheres to approximately 10% w/v. This is done so only a minimal volume is added to the samples to minimize concentration changes.

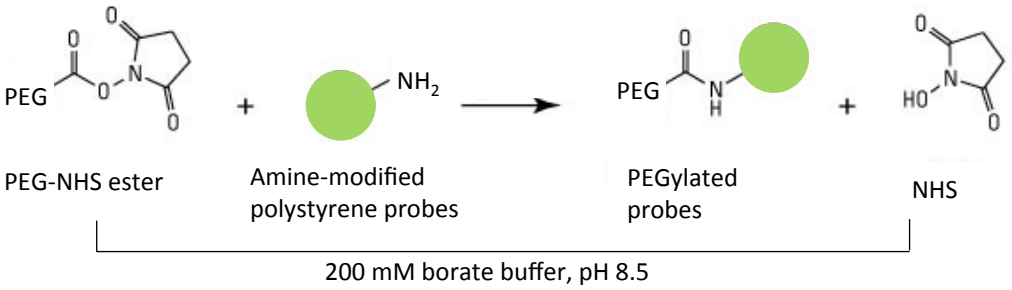

Figure 2.1: Carbodiimide reaction with amine-modified polystyrene microspheres as starting material.

2.1.1.1 PEGylation reactions on microspheres

Polystyrene (PS) microspheres grafted with poly(ethylene glycol) (PEG) are synthesized via carbodiimide reactive chemistry to make PEGylated microspheres (PS-PEG). Two starting microspheres with different surface modifications (amine and carboxylate, respectively) are used and their reactions are compared here.

The steps to covalent coupling of PEG to amine-modified PS microspheres are adapted from Huh and Furst [1] and shown in Fig. 2.1. Amine-modifed PS particles (2a = 0.97 ± 0.022 μm, 2.0% w/v, Molecular Probes) are first washed 3 times in Milli Q water. PEG with N-hydroxysuccinimidyl ester end groups (mPEG-succinimidyl carboxyl methyl ester, MW = 5000, CreativePEGWorks, Winston-Salem, NC) is dissolved in borate buffer (pH 8.5, 100 mM boric acid, 75 mM sodium chloride, 25 mM sodium tetraborate) at 200 mg/ml (1mL in volume) and immediately mixed with 100 μL 2.0% w/v amine-modified PS particles to react for 90 minutes. The probes are then washed with pure borate buffer and Milli-Q water three times each.

An alternative carbodiimide reaction starts with carboxylate modified microspheres [2, 3] and is shown in Figure 2.2. Carboxylate-modified latex (CML) beads (2a = 1.0 μm, Molecular Probes) are PEGylated with amine-functionalized polyethylene glycol (amine-PEG 5kDa, Creative PEGWorks, Winston Salem, NC). Beads are first washed 3 times in Milli Q water, then suspended in PolyLink coupling buffer (50 mM MES, pH 5.2, 0.05% Proclin-300, Polyscience Inc.) at 2% w/v and are sonicated until

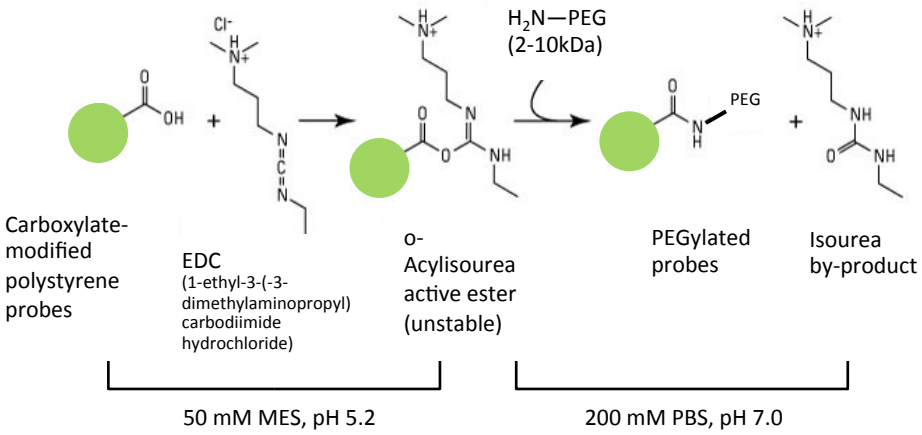

Figure 2.2: Carbodiimide reaction with carboxylated-modified polystyrene microspheres as starting material.

there is no visible precipitate. Carboxyl groups on beads are activated at this low pH by addition of 1- ethyl-3-(3-dimethylaminopropyl) carbodiimide hydrochloride (EDC) to form O-acylisourea intermediate. 50 μL of 200 mg/mL EDC are added to 500 μL 2% probes, and incubated at room temperature for 30 min under rotation. Excess EDC is removed by repeated centrifugation at 3200 G for 5 mins and washing with water (at least 3 times). 500 μL of 200 mg/mL amine-PEG, dissolved in 200 mM PBS, pH 7, is added to resuspend the beads in solution at 10$\times$ excess. Raising the pH from the initial activation step helps drive the PEGylation reaction. The reaction between the amine-PEG and the beads is allowed to occur overnight at room temperature, under rotation and shielded from light with metal foil. Unreacted amine-PEG is removed by repeated washing with DI water at least 3 times.

2.1.2 Sucrose solutions

The sucrose crystals (ACS reagents grade, #84100, Sigma-Aldrich) are dissolved in ultra-pure Milli-Q water (resistivity $\leq$ 18.2 M Ω cm) at 0, 10, 25, 40, 55, 60, 65 wt% in 20 mL vials with stirring and gentle heating at 35°C. The Milli-Q water is filtered

using a centrifuge tube-top filter unit (EMD Millipore Steriflip-GP, 0.22 μm pore size, polyethersulfone, #SCGP00525) to prevent mold and bacteria growth.

2.1.3 Poly(ethylene oxide) solutions

Poly(ethylene oxide) (PEO) solutions are prepared from 2.0 MDa PEO (Aldrich Chemistry, Lot No. MKBQ3351V). An amount of PEO for a given weight percent (0.2, 0.5, 1, 2, and 5 wt%) is added to 10 mL of ultra-pure water in a 20 mL scintillation vial at room temperature ($\sim$23°C). Samples will appear to have separate layers as the PEO slowly dissolves. The sample vials are placed on a stir plate at a medium speed for 30 minutes, until the solutions look visibly uniform; the vials then are incubated at 60°C overnight.

2.1.4 Polyacrylamide gel

Acrylamide monomer, bis-acrylamide crosslinker, ammonium persulfate initiator, and tetramethylethylenediamine (TEMED) catalyst are obtained commercially (Sigma-Aldrich). Oxygen is known to inhibit the polymerization process, so stock solutions are made fresh and degassed by vacuum prior to each use. Samples are prepared at 5.0 wt% total acrylamide, with up to 0.1 wt% bis-acrylamide crosslinker, 0.5 wt% ammonium persulfate, and 0.1% TEMED. This polyacrylamide gel has an estimated shear modulus of 1.5 kPa [4]; at this modulus, the expected MSD for 1 μm diameter probe particles is 2.9 $\times 10^{-13}$ nm^2 (or a root mean square = 5.4 $\times 10^{-7}$ nm).

The order of mixing in Milli-Q water should be acrylamide monomer, ammonium persulfate and bis-acrylamide; the solution needs to be degassed for at least 15 minutes. The probe particles used for microrheology are added to the precursor solution and mixed gently with vortex. The addition of TEMED will initiate the gelation process. The TEMED is mixed quickly and gently (avoiding air bubbles) into the precursor-and-probe solution, and sealed into capillary tubes or sample chamber with NOA optical glue (NOA81, Norland Products, Cranbury, NJ). The polyacrylamide gel is allowed to cure for 6 hours under the fume hood in a well-ventilated setting.

Table 2.1: Monoclonal antibodies used in this thesis and their properties

Molecule	MW (kDa)	Ext. Coefficient (mg/mg-cm)	Theoretical pI
mAb1	146.5	1.577	7.85
mAb2	145.4	1.492	9.80
mAb3	145.2	1.540	9.25
mAb4	144.4	1.636	8.95
mAb-A	145.0	1.430	6.25
mAb-B	145.2	1.540	9.25
mAb-C	144.9	1.353	6.95
BsAb-A/B	145.2	1.528	7.40
BsAb-A/C	144.9	1.430	6.45

2.1.5 Formulation buffers

The formulation buffers are made with ultra-pure Milli-Q water that is filtered using a bottle-top filter unit prior to use (Nalgene rapid-flow sterile disposable filter units, surfactant-free cellulose acetate membrane, 0.2 μm pore size, #161-0020, Thermo Fisher Scientific). The 30 mM histidine buffer is prepared and adjusted to pH 5.4 by combining 5 mM L-histidine free-base and 25 mM L-histidine-HCl. The 20 mM histidine buffer is prepared and adjusted to pH 6.0 by combining 9 mM L-histidine free-base and 11 mM L-histidine-HCl (Sigma Aldrich).

2.1.6 Monoclonal antibody solutions

All the monoclonal antibodies used in this thesis are supplied by Genentech Inc. (South San Francisco, CA). The protein properties are reported in Table 2.1. The proteins are first buffer-exchanged into the formulation buffer using Slide-A-Lyzer^{TM} dialysis cassettes (10k molecular weight cut off, catalog #66385, Thermo Fisher Scientific). The protein solutions are then diluted serially with the formulation buffer.

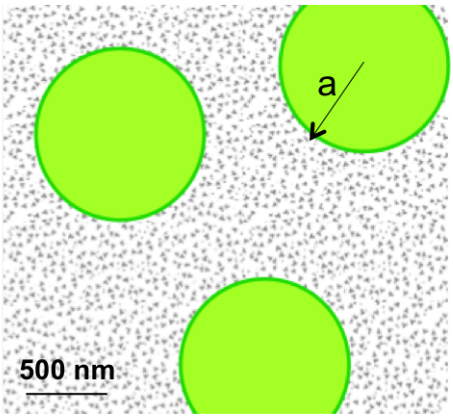

Figure 2.3: The chosen probe particles ($2a = 1$ μm) must be much larger than its surrounding material's characteristic length scale ($R_{\mathrm{g,mAb}} \sim 10$ nm).

2.2 Experimental methods

2.2.1 Multiple particle tracking microrheology

2.2.1.1 Necessary conditions

The choice of the proper colloidal probe is essential to a microrheology experiments, as there are four requirements that need to be considered: (1) The Stokes continuum assumption in calculating the hydrodynamic drag force on the particles (see Eq. 1.1 on pg. 13) requires that the probe size be much greater than the characteristic length scale of the material, (2) the probe particles are not interacting with the material and (3) the wall, and (4) the addition of the probe particles does not affect the interactions within the material itself.

- **Stokes continuum assumption:** The Stokes component of the Stokes-Einstein relation can be satisfied by using probes that are much bigger than the characteristic length scale of the material. With the radius of gyration of mAbs $R_g \sim$ 10 nm, 1 μm size probes are used to satisfy the continuum assumption in the Stokes equation (Fig. 2.3).
- **Probe-material interaction:** If the probes are aggregating, the tracking algorithm cannot be used, so aggregation needs to be mitigated before the viscosity can be measured. Thus, a PEG layer is grafted onto the probe surface using carbodiimide crosslinker chemistry to prevent interaction between protein and probe particles (see Sec. 2.1.1.1). The discussion on probe stability is detailed in Chapter 3.

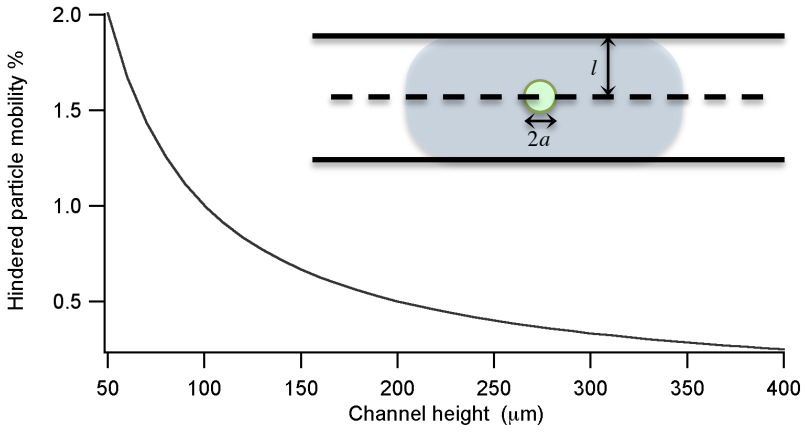

Figure 2.4: Faxén's solution for 1 μm particles to calculate the error tolerance as a function of channel height.

- **Probe-wall interaction:** In a microfluidic channel, the particle mobility is hindered by the wall. For a sphere halfway between two walls, Faxén [5] has solved analytically the percentage of hindered particle motions as

$$\frac{M_h}{M} = \frac{1}{1 - 1.004\left(\frac{a}{l}\right) + 0.418\left(\frac{a}{l}\right)^3 + 0.21\left(\frac{a}{l}\right)^4 - 0.169\left(\frac{a}{l}\right)^5} \tag{2.2}$$

  In Fig. 2.4 we show the percentage of hindered 1 μm particles as a function of channel height in μm [5–7]. For the 1 μm diameter probe, the channel height needs to be at least 100 μm for a 1% error tolerance in probe mobility. In the experiments, the actual channel height is 125 μm to ensure that this source of error is not significant.

- **Change in material after probe addition:** Proteins in solution can sometimes be unstable even in the presence of benign surfaces such as stainless steel used in fill-finish processing steps [8]. The addition of the probes used in microrheology increases the free surface area available for protein-surface interactions, and may induce protein aggregation. DLS experiments should always be performed to examine the size of the antibodies before and after the addition of the probes (see Chapter 3 for examples of DLS checks).

2.2.1.2 Microrheology sample preparation

Once the probe particles are carefully prepared (see Section 2.1.1) and chosen, a small volume (0.2 μL) of approximately 10% w/v probe particles is dispersed in a

20 μL sample. The final particle concentration is approximately 0.1% w/v, and this concentration range is used to prevent brightness saturation in the camera and to obtain 80-100 particles in the plane of view for good particle tracking statistics.

The samples are then loaded by capillary action into capillary tubes (Vitrocom, Inc., 0.2 $\times$ 2.0 mm inner diameter) or microfluidic sticker channels (Section 2.2.2), fixed to microscope slides, and sealed with NOA 81 (Norland Products, Cranbury, NJ). Probe particles are imaged with a 40$\times$ objective (EC Plan-Neofluar, NA 0.75, Carl Zeiss) and an inverted microscope (Axiovert 200, Carl Zeiss). This objective is selected due to its ability to magnify the probe particles sufficiently while retaining an adequate number of pixels to achieve the Gaussian illumination profile necessary for particle tracking ($\geq$ 4 pixels/μm) [9]. A CMOS high-speed camera (Phantom v5.1, 1024 $\times$ 1024 pixels, Vision Research, Wayne, NJ) is used to record videos of the particles in the two dimensional focal plane at a shutter time σ between 1 ms to 5 ms and at acquisition rate f = 30 or 50 frames per second. These settings are selected to minimize static and dynamic error of the particle tracking measurement [10].

2.2.1.3 Brightness weighted centroid algorithm

The brightness-weighted centroid algorithm [9] enables multiple particle tracking experiments. The IDL code is maintained by Crocker and Weeks [11], and the MATLAB code is available through Blair and Dufresne [12] and Kilfoil [13]. This algorithm rigorously eliminates sources of error to generate trajectories from a stack of images, an example of which is shown in Fig. 2.5A, with circles highlighting tracked particles. The following steps are used to transform the raw images into particle trajectories: restoration of the image, location of the particles, refining of particle positions, identification of particles from noise and measuring particle depth, and linking particle positions into trajectories.

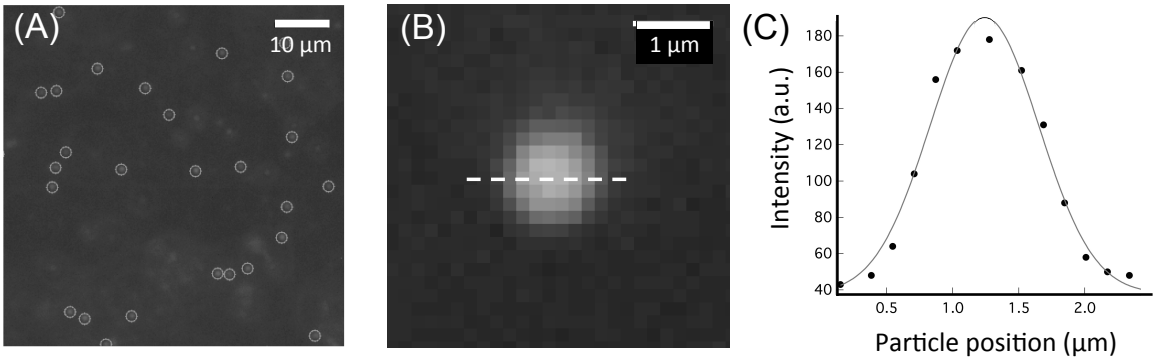

Figure 2.5: Identification of probe particles to track using multiple particle tracking microrheology. (A) Fluorescence image of a single frame of probe particles, with circles identify particles that are tracked and are centered around their brightness-weighted centroid. (B) An image of a single particle enlarged to show the Gaussian illumination profile. (C) Brightness profile of a probe particle.

2.2.1.3.1 Image restoration

Distortions inherent to the camera setup, including the background, digitization noise, and image mask must first be removed. These lead to errors in the particle trajectories unless steps are taken to remove them. Nonuniform contrast in the background arises from differences in sensitivity of the camera's pixels, as well as uneven illumination from the light source. Because the particles are small and well separated in a colloidal sample, the background can be easily subtracted using a boxcar average over $2w + 1$, where w is the tracking parameter, a user-selected integer chosen to be larger than the radius of the particles, but smaller than the separation distance between particles. Each pixel is given a new intensity

$$I_w(x, y) = \frac{1}{(2w+1)^2} \sum_{i,j=-w}^{w} I(x+i, y+j) \tag{2.3}$$

Random noise due to digitization of the image is reduced by averaging the values of nearby pixels. This is accounted for using a Gaussian function of half width of $\lambda_n = 1$

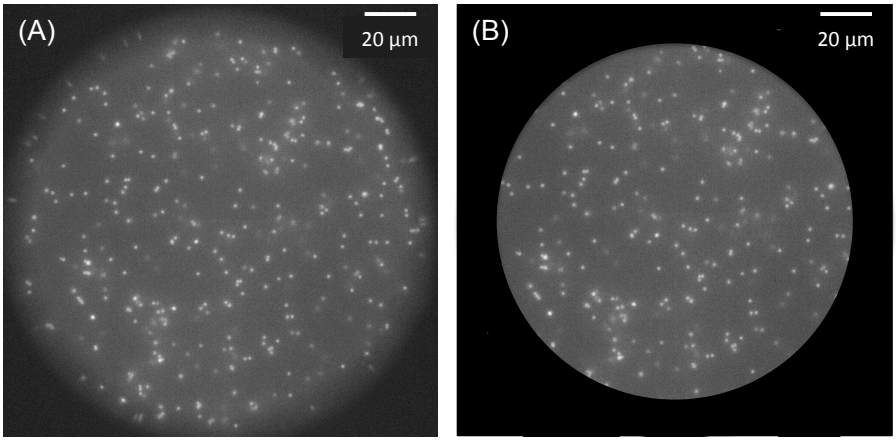

Figure 2.6: (A) A raw image of 1 μm particles in water. (B) A black mask over the image in A.

pixel, and over the range of the tracking parameter w,

$$I_{\lambda_n}(x,y) = \frac{\sum_{i,j=-w}^{w} I(x+i, y+j)\exp(-\frac{i^2+j^2}{4{\lambda_n}^2})}{[\sum_{i=-w}^{w}\exp(-i^2/4{\lambda_n}^2)]^2} \tag{2.4}$$

The corrected image is computed by subtracting I_{λ_n} from I_w [9]. Finally, the data collected by the camera is restricted to a circular field of view by the microscope (Fig. 2.6A). Data near the edge of the field of view is distorted as particles images are stretched, so a black mask (Fig. 2.6B) covers the edges of the image to restrict the particle tracking to undistorted particles.

2.2.1.3.2 Locating and refining particle positions

Initial guesses for particle locations are identified by comparing the brightness of a pixel with its neighbors; particle centers are approximately located at pixels in the top 20% of the image brightness. Of these pixels, those with local maxima in brightness are identified by checking the brightness of all the neighboring pixels [9]. These initial guesses are refined by calculating the centroid of the brightness profile of the particle to within 0.1 pixels [9]. The offset between the brightest pixel location (x, y) and the

geometric center of the particle (x_0, y_0) is calculated using

$$\begin{bmatrix} \epsilon_x \\ \epsilon_y \end{bmatrix} = \frac{1}{m_0} \sum_{i^2+j^2 \leq w^2} \begin{bmatrix} i \\ j \end{bmatrix} I(x+i, y+j) \tag{2.5}$$

where m_0 is the first moment of the particle brightness, $m_0 = \sum_{i^2+j^2 \leq w^2} I(x+i, y+j)$. The final location is calculated as $(x_0, y_0) = (x + \epsilon_x, y + \epsilon_y)$ [9].

2.2.1.3.3 Separation of particles from noise

As the particle position is being refined using Eq. 2.5, the brightness moment m_0 is already being calculated. The moment m_2 is given by

$$m_2 = \frac{1}{m_0} \sum_{i^2+j^2 \leq w^2} (i^2 + j^2) I(x+i, y+j) \tag{2.6}$$

In the (m_0, m_2) plane, colloidal particles cluster together, while aggregates or other noise appear outside this cluster, enabling rejection of the noise [9]. An example of a tracked particle and its corresponding Gaussian illumination profile is shown in Fig. 2.5B-C.

2.2.1.3.4 Tracking vertical depth

The distribution of particles in the m_0 and m_2 plane is also affected by the depth of the particles, causing the brightness of particles to vary. Crocker and Grier performed calibration experiments with single-layer samples of colloidal suspensions confined between parallel glass walls, with a microscope stage mobile in the z direction. The resulting distributions of (m_0, m_2) from known z can be used in estimating z for other particles using

$$z = \sum_i P(z_i | m_0, m_2) z_i. \tag{2.7}$$

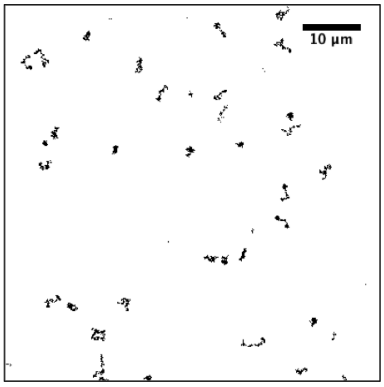

Figure 2.7: Trajectories of 1 μm particles diffusing in water, corresponding to the particles shown in Fig. 2.5A.

2.2.1.3.5 Linking locations into trajectories

Finally, the individual particle locations must be connected together to form trajectories for analysis. This involves estimating the likelihood that a particle in a subsequent frame is the same particle as one in the previous frame, taking into account Brownian motion of the colloidal particles [9]. The probability distribution of N non-interacting spherical particles diffusing a distance δ in time τ is given by

$$P(\{\delta_i\}|\ \tau) = \left(\frac{1}{4\pi D\tau}\right)^N \exp\left(-\sum_{i=1}^{N}\frac{\delta_i^2}{4D\tau}\right) \tag{2.8}$$

The most likely assignment of particle labels is the one that maximizes Eq. 2.8. Generally, maximizing this function would require $\mathcal{O}(N!)$ computations, but considerable savings can be realized by only considering particles within a particular length scale L [9]. This enables calculation of individual particle trajectories, as shown in Fig. 2.7 from the particles shown in Fig. 2.5A.

2.2.1.4 Particle tracking analysis

After particle trajectories have been calculated, the mean-squared displacement (MSD), $\langle \Delta x(\tau)^2 \rangle$, is calculated across a range of τ. The MSD is related to the material

property by

$$\langle \Delta x(\tau)^2 \rangle = 2D\tau \tag{2.9}$$

The diffusion coefficient D is

$$D = k_B T / 6\pi a \eta \tag{2.10}$$

where $k_B T$ is the thermal energy, a is the radius of the probe particle, and η is the viscosity of the material.

The logarithmic slope of the MSD, $d \ln\langle \Delta x(\tau)^2 \rangle / d \ln \tau$, enables characterization of the state of the material. When the MSD has a logarithmic slope of 1, the fluid is Newtonian. A MSD with a logarithmic slope greater than 0 but less than 1 indicates a viscoelastic fluid. A logarithmic slope of zero indicates that the particle is immobile and that a gel has formed. Motion is still detected due to the noise floor of the camera setup, which is described at length in Chapter 4. Logarithmic slopes > 1 are encountered when a sample is drifting or dominated by dynamic error (discussed below), or in the rare cases of super-diffusive particles, such as in tracking of motile bacteria [14].

2.2.1.5 Static and dynamic error

Savin and Doyle [10] analyzed the sources and impact of static and dynamic error. Static error arises from random noise in the experimental setup, and creates a deviation in the image particle position $x(t)$ from the true particle position $\hat{x}(t)$ by a random error $\chi(t)$

$$\hat{x}(t) = x(t) + \chi(t) \tag{2.11}$$

Strategies for reducing static error, and a new method for measuring it in situ, are presented in Chapter 4.

Dynamic error is a result of the shutter speed of the camera system required to measure the particle positions. During the finite time in which the shutter is open, the particles continue to diffuse, introducing a source of error which is dependent on the properties of the fluid. Savin and Doyle [10] developed models and corrections

for dynamic error in fluids with known properties. For Newtonian fluids of unknown properties, a calibration of the equipment and shutter speed on a known fluid can ensure that static and dynamic error are minimized or cancel each other.

Increasing the shutter time will increase dynamic error, while decreasing the shutter time reduces the dynamic error. Long exposure times create the most significant deviations in the MSD at short lag times. Larsen conducted a study with glycerine solutions on our equipment, varying the shutter time from 10 ms to 100 ms [15]. The dynamic error is found to be minimized near 10 ms, so all multiple particle tracking data collected at the University of Delaware are acquired at 30–50 frames per second and 10–20 ms shutter time to ensure minimization of these errors (unless otherwise noted). Experiments at Genentech in South San Francisco are performed on different equipment, so additional experiments establish the operating parameters of 30 frames per second and 10 ms shutter time.

2.2.1.6 Drift correction

If particles are translating across the field of view, a logarithmic slope greater than one, even approaching two, is observed. For samples with small amounts of drift (excessive drift occurs from leaky samples, which are discarded in exchange for new samples), a detrending algorithm is used to correct the trajectories [13]. The total change in the x and y coordinates are monitored over time, and any net change is subtracted from the particle trajectories using linear interpolation [16]. This is a subtle correction, as seen in Figure 2.7, where uncorrected and corrected trajectories are plotted together.

2.2.1.7 Application notes

While actually doing a particle tracking experiment, there are things that might go wrong. Take note of the following best practices:

- **Drift:** If the sample is not sealed correctly, and your eyes *alone* can detect the superdiffusion in the probes, the sample cannot be used. The drift correction algorithm will not correct severe drift. One way to try to correct this error would

be to measure the displacement of the probe particles from one image to another and divide it by the time step; the approximate velocity at which the probes are traveling can be estimated. However, this is extremely time-consuming and is not very reliable.

- **Bump:** Avoid touching or bumping into the air table as the video is being taken. If this happens, the data will show an artificial jump on the time scale of ∼1 s. The data at that lag time is not usable.
- **Occasional, random probes that are bigger than the rest of the population:** This is likely polydispersity from the manufacturing of the particles.
- **Occasional, small clumps of particles:** Always check for probe stability after washing procedures, prior to using probes in scarce samples. If small clumps of particles persist throughout the sample, then the sample's environment is causing the aggregation. (See Chapter 3 for more details.)
- **Non-uniform mixing of probes, resulting in non-uniform background fluorescence:** If this is not due to heterogeneity in the sample material itself, check for other areas in the sample for imaging. If microheterogeneity persists throughout sample, see Valentine et al. [17] for F-test analysis.
- **Probes not moving locally:** Check the imaging plane to make sure this is not the glass slide. Probe particles can get stuck on glass slide.
- **Probes not bright enough:** Adjust light intensity filter. If light intensity is at 100%, consider using probes with brighter fluorescence (ex. Alexa dye), especially in materials that are opaque.

2.2.2 Microfluidic sticker

2.2.2.1 Stamp fabrication using soft photolithography

Polydimethylsiloxane (PDMS) is used as the master stamp for the basis of the microfluidic sticker in the next section. PDMS stamp fabrication is fast and efficient, and has been a staple in the microfluidics literature since 1998 [18].

To start up the photolithography process, the spin speed and exposure dosage have to be optimized for the desired feature size and height. A negative epoxy resist SU-8 2035 (Microchem) is used for the fabrication of all master PDMS stamps. A standard ramp program is chosen: ramp to 500 rpm at 100 rpm/s, accelerate to final speed at 300 rpm/s, and finally, hold at final speed for 30 s. The resist film is then

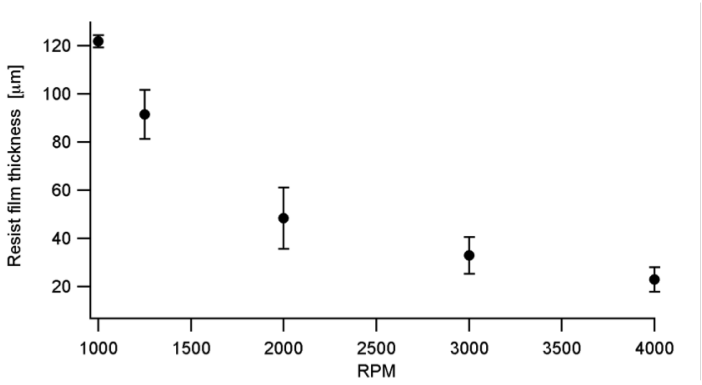

Figure 2.8: SU-8 2035 spin speed optimization.

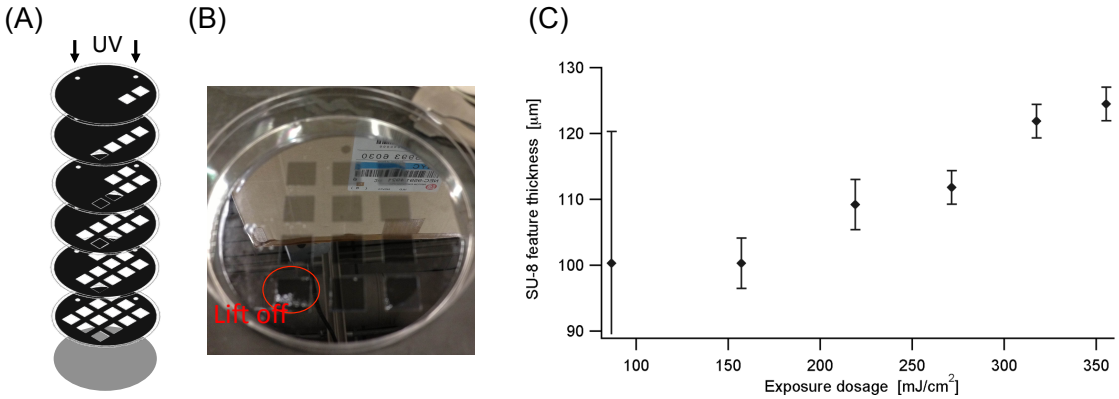

Figure 2.9: (A) Schematic of the stack of masks with square designs. (B) Image of silicon wafer after exposure optimization. (C) Feature height as a function of exposure dosage (mJ/cm^2).

solidified by heating on hot plate at 95°C for 80 minutes. The resulting film thickness is measured using a micrometer and is shown in Fig. 2.8.

For the exposure dosage optimization, a series of square features are made as a mask design. A stack of 6 masks with increasing amount of squares are stacked together, so that the top two squares are the most exposed and the last two squares are the least exposed (Fig. 2.9A-B). The channel designs are drawn in Adobe Illustrator and printed on Mylar at 10k DPI resolution (Fineline Imaging). The exposure dosage is measured using a UV power meter (365 nm) (Oai Instruments); the dosage through a dark mask and a clear mask is measured to calibrate the total exposure dosage. The resulting feature thickness as a function of exposure dosage is shown in Fig. 2.9C.

The pattern is made on a silicon wafer. The wafer is only to be handled with handling tweezers (TDI International, wafer handlers 4WL-SA & 45WF-SA, and flat tip tweezer 34A-SA). The wafer is first pretreated with a soak in acetone for 10 minutes, followed by a rinse with isopropyl alcohol (IPA), and dried with nitrogen gas. The wafer is then dried in a 120°C oven for 10 mins, and allowed to cool for 10 mins. A pre-cleaned petri dish is used to temporary storage and transport of the wafer.

To begin patterning the wafer with photoresist, preheat two hot plates at 65°C and 95°C, and turn on the ultraviolet flood lamp (Spectronics Corp., 365 nm, 120 V, 1.05 Amps). The wafer is centered on the spin coater. The SU-8 photoresist is spin-coated onto the wafer (pour ∼1 mL of SU-8 per inch of wafer diameter); the spin speed should be optimized to the desired feature height (Fig. 2.8). After the spin coating is completed, the resist film is soft baked first at 65°C, then at 95°C, according to Table 2.2. Before UV exposure, SU-8 can be cleaned off with repeated wash of acetone and IPA.

The ink side of the patterned mask should be placed on the wafer. The exposure time and dosage should follow Fig. 2.9. After UV exposure, the mask should be removed, and the wafer is baked at 95°C (Table 2.2). The photoresist is then developed with a SU-8 developer (Microchem) in a petri dish; the time for the development is dependent on the feature height, according to Table 2.3. The developed image should

Table 2.2: Bake times needed as a function of feature thickness.

Thickness (μm)	Soft bake times (mins)		Post exposure bake (min)
	65°C	95°C	95°C
25–40	0–3	5–6	5–6
45–80	0–3	6–9	6–7
85–110	5	10–20	8–10
115–150	5	20–30	10–12
160–225	7	30–45	12–15

Table 2.3: Development time needed as a function of feature thickness.

Thickness (μm)	Development time (min)
25–40	4–5
45–80	5–7
85–110	7–10
115–150	10–15
160–225	15–17

become clearer. At the end of the development time, spray wash the developed wafer with fresh developer solution for 10s, followed by IPA for 10 s. If a white streak occurs, the development is not completed; rinse with developer solution to remove the white film, and return to the developer bath. A post-develop bake (hard bake) is advised at 120°C for 5–10 mins. The pattern is complete at this point, and is ready for PDMS pour.

PDMS (Dow Corning, Sylgard 184) is used as received. The cross-linking agent and silicone elastomer base are mixed at a ratio of 1:10 by weight. The PDMS is degassed under vacuum, and then poured over the patterned wafer and cured for 4 hours at 65°C in a vacuum oven. This PDMS "master stamp" is released from the wafer and cut to fit a regular glass slide size (75 × 25 mm).

2.2.2.2 Microfluidic sticker fabrication

Microfluidic stickers are fabricated to produce multiple sample channels on a single microscope slide, as shown in Fig. 5.1. Each channel holds a volume of approximately 2 μL. The microfluidic stickers are made following the procedures of [19] and [20], using soft imprint lithography. A drop of ultraviolet-cured thiolene resin (NOA 81, Norland Products, Cranbury, NJ) is placed on a flat substrate made with polyethylene (PE) and polydimethylsiloxane (PDMS). A structured PDMS mold, made with traditional photolithography techniques, is gently pressed onto the thiolene drop with the help of a roller. Oxygen inhibits the photocuring reaction, and the polymers were selected based on their permeability to allow a two-step peeling process and greater control and maneuverability of the microfluidic sticker. The permeability of polyethylene is $\sim 10^{-3}$ less than that of PDMS, and after the first curing step the sticker preferentially attaches to the substrate rather than the channel mold. The substrate (with channel sticker) is then placed on a cover slip (25 $\times$ 75 $\times$ 0.15 mm, Fisher Scientific), where the thiolene resin completely cures. The substrate is then peeled off, leaving the microfluidic sticker on the microscope slide.

One requirement for MPT is that the probe motion is due solely to thermal forces and the local drag of the fluid. Other interactions, such as hydrodynamic interactions with the sample walls, should be minimized. Using Faxén's solution for the mobility of a sphere halfway between two walls (Sec. 2.2.1.1) [5–7], we calculate the minimum channel height needs to be at least 100 μm for 1% error tolerance in particle mobility. In designing the channel, its height is set at 125 μm to ensure this source of error is insignificant.

A typical microfluidic sticker is shown in Fig. 2.10; a total of 10 channels are on the sticker, and each channel is 0.35 $\times$ 30 $\times$ 0.125 mm, or approximately 2 μL in volume. A dense network of pillars surrounds the channel pattern (shown in gray scale for clarity); the porous pillar structure enhances the local curvature of the liquid meniscus, increases the Laplace pressure, and speeds up the capillary spreading of the resin.

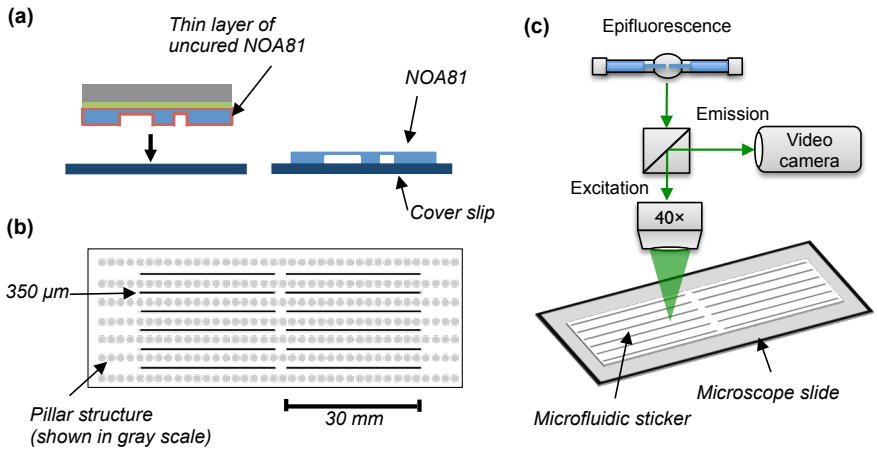

Figure 2.10: The design of microfluidic stickers used as sample chambers. (a) Microfluidic channels made of thiolene resin are sealed by a cover slip. (b) The design of microfluidic sticker. The channels are 0.35 × 30 × 0.125 mm and contain 2 μL of solution. (c) A schematic representation of the experimental microrheology setup.

2.2.3 Sample temperature control on microscope

2.2.3.1 Equipment setup

The temperature control unit (Fig. 2.11) is built with a thermoelectric (Peltier) module with lapped ceramic faces (50 × 50 × 5.2 mm, $T_{\max}$ = 200°C, $DT_{\max}$ = 68°C, Custom Thermoelectric, Bishopville, MD). The Peltier module is sealed between an aluminum contact plate (3 × 3 × 0.25 inch, Custom Thermoelectric) and a copper heat sink maintained at 12°C (3 × 3 × 0.85 inch, Custom Thermoelectric). The Peltier module is controlled by a PID controller (TC-48-20, TE Technology Inc., Traverse City, MI) that is powered by a DC power supply (PS-12-8.4A, output voltage = 12 V, max output current = 8.4 A, TE Technology Inc.). A thermistor sensor (15K Ω at 25°C, temperature range -20°C to 100°C, TE Technology Inc.) on the side of the contact plate measures the temperature on the stage (and in the samples, assuming steady state temperature equilibration).

A LabVIEW program records the calibrated PID parameters and the real-time thermistor temperature. A stream of dry air (22°C and 13% relative humidity) blows

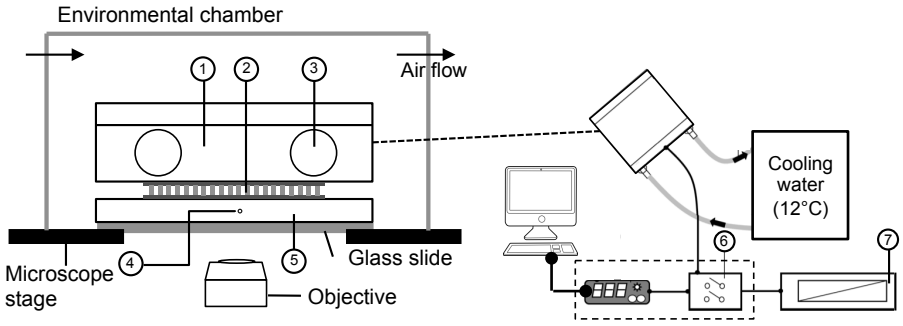

Figure 2.11: Schematic of temperature control setup. The components are: 1. copper cooling body, 2. Peltier module, 3. water circulation inlet/outlet, 4. thermistor hole, 5. aluminum contact plate, 6. PID controller with relay unit, 7. DC power.

across an environmental chamber and above the microscope stage to control the local humidity and eliminate condensation at low temperatures. The entire unit is clamped on the microscope stage to minimize vibrations from the circulating water bath. No vibrations are detected by tracking probes embedded inside a stiff gel sample. An example transient temperature ramp program is shown in Fig. 2.12. A 5°C step change is applied to change the temperature in cooling mode; in contrast, five continuous 1°C step changes are used in the heating mode to prevent temperature overshoot. The measured temperature typically reaches each set point (T_{set}) within 2 minutes.

In the experimental setup, the bottleneck lies in the time to reach thermal steady state for the samples. We first investigate the thermal performance of the Peltier module. On average, it takes approximately 40-60 seconds for the Peltier to change temperature by 1°C (Fig. 2.12). The temperature is measured from a thermistor inside the aluminum block and is not in sample materials. However, the heat transfer time in the aluminum block should be negligible, since its thermal diffusivity is $\alpha = 85\text{mm}^2/\text{s}$.

To verify that the sample reaches thermal equilibrium with the aluminum block, we developed a heat transfer model of the system in its exact dimensions. We start with the time dependent heat transfer PDE in one dimension for a solid with thermal

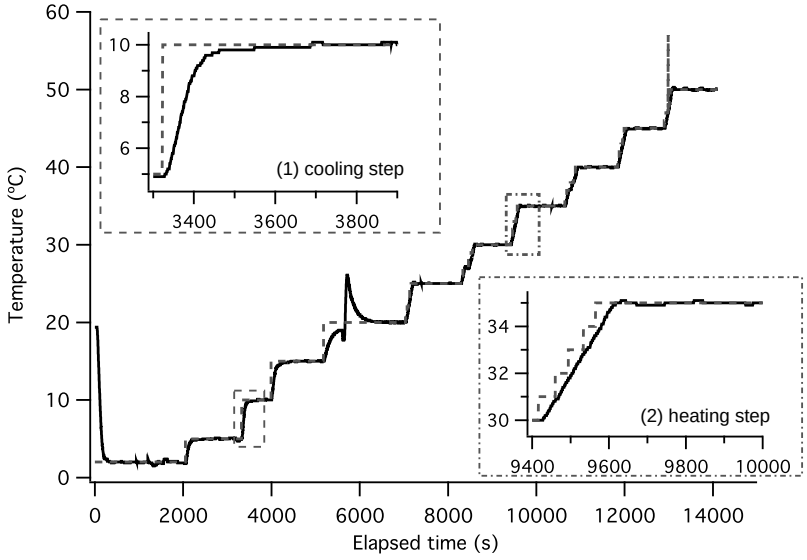

Figure 2.12: Transient temperature ramp; dashed line indicates set point temperature, and solid line shows temperature measured from thermistor in aluminum block. Inset (1) shows an example cooling step and inset (2) shows an example heating step. Note that incremental steps in the heating mode to prevent temperature overshoot. The spike at ∼5500 s occurred when the polarity of the Peltier module is switched.

diffusivity α and no generation term,

$$\frac{\partial T}{\partial t} = \alpha_i \frac{\delta^2 T}{\delta x^2}. \tag{2.12}$$

Taking the Laplace transform of each side,

$$s\tau(x,s) - T(x,0) = \alpha_i \frac{\delta^2 \tau(x,s)}{\delta x^2} \tag{2.13}$$

the PDE is transformed into an ODE of $\tau(x,s)$. Assuming all materials begin at an initial temperature of 298 K, we set this as T_{ref}, $T(x,0) = 0$. Henceforth, T refers to temperature difference; a negative T is cooler than T_{ref} and a positive T is warmer than T_{ref}. Applying this initial condition, we now have the ODE

$$s\tau(x,s) = \alpha_i \frac{\delta^2 \tau(x,s)}{\delta x^2}. \tag{2.14}$$

This ODE has the general solution

$$\tau(x,s) = A(s)e^{-\frac{\sqrt{s}}{\sqrt{\alpha_i}}x} + B(s)e^{-\frac{\sqrt{s}}{\sqrt{\alpha_i}}x} \tag{2.15}$$

where $A(s)$ and $B(s)$ are prefactors. Each material (aluminum, glass, thiolene) obeys this ODE in each respective domain; $0 < x < L_1$ refers to the aluminum contact plate (L_1 is half the thickness of aluminum plate), $L_1 < x < L_2$ to the glass cover slip, and $L_2 < x < L_3$ to the thiolene sticker. At t = 0 s, the thermistor (x = 0) has already detected the set point temperature; the temperature and flux are equal at the material boundaries, and at the interface with dry air, there is convective heat transfer.

The set of ODEs are solved numerically using the geometry of our temperature control module using COMSOL. The time-dependent temperature profile is shown in Fig. 2.13. At the extremes of cooling (15°C) and heating mode (40°C), the simulation results confirm that as the core of aluminum contact plate (the location of thermistor) reaches T_{set}, the temperature in the thiolene microfluidic sticker equilibrates within 1

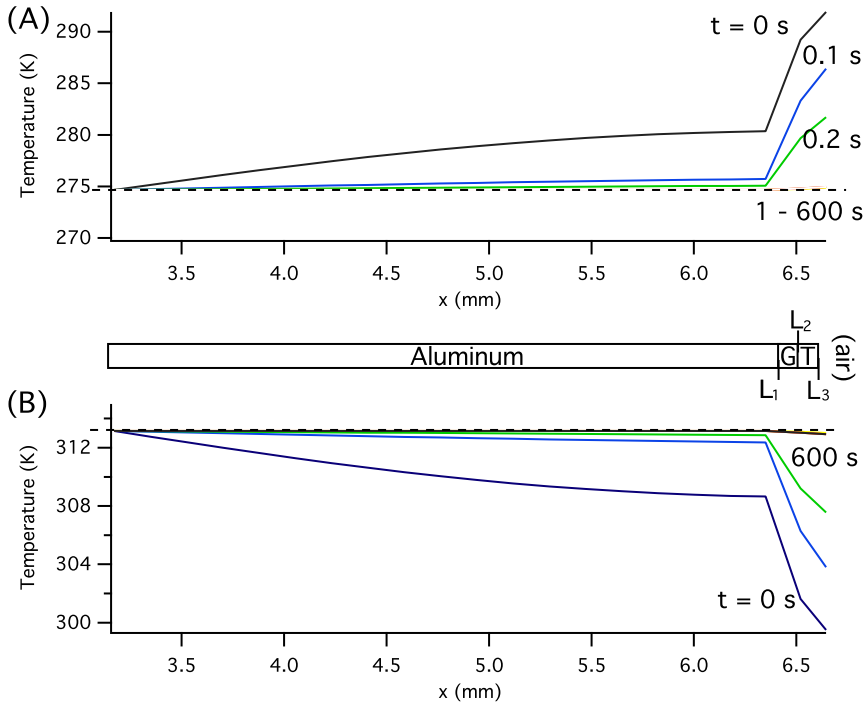

Figure 2.13: Heat transfer model in exact dimensions solved with COMSOL; module geometry is shown in the middle. $L_1 = 0.125$ in (half thickness of aluminum), $L_2 = 150$ μm (glass), and $L_3 = 125$ μm (thiolene microfluidic sticker). Dry air is at $L > L_3$. Dash line indicates set point temperature, and $T_{ref} = 298$ K. (A) $T_{set} = 274.7$ K (cooling mode): once the thermistor in aluminum contact plate measures T_{set}, the sample in the microfluidic channel achieves temperature equilibrium rapidly within 1 s. (B) $T_{set} = 313.15$ K (heating mode).

s, and there are no discernible temperature differences between 1 s and 600 s. This shows that the temperature control bottleneck lies in the response of the Peltier module to the PID controller. To account for differences in sample composition, the variable speed at which dry air blows across the stage and also any 2-dimensional heat transfer effects (though we expect none), microrheology measurements are taken 7-10 minutes after T_{set} is registered to ensure equilibration across samples in the microfluidic sticker.

2.2.3.2 Temperature control validation and calibration

Heat transfer effects may result in the sample temperature being inconsistent with the temperature of the Peltier. While a second thermistor at another location on the Peltier can verify the temperature control, it cannot measure the actual temperature of the sample. In order to obtain an in situ temperature measurement, we introduce a calibration fluid in a channel on the same microfluidic device as the protein samples. A 55% sucrose solution is used as the calibration fluid because its viscosity range in the target temperature range is well within the operating regime of detectable viscosity without inducing significant static error at short lag times [21]. It is also aqueous, making temperature equilibration time comparable to aqueous protein samples. In Fig. 2.14A the ensemble averaged mean squared displacement (MSD) is plotted as a function of lag time τ for 55% sucrose solution at 9 set point temperatures, T_{set}, from 5°C to 45°C. The probe displacements are all above the noise floor measured from particles trapped in a gel, and the logarithmic slopes of 1 of the MSDs show that the sucrose solution is a Newtonian fluid, as expected.

Given a measured mean-squared displacement, the true temperature of the sample can be calculated by rearranging Eq. 2.10 to $T = 3\pi a\eta\langle\Delta x^2\rangle/k\tau$. However, since viscosity η is also a function of temperature, the temperature of the sample cannot be directly calculated from the measured MSD. Instead, a calibration curve is used to correlate the MSD (the measured parameter) and temperature (the desired parameter) of sucrose solution. Taking the tabulated viscosity data of 55% sucrose [22], the expected MSD at $\tau = 0.5$ s is calculated using the Stokes-Einstein-Sutherland relation

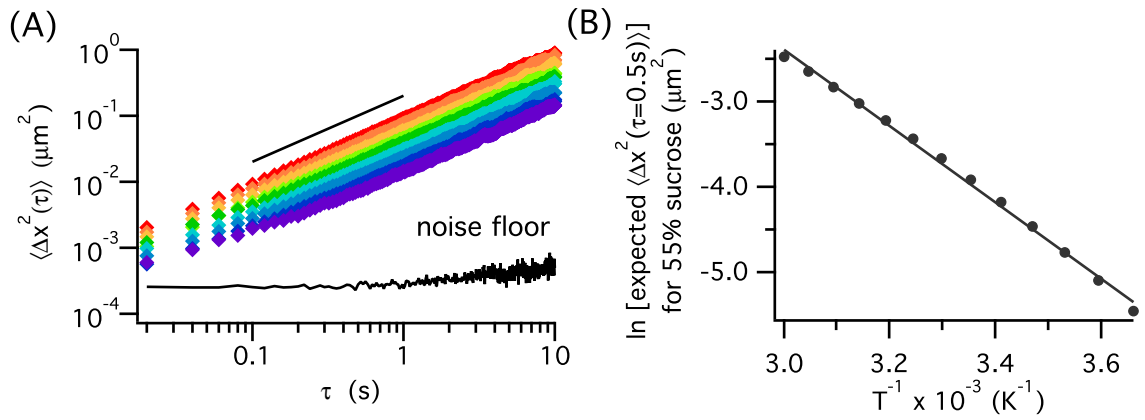

Figure 2.14: Temperature control stage validation. (A) Mean squared displacements of 55% sucrose solution at 9 set point temperatures (T_{set} = 5 – 45°C). Black line indicates a logarithmic slope of 1. (B) Calibration curve of temperature as a function of the expected MSD (τ = 0.5s) of 55% sucrose solution from tabulated data [22] and its Arrhenius fit.

(Eq. 2.10) from 273.15 K to 333.15 K in 5 K increments and plotted in Fig. 2.14B. The linearized Arrhenius equation

$$\ln(\langle \Delta x^2(\tau = 0.5s) \rangle) = \ln A + \frac{-E_a}{R} \frac{1}{T_{\text{MSD}}} \tag{2.16}$$

is used as a calibration curve to back calculate temperature based on MSD, with parameters $\ln A = 11.1 \pm 0.568$ and $-E_a/R = -4490 \pm 171$ at 95% confidence interval, and a a chi-square goodness of fit test of $\chi^2 = 0.036$. The simple two-parameter Arrhenius model is chosen because it works well for 55% sucrose in this range of temperature, with the extracted activation energy $E_a = 37.3 \pm 1.4$ kJ/mol in close agreement with the published value [23]. However, for calibration fluids that exhibit super-Arrhenius behavior at a wider temperature range, other viscosity models (e.g. Vogel-Fulcher-Tammann equation [24–26], Williams-Landel-Ferry equation [27], Avramov-Milchev equation [28], etc.) are needed. Longinotti and Corti [29] and Mauro *et al.* [30] discussed the different viscosity models for sucrose and glass-forming liquids extensively.

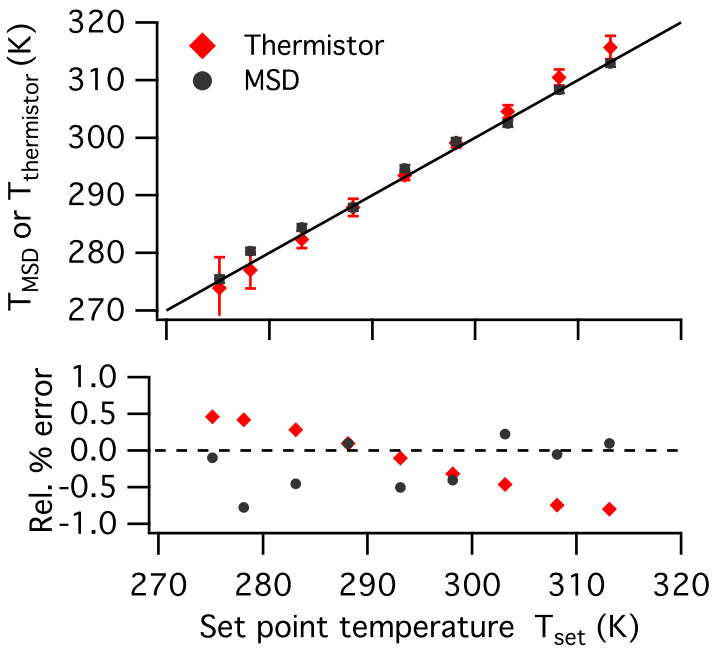

Figure 2.15: Comparison of the measured temperatures from MSD and thermistor, T_{MSD} and $T_{\mathrm{thermistor}}$, to the set point temperature T_{set}. The solid line (top) is a parity line, and the dashed line (bottom) indicates 0% error.The error bars for T_{MSD} come from error propagation from particle tracking and Arrhenius fit, and the error bars for $T_{\mathrm{thermistor}}$ come from the temperature fluctuations during the 30-second measurements.

In developing the calibration curve with the Arrhenius equation, the specific lag time τ for the MSD used in the equation depends on the viscosity of the chosen calibration fluid. We find that for 55% sucrose, $\tau = 0.5$ s balances between minimizing tracking error across all temperatures while maximizing the number of observed particle displacements.

The MSDs at $\tau = 0.5s$ of the sucrose solution at various temperatures from Fig. 2.14A are used in Eq. 2.16 to calculate T_{MSD}. A second thermistor secured on the edge of the contact plate using aluminum tape (not shown in Fig. 5.2) is also used to monitor the temperature of the samples, denoted as $T_{\mathrm{thermistor}}$. The thermistor measurements are taken at the same time as the video microscopy for 30 seconds.

Fig. 2.15 compares T_{MSD} and $T_{\text{thermistor}}$ to T_{set}, as well as the calculated relative error, defined as

$$\text{Relative temperature \% error} = \frac{T_{\text{set}} - T_i}{T_{\text{set}}} \cdot 100\%, \tag{2.17}$$

where i = MSD or thermistor. At room temperature (25 °C), there are negligible differences between the measured temperatures and set point temperature. However, at the extremes of the temperatures studied (i.e. T_{set} =5°C and 45 °C), $T_{\text{thermistor}}$ fluctuates more than T_{MSD}, with bigger absolute error bars. The relative error of $T_{\text{thermistor}}$ compared to T_{set} also shows a systematic error, decreasing steadily as set point temperature increases. The systematic error is likely due to the contact plate edge losing heat to its surroundings with the constant air flow. In contrast, T_{MSD} from the sucrose sample does not have a systematic error relative to T_{set}. Since the sucrose sample is embedded in the same microfluidic sticker as the protein samples, the temperature of the sucrose sample represents that of the samples, and T_{MSD} is used as the true temperature of the samples across the microfluidic sticker, corrected from T_{set}.

2.2.4 Rheology

2.2.4.1 Rotational rheometry

Protein solution viscosities are measured using a stress-controlled rheometer (AR-G2, TA Instruments, Newark, DE). A cone-and-plate geometry with a solvent trap is used due to the low sample viscosities, which are in an expected range of 0.9 $\times$ 10^{-3} - 15 $\times$ 10^{-3} Pa s, and evaporation rate. Measurements are made at shear rates from 100 - 1000 s^{-1}. The viscosity does not depend on shear rate over this range. The Pèclet number, $\text{Pe} = 6\pi a^3 \eta_0 \dot{\gamma}/kT$, which scales the shear rate by the characteristic relaxation time of the solution by the diffusion of the protein molecules, satisfies $\text{Pe} \ll 1$. This is consistent with the observation that *concentrated* protein solutions exhibit shear-thinning at shear rates above 1000 s^{-1} [31]. Therefore, the steady-state shear viscosity is estimated from the average over the range of shear rates.

Bulk rheology is performed using a steady shear method because the samples lacked the sufficient torque required for oscillatory measurements.

2.2.5 Light scattering

2.2.5.1 Dynamic light scattering

Dynamic light scattering measurements are performed in DAWN-HELEOS II with a QELS attachment (Wyatt Technologies, Santa Barbara, CA) to examine the size of the antibodies before and after the addition of the probes used in microrheology. The protein samples (50 μL) are mixed with either 0.5 μL Milli-Q water (sample "without probes") or 0.5 μL of 10% w/v PS-PEG (sample "with probes"). The samples are incubated for 10 minutes at 20°C, and then centrifuged for 2 minutes at 6000 G. The top 45 μL of the samples are removed from the centrifuge tube and used in the DLS experiments.

The autocorrelation function data are analyzed using non-linear regression to the cumulant expansion

$$g_2(t) = \alpha + \beta \exp(-2Q^2 D_0 t)\left(1 + \frac{\mu_2}{2!}t^2\right)^2, \tag{2.18}$$

where Q is the magnitude of the scattering vector

$$Q = \frac{4\pi n}{\lambda} \sin\left(\frac{\theta}{2}\right), \tag{2.19}$$

α is a short delay-time baseline constant, β is an instrument-specific constant, D_0 is the self-diffusion coefficient at dilute protein concentrations, n is the refractive index of solvent, λ is the laser wavelength at 658.9 nm, θ is the scattering angle at 96.7°, t is the decay time, and μ_2 is the second cumulant and related to the sample polydispersity index. The hydrodynamic radius of the protein molecules is calculated from the measured D_0 using the Stokes-Einstein relation

$$R_h = \frac{k_b T}{6\pi\eta D_0}. \tag{2.20}$$

2.2.5.2 Static light scattering

Static light scattering (SLS) experiments are conducted using a DAWN-HELEOS II Multi-Angle Light Scattering (Wyatt, Santa Barbara, CA) instrument (MALS) with laser wavelength of 658.9 nm with temperature maintained at 25°C to quantify protein-protein interactions (PPI). In SLS, the average scattered intensity at a given angle can be determined and used to calculate the excess Rayleigh scattering, R_{90}^{ex} , as previously reported [32, 33], by

$$\frac{R_{90}^{\text{ex}}}{K} = M_{\text{w,app}} c_2 - 2 M_w B_{22} {c_2}^2 \tag{2.21}$$

where $\frac{R_{90}^{\text{ex}}}{K}$ is the excess Rayleigh scattering, $M_{\text{w,app}}$ and M_w are the apparent and true molecular weight of the protein, c_2 is concentration of protein, and B_{22} is the osmotic second virial coefficient, a protein-protein interaction parameter. The osmotic second virial coefficient describes the deviation from ideality caused by PPI. In this instance, a positive and negative value of B_{22} correspond to repulsive and attractive interactions, respectively.

2.2.6 Size exclusion chromatography with short guard columns

The size exclusion chromatography (SEC) method uses a high-performance liquid chromatography (HPLC) guard column (4.6 mm inside diameter, 3.5 cm length) packed with 4 μm silica particles (TSKgel SuperSW3000, Tosoh Bioscience, #18762). The mobile phase is 0.1 M K_3PO_4/0.125 M KCl, pH 6.2. Flow rates are varied from 0.0625 to 2.0 mL/min. The column pressure is maintained below 75 bar and the column temperature is maintained at 25°C. The injection volume is 5.0 μL. Detection wavelengths of 214 and 280 nm are used. Freshly prepared mobile phases are equilibrated with the column for 30 min at a flow rate of 1.0 mL/min. A Waters Alliance HPLC System with an autosampler is used for all experiments.

2.2.7 Protein processing and characterization

2.2.7.1 Buffer exchange

The proteins are buffer-exchanged into the formulation buffer (20 mM histidine chloride, pH 6.0) using Slide-A-Lyzer dialysis cassettes (10k molecular weight cut off, #66385, Thermo Fisher Scientific). For every 1 mL sample, an ion exchange factor of $(2 \times 10^3)^3$ is used. The dialysis cassettes are placed in a 2 L beaker filled with the desired buffer, and stirred on magnetic stir plate gently at 80 rpm. The solutions are shielded from light and the buffer exchange takes place in a cold room (4°C).

2.2.7.2 Ultrafiltration

Amicon Ultra centrifugal filters (EMD Millipore) are used for ultrafiltration of the proteins. The centrifugal filter unit is first wetted and spun down. The protein solution is centrifuged at 2000 rpm for 10 minutes, with careful pipette mixing in between every spin.

2.2.7.3 Concentration determination

The protein concentrations are determined from the average of 5 measurements in Nanodrop 2000c (Thermo Fisher Scientific) at 1:10 dilution factor.

REFERENCES

[1] J. Y. Huh and E. M. Furst. Colloid dynamics in semiflexible polymer solutions. *Physical Review E*, 74(3), 2006.

[2] M. T. Valentine, Z. E. Perlman, M. L. Gardel, J. H. Shin, P. Matsudaira, T. J. Mitchison, and D. A. Weitz. Colloid Surface Chemistry Critically Affects Multiple Particle Tracking Measurements of Biomaterials. *Biophysical Journal*, 86(6):4004–4014, 2004.

[3] M. A. Kotlarchyk, E. L. Botvinick, and A. J. Putnam. Characterization of hydrogel microstructure using laser tweezers particle tracking and confocal reflection imaging. *Journal of Physics Condensed Matter*, 22(19):194121, 2010.

[4] R. S. Fischer, K. A. Myers, M. L. Gardel, and C. M. Waterman. Stiffness-controlled three-dimensional extracellular matrices for high-resolution imaging of cell behavior. *Nature Protocols*, 7(11):2056–2066, 2012.

[5] H. Faxén. Der Widerstand gegen die Bewegung einer starren Kugel in einer zähen Flüssigkeit, die zwischen zwei parallelen ebenen Wänden eingeschlossen ist. *Annalen der Physik*, 373(10):89–119, 1922.

[6] J. Happel and H. Brenner. *Low Reynolds Number Hydrodynamics: with special applications to particulate media*. Prentice-Hall, 1965.

[7] K. M. Schultz and E. M. Furst. High-throughput rheology in a microfluidic device. *Lab on a Chip*, 11(22):3802–3809, 2011.

[8] A. Nayak, J. Colandene, V. Bradford, and M. Perkins. Characterization of Subvisible Particle Formation During the Filling Pump Operation of a Monoclonal Antibody Solution. *Journal of Pharmaceutical Sciences*, 100(10):4198–4204, 2011.

[9] J. C. Crocker and D. G. Grier. Methods of digital video microscopy for colloidal studies. *Journal of Colloid and Interface Science*, 179(1):298–310, 1996.

[10] T. Savin and P. S. Doyle. Static and Dynamic Errors in Particle Tracking Microrheology. *Biophysical Journal*, 88(1):623–638, 2005.

[11] J. C. Crocker and E. R. Weeks. Particle tracking using IDL, 2007. URL http://www.physics.emory.edu/faculty/weeks//idl/tracking.html.

[12] D. Blair and E. Dufresne. The Matlab Particle Tracking Code Repository. *site.physics.georgetown.edu*.

[13] M. Kilfoil. Microrheology Dedrifting Tools. URL http://people.umass.edu/kilfoil/downloads.html.

[14] H. Kurtuldu, J. S. Guasto, K. A. Johnson, and J. P. Gollub. Enhancement of biomixing by swimming algal cells in two-dimensional films. *Proceedings of the National Academy of Sciences*, 108(26):10391–10395, 2011.

[15] T. H. Larsen. *Microrheology of responsive hydrogels*. PhD thesis, 2008.

[16] J. C. Crocker and B. D. Hoffman. Multiple-particle tracking and two-point microrheology in cells. *Methods in cell biology*, 83:141–178, 2007.

[17] M. T. Valentine, P. D. Kaplan, D. Thota, J. C. Crocker, T. Gisler, R. K. Prud'homme, M. Beck, and D. A. Weitz. Investigating the microenvironments of inhomogeneous soft materials with multiple particle tracking. *Physical Review E*, 64(6):061506, 2001.

[18] D. C. Duffy, J. C. McDonald, O. J. Schueller, and G. M. Whitesides. Rapid Prototyping of Microfluidic Systems in Poly(dimethylsiloxane). *Analytical Chemistry*, 70(23):4974–4984, 1998.

[19] D. Bartolo, G. Degre, P. Ngheb, and V. Studer. Microfluidic stickers. *Lab on a Chip*, 8:274–279, 2008.

[20] M. Natali, S. Begolo, T. Carofiglio, and G. Mistura. Rapid prototyping of multilayer thiolene microfluidic chips by photopolymerization and transfer lamination. *Lab on a Chip*, 8(3):492, 2008.

[21] K. M. Schultz and E. M. Furst. Microrheology of biomaterial hydrogelators. *Soft Matter*, 8(23):6198, 2012.

[22] J. F. Swindells, C. F. Snyder, R. C. Hardy, and P. E. Golden. Viscosities of sucrose solutions at various temperatures: Tables of recalculated values. Technical report, National Bureau of Standards, 1958.

[23] V. R. N. Telis, J. Telis-Romero, H. B. Mazzotti, and A. L. Gabas. Viscosity of Aqueous Carbohydrate Solutions at Different Temperatures and Concentrations. *International Journal of Food Properties*, 10(1):185–195, 2007.

[24] V. H. *Phys. Zeit*, 22:645, 1921.

[25] G. S. Fulcher. Analysis of recent measurements of the viscosity of glasses. *Journal of the American Ceramic Society*, 8(6):339–355, 1925.

[26] G. Tammann and W. Hesse. Die Abhängigkeit der Viscosität von der Temperatur bie unterkühlten Flüssigkeiten. *Zeitschrift für anorganische und allgemeine Chemie*, 156(1):245–257, 1926.

[27] M. L. Williams, R. F. Landel, and J. D. Ferry. The Temperature Dependence of Relaxation Mechanisms in Amorphous Polymers and Other Glass-forming Liquids. *Journal of the American Chemical Society*, 77(14):3701–3707, 1955.

[28] A. I and M. A. Effect of disorder on diffusion and viscosity in condensed systems. *J. Non-Cryst Solids*, 104:253–260, 1988.

[29] M. P. Longinotti and H. R. Corti. Viscosity of concentrated sucrose and trehalose aqueous solutions including the supercooled regime. *Journal of Physical and Chemical Reference Data*, 37(3):1503, 2008.

[30] J. C. Mauro, Y. Yue, A. J. Ellison, P. K. Gupta, and D. C. Allan. Viscosity of glass-forming liquids. *Proceedings of the National Academy of Sciences of the United States of America*, 106(47):19780–19784, 2009.

[31] I. E. Zarraga, R. Taing, J. Zarzar, J. Luoma, J. Hsiung, A. Patel, and F. J. Lim. High Shear Rheology and Anisotropy in Concentrated Solutions of Monoclonal Antibodies. *Journal of Pharmaceutical Sciences*, 102(8):2538–2549, 2013.

[32] M. A. Blanco, T. Perevozchikova, V. Martorana, M. Manno, and C. J. Roberts. Protein-protein interactions in dilute to concentrated solutions: α-chymotrypsinogen in acidic conditions. *Journal of Physical Chemistry B*, 118 (22):5817–5831, 2014.

[33] R. Ghosh, C. Calero-Rubio, A. Saluja, and C. J. Roberts. Relating Protein-Protein Interactions and Aggregation Rates From Low to High Concentrations. *Journal of Pharmaceutical Sciences*, 105(3):1086–1096, 2016.

Chapter 3

PARTICLE TRACKING MICRORHEOLOGY OF THERAPEUTIC PROTEIN SOLUTIONS

3.1 Introduction

This chapter provides a detailed discussion of the accuracy and precision of multiple particle tracking microrheology, a technique used extensively throughout this thesis.

This chapter will first briefly review particle tracking microrheology methods and describe the sample preparation. The stability of probe particles is then discussed, including its dependence on the probe particle surface chemistry. The stability of the proteins upon addition of the probes was verified using dynamic light scattering (DLS). To analyze the experiments, we develop the use of excess kurtosis and its test statistic Z_{α_2} to identify a lag time with a maximum number of independent probe displacement measurements and minimum tracking error. Microviscosity measurements of two monoclonal antibody solutions are compared to bulk rheometry, and we demonstrate the accuracy of particle tracking microrheology with analysis of covariance (ANCOVA). We conclude by discussing the uncertainty of viscosity measurements using particle tracking microrheology.

The dynamic light scattering measurements were conducted by Mahlet Woldeyes (co-advised by Eric M. Furst and Christopher J. Roberts) at the University of Delaware. Parts of this chapter were originally published in the *Journal of Rheology* in a paper titled "Particle tracking microrheology of protein solutions." Reprinted with permission from [1].

3.2 Experimental Methods

3.2.1 Materials

Fluids used in the experiments are ultra-pure water (Milli-Q, Millipore, resistivity = 18.2 M $\cdot\Omega$ cm), aqueous sucrose solution, and two humanized IgG1 monoclonal antibodies (mAb1 and mAb2 supplied by Genentech, South San Francisco, CA). The chemicals (sucrose, L-histidine, L-histidine monohydrochloride monohydrate and Tween 20) are used as received (Sigma-Aldrich). Stock protein solutions in 0.5 mL aliquots (up to 93.3 mg/ml) are stored at -80°C for several months, then thawed to room temperature (23 °C) for two hours. The protein solutions are diluted serially with 30 mM histidine buffer at pH 5.4, with 0.02% Tween 20, and are stored at 4°C prior to use for up to three months. The 30 mM histidine buffer is prepared and adjusted to pH 5.4 by combining 5 mM L-histidine free-base and 25 mM L-histidine-HCl.

One-micrometer diameter ($2a = 1.063 \pm 0.01$ μm) fluorescently labeled polystyrene (PS) particles (Polysciences, Wallingford, PA) and amine-modified PS particles ($2a = 0.97 \pm 0.022$ μm, Invitrogen Molecular Probes) are prepared by first washing them to remove excess fluorescent dye and possible contaminants from their manufacturing and storage. The PS particles are taken from stock solution (2.5% w/v) and are centrifuged for 6 minutes at 5000 G. The PS-amine particles are taken from the stock solution (2.0% w/v) and are centrifuged for 10 minutes at 5000 G. Centrifugation time depends on probe size and colloidal stability, and the washing procedures should be monitored carefully to prevent aggregation. The supernatant is discarded and particles are redispersed in the same volume of ultra-pure Milli-Q water. This washing procedure is repeated three times.

A third batch of probe particles is chemically grafted with poly(ethylene glycol) (PEG). PEG coating is expected to reduce protein adsorption on the particle surface [2–4]. PEG with N-hydroxysuccinimidyl ester end groups (mPEG-succinimidyl carboxyl methyl ester, MW=5000, Creative PEGWorks, Winston-Salem, NC) is dissolved in borate buffer (pH 8.5) at 200 mg/ml and mixed with amine-modified PS particles to react for 90 minutes. The probes are then washed with pure borate buffer three

times. The PS-PEG particles are observed under a microscope to verify that they do not aggregate in solution. Zeta potential measurements of PS-PEG particles in 1 mM NaCl (ZetaPALS, Malvern Instruments) give $\zeta = -30 \pm 2$ mV. The zeta potential of bare PS probes is $\zeta = -50 \pm 4$ mV.

The final stock concentrations of the probes are approximately 10% w/v, so only a small volume (0.2 μL) is added to each sample to minimize concentration changes. The probes are dispersed in 20 μL of solution, with the final particle concentrations ranging from 0.1 % w/v to 0.2% w/v. This range of particle concentration is used to prevent brightness saturation in the camera and to obtain approximately 100 particles in the plane of the fluorescence microscope for good particle tracking statistics.

3.2.2 Microfluidic stickers

Microfluidic stickers are fabricated to produce multiple sample channels on a single microscope slide, as shown in Fig. 3.1. Each channel holds a volume of approximately 2 μL. The microfluidic stickers are made following the procedures of Bartolo et al. [5] and Natali et al. [6], using soft imprint lithography. A drop of ultraviolet-cured thiolene resin (NOA 81, Norland Products, Cranbury, NJ) is placed on a flat substrate made with polyethylene (PE) and polydimethylsiloxane (PDMS). A structured PDMS mold, made with traditional photolithography technique, is gently pressed onto the thiolene drop with the help of a roller. Oxygen inhibits the photocuring reaction, and the polymers were selected based on their permeability to allow a two-step peeling process and greater control and maneuverability of the microfluidic sticker. The permeability of polyethylene is $\sim 10^{-3}$ less than that of PDMS, and after the first curing step the sticker preferentially attaches to the substrate rather than the channel mold. The substrate (with channel sticker) is then placed on a cover slip (25 $\times$ 75 $\times$ 0.15 mm, Fisher Scientific), where the thiolene resin completely cures. The substrate is then peeled off, leaving the microfluidic sticker on the microscope slide.

One requirement for MPT is that the probe motion is due solely to thermal forces and the local drag of the fluid. Other interactions, such as hydrodynamic interactions

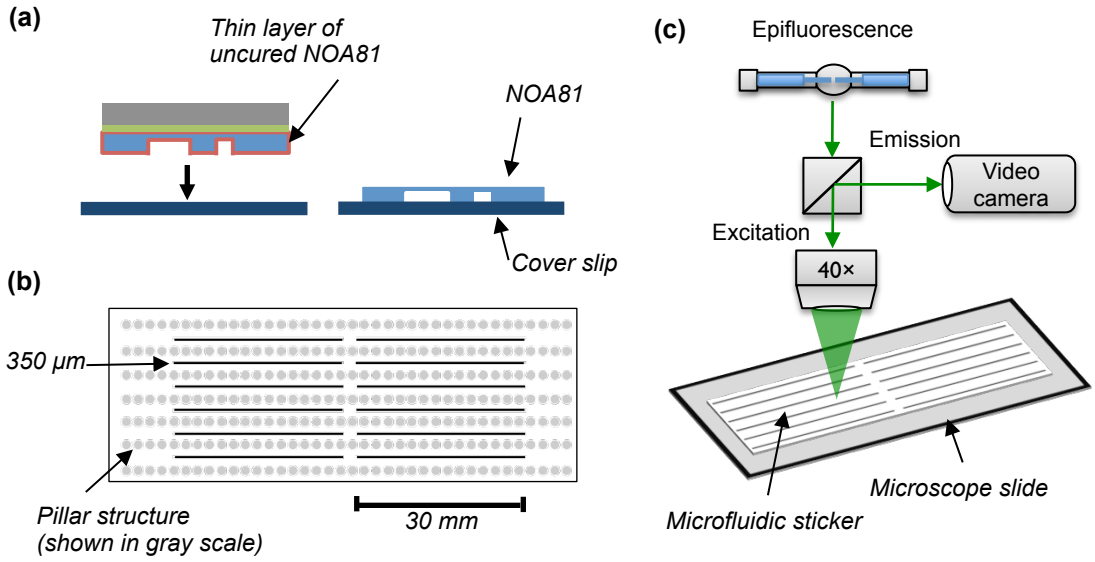

Figure 3.1: The design of microfluidic stickers used as sample chambers. (a) Microfluidic channels made of thiolene resin are sealed by a cover slip. (b) The design of microfluidic sticker. The channels are 0.35 × 30 × 0.125 mm and contain 2 μL of solution. (c) A schematic representation of the experimental microrheology setup.

with the sample walls, should be minimized. Using Faxén's solution for the mobility of a sphere halfway between two walls [7–9], we calculate the minimum channel height needs to be at least 100 μm for 1% error tolerance in particle mobility. In designing the channel, its height is set at 125 μm to ensure this source of error is insignificant.

A typical microfluidic sticker is shown in Fig. 3.1b; a total of 12 channels are on the sticker, and each channel is 0.35 × 30 × 0.125 mm, or approximately 2 μL in volume. A dense network of pillars surrounds the channel pattern (shown in gray scale for clarity); the porous pillar structure enhances the local curvature of the liquid meniscus, increases the Laplace pressure, and speeds up the capillary spreading of the resin.

3.2.3 Multiple particle tracking experiments

Samples are loaded by capillary action into the channels of the microfluidic sticker fixed to microscope slides, and sealed with NOA 81. Probe particles are imaged with a 40× objective (EC Plan-Neofluar, NA 0.75, Carl Zeiss) and an inverted microscope (Axiovert 200, Carl Zeiss). This objective is selected due to its ability to magnify the probe particles sufficiently while retaining an adequate number of pixels to achieve the Gaussian illumination profile necessary for particle tracking ($\geq$ 4 pixels/μm) [10]. A CMOS high-speed camera (Phantom v5.1, 1024 pixels, Vision Research, Wayne, NJ) is used to record videos of the particles in the two dimensional focal plane at a shutter time σ between 1 ms to 5 ms and at acquisition rate $f = 50$ frames per second. These settings are selected to minimize static and dynamic error of the particle tracking measurement [11]. The probe positions are tracked by a brightness-weighted centroid algorithm, and trajectories are formed by linking the probe positions found in consecutive video frames [10].

The goal of passive microrheology is to extract the linear viscoelastic properties of a material from the motion of embedded colloidal probes. Compared to macroscopic rheometers, a passive microrheology experiment minimally perturbs the material, and its rheological responses are measured over a wide range of frequencies simultaneously [12]. From the particle trajectories, the one-dimensional projection of the mean squared displacement (MSD) is calculated as

$$\langle \Delta x^2(\tau) \rangle = \langle (x(\tau) - x(0))^2 \rangle, \tag{3.1}$$

where x is the position of particle, τ is the lag time, and the average is taken over all particles and independent trajectory segments. The MSD is proportional to the macroscopic creep compliance of the material, $J(\tau)$, by the generalized Stokes-Einstein relation (GSER) [12, 13],

$$J(\tau) = 3\pi a \langle \Delta x^2(\tau) \rangle / kT, \tag{3.2}$$

where a is the probe radius, k is the Boltzmann constant, and T is the absolute

temperature. The creep compliance is the strain response $\gamma(\tau)$ of a material under an applied stress $\sigma(\tau)$, defined as

$$\gamma(\tau) = \int_0^\tau J(\tau - \tau')\sigma(\tau')d\tau'. \tag{3.3}$$

In the case of a constant stress σ_0, the material creep compliance is $J(\tau) = \gamma(\tau)/\sigma_0$. For a Newtonian fluid with viscosity η, $J(\tau) = \tau/\eta$, and for an elastic solid, $J = 1/G$, where G is the equilibrium shear modulus. The creep compliance can be converted to the frequency dependent storage and loss moduli, $G'(\omega)$ and $G"(\omega)$, in the cases where samples exhibit viscoelastic behavior [13].

The continuum approximation of the Stokes component in the GSER requires that the length scale of the probes be much larger than the length scale of the mAb proteins (radius of gyration, $R_g \sim 50$ Å), so that the probes measure the average macroscopic rheological properties of the protein solution [12]. Where there is significant structure in the fluid, probe surface chemistry is also important such that the probes do not interact with the material in a manner that alters their local microenvironment [3, 14, 15]. In the cases reported here, protein adsorption to the probe surfaces does not significantly change the hydrodynamic radius of the particles; however, the proteins may induce interactions between probes that destabilize them. For this reason, we use probe particles with several surface chemistries and select the probes that provide the greatest stability.

3.2.4 Bulk rheology

Protein solution viscosities are measured using a stress-controlled rheometer (AR-G2, TA Instruments, Newark, DE). A cone-and-plate geometry with a solvent trap is used due to the low sample viscosities, which are in an expected range of $0.9 \times 10^{-3} - 15 \times 10^{-3}$ Pa s, and evaporatation rate. Measurements are made at shear rates from $100 - 1000$ s^{-1}. The viscosity does not depend on shear rate over this range. The Pèclet number, $\mathrm{Pe} = 6\pi a^3 \eta_0 \dot{\gamma}/kT$, which scales the shear rate by the

characteristic relaxation time of the solution by the diffusion of the protein molecules, satisfies Pe $\ll 1$. This is consistent with the observation that *concentrated* protein solutions exhibit shear-thinning at shear rates above 1000 s^{-1} [16]. Therefore, the steady-state shear viscosity is estimated from the average over the range of shear rates.

Bulk rheology is performed using a steady shear method because the samples lack the sufficient torque required for oscillatory measurements.

3.2.5 Dynamic light scattering

Dynamic light scattering measurements are performed in DAWN-HELEOS II with a QELS attachment (Wyatt Technologies, Santa Barbara, CA) to examine the size of the antibodies before and after the addition of the probes used in microrheology. The protein samples (50 μL) are mixed with either 0.5 μL Milli-Q water (sample "without probes") or 0.5 μL of 10% w/v PS-PEG (sample "with probes"). The samples are incubated for 10 minutes at 20°C, and then centrifuged for 2 minutes at 6000 G. The top 45 μL of the samples are removed from the centrifuge tube and used in the DLS experiments.

The autocorrelation function data are analyzed using non-linear regression to the cumulant expansion

$$g_2(t) = \alpha + \beta \exp(-2Q^2 D_0 t)\left(1 + \frac{\mu_2}{2!}t^2\right)^2, \tag{3.4}$$

where Q is the magnitude of the scattering vector

$$Q = \frac{4\pi n}{\lambda} \sin\left(\frac{\theta}{2}\right), \tag{3.5}$$

α is a short delay-time baseline constant, β is an instrument-specific constant, D_0 is the self-diffusion coefficient at dilute protein concentrations, n is the refractive index of solvent, λ is the laser wavelength at 658.9 nm, θ is the scattering angle at 96.7°, t is the decay time, and μ_2 is the second cumulant and related to the sample polydispersity index. The hydrodynamic radius of the protein molecules is calculated from the

measured D_0 using the Stokes-Einstein-Sutherland relation

$$R_h = \frac{k_b T}{6\pi\eta D_0}. \tag{3.6}$$

3.3 Results and Discussion

3.3.1 Probe stability

Microrheology requires the probe particles to be dispersed throughout the samples and not aggregated. Multiple particle tracking provides immediate visual confirmation of the stability and dispersion of the probes. Probe stability in mAb solution samples was characterized as stable, small clusters, and large clusters (see Fig. 3.2 for example images). Samples with stable, freely dispersed particles can be used for multiple particle tracking without further consideration. Samples with small clusters are typically distributed with a modest number of freely diffusing single particles, and thus are candidates for subsequent refinement of the particle tracking, for instance, by selecting single-particle trajectories based on the ratio of first and second moments of the intensity distribution for each tracked object [10]. The drawback of this approach is the reduction of tracking statistics due to fewer probes, which reduces the accuracy of the measurement. The existence of large clusters in a sample indicates strong attractive interactions between probes.

We examined the stability of the untreated, bare PS and PEGylated PS probes, for mAb1 and mAb2 from 5.6 mg/ml to 90 mg/ml with and without Tween 20 in solution. Untreated PS probes performed poorly over all conditions. Probes were unstable for all conditions of the protein mAb1, which is known to be strongly self-associating [17]. The mAb2 samples generally produced weak aggregation of untreated probes, but the highest protein solution concentration (90 mg/ml) exhibits strong aggregation.

The aggregation behavior of the probes is sometimes difficult to predict. For example, formulations of mAb1 with and without Tween 20 have different behaviors of the aggregation of PS probes over the identical concentration range. Compared to

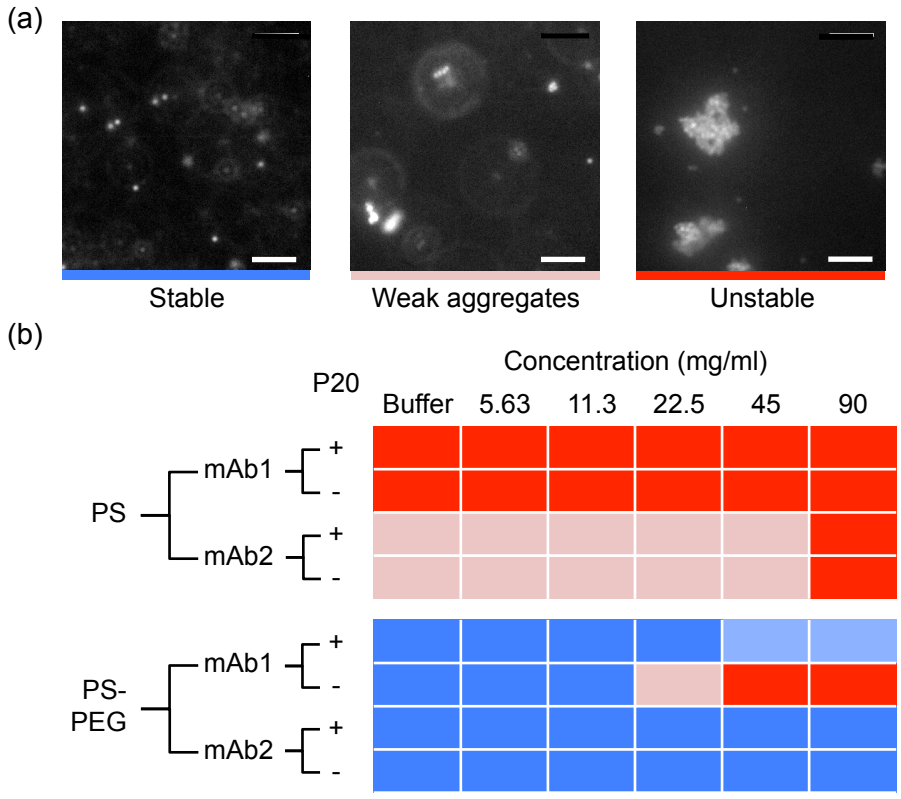

Figure 3.2: Probe stability in 72 mAb solutions. (a) Sample microscope images of probes in solution in three conditions: stable, weakly aggregating, and unstable. The scale bar is 10 μm. (b) Probe stability of polystyrene and PEGylated polystyrene in different concentrations of mAb1 and mAb2, with and without Tween 20 (indicated as P20). At 45 and 90 mg/ml of mAb1 in the presence of surfactant, the probes are mostly stable with a few doublets present, and are indicated in light blue.

the untreated PS, PS-PEG probes are more stable overall under different conditions, but surprisingly, the steric layer alone does not make the probes completely immune to aggregation, as shown at high concentration of mAb1. Although it is not immediately apparent under what conditions the probes are stable, the advantage of multiple particle tracking is that aggregation can be assessed to directly identify samples that can be used for calculations. Currently, viscosity measurements are only performed for samples with stable probes.

3.3.2 Protein stability after probe addition

Proteins in solution can sometimes be unstable even in the presence of benign surfaces such as stainless steel used in fill-finish processing steps [18]. The addition of the probes used in microrheology increases the free surface area available for protein-surface interactions, and may induce protein aggregation. DLS experiments were performed to examine the size of the antibodies before and after the addition of the probes. In Fig. 3.3, the scattering correlation functions and size distributions (calculated using CONTIN regularization) are plotted for mAb1 and mAb2. For mAb1, the correlation intercepts with and without probes (Fig. 3.3a) are due to slight concentration differences; the decay times for both samples agree. The calculated hydrodynamic radius of mAb1 with and without probes (calculated using the cumulant expansion) is 4.9 $\pm$ 0.2 nm and 4.8 $\pm$ 0.1 nm respectively, and Fig. 3.3b shows the size distribution profiles match completely. There is no evidence of larger protein aggregates. The mAb2 sample with probes still had traces of the 1 μm-diameter probes, shown in Fig. 3.3d; the presence of the probes affected the decay time in Fig. 3.3c. However, the size analysis still shows a good agreement between the mAb2 with and without probes, with the calculated hydrodynamic radii of 5.8 $\pm$ 0.3 nm and 6.0 $\pm$ 0.3 nm, respectively.

The DLS experiments verify that the antibodies are stable and have not aggregated as a result of the addition of probe particles.

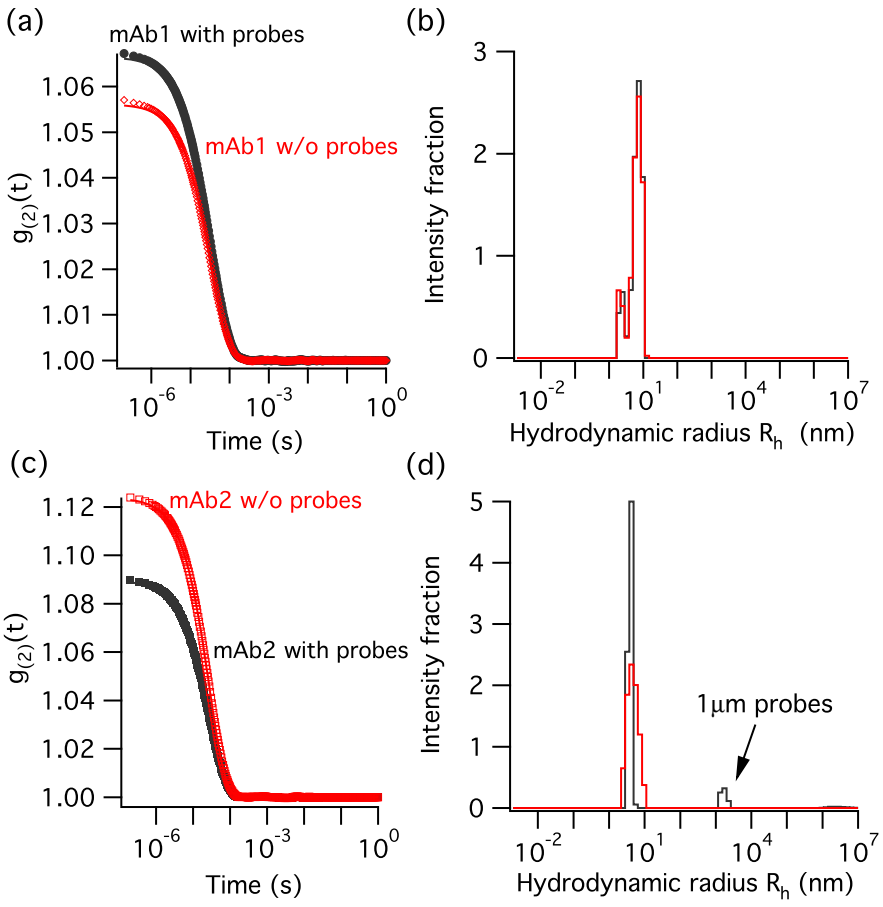

Figure 3.3: Scattering correlation functions and size distributions for mAb1 (a-b) and mAb2 (c-d), at 30 mM histidine-HCl, pH 5.3.

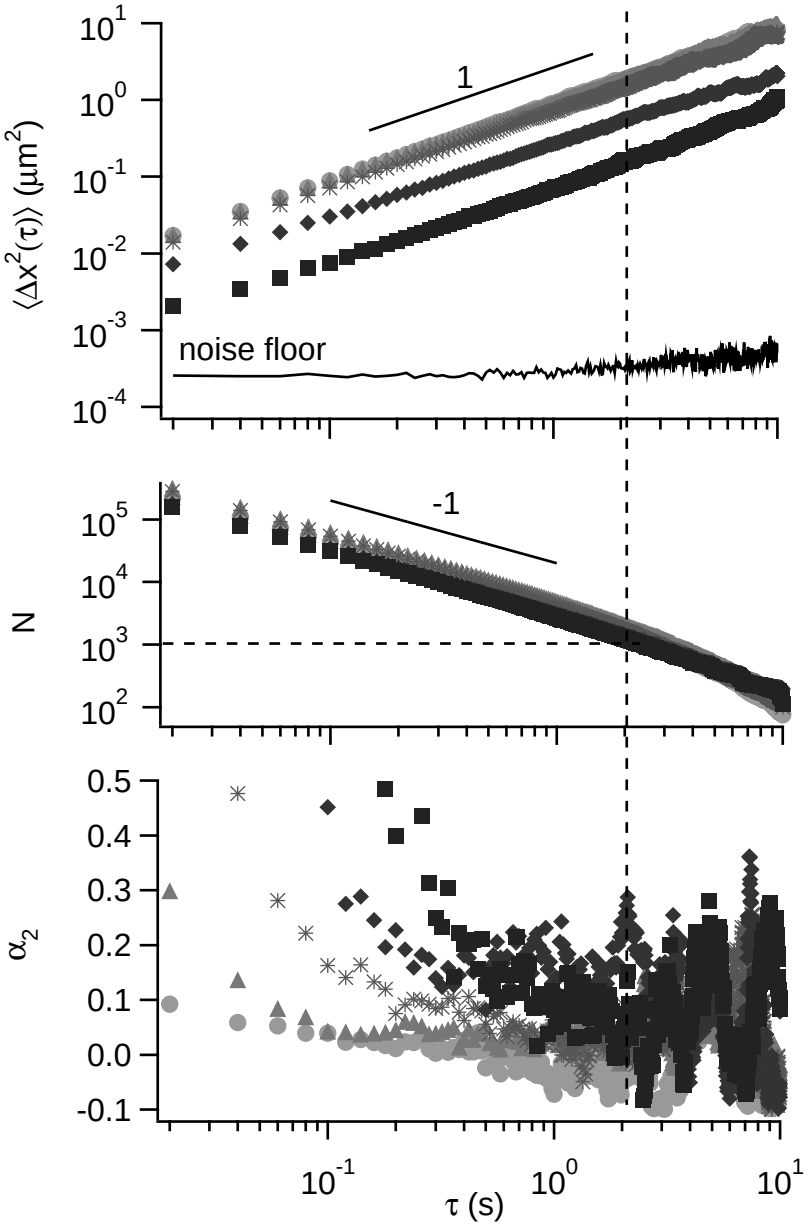

Figure 3.4: Mean squared displacements, number of observations and excess kurtosis of mAb1 solutions at 5.6 (•), 11.3 (▲), 22.5 (⁎), 45 (⧫), and 90 (■) mg/mL in 30 mM histidine buffer, pH 5.4 with 0.02% Tween 20. The solid lines indicate logarithmic slopes. The horizontal dash line indicates where the number of observation is 1000, and the vertical dash line indicates the lag times below which do not have enough statistics for viscosity calculations.

3.3.3 Particle tracking mean-squared displacement

For samples with good probe stability, we measure the microviscosity of mAb1 and mAb2. In Fig. 3.4 we plot the mean-squared displacement (MSD) and corresponding number of displacement observations, as a function of lag time τ for five concentrations of mAb1. The inherent noise in determining a particle's position is also indicated. The noise floor, or static error, primarily comes from background fluorescence, photon shot noise, camera readout noise, and digitization noise [11]. We measure the static error by tracking the positions of particles trapped in a 1.5 kPa polyacrylamide gel cross-linked with bis-acrylamide. Since the stiff gel modulus lies outside of the operating regime of MPT with 1μm probes [19], any apparent particle displacement detected in the gel is considered the inherent noise. The static error is estimated to be $\epsilon \sim 10$ nm. The increasing noise floor fluctuations at larger lag times arise from a decrease in the number of lag-time observations and a corresponding increase in the standard error of the mean, which scales as $\sim 1/\sqrt{N}$ for N observations.

The MSDs of the protein solutions at all concentrations have a logarithmic slope of 1, indicating that the solutions are Newtonian, and are greater than the particle tracking noise floor. At large lag times, the MSD fluctuates and deviates slightly from the power law, which arises from probes moving in and out of the focal plane and the corresponding loss of statistics. The lag time where fluctuations become apparent coincides approximately with $N \leq 1000$ measured displacements, indicated by the dashed lines in Fig. 3.4.

In the remainder of the discussion, we focus on the technique's capabilities and not on the rheological behavior of the protein solutions; the main variable examined in this work is protein concentration, and we leave to future work the details of high throughput development and multiple variables in the composition space (temperature, pH, salt, etc.)

3.3.4 Precision of particle tracking microrheology

In a typical MPT experiment, the maximum number of independent displacement measurements is $N \approx n_p T/\tau$, where n_p is the average number of probes being tracked, T is the total trajectory duration, and τ is lag time. At short lag times the number of observations N decays as $1/\tau$, but some probe displacements may not exceed the noise level. As τ increases, the number of independent displacement measurements decreases. This decrease accelerates at the longest τ, and the number of measurements falls below the power-law scaling (Fig. 3.4) as particles move in and out of the focal plane. The observed MSD also begins to fluctuate and lose accuracy. Thus there is a range of lag times for which the tracking error is minimized while a maximum number of independent observations can be made. These conditions give the most precise measurement.

The random walk of a probe particle in complex fluids can be characterized as the probability G_s that a particle will move in the vicinity $\boldsymbol{r}$ within time τ, $G_s(\boldsymbol{r}, t) = \langle \delta(\boldsymbol{r} - \Delta \boldsymbol{r}_j) \rangle$, known as the Van Hove self space-time correlation function [20, 21]. With a sufficiently large sample of displacements, the central limit theorem states that the probability of a probe displacement is expected to be Gaussian, and the one-dimensional Van Hove self-correlation is

$$G_s(\Delta x, \tau) = (2\pi \langle \Delta x^2(\tau) \rangle)^{-1/2} \exp\left(\frac{-\Delta x^2}{2\langle \Delta x^2(\tau) \rangle} \right). \tag{3.7}$$

Equation 3.7 can be applied to any complex fluid for which the GSER (Eq. 3.2) is valid, only assuming the probe displacement is isotropic in space. For a Newtonian fluid, the generalized Stokes-Einstein equation (Eq. 3.2) becomes

$$\langle \Delta x^2(\tau) \rangle = 2D\tau = (kT/3\pi a\eta)\tau. \tag{3.8}$$

where D is the diffusion coeffcient, from which the viscosity can be calculated. For each sample, the variance of the Van Hove self-correlation (note that the variance

is equivalent to the MSD, $\langle \Delta x^2(\tau) \rangle$), is calculated at a specific lag time τ, and the viscosity is calculated using the Stokes-Einstein relation (Eq. 3.8). Typically, the logarithmic intercept of the MSD is used to calculate the microviscosity, but such an analysis is weighted by less accurate displacement observations that occur especially at long lag times. The use of the Van Hove correlation to calculate viscosity excludes such bias since it only utilizes data at a specific lag time, which is selected to provide the most precise measurement. The excess kurtosis α_2 and its test statistic Z_{α_2} are used to identify the specific lag time that achieves a maximum number of measurements with the highest precision of each displacement measurement. Since MPT should only observe random Brownian motion of the probes, deviation from a Gaussian distribution of the probe displacements indicates that the probe displacement distribution at that particular τ is not suitable for the viscosity calculation. The departure of measured Van Hove functions from Gaussian behavior can indicate sample heterogeneity [22], probe-material interactions, incorrect parameters in particle tracking algorithm [10], or the inherent measurement error of video microscopy.

The excess kurtosis α_2, formally defined as the standardized fourth centralized moment, is commonly used in statistical analysis and reflects "tailedness" and "peakedness" in a distribution. It is derived from the the ratio of successive moments [21]

$$\alpha_n(t) = \frac{\langle \Delta x^{2n} \rangle}{C_n \langle \Delta x^n \rangle^n} - 1 \tag{3.9}$$

where $n = 1, 2, 3, ...$ and $C_n = 1 \times 3 \times 5 \times 7 \times ... \times (2n+1)/3^n$. For a normal distribution, $\alpha_2 = 0$ [23]. The excess kurtosis is used to determine the lag time at which the ensemble of probe displacements is closest to the normal distribution. A test statistic Z_{α_2} determines how far α_2 must be from 0 to be considered nonzero, and is defined as $Z_{\alpha_2} = \alpha_2 / \sigma_{\alpha_2}$, where

$$\sigma_{\alpha_2} = \sqrt{\frac{24N(N-1)^2}{(N-3)(N-2)(N+3)(N+5)}} \tag{3.10}$$

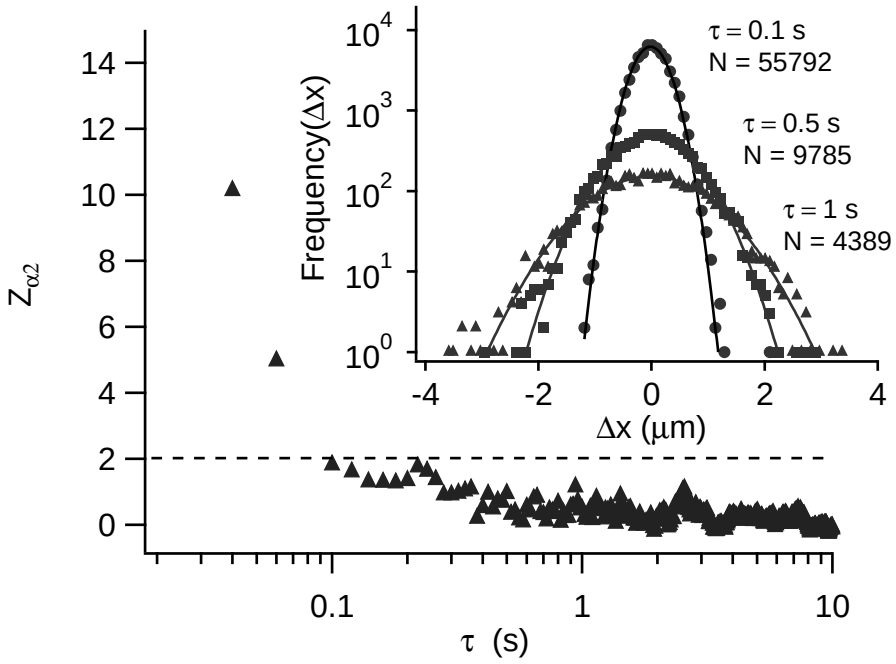

Figure 3.5: Test statistic Z_{α_2} for 11.3 mg/mL mAb1. The horizontal dash line indicates where Z_{α_2} is 1.96, above which the excess kurtosis is significantly different from zero. The inset shows the Van Hove correlations at τ = 0.1 s for 11.3 mg/mL mAb1. The solid lines are Gaussian distributions fitted to the data.

is the standard error of kurtosis (SEK) and N is the number of probe displacements at lag time τ. The critical value of Z_{α_2} is 1.96 at 0.05 significance level; when $|Z_{\alpha_2}| > 1.96$, the excess kurtosis is significantly different from zero, and the probe displacement distribution is therefore not fitted for viscosity calculations. For an ensemble of $N = 10^5$ displacements (typical at short τ), the limit of excess kurtosis is $|\alpha_2| < 0.03$ (Table. 3.1).

The excess kurtosis is used to examine the probe displacements statistics of the protein solutions, and is plotted against the lag time (Fig. 3.4). All the curves have a similar shape, starting at a positive α_2 value, are minimized over a range of lag times, and fluctuate as τ increases further. The higher value of α_2 at short lag times

Table 3.1: Example of excess kurtosis limits for different number of observations at 0.05 significance level (Z_{α_2} =1.96).

N	σ^2 (μm^2)	$\lvert\alpha_2\rvert$ limit
1000	0.023880836	0.303
5000	0.004795207	0.136
10000	0.002398801	0.096
25000	0.000959808	0.061
50000	0.000479952	0.043
100000	0.000239988	0.030
200000	0.000119997	0.021

(here, $\tau \leq 0.1s$) indicates that not all the probes have moved beyond the minimum measurable displacement characterized by the static error. At short lag times, many particles move a distance beyond the resolution set by the static error, but some do not. As the lag time decreases and the Van Hove distribution becomes narrower, these "unresolved" displacements exert a greater bias. Its "peakedness" increases above the expected Gaussian distribution.

This effect is more pronounced at the higher concentration solutions, because in a medium with a higher viscosity, the probes experience slower dynamics, and many take longer to move beyond the static error. At the other extreme, at $\tau > 1.5$ s, α_2 values fluctuate due to the reduced numbers of observations, and in this region of large τ, the average number of independent observations N typically falls below 1000. Using the test statistic for excess kurtosis, we identify the first lag time at which $|Z_{\alpha_2}| < 1.96$, i.e. the excess kurtosis is not significantly different from zero and the displacement distribution is a normal distribution (Fig. 3.5). The variance of Van Hove self-correlation and solution viscosity are calculated at that lag time. The first lag time that has a Gaussian distribution of probe displacement is chosen because the number of observations is always greater at smaller lag times, and thus produces a more precise measurement of solution viscosity.

The Van Hove self-correlations are examined between $\tau = 0.08$ s and $\tau = 0.56$

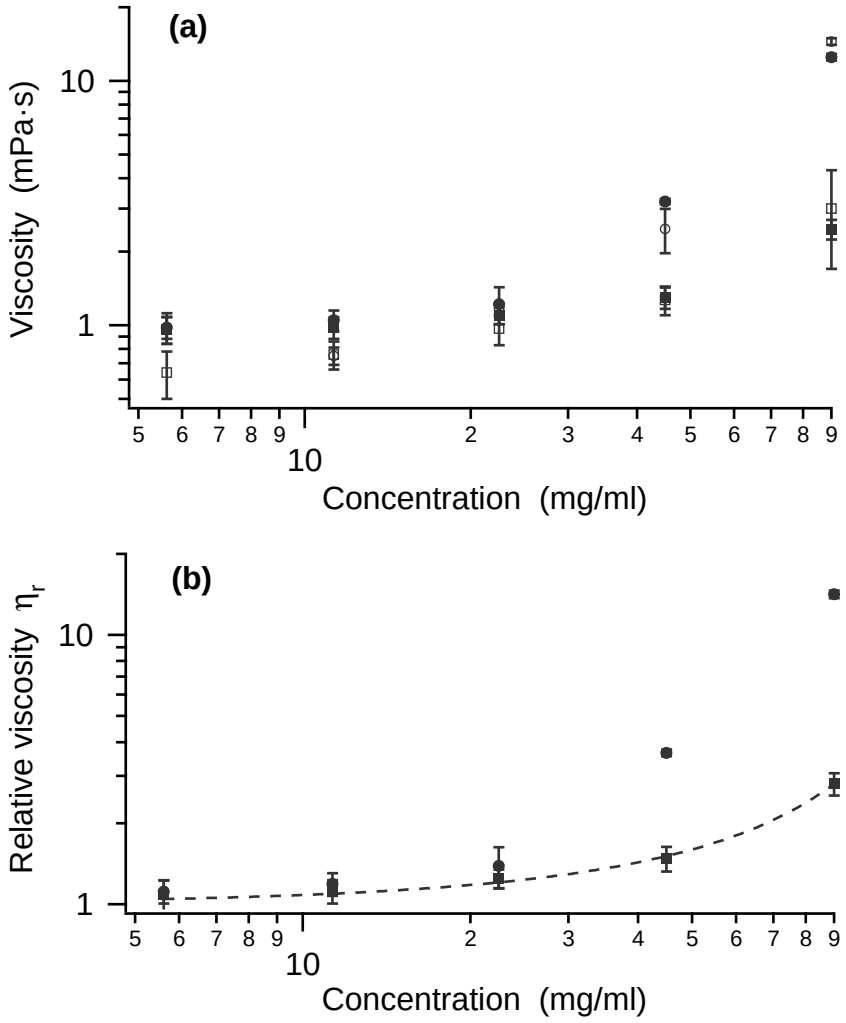

Figure 3.6: (a) Viscosity as a function of concentration for mAb solutions in 30 mM histidine, pH 5.4 with 0.02% Tween 20 (critical micellar concentration = 0.0074 mg/mL); microrheology results are indicate for mAb1 (•) and mAb2 (■), and cone-and-plate bulk rheometry results are indicated for mAb1 (○) and mAb2 (□). (b) Relative viscosity of mAb1 (•) and mAb2 (■), calculated with measured buffer microviscosity η_0 = 0.88 mPa·s; dash line is fit to modified Mooney equation (Eq. 3.11).

s for different concentrations of the protein solutions. The lag time τ is determined by the Z-statistic, as described above. We compare microrheology data to rotational rheometry (Fig. 3.6a). The reported uncertainties for microrheology are determined from the fit to the Van Hove correlation functions. The steady-state shear viscosity is taken as an average over the range of shear rates examined, and the uncertainty reflects one standard deviation of the averaged viscosity. Both measurements are reported here without sample replicates. The rotational rheology and microrheology measurements agree well, and the two techniques are within statistical error as discussed below in Sec. 3.3.5. However, the microrheology data exhibits less uncertainty at most concentrations.

Microrheology provides excellent sensitivity at low concentrations and correspondingly low viscosities. At low concentrations, some viscosities measured by bulk rheology are below that of water and even the buffer. These anomalies are due to the lower limit of torque sensitivity in the rheometer. Precise measurements at low viscosities for a cone-and-plate rheometer can be complicated due to artifacts arising from surface tension and interfacial adsorption; the rheometer needs to be sensitive to slight changes in torque [24, 25], and often requires larger sample sizes (typically > 100 μL) to capture changes in the viscosity. In contrast, microrheology accurately measures these low viscosities, since its sensitivity is only related to the particle tracking noise level and not of mechanical sensitivity. Increasing number of samples and the sample volume would improve the measurement precision, but may not be feasible in the early stage therapeutics development, where the availability of material is limited.

The viscosity of the protein solutions relative to the buffer is reported in Fig. 3.6b. The viscosity increases with increasing protein concentration. The concentration dependence of mAb2 is fitted using a modified Mooney equation [26],

$$\eta/\eta_0 = \exp\left(\frac{c[\eta]}{1-(k/\nu)c[\eta]}\right) \tag{3.11}$$

where η is the solution viscosity in mPa s, η_0 is the buffer viscosity in mPa s, c is

protein concentration in mg/ml, $[\eta]$ is the protein intrinsic viscosity in ml/mg, k is a crowding factor, and ν is a shape-determining factor. We find $k/\nu = 0.48 \pm .14$ and $[\eta] = (7.6 \pm 0.8) \times 10^{-3}$ ml/mg; the latter value is in close agreement with the reported intrinsic viscosity of the identical IgG1 antibody (mAb-G in 30 mM histidine-chloride, pH 6.0 [27]) $[\eta] = (7.4 \pm 0.6) \times 10^{-3}$ ml/mg, measured using a capillary rheometer and extrapolated to zero concentration using the Huggins relation.

The modified Mooney equation for nonspherical molecules accurately describes the viscosity dependence on concentration of mAb2. In contrast, mAb1 has a stronger dependence on concentration and the model does not capture the behavior as accurately; the protein self-association is not accounted for in the ideal non-associating model.

3.3.5 Accuracy of particle tracking microrheology

The micro and bulk viscosities reported in Sec. 3.3.4 are generally in good agreement, but how accurate are the microrheology measurements? We estimate the uncertainty of particle tracking by performing an analysis of covariance (ANCOVA) to compare microrheology experimental data to the expected viscosity values. The covariance is a measure of association between two variables, and in general, ANCOVA is an extension of analysis of variance that provides a way of statistically controlling the effect of covariates (or nuisance variables) by using regression to partial out those effects. In our study, we evaluate whether the dependent variable (viscosity) is equal across a categorial independent variable (measurement methods), while statistically controlling for the effects of the covariate (concentration). At a 95% confidence level, the p-value $p < 0.05$ is necessary to reject the null hypothesis, that the data sets derive from the same population.

Since highly accurate sucrose viscosity data are available [28], we first compare the microrheology measurement of aqueous sucrose solutions ranging from 10% w/v to 68% w/v to tabulated values. Fig. 3.7a shows the comparison between measured and tabulated viscosity of sucrose solutions as a function of concentration. Qualitatively,

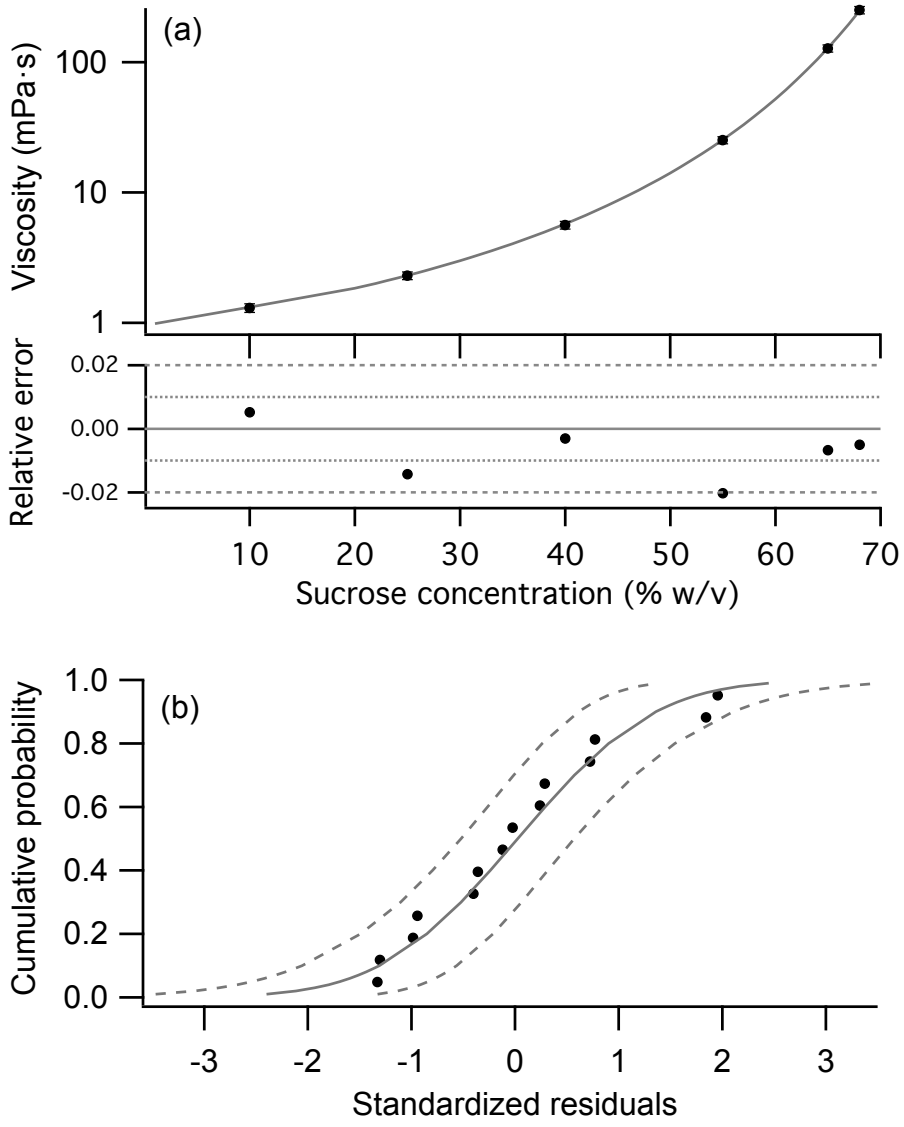

Figure 3.7: (a) Viscosity as a function of concentration for aqueous sucrose solutions, comparing microrheology results (•) and tabulated data (solid line). The lower subplot shows the relative error $\delta\eta$ of the measurements. (b) The cumulative probability distribution of the standard residuals calculated from ANCOVA to compare microrheology and tabulated sucrose data. The solid line is fit for a normal distribution, and the dash lines are the 95% confidence interval of the fit.

the microrheology results compare well with the tabulated data. A covariance calculation gives a p-value of $p = 0.941$, indicating that there is no significant difference between microrheology and the tabulated data. Further examination of the residuals resulting from ANCOVA (Fig. 3.7b) shows that the residuals are normally distributed ($p = 0.533$), indicating that there is no structural error or bias. Using a similar ANCOVA analysis, we find $p = 0.906$ for mAb1 and $p = 0.516$ for mAb2, suggesting there is no difference between the bulk rheology and microrheology data sets other than that due to random variation.

Finally, the relative error between tabulated sucrose viscosity data (η_{tab}) and microrheology measurements (η_{micro}),

$$\delta\eta = \frac{\eta_{\text{micro}} - \eta_{\text{tab}}}{\eta_{\text{tab}}}. \tag{3.12}$$

provides an estimate of the measurement uncertainty. The relative error is shown in Fig. 3.7a. Over the range of viscosities of the sucrose solutions, which are between approximately 1 and 200 mPa·s, particle tracking microrheology is consistently capable of measuring the viscosity with less than 2% error for all samples, and four of the six samples have errors below 1%. Notably, the measurement uncertainty of particle tracking is lower than the 7% bias errors typical of measurements at low viscosities using bulk rheology [29].

3.4 Conclusions

We demonstrated the capability of particle tracking microrheology to obtain precise and accurate viscosity data using small volumes of protein samples. The experiments are straightforward to perform, and require only a microscope and a video camera. Imaging provides an immediate assessment of the probe particle stability. We demonstrated its use with two monoclonal antibody solutions, which were measured as a function of the protein concentration. Conditions for making precision microrheology measurements can be assessed using the excess kurtosis of probe displacement

probability distribution (Van Hove correlation function). The resulting microviscosity measurements are more accurate than bulk rheometry, especially at low protein concentrations, and other low viscosity samples. The ease of use and high throughput capability of microrheology will be beneficial for screening formulations with various excipients and solution conditions. Future work will focus on understanding and controlling the effect of probe surface chemistry to expand the types of proteins, range of protein concentration, buffer composition, and excipient concentrations that can be measured using particle tracking microrheology. A key limitation of *passive* microrheology is its inability to measure non-linear rheology, including shear thinning. Second, the colloidal stability of probe particles could be improved. Even with a pegylated surface chemistry, probe aggregation prevents microrheology measurements in 20% of the samples studied in this work.

REFERENCES

[1] L. L. Josephson, E. M. Furst, and W. J. Galush. Particle tracking microrheology of protein solutions. *Journal of Rheology*, 60(4):531–540, 2016.

[2] J. L. McGrath, J. H. Hartwig, and S. C. Kuo. The mechanics of F-actin microenvironments depend on the chemistry of probing surfaces. *Biophysical Journal*, 79 (6):3258–3266, 2000.

[3] M. T. Valentine, Z. E. Perlman, M. L. Gardel, J. H. Shin, P. Matsudaira, T. J. Mitchison, and D. A. Weitz. Colloid Surface Chemistry Critically Affects Multiple Particle Tracking Measurements of Biomaterials. *Biophysical Journal*, 86(6):4004–4014, 2004.

[4] B. S. Chae and E. M. Furst. Probe Surface Chemistry Dependence and Local Polymer Network Structure in F-Actin Microrheology. *Langmuir*, 21(7):3084–3089, 2005.

[5] D. Bartolo, G. Degre, P. Ngheb, and V. Studer. Microfluidic stickers. *Lab on a Chip*, 8:274–279, 2008.

[6] M. Natali, S. Begolo, T. Carofiglio, and G. Mistura. Rapid prototyping of multilayer thiolene microfluidic chips by photopolymerization and transfer lamination. *Lab on a Chip*, 8(3):492, 2008.

[7] H. Faxén. Der Widerstand gegen die Bewegung einer starren Kugel in einer zähen Flüssigkeit, die zwischen zwei parallelen ebenen Wänden eingeschlossen ist. *Annalen der Physik*, 373(10):89–119, 1922.

[8] J. Happel and H. Brenner. *Low Reynolds Number Hydrodynamics: with special applications to particulate media*. Prentice-Hall, 1965.

[9] K. M. Schultz and E. M. Furst. High-throughput rheology in a microfluidic device. *Lab on a Chip*, 11(22):3802–3809, 2011.

[10] J. C. Crocker and D. G. Grier. Methods of digital video microscopy for colloidal studies. *Journal of Colloid and Interface Science*, 179:298–310, 1996.

[11] T. Savin and P. S. Doyle. Static and Dynamic Errors in Particle Tracking Microrheology. *Biophysical Journal*, 88(1):623–638, 2005.

[12] T. M. Squires and T. G. Mason. Fluid Mechanics of Microrheology. *Annual Review of Fluid Mechanics*, 42(1):413–438, 2010.

[13] T. G. Mason and D. A. Weitz. Optical measurement of frequency-dependent linear viscoelastc moduli of complex fluids. *Physical Review Letters*, 74(7):1250–1253, 1995.

[14] M. T. Valentine, P. Kaplan, D. Thota, J. G. Crocker, T. Gisler, R. Prud'homme, M. Beck, and D. A. Weitz. Investigating the microenvironments of inhomogeneous soft materials with multiple particle tracking. *Physical Review E*, 64(6):061506, 2001.

[15] J. Y. Huh and E. M. Furst. Colloid dynamics in semiflexible polymer solutions. *Physical Review E*, 74(3), 2006.

[16] I. E. Zarraga, R. Taing, J. Zarzar, J. Luoma, J. Hsiung, A. Patel, and F. J. Lim. High shear rheology and anisotropy in concentrated solutions of monoclonal antibodies. *Journal of Pharmaceutical Sciences*, 102(8):2538–2549, 2013.

[17] S. Yadav, A. Sreedhara, S. Kanai, J. Liu, S. Lien, H. Lowman, D. S. Kalonia, and S. J. Shire. Establishing a Link Between Amino Acid Sequences and Self-Associating and Viscoelastic Behavior of Two Closely Related Monoclonal Antibodies. *Pharmaceutical Research*, 28(7):1750–1764, 2011.

[18] A. Nayak, J. Colandene, V. Bradford, and M. Perkins. Characterization of Subvisible Particle Formation During the Filling Pump Operation of a Monoclonal Antibody Solution. *Journal of Pharmaceutical Sciences*, 100(10):4198–4204, 2011.

[19] K. M. Schultz and E. M. Furst. Microrheology of biomaterial hydrogelators. *Soft Matter*, 8(23):6198, 2012.

[20] L. Van Hove. Correlations in Space and Time and Born Approximation Scattering in Systems of Interacting Particles. *Physical Review*, 95(1):249–262, 1954.

[21] A. Rahman. Correlations in the Motion of Atoms in Liquid Argon. *Physical Review*, 136(2A):A405–A411, 1964.

[22] E. R. Weeks. Three-Dimensional Direct Imaging of Structural Relaxation Near the Colloidal Glass Transition. *Science*, 287(5453):627–631, 2000.

[23] L. T. DeCarlo. On the meaning and use of kurtosis. *Psychological Methods*, 2(3): 292, 1997.

[24] M. T. Johnston and R. H. Ewoldt. Precision rheometry: Surface tension effects on low-torque measurements in rotational rheometers. *Journal of Rheology*, 57(6): 1515–1532, 2013.

[25] R. H. Ewoldt, M. T. Johnston, and L. M. Caretta. Experimental challenges of shear rheology: how to avoid bad data. In S. E. Spagnolie, editor, *Complex Fluids in Biological Systems*, pages 207–244. Springer, 2015.

[26] A. P. Minton. Hard Quasispherical Particle Models for the Viscosity of Solutions of Protein Mixtures. *Journal of Physical Chemistry B*, 116(31):9310–9315, 2012.

[27] S. Yadav, S. J. Shire, and D. S. Kalonia. Factors affecting the viscosity in high concentration solutions of different monoclonal antibodies. *Journal of Pharmaceutical Sciences*, 99(12):4812–4829, 2010.

[28] J. F. Swindells, C. F. Snyder, R. C. Hardy, and P. E. Golden. Viscosities of sucrose solutions at various temperatures: Tables of recalculated values. Technical report, National Bureau of Standards, 1958.

[29] L. H. O. Hellström, M. A. Samaha, K. M. Wang, A. J. Smits, and M. Hultmark. Errors in parallel-plate and cone-plate rheometer measurements due to sample underfill. *Measurement Science & Technology*, 26(1):015301, 2015.

Chapter 4

IN SITU MEASUREMENTS OF STATIC ERROR IN PARTICLE TRACKING MICRORHEOLOGY

4.1 Introduction

Particle tracking is one of the most common microrheology methods, due to its ease of implementation and fast data acquisition. The use of video microscopy has come a long way in advancing the field of particle tracking since Jean Perrin performed his particle tracking experiment in 1909 [1]. His experiment required two people; the main researcher looked into the microscope and drew the particle position on a gridded paper, and the other counted the time steps at 30-second intervals.

The work of Crocker and Grier [2] has contributed to the popularity of video-based particle tracking microrheology; since then, multiple particle tracking has seen numerous applications, such as resolving microheterogeneity in actin filaments [3, 4], understanding the microstructure of hydrogels [5–7], investigating the dynamics of colloidal depletion gels [8], and measuring biofluids such as mucus [9] and vitreous humor [**?**]. However, in analyzing complex fluids, great care must be taken to interpret the results from particle tracking experiments; Martin et al. [10] showed that the limited spatial resolution in video microscopy leads to errors that can significantly alter the physical interpretations. For example, a particle tracking experiment generated an artifactual elastic-like signature, and without careful correction during the analysis, led to an incorrect conclusion that phospholipid bilayers are viscoelastic [11].

Savin and Doyle [12] introduced the analysis of static and dynamic error for multiple particle tracking. Static error arises from the camera setup and its random

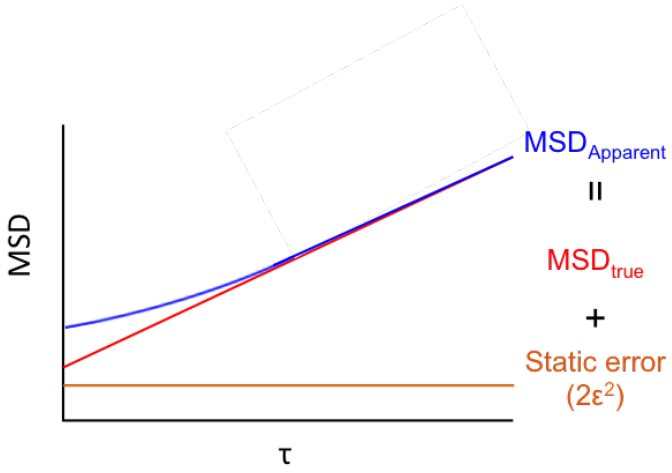

Figure 4.1: A schematic on how the localization or static error affects the true mean squared displacement as a function of lag time τ.

noise. The apparent position of the particle $\hat{x}(\tau)$ is

$$\hat{x}(\tau) = x(\tau) + \chi(\tau) \tag{4.1}$$

where $x(\tau)$ is the true particle position and $\chi(\tau)$ is the random error, with $\langle\chi\rangle = 0$ and $\langle\chi^2\rangle = \epsilon^2$, where ϵ represents the static error, or the inherent inaccuracy to track the position of a particle within a spatial resolution. For a Newtonian fluid,

$$\langle\Delta\hat{x}^2(\tau)\rangle = \langle\Delta x^2(\tau)\rangle + 2\epsilon^2. \tag{4.2}$$

Fig. 4.1 shows how the apparent mean squared displacement (MSD) is affected by ϵ. The spatial resolution also sets the operating regime of particle tracking microrheology, limiting the maximum viscosity that can be probed [13].

Besides the random noise in the microscopy setup, the static error is also influenced by digitization of a spherical feature as well as the parameters used in the brightness-weighted centroid algorithm calculation [2]. The expected probe width w is one of the user-selected parameters in the particle tracking algorithm, and it limits

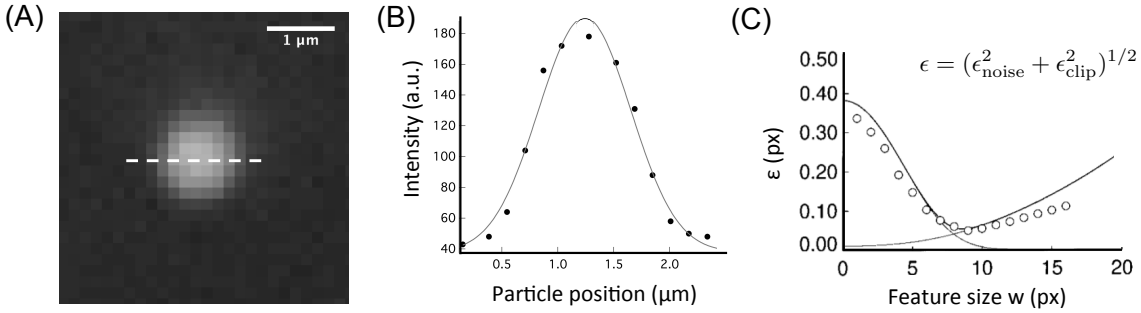

Figure 4.2: (A) Sample in-focus particle image during a typical experiment. (B) The corresponding brightness profile along the white dashed line in the particle image. (C) The effect of the tracking parameter w on static error. Adapted from [12].

the search on how wide the Gaussian-like feature should be. Fig. 4.2A shows a typical in-focus particle image, with w tested at 11 pixels. The spherical probe has jagged edges due to pixelation. The corresponding brightness profile of this particle is shown in Fig. 4.2B along with the Gaussian profile that the centroid algorithm uses to refine the particle's location (to subpixel resolution). The static error ϵ grows larger as the expected feature size w increases, suggesting that smaller w values improve tracking resolution (Fig. 4.2C). However, as w decreases, a second contribution arises due to clipping at the edges of the particle in the centroid calculation [12]. For the case tested, the optimal value of w is 9–11 pixels.

Currently there are two main methods to determine the static error ϵ experimentally. The first method is to track immobilized probes in a sufficiently strong gel or a dried-out sample [12, 14, 15]; since the probe particles are moving a distance smaller than what the microscopy setup can detect, any "displacement" detected will be the random noise that is induced by the system. This is the most widely-used method to benchmark the noise floor in the experimental setup. However, to truly account for the the sample's static error, the imaging condition in the gel sample needs to be extremely similar to that in the sample of interest – including particle brightness and radius a,

particle volume fraction ϕ, the amount of illumination in the sample, focal plane distance, etc. The second method is to combine the experimental data with simulation data, as developed by Savin and Doyle [12], Wu et al. [16]. This process retrieves tracked parameters from a raw particle image, maps the adequate parameters to simulate experimental images, and applies Monte Carlo simulation to estimate the static error. While this method yields an accurate localization error, it is time-consuming and significantly increases the computational resources needed for a particle tracking experiment.

Here we present a method to measure the static error ϵ *in situ*, simultaneously with the particle tracking experiment for the sample of interest. Since the experiment is done in the same sample, the static error is measured under the same imaging conditions and no additional experimental time is needed. Previously we developed the use of excess kurtosis α_2 to identify an optimal lag time τ to calculate viscosity of the samples [17]; this theory of estimating the static error *in situ* also uses the excess kurtosis. This chapter will describe the theory on the relationship between excess kurtosis and the static error. The MSD corrections based on our method are compared to the current benchmarking method with a polyacrylamide gel.

James W. Swan (previous post-doc advised by Eric M. Furst, now a faculty member at Massachusetts Institute of Technology) developed the theory, and the author executed and analyzed the experiments.

4.2 Materials

Sucrose (ACS reagents grade, #84100) is bought from Sigma-Aldrich and used as is. The sugar crystals are dissolved in filtered ultra-pure Milli-Q water (resistivity $\leq$ 18.2 M Ω cm) at 55, 60, and 65 wt% in 20 mL vials with stirring and gentle heating at 35°C. The tabulated viscosities at 23°C are 24, 49, and 120 mPa-s, respectively [18].

Acrylamide monomer, bis-acrylamide crosslinker, ammonium persulfate initiator, and tetramethylethylenediamine (TEMED) catalyst are obtained (Sigma-Aldrich) to make the polyacrylamide gel as a benchmarking fluid for noise floor characterization.

Oxygen is known to inhibit the polymerization process, so stock solutions are made fresh and degassed by vacuum prior to each use. Samples are prepared at 5.0 wt% total acrylamide, with 0.1 wt% bis-acrylamide crosslinker, 0.5 wt% ammonium persulfate, and 0.1% TEMED. This polyacrylamide gel has an estimated shear modulus of 1.5 kPa [19]; at this modulus, the expected MSD for 1 μm diameter probe particles is 2.9 $\times 10^{-13}$ nm (or a root mean square = 5.4 $\times 10^{-7}$ nm).

4.3 Methods

4.3.1 Multiple particle tracking experiment

Samples are loaded into the microcapillary channels (internal dimensions = 2.0$\times$ 0.2 $\times$ 50 mm, glass thickness = 0.14 mm, part #3520, Vitrocom, Mountain Lakes, NJ) and sealed with NOA81 (Norland Products, Cranbury, NJ). Probe particles are imaged on a Nikon Ti-E perfect focus inverted microscope equipped with a motorized X,Y stage and a high-speed camera (Clara interline CCD camera, Andor, Oxford Instruments, f = 30 frames per second, σ = 10 ms); the Brownian motion of the probe particles is captured at 40$\times$ magnification with a pixel size of 0.252 μm/px (ELWD Plan Fluor objective, NA 0.6, Nikon). The camera settings are selected so that dynamic error of particle tracking experiments is minimized ($\sigma \ll f$) [12, 20, 21], and that time step is constant at the desired frames per second. As each movie is saved, the microscope stage is moved to the next sample and refocused. The image stacks are analyzed in MATLAB [22], where the probe positions are tracked by a brightness-weighted centroid algorithm first developed by Crocker and Grier [2], and trajectories are formed by linking the probes found in consecutive video frames.

The description of the brightness-weighted centroid algorithm is detailed in Ch. 2. The analysis of particle tracking trajectories and statistics using the Van Hove self-correlation and excess kurtosis is described in Ch. 3.

4.3.2 The relation between excess kurtosis and static error

In a particle tracking experiment, the random walk of a probe particle in a complex fluid is captured on video. The particle displacements or trajectories are characterized as the probability P_s that a particle will move in the vicinity $\boldsymbol{r}$ within time t, $P_s(\boldsymbol{r}, t) = \langle \delta(\boldsymbol{r} - \Delta \boldsymbol{r}_j) \rangle$. This distribution is also known as the Van Hove self space-time correlation function [23, 24]. With a sufficiently large sample of displacements, the probability of a probe displacement is expected to be Gaussian, by the central limit theorem. This statement applies specifically to particles experiencing thermal forces that are uncorrelated, and holds for complex as well as simple fluids.

For simplicity's sake, let us consider an ensemble of colloidal particles undergoing Brownian motion in a fluid. The self-diffusivity is $D = kT/6\pi a\eta$. The probability distribution of the particle displacements in one dimension Δx at a specific lag time τ is $P(\Delta x, \tau)$. Because of the inherent random error, the experiment cannot distinguish displacements within a spatial resolution $|\epsilon|$ (with units of distance).

This particle displacement probability distribution can be written as

$$P(\Delta x, \tau) = \begin{cases} A\delta(\Delta x) & |\Delta x| \leq \epsilon \\ B \exp\left(\frac{-(\Delta x)^2}{2D\tau}\right) & |\Delta x| > \epsilon. \end{cases} \tag{4.3}$$

A Gaussian distribution of particle displacements is recovered when $|\Delta x| > \epsilon$ (displacements have moved beyond the noise floor) or as $\epsilon \to 0$. For all probability distributions, $\int_{-\infty}^{\infty} P(\Delta x, \tau)\ d(\Delta x) = 1$. The ensemble-averaged mean squared displacement $\langle \Delta x^2 \rangle$ can then be calculated and expanded based on Eq. 4.3,

$$\begin{aligned} \langle \Delta x^2 \rangle &= \int_{-\infty}^{\infty} P \cdot (\Delta x)^2\ d(\Delta x) \\ &= 2\int_{\epsilon}^{\infty} B \exp\left(\frac{-\Delta x^2}{2D\tau}\right)(\Delta x)^2\ d(\Delta x) + \int_{-\epsilon}^{\epsilon} A\delta(\Delta x)^2\ d(\Delta x). \end{aligned} \tag{4.4}$$

The integral of the Dirac delta function on the right hand side of Eq. 4.4 becomes zero

and drops out of the equation. Similarly,

$$\langle \Delta x^4 \rangle \;=\; \int_{-\infty}^{\infty} P \cdot (\Delta x)^4 \; d(\Delta x) = 2 \int_{\epsilon}^{\infty} B \exp\left(\frac{-\Delta x^2}{2D\tau}\right)(\Delta x)^4 \; d(\Delta x). \quad (4.5)$$

The excess kurtosis is defined as

$$\alpha_2 \;=\; \frac{\langle \Delta x^4 \rangle}{3\langle \Delta x^2 \rangle^2} - 1 \quad (4.6)$$

Substituting $\langle \Delta x^2 \rangle$ from Eq. 4.4 and $\langle \Delta x^4 \rangle$ from Eq. 4.5, the excess kurtosis α_2 becomes

$$\alpha_2 = -1 + \frac{\sqrt{D\tau}\left[(2\epsilon^3 + 6D\epsilon\tau)\exp\left(-\epsilon^2/2D\tau\right) + 3\sqrt{2\pi}(D\tau)^{-3/2}\,\mathrm{erfc}(\frac{\epsilon}{\sqrt{2D\tau}})\right]}{12\sqrt{2\pi}\left[\frac{\exp\left(-\epsilon^2/2D\tau\right)\sqrt{D\epsilon^2\tau}}{\sqrt{2\pi}} + \frac{1}{2}(D\tau)\,\mathrm{erfc}(\frac{\epsilon}{\sqrt{2D\tau}})\right]^2} \quad (4.7)$$

As expected, Eq. 4.7 reduces to 0 as $\epsilon \to 0$. This complicated expression is expanded using a Taylor series expansion as $\epsilon \to 0$ and solved in Mathematica; α_2 then simplifies to

$$\alpha_2 \;\cong\; \sqrt{\frac{8}{9\pi}}(D\tau)^{-\frac{3}{2}}\epsilon^3 + \mathcal{O}(\epsilon^4). \quad (4.8)$$

Eq. 4.8 relates the excess kurtosis α_2, a measured quantity in a particle tracking experiment, directly to the static error ϵ in the sample. Because $\langle \Delta x^2 \rangle = 2D\tau$ [2], Eq. 4.8 can be solved for ϵ:

$$\epsilon = \left(\sqrt{\frac{9\pi}{8}}\alpha_2\right)^{\frac{1}{3}}\left(\frac{\langle \Delta x^2 \rangle}{2}\right)^{\frac{1}{2}} \quad (4.9)$$

Alternatively, Eq. 4.8 can be linearized into the form $y = \epsilon x$

$$\left(\sqrt{\frac{9\pi}{8}}\alpha_2\right)^{\frac{1}{3}} = \epsilon\left(\frac{\langle \Delta x^2 \rangle}{2}\right)^{-\frac{1}{2}} \quad (4.10)$$

This enables the calculation of the static error ϵ using the MSD and excess kurtosis, both quantities already measured during a particle tracking experiment under

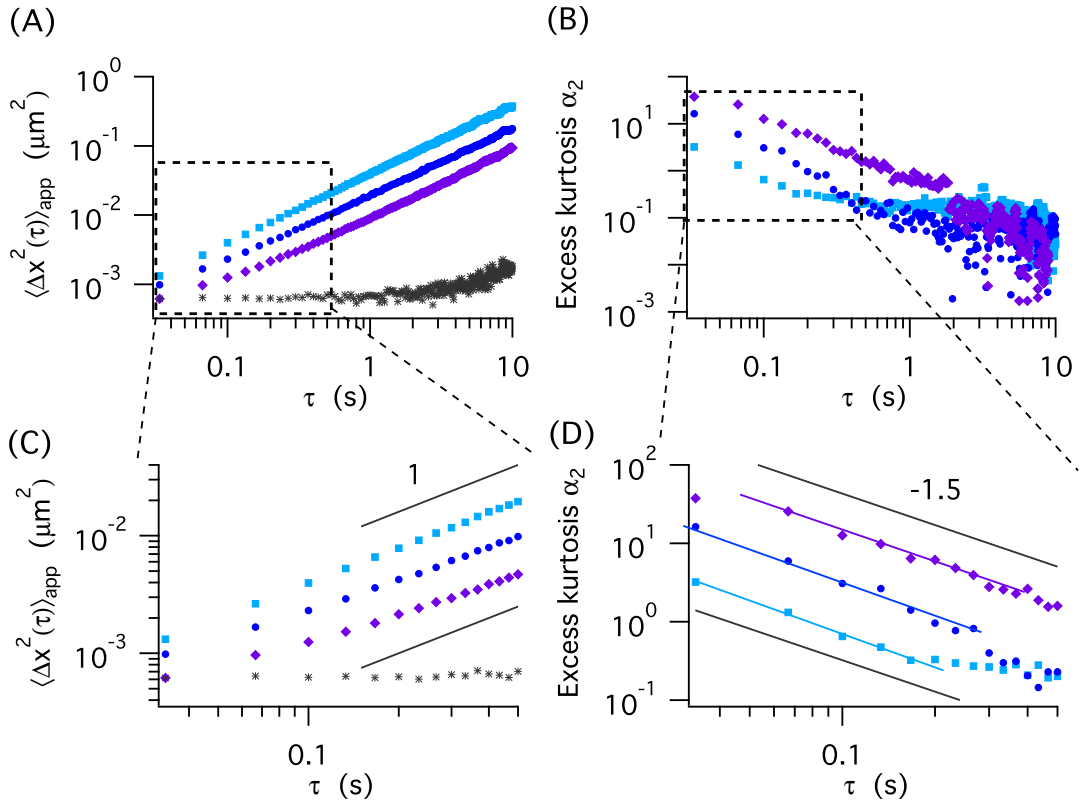

Figure 4.3: The apparent mean squared displacements (A) and excess kurtosis (B) of 55 wt% (■), 60 wt% (•), and 65 wt% (⧫) sucrose solutions, with insets to show short lag time behavior. The noise floor or static error of this imaging system, measured using the polyacrylamide gel, is also indicated (⁕). (C-D) Insets from $\tau = 0.03 - 0.5$ s.

dilute particle concentrations (< 0.1w/v%). Because it is derived without assuming Newtonian behavior, it is valid for complex fluids, as well.

4.4 Results and Discussion

To test the hypothesis that the static error can be measured from MSD measurements, high-viscosity sucrose solutions, in which static error effects will be most pronounced, are characterized using multiple particle tracking. In Fig. 4.3A we show the apparent mean-squared displacement of 55, 60, 65 wt% sucrose solutions, as well as that of the polyacrylamide gel. Examination of the short lag time region in the inset of

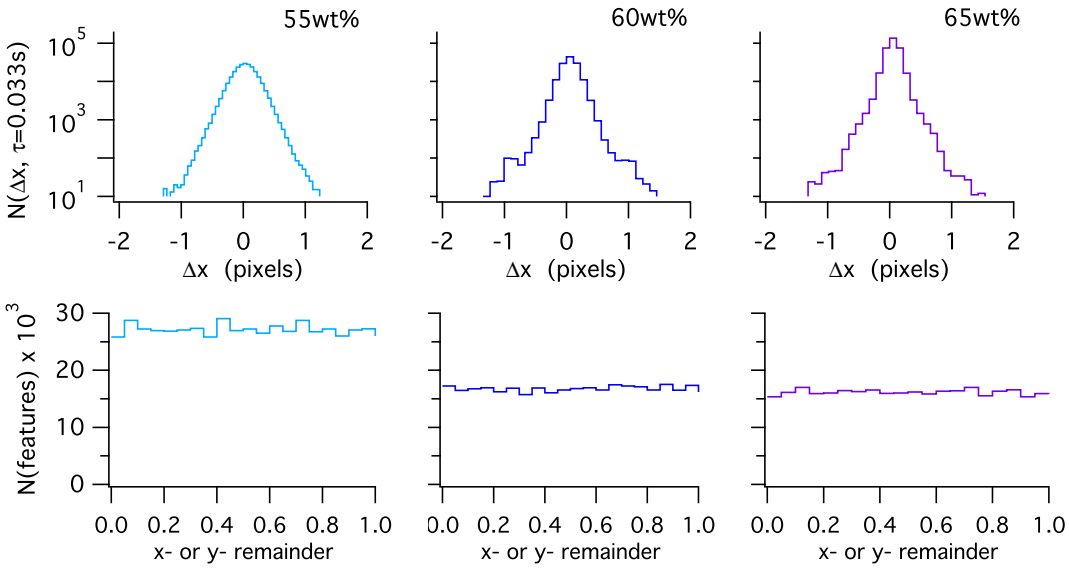

Figure 4.4: (Top) The particle displacement distributions at $\tau = 0.033$ s for 55, 60, and 65 wt%. (Bottom) Histogram of particle position remainders after the centroid confinement.

Fig. 4.3C shows the increasing deviation from the expected logarithmic slope of 1 with increasing sucrose concentration. At the shortest lag times, the probe displacement in the gel has comparable magnitude to that in the 65 wt% solution. Fig. 4.3B shows the excess kurtosis for the sucrose solutions. The excess kurtosis α_2 is proportional to $\tau^{-1.5\pm0.3}$, in agreement with Eq. 4.8, and providing experimental support for this theory and technique. However, α_2 for the 55 and 60 wt% sucrose solution begins to depart from the $\tau^{-3/2}$ scaling above $\tau > 0.2$ s, marking a regime in which this static error estimate is valid. To better demonstrate why α_2 is so high, the particle displacement distributions at the shortest lag time $\tau = 0.033$ s for all 3 sucrose samples are shown in the top row of Fig. 4.4. Each distribution has a different bin width, determined based on 2ϵ estimated from the *in situ* measurement. As concentration increases, the peak in the middle becomes more apparent, which correlates with the increase in excess kurtosis shown in Fig. 4.3. To verify that the feature tracking parameter w is not too small (and causing biased centroid corrections and peaked Van Hove distributions), the

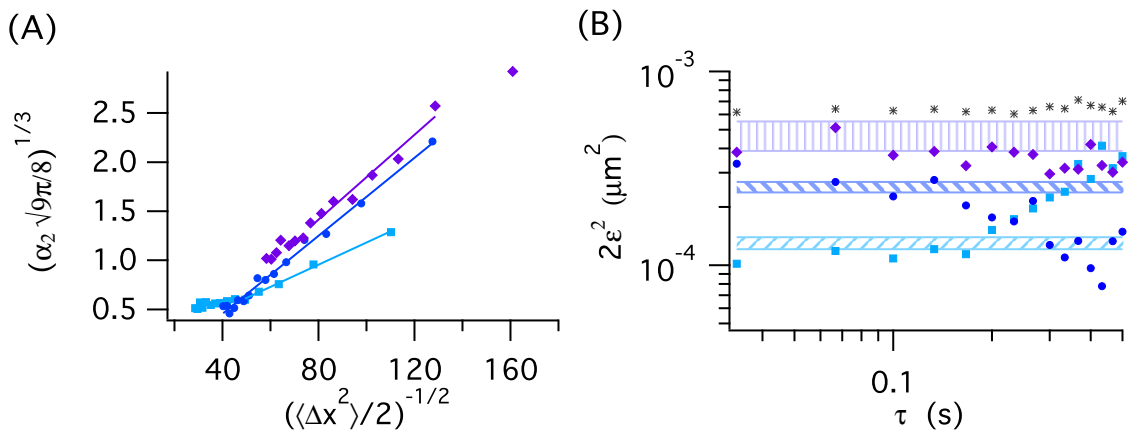

Figure 4.5: (A) Rescaled MPT data for 55 wt% (■), 60 wt% (●), and 65 wt% (♦) sucrose solutions. The lines correspond to the range of data used to fit the line $y = \epsilon x$, determined from Fig. 4.3. (B) The static error calculated based on Eq. 4.9 for each sucrose sample. The shaded regions come from the estimated ϵ using the fit from A and Eq. 4.10.

bottom row of Fig. 4.4 shows the histogram of particle location corrections made by the centroid algorithm. When the user-selected w is too small, the x- and y-coordinates will round off to the nearest integer value, causing a "dip" at 0.5 in the histogram [25]. At $w = 11$ pixels, the histograms are relative flat, indicating that the w did not cause bias in the particle locations, and thus is not the cause of the static error.

Using Eq. 4.10, the MPT results from Fig. 4.3 are rescaled and shown in Fig. 4.5A. The range of data used to calculate the slope of the line is based on where $\alpha_2 \sim \tau^{-3/2}$ no longer holds true in Fig. 4.3D. The estimated ϵ are $\epsilon_{55\%}$ =11.4 ± 0.4 nm, $\epsilon_{60\%}$ = 15.9 ± 0.5 nm, $\epsilon_{65\%}$ = 21.6 ± 1.9 nm, as compared to the gel estimation at ϵ_{gel} = 24.8 nm. Fig. 4.5B shows the static error ϵ^2, calculated using Eq. 4.9 (data points) and Eq. 4.10 (shaded region) for each sucrose sample, as well as for the gel. As in Fig. 4.3, Fig. 4.5B shows that the estimate for ϵ is invalid for $\tau > 0.2$ s for 55 and 60 wt% sucrose solutions. The estimated static error from the polyacrylamide gel is 2× higher than the static error measured *in situ* in the 55 wt% sucrose solution. In addition, there are more fluctuations in our calculated ϵ^2 using Eq. 4.9 than the MSD

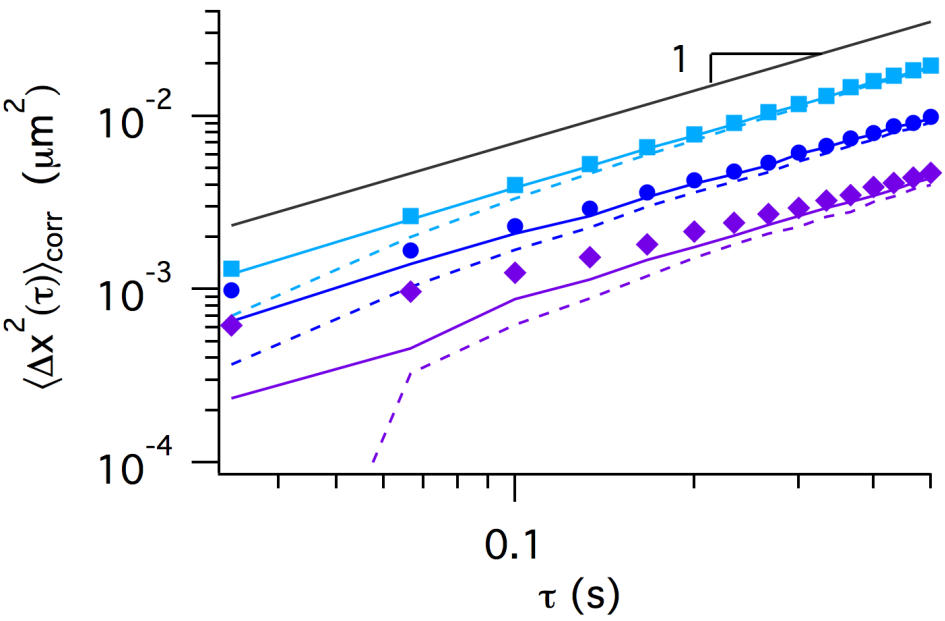

Figure 4.6: The corrected mean squared displacement based on the *in situ* measurement (solid lines) and gel estimation (dash lines) for 55 wt% (■), 60 wt% (●), and 65 wt% (♦) sucrose solutions. The *in situ* calculation is based on Eq. 4.9, i.e. the fluctuating points in Fig. 4.5B.

in the polyacrylamide gel, capturing the idea that the noise floor is dependent on the imaging condition of the sample at the moment of acquisition. Because each image has a slightly different noise-to-signal ratio (N/S) due to the background fluorescence from out-of-focus particles, these fluctuations are in agreement with Savin and Doyle [12], which showed that ϵ varies linearly with N/S.

To compare the two static error estimations, Eq. 4.2 is rearranged to calculate the corrected MSD, $\langle \Delta x^2(\tau) \rangle_{\text{corr}} = \langle \Delta \hat{x}^2(\tau) \rangle - 2\epsilon^2$. Fig. 4.6 compares the MSDs with their corrections, either from the *in situ* measurement (Fig. 4.5B) or from the gel approximation. After applying the *in situ* measurement, all samples now closely follow logarithmic slopes of 1 (solid lines in figure). However, estimating the static error using the gel overcorrects and gives slopes greater than 1 at the two shortest lag times τ from 0.033 to 0.066 s. This demonstrates the improvement of the estimate of the static error

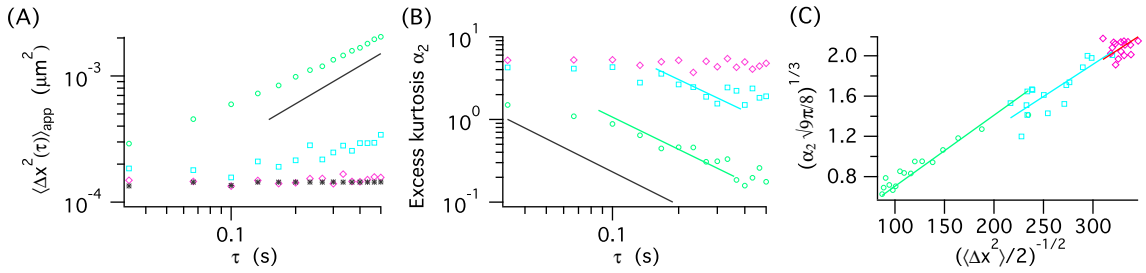

Figure 4.7: The apparent mean squared displacements (A) and excess kurtosis (B) of 1 wt% (•), 2 wt% (•)(■), and 5 wt% (⧫) 2MDa PEO solutions, from $\tau = 0.03 - 0.5$ s The noise floor or static error of this imaging system, measured using the polyacrylamide gel, is also indicated (⁕).(C) Rescaled data according to Eq. 4.10.

from the *in situ* measurement relative to the estimate from the gel.

To test the limits of the *in situ* method of measuring ϵ, Fig. 4.7 shows the short time MPT results from 1, 2, and 5 wt% 2MDa PEO.[1] At longer τ, we estimate the viscosity of these PEO solutions to be 145 ± 3.5, 1140 ± 71, and 14550 ± 645 mPa-s, respectively. At $\tau = 0.033$ s and $\epsilon = 10$ nm, $\eta_{\max} = kT\tau/3\pi a\epsilon^2 \approx 146$ mPa-s. For 1 wt% PEO solution, we see the curvature in MSD that is induced by the static error, as expected; its kurtosis also follows $\alpha_2 \sim \tau^{-3/2}$. The MSD for the 2 wt% PEO solution barely have any motions greater than what can be captured by the video, and after the initial plateau, its kurtosis also has a small region that follows $\alpha_2 \sim \tau^{-3/2}$. The MSD for the 5 wt% PEO overlaps that of the gel sample (tested in that microscopy system). From the 5 wt% and gel's MSD, the estimated static error is $\epsilon \approx 13$ nm. The scaled MSD and kurtosis data are shown in Fig. 4.7C; the 1 wt% and 2 wt% solutions data are fitted to Eq. 4.10, and the estimated static error is $\epsilon = 14.1 \pm 0.2$ nm and $\epsilon = 12.8 \pm 0.3$ nm, respectively. The kurtosis is also based on measurable displacements (Eq. 4.6); similar to the mean squared displacement, the excess kurtosis plateaus as a function of τ, and the 5 wt% PEO solution could not be fitted to Eq. 4.10. However,

[1] These experiments are done with a different microscope setup. See details in Chapter 7.

it is clear that the MSD measured for the 5 wt% PEO sample at this time scale *is* the static error, since the PEO's viscosity (14.5×10^3 mPa-s) is much greater than that of the theoretical limit (145 mPa-s).[2] This experiment has shown that, as long as there are measurable motions beyond the static error, and that the kurtosis values are not at a plateau as a function of τ, the *in situ* method will yield an estimation of ϵ and the operating regime of particle tracking microrheology (Sec. 1.5.1).

4.5 Conclusions and Outlook

This new method enables measurement of static error under *in situ* conditions, improving accuracy of the estimation of ϵ and eliminating the need for additional experiments in gel samples that are under different sample and imaging conditions. Subtracting the static error corrects the measured mean-squared displacement to recover the true mean-squared displacement, especially at lag times $\tau < 0.1$ s, where static error is most pronounced. For such viscous solutions, the optimal lag time τ for calculating the viscosity is still at $\tau > 0.5$ s, using the excess kurtosis method described in Ch. 3. However, the main advantage of this technique would be for complex fluids with an estimated longest relaxation time τ_s on the order of 0.01 – 0.1 s (i.e. the lower end of lag times that can be probed with MPT). The *in situ* measurement of ϵ accounts for the noise floor precisely, so that the true curvature of the mean-squared displacement and the non-Newtonian behavior of the fluid can be observed and analyzed. Future work should demonstrate the utility of this method in a non-Newtonian fluid with τ_s that is in the range of time scale for particle tracking experiments, such as low concentration higher molecular weight polymer solution or worm-like micellar solution.

---

[2] See corrected MSD for these PEO solutions and the discussion on emerging non-Newtonian behavior at $\tau < \tau_s$ in Chapter 7. In short, the experimental time scale is too large to detect the cross to non-Newtonian behavior.

REFERENCES

[1] J. Perrin. Mouvement brownien et réalité moléculaire. *Ann. de Chim. et Phys.*, 1909.

[2] J. C. Crocker and D. G. Grier. Methods of digital video microscopy for colloidal studies. *Journal of Colloid and Interface Science*, 179(1):298–310, 1996.

[3] J. Apgar, Y. Tseng, E. Fedorov, M. B. Herwig, S. C. Almo, and D. Wirtz. Multiple-Particle Tracking Measurements of Heterogeneities in Solutions of Actin Filaments and Actin Bundles. *Biophysical Journal*, 79(2):1095–1106, 2000.

[4] M. T. Valentine, P. D. Kaplan, D. Thota, J. C. Crocker, T. Gisler, R. K. Prud'homme, M. Beck, and D. A. Weitz. Investigating the microenvironments of inhomogeneous soft materials with multiple particle tracking. *Physical Review E*, 64(6):061506, 2001.

[5] K. M. Schultz, A. D. Baldwin, K. L. Kiick, and E. M. Furst. Rapid rheological screening to identify conditions of biomaterial hydrogelation. *Soft Matter*, 5(4): 740–742, 2009.

[6] G. Balakrishnan, D. Durand, and T. Nicolai. Particle Diffusion in Globular Protein Gels in Relation to the Gel Structure. *Biomacromolecules*, 12(2):450–456, 2011.

[7] A. Aufderhorst-Roberts, W. J. Frith, M. Kirkland, and A. M. Donald. Microrheology and Microstructure of Fmoc-Derivative Hydrogels. *Langmuir*, 30(15):4483–4492, 2014.

[8] C. J. Dibble, M. Kogan, and M. J. Solomon. Structure and dynamics of colloidal depletion gels: coincidence of transitions and heterogeneity. *Physical review. E, Statistical, nonlinear, and soft matter physics*, 74(4 Pt 1):041403, 2006.

[9] S. K. Lai, Y.-Y. Wang, D. Wirtz, and J. Hanes. Micro- and macrorheology of mucus. *Advanced Drug Delivery Reviews*, 61(2):86–100, 2009.

[10] D. S. Martin, M. B. Forstner, and J. A. Käs. 12324428. *Biophysical Journal*, 83 (4):2109–2117, 2002.

[11] C. W. Harland, M. J. Bradley, and R. Parthasarathy. Phospholipid bilayers are viscoelastic. *Proceedings of the National Academy of Sciences of the United States of America*, 107(45):19146–19150, 2010.

[12] T. Savin and P. S. Doyle. Static and Dynamic Errors in Particle Tracking Microrheology. *Biophysical Journal*, 88(1):623–638, 2005.

[13] K. M. Schultz and E. M. Furst. Microrheology of biomaterial hydrogelators. *Soft Matter*, 8(23):6198, 2012.

[14] M. K. Cheezum, W. F. Walker, and W. H. Guilford. Quantitative comparison of algorithms for tracking single fluorescent particles. *Biophysical Journal*, 81(4): 2378–2388, 2001.

[15] H. A. Houghton, I. A. Hasnain, and A. M. Donald. Particle tracking to reveal gelation of hectorite dispersions. *The European Physical Journal E*, 25(2):119–127, 2002.

[16] P.-H. Wu, S. H. Arce, P. R. Burney, and Y. Tseng. A Novel Approach to High Accuracy of Video-Based Microrheology. *Biophysical Journal*, 96(12):5103–5111, 2009.

[17] L. L. Josephson, E. M. Furst, and W. J. Galush. Particle tracking microrheology of protein solutions. *Journal of Rheology*, 60(4):531–540, 2016.

[18] J. F. Swindells, C. F. Snyder, R. C. Hardy, and P. E. Golden. Viscosities of sucrose solutions at various temperatures: Tables of recalculated values. Technical report, National Bureau of Standards, 1958.

[19] R. S. Fischer, K. A. Myers, M. L. Gardel, and C. M. Waterman. Stiffness-controlled three-dimensional extracellular matrices for high-resolution imaging of cell behavior. *Nature Protocols*, 7(11):2056–2066, 2012.

[20] T. H. Larsen. *Microrheology of responsive hydrogels*. PhD thesis, 2008.

[21] K. M. Schultz. *High-throughput microrheological characterization of biocompatible hydrogelators*. PhD thesis, 2011.

[22] D. Blair and E. Dufresne. The Matlab Particle Tracking Code Repository. *site.physics.georgetown.edu*.

[23] L. Van Hove. Correlations in Space and Time and Born Approximation Scattering in Systems of Interacting Particles. *Physical Review*, 95(1):249–262, 1954.

[24] A. Rahman. Correlations in the Motion of Atoms in Liquid Argon. *Physical Review*, 136(2A):A405–A411, 1964.

[25] J. C. Crocker and E. R. Weeks. Particle tracking using IDL, 2007. URL http://www.physics.emory.edu/faculty/weeks//idl/tracking.html.

Chapter 5

PARALLEL TEMPERATURE-DEPENDENT MICRORHEOLOGICAL MEASUREMENTS IN A MICROFLUIDIC CHIP

5.1 Introduction

Parts of this chapter were originally published in *Biomicrofluidics* in a paper titled "Parallel temperature-dependent microrheological measurements in a microfluidic chip." Reprinted with permission from [1]. Copyright © 2016 American Institute of Physics (AIP) Publishing.

The production and use of high concentration monoclonal antibody (mAb) therapeutics have grown rapidly in the pharmaceutical industry over the past decade [2]. Protein solution rheology is one of the critical physical properties that is measured during early stage development, as viscosity affects syringeability [3] and manufacturability [4], and may indicate self-associating protein-protein interactions [5], thermal stability [6], or protein aggregation propensity [7]. The effects of temperature on solution viscosity require thorough examination, as drug product manufacturing units operate at different temperatures: tangential flow filtration and thermal stability studies are often conducted at elevated temperatures (>30°C) [8, 9], whereas protein solutions are refrigerated during storage and transportation [10].

Various buffer conditions, excipients, pHs, and temperatures are found to affect solution viscosity significantly [11]. However, rheometry typically requires sample volumes greater than 100 μL, and such volume requirements limit the number of samples that can be measured. In studies of the effects of temperature, the bottleneck lies in the time needed for temperature equilibration; many viscosity measurements are not able to equilibrate multiple samples at the same time, which significantly decreases

throughput. To date, only He and coworkers [11] have demonstrated parallel temperature equilibration (30 minutes) for rheological samples in a dynamic light scattering system with block-heating. There is clearly a need for a small volume, high throughput rheological technique for protein solutions that is capable of rapid parallel temperature equilibration.

Here we demonstrate high-throughput temperature-dependent mAb viscometry by combining microrheology and microfluidics. Microrheology requires small samples, on the order of 10 μL or less, which fits the needs of early pharmaceutical development, and the micrometer dimensions of microfluidics enable rapid temperature equilibration. In the following sections, we briefly review particle tracking microrheology methods and the experimental analysis using excess kurtosis. The microfluidic sticker design and fabrication material choice are detailed. We introduce a temperature control stage using a Peltier module, locally controlling the surrounding environment of the samples and enabling us to rapidly equilibrate to a set temperature for multiple samples in a microfluidic device. Sucrose solutions are used to validate the temperature control and to develop a calibration curve. Using a biocompatible microfluidic device and our temperature control setup, 72 temperature-concentration viscosity measurements of monoclonal antibody solutions are obtained using 2 μL samples in approximately 6 hours.

5.2 Experimental methods

5.2.1 Materials

Two humanized monoclonal antibodies (mAb1 and mAb2) are supplied by Genentech Inc. (South San Francisco, CA) and stored at -80°C. The proteins are diluted serially with buffer (30 mM histidine, 0.02% Tween 20, pH 5.4). Sucrose, histidine, histidine-HCl and Tween 20 are used as received (Sigma-Aldrich).

Fluorescently labeled tracer particles are obtained from Invitrogen; the surface of the amine-modified polystyrene ($2a = 0.97 \pm 0.022$ μm) particles is chemically grafted

with poly(ethylene glycol) (PEG) through NHS ester-amine reactions using mPEG-succinimidyl carboxyl methyl ester (MW=5000, Creative PEGWorks, Winston-Salem, NC). The particles are washed by centrifuging the solution for 6 minutes at 6000 G, discarding the supernatant, and redispersing in the same volume of ultra-pure Milli-Q water (resistivity 18.2 M Ω cm, Millipore EMD). The washing procedure removes excess fluorescent dye and possible contaminants from their synthesis and storage. The PS-PEG particles are sonicated for 20 minutes and observed under a microscope to verify their colloidal stability. The final particle concentrations needed in the samples are approximately 0.1%w/v; this particle concentration prevents brightness saturation in the camera. The stock solutions of the probes are concentrated to approximately 10%w/v, so only a small volume is added to each sample.

The 1 μm size probes are chosen to satisfy the continuum assumption in the Stokes equation to measure the bulk rheological properties of the protein samples. The PEG grafted surface chemistry for the probes is selected to prevent surface adsorption by proteins. Although protein adsorption to probe surfaces does not significantly alter the hydrodynamic radius of the probes, it may induce additional interactions between probes [12].

5.2.2 Microfluidic stickers

Microfluidic stickers are used to create 12 channels, each containing 2 μL, on a single microscope coverslip. The soft imprint lithography process used to fabricate stickers is adapted from Bartolo et al. [13] and Natali et al. [14]. The structured polydimethylsiloxane (PDMS) mold is fabricated using standard photolithography methods. First, a layer of SU-8 2035 photoresist (Microchem) is spin-coated onto a silicon wafer; the photoresist film is exposed to ultraviolet light (365 nm) through a patterned mask (Fineline Imaging). PDMS is mixed in a 10:1 ratio of monomer and curing agent (Sylgard 184, Dow Corning), poured over the etched photoresist, degassed, and cured at 65°C overnight. The PDMS mold serves as the device master from which the microfluidic stickers are fabricated. Approximately 100 μL of thiolene resin (Norland

Products, NOA 81) is deposited on a flat substrate made with polyethylene (3M, film tape 483, 5.3 mm thick × 1 in wide) supported on PDMS. The master PDMS mold is gently pressed onto the thiolene resin with the help of a roller [15] and the module is exposed to UV light for 5 seconds to partially cure NOA 81. Since oxygen inhibits the free-radical polymerization in the photocuring reaction [16], the gas permeability of PDMS versus the substrate polymer is an important parameter to consider for the ease of handling of the microfluidic sticker. Polyethylene (PE) is chosen as the top layer of the substrate because its permeability is significantly less than PDMS. The sticker preferentially sticks to the PE substrate rather than the PDMS mold, which makes handling of thin sheets of microfluidic device easier. The PDMS mold is peeled away, leaving the channel sticker on the substrate. Access inlets to channels are carved on the sticker, before the assembly onto a rigid glass substrate (25 × 75 × 0.15 mm, Fisher Scientific) and final curing under UV light. The PE substrate is then peeled off, leaving the sticker on the cover slip. The process can be repeated to assemble multiple stickers comprising different microfluidic networks.

The channel height is set at 125 μm to account for 1% error in hindered particle mobility in a microfluidic channel wall [17–19]. The microfluidic sticker has 12 channels, each with dimensions 0.35 × 30 × 0.125 mm and holds approximately 2 μL sample volume (Fig. 5.1). The multiple-channel design enables the parallel temperature equilibration of multiple samples and increases the throughput of the experiments.

The choice of thiolene chemistry over the traditional PDMS serves multiple purposes. Thiolene stickers can be rapidly fabricated without heating, compared to curing of PDMS at 150°C for 10 minutes. Thiolene is impermeable to air and water vapor, preventing evaporation in the channels and is suitable for temperature studies. These advantages of the thiolene sticker decrease device fabrication time, resulting in increased overall throughput.

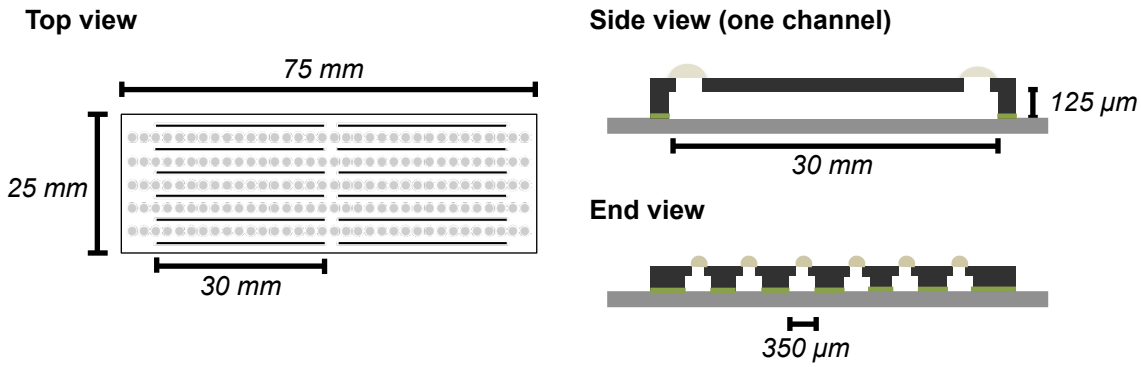

Figure 5.1: Scheme of 12-channel microfluidic sticker design. Pre-cured "sticky" layer is indicated in green, and is pressed onto a glass cover slip. Inlets are carved prior to final curing, and are sealed with additional thiolene drops.

5.2.3 Temperature control

The temperature control unit (Fig. 5.2) is built with specifications and validated as detailed in Chapter 2.

In the experimental setup, the bottleneck lies in the time to reach thermal steady state for the samples. We investigated the thermal performance of the Peltier module. On average, it takes approximately 40-60 seconds for the Peltier to change temperature by 1°C (see pg. 57 for an example of temperature ramp). The temperature is measured by a thermistor inside the aluminum block and is not in the samples. However, the heat transfer time in the aluminum block should be negligible, since its thermal diffusivity is $\alpha = 85\text{mm}^2/\text{s}$.

To verify that the sample reaches thermal equilibrium with the aluminum block, we developed a heat transfer model (see Chapter 2 for details). The set of ODEs are solved numerically using the geometry of our temperature control module using COMSOL. The simulation results confirm that as the core of the aluminum contact plate (the location of thermistor) reaches T_{set}, the temperature in the thiolene microfluidic sticker equilibrates within 1 s, and there are no discernible temperature differences between 1 s and 600 s. This shows that the temperature control bottleneck lies in

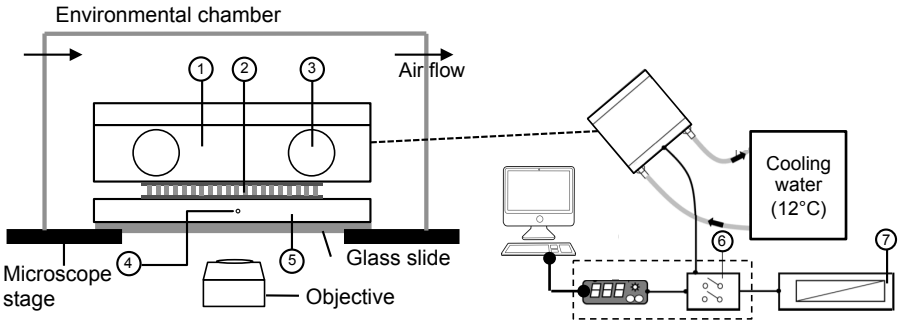

Figure 5.2: Schematic of temperature control setup. The components are: 1. copper cooling body, 2. Peltier module, 3. water circulation inlet/outlet, 4. thermistor hole, 5. aluminum contact plate, 6. PID controller with relay unit, 7. DC power.

the response of the Peltier module to the PID controller. To account for differences in sample composition, the variable speed at which dry air blows across the stage and also any 2-dimensional heat transfer effects (though we expect none), microrheology measurements are taken 7-10 minutes after T_{set} is registered to ensure equilibration across samples in the microfluidic sticker.

5.2.4 Multiple particle tracking experiments

Multiple particle tracking measurements are taken from each equilibrated sample in the microfluidic sticker. Samples are pipetted into the microfluidic channels through carved inlets, and sealed with thiolene resin. Fluorescence video microscopy with a CMOS high-speed camera (Phantom v5.1, 50 frames per second, $\sigma = 5$ ms) is used to capture the Brownian motion of the probe particles at 40 times magnification (EC Plan-Neofluar, NA 0.75, Carl Zeiss). The camera settings are selected so that the static and dynamic error of particle tracking experiments are minimized [20]. As each movie is saved, the microscope stage is moved to the next sample and refocused. The probe positions are tracked by a brightness-weighted centroid algorithm, and trajectories were formed by linking the probes found in consecutive video frames

[21].

The details of the particle tracking experiment analysis using Van Hove self-correlation and its statistical parameter excess kurtosis are described in a recent publication [22]. Here, we briefly review key aspects of the method. The rheological properties of a sample are calculated from the embedded probe particles' dynamics. The ensemble-averaged mean square displacement (MSD), $\Delta x^2(\tau)$, is calculated from the probe trajectories at each lag time τ. The generalized Stokes-Einstein relation (GSER) relates the MSD to bulk rheological properties by $J(\tau) = 3\pi a\langle\Delta x^2\rangle/kT$, where J is the material creep compliance, τ is the lag time, a is the probe radius, kT is the thermal energy. In the limit for a material with Newtonian viscosity η, $J(\tau) = \tau/\eta$, and the GSER simplifies to

$$\eta = \frac{kT}{3\pi a\langle\Delta x^2(\tau)\rangle}\tau. \tag{5.1}$$

With a sufficiently large sample of displacements, the distribution of probe displacement is expected to be a normal distribution [23], and can be written as the one-dimensional Van Hove space-time correlation function,

$$G_s(x,\tau) = (2\pi\langle\Delta x^2(\tau)\rangle)^{-1/2}\exp\left(\frac{-x^2}{2\langle\Delta x^2(\tau)\rangle}\right). \tag{5.2}$$

The Van Hove self-correlation is valid for any material that satisfies the GSER provided the probes move isotropically in space. The deviation from normal distribution of the Van Hove correlations may indicate sample heterogeneity [24] or incorrect algorithm parameters in tracking probe particles [25], and can be quantified using the excess kurtosis,

$$\alpha_2(\tau) = \frac{\langle\Delta x^4\rangle}{3\langle\Delta x^2\rangle^2} - 1, \tag{5.3}$$

to reflect tailedness and peakedness in a distribution. For a perfect normal distribution [26], $\alpha_2 = 0$. The excess kurtosis and its test statistic Z_{α_2} (calculated from the standard error of α_2) are used to determine the lag time τ at which the probe displacement distribution is closest to being Gaussian. The critical value of Z_{α_2} is 1.96 at 95%

confidence; when $|Z_{\alpha_2}| > 1.96$, α_2 is considered significantly different from zero, and the probe displacement distribution is therefore not close enough to a normal distribution for viscosity calculations. This lag time maximizes the number of displacements while minimizing the static particle tracking error.

5.3 Results and Discussion

To measure the true sample temperature on chip, it is necessary to include a standard calibration fluid alongside the samples (the details of calibration are discussed in Chapter 2). The calibration fluid validates the temperature control setup and corrects for temperature variations on chip. The choice of calibration fluid depends on the application and the range of temperatures for the experiment. An appropriate calibration fluid must have: (1) accurate viscosity data or model in the desired operating temperatures available; (2) viscosity within the operating regime of particle tracking microrheology [19]; and (3) similar thermal properties to the sample fluids (e.g. aqueous calibration fluid for aqueous samples).

5.3.1 Arrhenius behavior of mAb solutions

The temperature-dependent viscosity profiles of mAb1 and mAb2 are examined at 6 temperatures ($T_{\mathrm{MSD}} = 0.9$°C - 40°C, measured from a sucrose sample on the same chip) and shown in Fig. 5.3A-B; the mAb solutions were serially diluted two-fold from 90 mg/mL to 5.6 mg/mL. The precise temperatures of the samples were measured in situ with a 55% sucrose sample in the same microfluidic sticker. The data for 72 experiments was acquired over approximately 5 hours; with 2 μL samples, only 1.5 mg of each mAb was used in total.

The protein solution viscosity increases rapidly as a function of concentration for both proteins. Fig. 5.3A-B show the important role of protein-protein self-association in the material rheological properties. Though both proteins are of the same IgG1 framework with only 2% sequence differences in the CDR regions[27, 28], the viscosity behavior at concentrations above 22 mg/mL differ drastically.

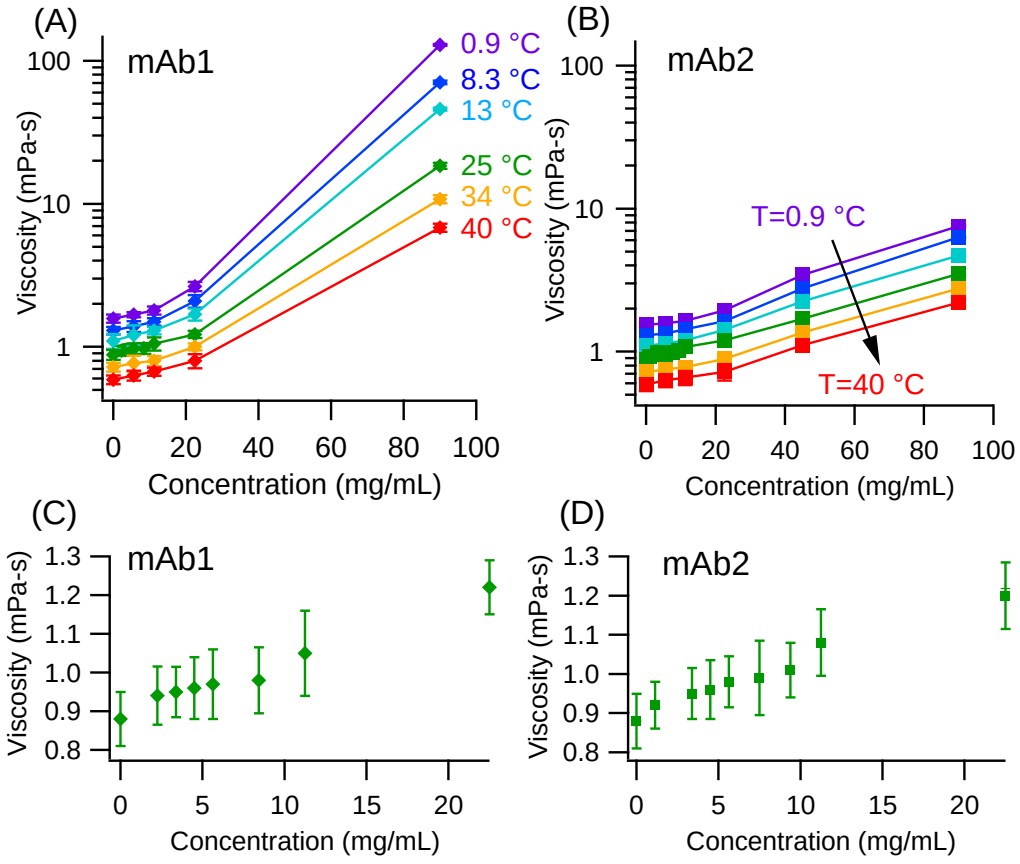

Figure 5.3: Viscosity profile for mAb solutions. (A-B) Viscosity of mAb1 and mAb2, respectively, as a function of concentration and temperature. The various colors represent data collected at 6 different temperatures, and the lines are drawn to guide the eye. (C-D) Viscosity of mAb1 and mAb2 from 0 mg/mL to 22 mg/mL at 25 °C. Note the axis only goes from 0.8 mPa-s to 1.3 mPa-s; microrheology can measure small incremental changes in viscosity.

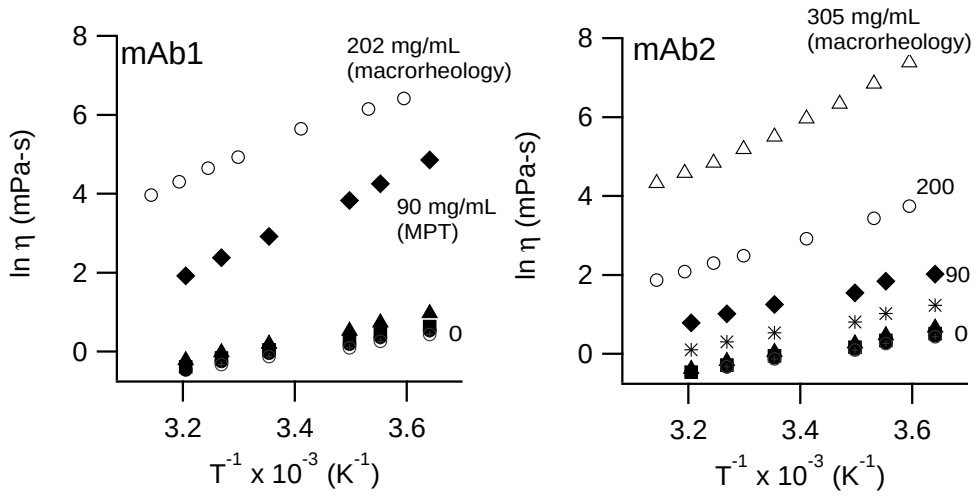

Figure 5.4: Semi-logarithmic plot of viscosity against inverse temperature. Open symbols are experiments performed with a cone-and-plate rheometer.

Particle tracking microrheology is sensitive in detecting small viscosity changes, as evident in the incremental changes in buffer viscosity (0.7 - 1.7 mPa-s) in the range of temperature examined. The mAb solutions are further diluted in the range of 1 - 10 mg/mL and their viscosity measured at 25°C (Fig. 5.3C-D), and the same observation holds. Microrheology is capable of measuring low viscosities, because its measurement sensitivity is only related to particle tracking noise level in the microscope setup [29]. Such sensitivity may not hold true for bulk rheometry, as the mechanical torque sensitivity sets the limit of the instrument, and Hellström *et al.* [30] show that sample underfilling leads to errors in rheometry measurements in low viscosity samples.

The effect of temperature on protein solution viscosity is illustrated in Fig. 5.4, with a plot of ln η as a function of $1/T$. A linear correlation is found between ln η and inverse temperature, indicating that the relation can be expressed by the Arrhenius equation, which views flow as an activated process and the motions between molecules depend exponentially on the temperature, with $\ln \eta = E_a/RT$, where E_a is the activation energy and R the gas constant. The solution viscosity of a material departs from

the Arrhenius equation when there is strong association between molecules, for example as water approaches its freezing point, or other long-range fluctuations leading to non-linear effects. Protein solutions typically exhibit nearly Arrhenius behavior, with an apparent activation energy dependent on the protein molecule, its concentration, and excipients in the solution [31, 32]. Temperature studies are therefore informative in evaluating whether protein solutions exhibit such behaviors.

We observe Arrhenius behavior for the two monoclonal antibody solutions, and similar values in the apparent activation energy between mAbs at low concentrations (5.6 - 22.5 mg/mL). However, 90 mg/mL mAb1 exhibits higher activation energy than mAb2 at the same concentration, and it takes $\sim$50% more mAb2 at 305 mg/mL to achieve a similar viscosity profile as 202 mg/mL mAb1. Data such as this may be useful in future understanding of protein-protein interaction and self-association in concentrated systems; here we simply demonstrate the capability of parallel temperature-dependent microrheological measurements in microfluidic channels. Our setup makes it possible to examine the effect of temperature on the material even when the amount of sample is too small (less than 10 μL) to be measured by macrorheology.

5.4 Conclusions

Accurate in situ measurement of temperature is obtained by inserting the calibration fluid in the same microfluidic device with protein samples. We demonstrate that 72 temperature-concentration viscosity measurements of mAb solutions can be made in a single day. Particle tracking microrheology combined with microfluidics can be used to explore the rheology of protein solutions as a function of concentration and temperature, and our setup increases experimental throughput significantly by eliminating temperature equilibration in each sample separately, such as in traditional rheometry. Interfacing with higher throughput sample preparation using droplet microfluidics would be straightforward, resulting in rapid acquisition of formulation or solution conditions library available at early stage pharmaceutical development.

REFERENCES

[1] L. L. Josephson, W. J. Galush, and E. M. Furst. Parallel temperature-dependent microrheological measurements in a microfluidic chip. *Biomicrofluidics*, 10(4): 043503, 2016.

[2] S. R. Aggarwal. What's fueling the biotech engine 2012 to 2013. *Nature Biotechnology*, 32(1):32–39, 2014.

[3] V. Burckbuchler, G. Mekhloufi, A. P. Giteau, J. L. Grossiord, S. Huille, and F. Agnely. Rheological and syringeability properties of highly concentrated human polyclonal immunoglobulin solutions. *European Journal of Pharmaceutical Sciences*, 76(3):351–356, 2010.

[4] S. J. Shire. Formulation and manufacturability of biologics. *Current Opinion in Biotechnology*, 20(6):708–714, 2009.

[5] S. Kanai, J. Liu, T. W. Patapoff, and S. J. Shire. Reversible self-association of a concentrated monoclonal antibody solution mediated by Fab-Fab interaction that impacts solution viscosity. *Journal of Pharmaceutical Sciences*, 97(10):4219–4227, 2008.

[6] C. Liu, C. Vailhe, N. Samuel, and Q. Min. A simple and reproducible approach to characterize protein stability using rheology. *International Journal of Pharmaceutics*, 374(1-2):1–4, 2009.

[7] W. Cheng, S. B. Joshi, N. K. Jain, F. He, B. A. Kerwin, D. B. Volkin, and C. R. Middaugh. Linking the Solution Viscosity of an IgG2 Monoclonal Antibody to

Its Structure as a Function of pH and Temperature. *Journal of Pharmaceutical Sciences*, 102:4291–4304, 2013.

[8] F. He, C. E. Woods, E. Trilisky, K. M. Bower, J. R. Litowski, B. A. Kerwin, G. W. Becker, L. O. Narhi, and V. I. Razinkov. Screening of monoclonal antibody formulations based on high-throughput thermostability and viscosity measurements: Design of experiment and statistical analysis. *Journal of Pharmaceutical Sciences*, 100(4):1330–1340, 2010.

[9] J. Rubin, A. Sharma, L. Linden, A. S. Bommarius, and S. H. Behrens. Gauging Colloidal and Thermal Stability in Human IgG1–Sugar Solutions through Diffusivity Measurements. *Journal of Physical Chemistry B*, 118(11):2803–2809, 2014.

[10] T. Palm, E. Sahin, and R. Gandhi. The Importance of the Concentration–Temperature–Viscosity Relationship for Development of Biologics, 2015. URL http://www.bioprocessintl.com/manufacturing/antibody-non-antibody/importance-concentration-temperature-viscosity-relationship-development-biologics/.

[11] F. He, C. E. Woods, J. R. Litowski, L. A. Roschen, H. S. Gadgil, V. I. Razinkov, and B. A. Kerwin. Effect of Sugar Molecules on the Viscosity of High Concentration Monoclonal Antibody Solutions. *Pharmaceutical Research*, 28(7):1552–1560, 2011.

[12] S. V. Sule, C. D. Dickinson, J. Lu, C.-K. Chow, and P. M. Tessier. Rapid Analysis of Antibody Self-Association in Complex Mixtures Using Immunogold Conjugates. *Molecular Pharmaceutics*, 10(4):1322–1331, 2013.

[13] D. Bartolo, G. Degre, P. Ngheb, and V. Studer. Microfluidic stickers. *Lab on a Chip*, 8:274–279, 2008.

[14] M. Natali, S. Begolo, T. Carofiglio, and G. Mistura. Rapid prototyping of multilayer thiolene microfluidic chips by photopolymerization and transfer lamination. *Lab on a Chip*, 8(3):492, 2008.

[15] R. Arayanarakool, S. Le Gac, and A. van den Berg. Low-temperature, simple and fast integration technique of microfluidic chips by using a UV-curable adhesive. *Lab on a Chip*, 10(16):2115, 2010.

[16] H. E. Jeong and K. Y. Suh. On the role of oxygen in fabricating microfluidic channels with ultraviolet curable materials. *Lab on a Chip*, 8(11):1787–1792, 2008.

[17] H. Faxén. Der Widerstand gegen die Bewegung einer starren Kugel in einer zähen Flüssigkeit, die zwischen zwei parallelen ebenen Wänden eingeschlossen ist. *Annalen der Physik*, 373(10):89–119, 1922.

[18] J. Happel and H. Brenner. *Low Reynolds Number Hydrodynamics: with special applications to particulate media*. Prentice-Hall, 1965.

[19] K. M. Schultz and E. M. Furst. High-throughput rheology in a microfluidic device. *Lab on a Chip*, 11(22):3802–3809, 2011.

[20] T. Savin and P. S. Doyle. Static and Dynamic Errors in Particle Tracking Microrheology. *Biophysical Journal*, 88(1):623–638, 2005.

[21] J. C. Crocker and D. G. Grier. Methods of digital video microscopy for colloidal studies. *Journal of Colloid and Interface Science*, 179:298–310, 1996.

[22] L. L. Josephson, E. M. Furst, and W. J. Galush. Particle tracking microrheology of protein solutions. *Journal of Rheology*, 60(4):531–540, 2016.

[23] L. Van Hove. Correlations in Space and Time and Born Approximation Scattering in Systems of Interacting Particles. *Physical Review*, 95(1):249–262, 1954.

[24] E. R. Weeks. Three-Dimensional Direct Imaging of Structural Relaxation Near the Colloidal Glass Transition. *Science*, 287(5453):627–631, 2000.

[25] J. C. Crocker and E. R. Weeks. Particle tracking using IDL, 2007. URL http://www.physics.emory.edu/faculty/weeks//idl/tracking.html.

[26] L. T. DeCarlo. On the meaning and use of kurtosis. *Psychological Methods*, 2(3): 292, 1997.

[27] S. Yadav, A. Sreedhara, S. Kanai, J. Liu, S. Lien, H. Lowman, D. S. Kalonia, and S. J. Shire. Establishing a Link Between Amino Acid Sequences and Self-Associating and Viscoelastic Behavior of Two Closely Related Monoclonal Antibodies. *Pharmaceutical Research*, 28(7):1750–1764, 2011.

[28] A. Chaudhri, I. E. Zarraga, S. Yadav, T. W. Patapoff, S. J. Shire, and G. A. Voth. The Role of Amino Acid Sequence in the Self-Association of Therapeutic Monoclonal Antibodies: Insights from Coarse-Grained Modeling. *Journal of Physical Chemistry B*, 117(5):1269–1279, 2013.

[29] K. M. Schultz and E. M. Furst. Microrheology of biomaterial hydrogelators. *Soft Matter*, 8(23):6198, 2012.

[30] L. H. O. Hellström, M. A. Samaha, K. M. Wang, A. J. Smits, and M. Hultmark. Errors in parallel-plate and cone-plate rheometer measurements due to sample underfill. *Measurement Science & Technology*, 26(1):015301, 2015.

[31] K. Monkos. Concentration and temperature dependence of viscosity in lysozyme aqueous solutions. *Biochimica et Biophysica Acta*, 1339(2):304–310, 1997.

[32] K. Monkos. Viscosity analysis of the temperature dependence of the solution conformation of ovalbumin. *Biophysical Chemistry*, 85(1):7–16, 2000.

Chapter 6

MICRORHEOLOGY OF BISPECIFIC MONOCLONAL ANTIBODIES AND THEIR MONOSPECIFIC MIXTURES

6.1 Introduction

The generation of human and humanized versions of monoclonal antibodies (mAbs), as well as improvements in processing and manufacturing, have contributed substantially to the landscape of mAbs as the ever growing class of biotherapeutics [1–5]. The next wave of mAb therapeutics aims to enhance efficacy and targeting to antigens, and one novel approach is dual targeting strategies with bispecific antibodies (BsAbs) [6]. Bispecific antibodies have two distinct binding antigens, and genetic engineering advances have resulted in over 60 different formats (for a comprehensive overview on the available formats, see [7–9]). BsAbs have several capabilities: (1) redirecting immune cells to tumor cells to enhance tumor killing, (2) blocking two mediators or pathways simultaneously, and (3) interacting with two different surface antigens to increase binding specificity [10].

There are more than 30 BsAbs currently in clinical trials for autoimmune, oncology, or chronic inflammatory indications. Because bispecific antibodies are still emerging therapeutics, much of the literature is focused on antibody engineering, overcoming synthesis challenges, and purification and production of BsAb. These topics are typically part of the technology platforms, which include: tandem diabody (TandAb) [11], nanobodies [12], "dock-and-lock" with kinase anchor protein [13], HSA-antibody fusion [14], dual variable domain immunoglobulin (DVD-Ig^{TM}) [15], "two-in-one" [16], Triomab® [17], IgG-scFv [18], CrossMab [19], immune mobilizing monoclonal T-cell receptors against cancer (ImmTac) [20], and bispecific T-cell engager (BiTE®) [21].

As BsAbs approach late-stage development, many issues may arise that are unique to these new antibody formats. For mAbs, in-depth studies on protein-protein interaction [22–25], solution microstructure [26–28], solvent interactions [29–31], and interfacial behavior (solid/liquid [32–34] or air/liquid [33, 35–37]) are done to provide deeper molecular insights and to aid the finalization of drug products. Although one study of aggregation kinetics and protein-protein interaction of a DVD-Ig^{TM} [38] has been published, such protein characteristics have not been well-established in the literature for BsAbs. These studies can be time consuming, and are typically reserved for molecules that are further in development (and more abundantly available for collaborations in academia). In contrast, quick screening studies are used in early stage development, and must satisfy time constraints when transitioning from late stage research to Phase 1.

Solution rheology is one such critical biophysical parameter that is screened during early therapeutics development, as downstream processing and manufacturing steps (such as filtration, pumping and filling) are substantially affected by the protein solution viscosity [39]. In early stages of development, material is scarce, and thus a small-scale rheology technique is needed to do these viscosity measurements. Unlike the vast literature on mAb viscosity and its molecular basis [22, 23, 25–28, 36, 40–59], there is only one dedicated viscosity study [60] on a bispecific antibody to date (in the DVD-Ig^{TM} format). The protein molecule used in this study had a larger molecular weight (∼200 kDa) than the comparison mAb, a normal monospecific IgG (∼150 kDa), and thus a larger size and intrinsic viscosity; the effect of molecule size on the viscosity was found to be significant at high concentrations, but Raut and Kalonia [60] did not directly compare therapeutic mAbs of similar size. This presents a new opportunity to study a bispecific antibody to compare with mAbs constructed with the same indications and molecular weight. These proteins are in the early stages of development, and microrheology enables viscosity measurements that would otherwise be difficult due to material constraints.

Multiple particle tracking (MPT) microrheology has been used to measure the

rheology of many biological fluids and biomaterials under different conditions, including concentrated genomic DNA solutions [61, 62], bovine serum albumin and its viscoelastic response with the addition of urea [63], protein–layer and network formation of amyloid fibrils [64–66]. MPT microrheology requires small sample volumes (on the order of μL), has short acquisition times (on the order of seconds), and can probe multiple frequencies simultaneously; these capabilities permit high-throughput characterization of scarce materials [63, 67, 68], which fills the need for small volume rheology in early pharmaceutical development stages. We have previously demonstrated the use of multiple particle tracking microrheology to measure mAb viscosity with 2 μL samples [69].

In this study, we discuss the discovery of surprising viscosity results of monospecific mAbs, bispecific mAbs, and mixtures thereof, using small-sample microrheology experiments. In the following sections of this chapter, we first briefly review particle tracking microrheology (MPT), short guard column size exclusion chromatography (SEC), and light scattering methods, and describe the mAbs and BsAbs. We measured the viscosity profiles of three monospecific mAbs, two bispecific antibodies BsAbs, and two mAb mixtures, and we discuss in two sections the non-interacting mAbs and the cross-interacting mAbs. The viscosity profiles are analyzed using the Arrhenius mixture rule, as well as a hard quasispherical model to estimate the intrinsic viscosity $[\eta]$ and infer the self-association of the antibodies. A short column SEC method is used in an attempt to observe the existence and dissociation of reversible dimers in the bispecific antibodies. The protein-protein interactions are examined using static and dynamic light scattering, and the resulting second virial coefficient B_{22}, interaction parameter (k_D), and collective diffusion coefficient (D_c) are analyzed in conjunction with the viscosity results. The measured protein-protein interaction parameters are not sufficient for predicting trends in mAb viscosity, and thus we conclude with a proposed explanation for the mechanism behind the rapid increase in viscosity as detected by microrheology.

6.2 Experimental methods

This section begins with a description of monoclonal antibodies and probe particles used in the experiments. The proteins used in these investigations are described in detail in Chapter 2 and briefly here. Characterization of the solution viscosity is done using multiple particle tracking microrheology, described in detail in the Experimental methods section of Chapter 2 and the analysis detailed in Chapter 3. The preparation of the formulation buffer and the protein solutions used in this study are described in Chapter 2. The specific solution compositions are described in this section.

6.2.1 Materials

Three humanized monospecific monoclonal antibodies (mAb-A, mAb-B, mAb-C) and two bispecific monoclonal antibodies (BsAb-A/B, and BsAb-A/C, produced through the knob-into-hole approach and the co-culture of bacterial strains [70]) are supplied by Genentech Inc. (South San Francisco, CA) and stored at 4°C. The protein properties are reported in Table 6.1. Ultra-pure water and formulation buffers are filtered using a bottle-top filter unit prior to use (Nalgene rapid-flow sterile disposable filter units, surfactant-free cellulose acetate membrane, 0.2 μm pore size, #161-0020, Thermo Fisher Scientific). The proteins are first buffer-exchanged into the formulation buffer (20 mM histidine chloride, pH 6.0) using Slide-A-Lyzer dialysis cassettes (10k molecular weight cut off, #66385, Thermo Fisher Scientific). The stock (concentrated) protein solutions are then diluted serially with the formulation buffer. Their concentrations are determined from the average of 5 measurements in a Nanodrop 2000c (Thermo Fisher Scientific) at 1:10 dilution factor. The extinction coefficient at 280 nm (A_{280}) used for the Nanodrop measurements is reported in Table 6.1. The 20 mM histidine buffer is prepared and adjusted to pH 6.0 by combining 9 mM L-histidine free-base and 11 mM L-histidine-HCl (Sigma Aldrich).

Fluorescently labeled tracer particles are obtained from Molecular Probes (Eugene, OR); the surface of the carboxylate-modified polystyrene (PS-CML) ($2a = 1.0 \pm 0.025$ μm, 2% solids) particles are chemically grafted with poly(ethylene glycol) (PEG)

Table 6.1: Properties of monoclonal antibodies in this chapter

Molecule	MW (kDa)	Ext. Coefficient (mg/mg-cm)	Theoretical pI
mAb-A	145.0	1.430	6.25
mAb-B	145.2	1.540	9.25
mAb-C	144.9	1.353	6.95
BsAb-A/B	145.2	1.528	7.40
BsAb-A/C	144.9	1.430	6.45

through carbodiimide reaction. The PS-CML particles (500 μL) are first washed with Milli-Q water three times, and then dispersed in 50 mM MES with 0.05% Proclin 300 at pH 5.2 (Polylink coupling buffer, Polysciences, Inc, Warrington, PA). A 100 μL solution of 200 mg/mL of 1-ethyl-3-(-3-dimethylaminopropyl) carbodiimide (EDAC, Polysciences) is made in the coupling buffer; 50 μL of this activation solution is added to the particle suspension immediately and the mixture is incubated at room temperature under rotation for 15 minutes. This step activates the carboxylate end-groups on the surface of the probe particles to become o-acylisourea intermediates; the acidic environment of the coupling buffer helps extend half-life of the intermediates. The supernatant in the probe-EDAC mixture is discarded, and the probe particles are immediately resuspended in the amine-modified PEG solution, which is made by dissolving 100 mg of methyl-PEG-amine (MW=5000 or 10000, Creative PEGWorks, Winston-Salem, NC) in 500 μL of 200 mM PBS buffer at pH 7.0. The reaction is allowed to proceed for at least 8 hours at room temperature, under rotation and shielded from light. Excess EDAC, and isourea by-products, unreacted amines are removed by washing the reacted probes in solution at least 3 times in Milli-Q water. The resulting PEGylated polystyrene (PS-PEG) particles are sonicated for 20 minutes and observed under a microscope to verify their colloidal stability in water and the formulation buffer. The stock solutions of the probes are concentrated to approximately 10% w/v, so only a small volume (0.1 μL) of probes is added to each 20 μL sample, resulting in a final

particle concentration of approximately 0.1% w/v.

6.2.2 Particle tracking microrheology and viscosity analysis

Multiple particle tracking measurements on the protein solutions are taken from each equilibrated sample in capillary tubes (inside diameter = 2.0 x 0.2 x 50 mm, glass thickness = 0.14 mm, part #3520, Vitrocom, Mountain Lakes, NJ) sealed with a fast-curing thiolene resin (NOA81, Norland Products, Cranbury, NJ) onto a microscope slide. Fluorescence video microscopy is performed on a Nikon Ti-E perfect focus inverted microscope equipped with a motorized X,Y stage and a high-speed camera (Clara interline CCD camera, Andor, Oxford Instruments, 30 frames per second, σ = 10 ms); the Brownian motion of the probe particles is captured at 40× magnification (ELWD Plan Fluor objective, NA 0.6, Nikon). The camera settings are selected so that the static and dynamic error of particle tracking experiments are minimized [71] and the time step is constant at the desired frames per second. As each movie is saved, the microscope stage is moved to the next sample and refocused. The image stacks are analyzed in MATLAB, where the probe positions are tracked by a brightness-weighted centroid algorithm first developed by Crocker and Grier [72], and trajectories are formed by linking the probes found in consecutive video frames.

The detailed analysis of the particle tracking trajectories and statistics using the Van Hove self-correlation and excess kurtosis, a statistical parameter, are described in Chapter 2 and 3, and reviewed in essence here. The rheology of the material of interest is extracted from the dynamics of the embedded probe particles. The ensemble-averaged mean square displacement (MSD), $\langle \Delta x^2(\tau) \rangle$, is calculated from the probe trajectories at each lag time τ. The Stokes-Einstein-Sutherland relation relates the MSD to bulk viscosity η by

$$\eta = \frac{kT}{3\pi a \langle \Delta x^2(\tau) \rangle} \tau. \tag{6.1}$$

where a is the probe radius and kT is the thermal energy. With a sufficiently large sample of displacements, the distribution of probe displacement is expected to be a

Gaussian distribution [73], and is mathematically equivalent to the one-dimensional Van Hove space-time correlation function,

$$G_s(x,\tau) = (2\pi\langle\Delta x^2(\tau)\rangle)^{-1/2}\exp\left(\frac{-x^2}{2\langle\Delta x^2(\tau)\rangle}\right). \tag{6.2}$$

Provided the probes move isotropically in space, Eq 6.2 is valid for any material that satisfies the Stokes-Einstein-Sutherland relation. The deviation from a Gaussian distribution of the Van Hove functions can be quantified using the excess kurtosis,

$$\alpha_2(\tau) = \frac{\langle\Delta x^4\rangle}{3\langle\Delta x^2\rangle^2} - 1, \tag{6.3}$$

which reflects tailedness and peakedness in a distribution, with the excess kurtosis of a perfect normal distribution being zero [74]. The parameter α_2 and its test statistic Z_{α_2}, calculated from the standard error of α_2 [69], are used to select the optimal lag time τ at which the probe displacement distribution is closest to being a normal distribution. At 95% confidence, Z_{α_2} has a critical value of 1.96; α_2 is considered statistically different from zero when $|Z_{\alpha_2}| > 1.96$, and the probe displacement distribution is therefore not used for viscosity calculations. The optimal lag time selected using this method maximizes the sample size of the displacement distribution while minimizing the particle tracking error induced by the noise floor.

To analyze the viscosity profiles of the bispecific antibodies and detect potential protein interactions, the viscosities of their 1:1 monospecific antibody mixtures are measured. The expected viscosity of the antibody mixtures can be calculated using Arrhenius's mixture model, which states that the logarithm of the viscosity of a mixture η_{mix} varies linearly with the proportions of its components,

$$\ln(\eta_{mix}) = \sum x_i \cdot \ln(\eta_i). \tag{6.4}$$

In other words, for a 1:1 binary mixture between component A and B,

$$\ln(\eta_{\text{mix}}) = x_{\text{A}} \cdot \ln(\eta_{\text{A}}) + x_{\text{B}} \cdot \ln(\eta_{\text{B}}) \tag{6.5}$$

where $x_{\text{A}} = x_{\text{B}} = 0.5$. Previously Galush et al. [75] tested this simple mixing relation on 3 different mAbs (at 250 mg/mL with 20 mM histidine chloride and 200 mM arginine chloride, $\eta_{\text{mAb1}} = 87.9$ cP, $\eta_{\text{mAb2}} = 139$ cP, $\eta_{\text{mAb3}} = 1670$ cP), and found that the Arrhenius rule predicts the viscosity of the antibody mixtures across different concentrations and compositions. Despite their own complex viscosity behaviors (especially at high concentrations), combinations of these proteins still agree well with Eq. 6.5, even though the equation does not contain terms that account for different interactions between the components. It may be that these IgG1 antibody molecules (with 99% sequence identity outside the complementarity determining region (CDR) and >91% sequence identity overall) do not experience cross-interactions that are fundamentally different from their own protein-protein interactions. Significantly different intramolecule interactions could give rise to a mixture viscosity that deviates from the predictions of the Arrhenius mixing relation (Eq. 6.4). Such deviations have been observed in mixtures of organic solvents [76–78].

6.2.3 Size exclusion chromatography with short guard columns

The size exclusion chromatography (SEC) method uses a high-performance liquid chromatography (HPLC) guard column (4.6 mm inside diameter, 3.5 cm length) packed with 4 μm silica particles (TSKgel SuperSW3000, Tosoh Bioscience, #18762). The mobile phase is 0.1 M K_3PO_4/0.125 M KCl, pH 6.2. Flow rates are varied from 0.0625 to 2.0 mL/min. The column pressure is maintained below 75 bar and the column temperature is maintained at 25°C. The injection volume is 5.0 μL. Detection wavelengths of 214 and 280 nm are used. Freshly prepared mobile phases are equilibrated with the column for 30 min at a flow rate of 1.0 mL/min. A Waters Alliance HPLC System with an autosampler is used for all experiments.

The stock solutions of 180 mg/mL BsAb-A/C and 100 mg/mL BsAb-A/B in the formulation buffer are directly diluted to 20 mg/mL using the mobile phase. The subsequent serial dilution to prepare the SEC samples is done in factors of $\sqrt{10}$, resulting in 6 concentrations at 0.01, 0.02, 0.06, 0.2, 0.63, 2.0, 6.3, and 20 mg/mL. The retention volume of proteins is determined as the product of retention time $\times$ mobile phase flow rate (0.0625 – 2.0 mL/min).

6.2.4 Static light scattering

Static light scattering (SLS) experiments are conducted using a DAWN-HELEOS II Multi-Angle Light Scattering (Wyatt, Santa Barbara, CA) instrument (MALS) with laser wavelength of 658.9 nm with temperature maintained at 25°C to quantify protein-protein interactions (PPI). In SLS, the average scattered intensity at a given angle can be determined and used to calculate the excess Rayleigh scattering, R_{90}^{ex} , as previously reported [79, 80], by

$$\frac{R_{90}^{\text{ex}}}{K} = M_{\text{w,app}} c_2 - 2 M_w B_{22} {c_2}^2 \tag{6.6}$$

where $\frac{R_{90}^{\text{ex}}}{K}$ is the excess Rayleigh scattering, $M_{\text{w,app}}$ and M_w are the apparent and true molecular weight of the protein, c_2 is the concentration of protein, and B_{22} is the osmotic second virial coefficient, protein-protein interaction parameter. The osmotic second virial coefficient describes deviation from ideality caused by PPI. In this instance, a positive and negative value of B_{22} corresponds to repulsive and attractive interactions, respectively.

6.2.5 Dynamic light scattering

Dynamic light scattering (DLS) experiments are conducted using a Wyatt DynaPro Plate Reader II (Wyatt, Santa Barbara, CA) at 833 nm laser wavelength, 158° scattering angle in 384 well plate with sample volume of 40 μL. An image of each well is taken during measurement and examined to make sure there are no bubbles or visible dust in all samples. In DLS, the time dependence of the fluctuation of the scattered light is measured using a detector and autocorrelator. The acquired

intensity autocorrelation function $g^2(t)$ is used to calculate the collective diffusion coefficient using the method of cumulants in Wyatt Technology Dynamics Software. DLS measurements were taken for protein concentrations of 1 to 170 mg/mL.

The collective diffusion coefficient is related to the protein interaction (k_D) parameter via a series expansion as a function of the protein concentrations in the dilute regime. At dilute condition,

$$D_C = D_0(1 + k_D c_2) \tag{6.7}$$

where D_c and D_0 are the mutual (collective) and infinite dilution-diffusion coefficient, respectively [25].

6.3 Results and Discussion

6.3.1 Viscosity results of non-interacting antibodies

Microrheology requires the probe particles to be dispersed throughout the samples, and through microscopy imaging, it provides immediate visual confirmation of the particle stability and dispersion. PS-PEG probe particles dispersed in all five monoclonal antibodies have good stability over the concentration range of 1 mg/mL to 150 mg/mL in the formulation buffer of 20 mM histidine chloride; thus, the samples are used for particle tracking experiments without further consideration.

We measure the viscosity of the three monospecific mAbs (A, B, C) and two bispecific antibodies (BsAb-A/B, BsAb-A/C). In Fig. 6.1 we first show the mean squared displacement (MSD) as a function of lag time τ for the first set of proteins – mAb-A, mAb-C, and BsAb-A/C. The inherent noise in determining the position of particles is also indicated; this noise floor primarily comes from fluorescence of particles outside the focal plane, photon shot noise, camera readout noise, and digitization noise [71]. The noise floor ($\epsilon \sim 10$ nm) is estimated by tracking the particle positions of identical 1 μm diameter probes trapped in a stiff polyacrylamide gel with a gel modulus that lies outside of the operating regime of particle tracking microrheology [81, 82].

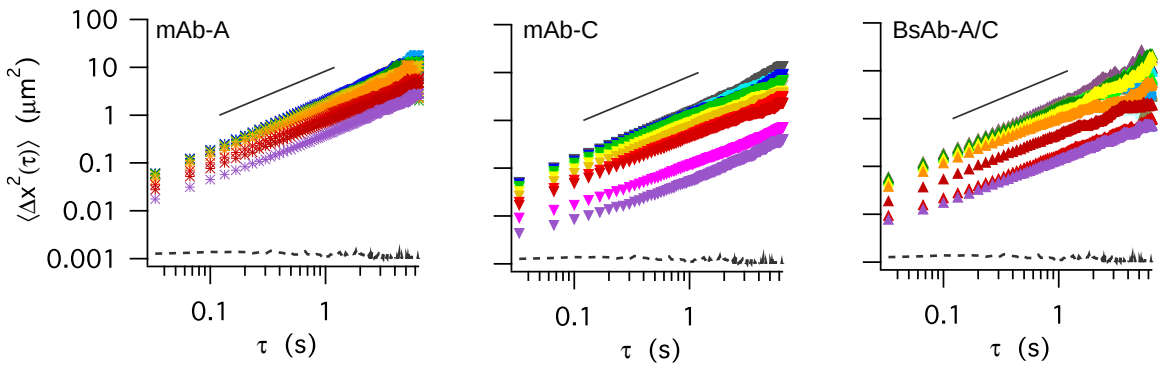

Figure 6.1: The mean squared displacements of mAb-A, mAb-C, and BsAb-A/C in 20mM histidine chloride, pH 6.0 at 23°C. Each monoclonal antibody has 12-15 concentrations, ranging from 1 mg/mL to approximately 150 mg/mL. The solid black line indicates logarithmic slope of 1, and the dash line indicates the noise floor of this imaging system.

The apparent MSDs of the three protein solutions at all concentrations are greater than the particle tracking noise floor, and have a logarithmic slope of 1, an indicator that the solutions are Newtonian, or that non-Newtonian behavior occurs on timescales smaller than the shortest lag time of the experiment. At small lag times ($\tau \leq 0.2$ s) the mean squared displacements of mAb-C at their highest concentration have a slight curvature due to static error in particle tracking, since not all the probes have moved beyond the minimum measurable displacement. The true MSDs can be recovered by subtracting the noise from the apparent MSD, $\langle \Delta x^2 \rangle_{\text{true}} = \langle \Delta x^2 \rangle_{\text{apparent}} - 2\epsilon^2$ [71]. At large lag times ($\tau > 5$ s), the MSDs fluctuate, which arises from probes diffusing in and out of the focal plane and the corresponding loss of statistics.

The excess kurtosis and its Z-statistic parameter are used to determine the optimal lag time τ for viscosity calculations, as described above in the methods section. The Van Hove self-correlations are calculated between $\tau = 0.08$ s and $\tau = 0.78$ s for different concentrations of the three antibody solutions in 20mM histidine chloride at pH 6.0. Fig. 6.2 shows the calculated viscosity of the three protein solutions, as well as the 1:1 mixtures of (mAb-A + mAb-C), as a function of concentration. Of the three

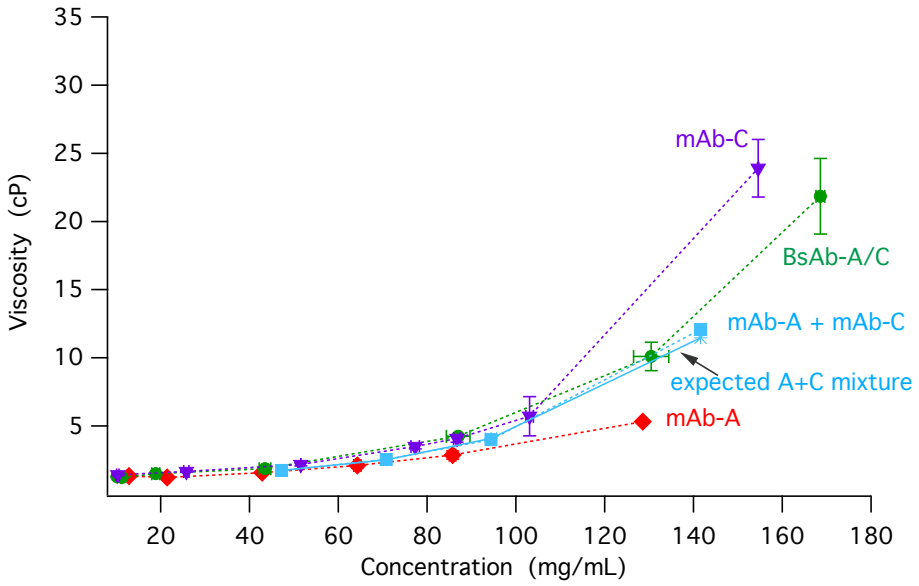

Figure 6.2: Viscosity as a function of concentration of mAb-A, mAb-C and the bispecific BsAb-A/C, formulated in 20mM histidine chloride, pH 6.0, at 23°C. The dotted lines between data points are just a guide for the eye, and do not represent any fitting; the solid lines indicate the predicted binary mixture viscosity by the Arrhenius mixing rule (Eq. 6.4).

protein molecules, mAb-C has the highest viscosity (23.9 ± 2.1 cP) at 150 mg/mL, as well as the sharpest rise in viscosity as concentration increases. It takes only 100 mg/mL of mAb-C to reach 5 cP in viscosity, whereas mAb-A requires more protein molecules in solution (∼130 mg/mL) to reach the same viscosity. This suggests a fundamental difference in protein-protein interactions for mAb-C as compared to mAb-A; they have similar isoelectric points (pI = 6.95 and 6.25, respectively), yet they exhibit very different viscosity behavior as a function of concentration. However, though mAb-A and mAb-C have different underlying interactions that lead to different viscosity behavior, the Arrhenius mixture relation describes their mixture perfectly. There is no appreciable difference between the measured viscosity of the mixture of (mAb-A + mAb-C) (■ in Fig. 6.2) and the expected viscosity of the mixture calculated by Eq. 6.5 (⁕ with solid line in Fig. 6.2). The viscosity of the bispecific antibody BsAb-A/C also tracks closely with the physical mixture (• in Fig. 6.2). These observations suggest that mAb-A and mAb-C are not experiencing non-additive cross-interactions that are fundamentally different from their own intermolecular protein-protein interactions.

6.3.2 Viscosity results of cross-interacting antibodies

The mean squared displacements (MSD) for the second set of proteins (mAb-A, mAb-B, and BsAb-A/B) are shown in Fig. 6.3, reported with the same imaging system noise. Similar to Fig. 6.1, the MSDs for all solutions are greater than the particle tracking error and have a logarithmic slope of 1, with the exception of the highest concentration of BsAb-A/B. The viscosity at different concentrations is calculated using Van Hove functions and excess kurtosis, and the results are demonstrated in Fig. 6.4. Though mAb-A and mAb-B have significantly different isoelectric points (pI = 6.25 and 9.25, respectively), the two molecules exhibit very similar viscosity behavior as a function of concentration.

The Arrhenius mixing rule (Eq. 6.4) predicts a similar viscosity for the mixture (mAb-A + mAb-B) (■ with solid line in Fig. 6.4) as compared to mAb-A and mAb-B (♦ and • in Fig. 6.4, respectively), but the microrheology results show that the mixture

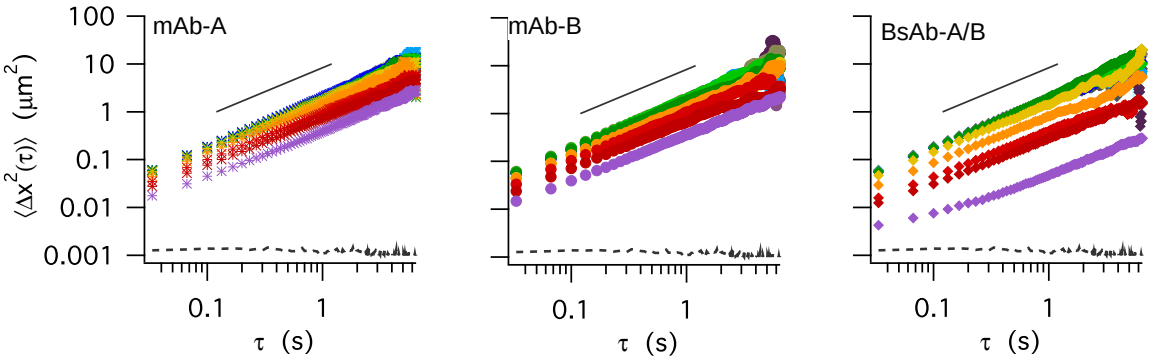

Figure 6.3: The mean squared displacements of mAb-A, mAb-B, and BsAb-A/B in 20mM histidine chloride, pH 6.0 at 23°C. Each monoclonal antibody has 12-15 concentrations, ranging from 1 mg/mL to approximately 150 mg/mL. The solid black line indicates logarithmic slope of 1, and the dash line indicates the noise floor of this imaging system.

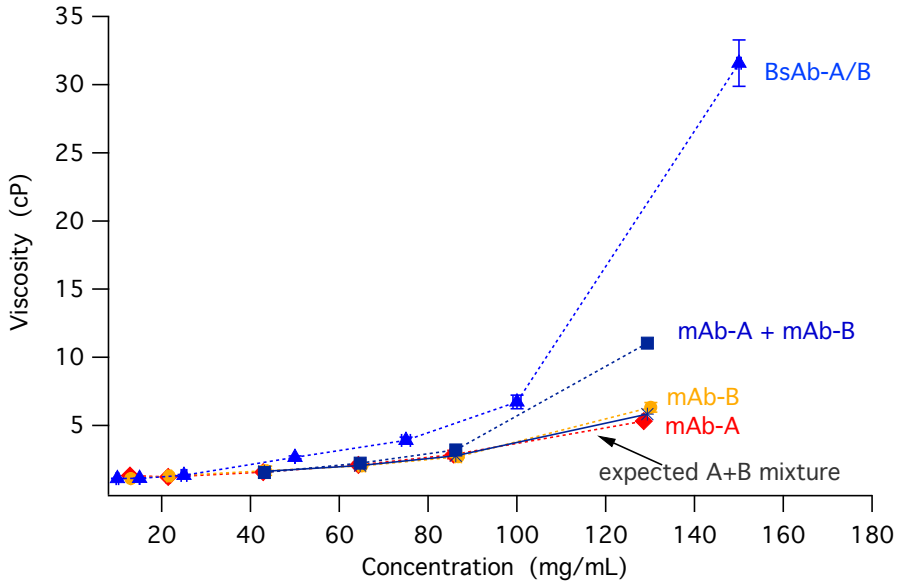

Figure 6.4: Viscosity as a function of concentration of mAb-A, mAb-B and the bispecific BsAb-A/B, formulated in 20mM histidine chloride, pH 6.0, at 23°C. The dotted lines between data points are just a guide for the eye, and does not represent any fitting; the solid lines indicate the predicted binary mixture viscosity by the Arrhenius mixing rule (Eq. 6.4).

viscosity (11.1 ± 0.5 cP) is approximately two times greater than the single species solutions. Moreover, the bispecific BsAb-A/B shows a significantly higher viscosity at 31.6 ± 1.7 cP. These observations suggest that mAb-A and mAb-B have stronger cross-interactions, which leads to a rise in viscosity in the mixture. Furthermore, by combining mAb-A and mAb-B into a single bispecific antibody, the strong interactions on the two arms of the antibody cause the protein molecules to self-associate, resulting in a significant increase in viscosity of BsAb-A/B compared to the single species and physical mixture.

6.3.3 Hard quasispherical particle models for viscosity of protein solutions and protein mixtures

Since the mixture viscosity of (mAb-A + mAb-B) deviates from the prediction of the Arrhenius mixing rule (Eq. 6.4), it could indicate significantly different intramolecular interactions. To infer information about these interactions, we used the Ross–Minton equation [83], a semi-empirical hard quasispherical particle model, which has been successful in fitting the concentration dependence of the viscosity of hemoglobin solutions [83], bovine serum albumin and ovalbumin [84], various mAbs [75, 85], and other non-associating protein species up to ca. 400 mg/mL, with only one adjustable parameter, the jamming limit c^*. In this model, the solution viscosity of a single protein species (modeled as hard quasispherical particles) as a function of concentration is described by the generalized Mooney equation [83, 86]

$$\ln \eta(c) = \ln \eta_0 + \frac{[\eta]c}{1 - c/c^*} \tag{6.8}$$

where c is the w/v concentration of the protein species, η_0 is the buffer viscosity, $[\eta]$ is the intrinsic viscosity of the protein, and c^* is the critical concentration or the jamming limit. For spherical or quasispherical particles, c^* is equal to 640 mg/mL (equivalent to a volume fraction of $\phi = 0.64$), the concentration above which spheres occupy a fractional volume so great that they cannot move past each other and can no longer

flow under shear. To account for particle shape and specific volume, the intrinsic viscosity can be further defined as

$$[\eta] = \nu N_A v_h / M_w \tag{6.9}$$

where N_A is Avogadro's number, M_w is the molar mass, v_h is the hydrodynamic volume of a protein molecule, and ν is the Simha factor [87], with a minimum value of 2.5 for spherical particles that increases as the particle shape deviates from sphericity. Minton [88] further extended Eq. 6.8 to account for mixtures of protein molecules with similar structure to become

$$\ln \eta_{\text{mix}} = \ln \eta_0 + \frac{[\eta]_{\text{avg}} c_{\text{tot}}}{1 - c_{\text{tot}}/c^*_{\text{tot}}} \tag{6.10}$$

where $c_{\text{tot}} = \sum_i c_i$ is the total w/v concentration for all protein species in the mixture, c^*_{tot} is the combined jamming limit from all the protein species, and $[\eta]_{\text{avg}} = \sum_i c_i [\eta_i] / c_{\text{tot}}$ is the weight-averaged intrinsic viscosity of the mixture. This equation provides a quantitative description for 3 different binary antibody mixtures and a 1:1:1 ternary antibody mixture [75, 88], where the various species in the mixture do not interact and can be approximated as hard quasispherical particles of similar volume.

Heterogeneity in size and shape of the solute species can cause variation in the parameter c^* or c^*_{tot}, departing from the value of 640 mg/mL as the system departs from the ideal case of monodisperse hard spheres. In addition, self-associating behavior results in an apparent decrease of c^*_{tot}, as shown in Fig. 6.5 [88]. The best-fit values of c^*_{tot} decrease markedly from 640 mg/mL in a model considering trimer formation of IgG. Thus $c^*_{\text{tot}} \ll 640$ mg/mL is expected to be a reliable indicator of self-association as the total protein concentration increases, because associating particles reach the jamming limit at a lower concentration. A significant decrease in c^*_{tot} and a corresponding increase in intrinsic viscosity could also indicate the presence of highly anisometric or aspherical solute species (such as a linear n-mer); in this case, the best-fit value of $[\eta]$ would increase significantly from the expected intrinsic viscosity value of a single protein molecule, due to an increase of the Simha factor ν and/or the hydrodynamic

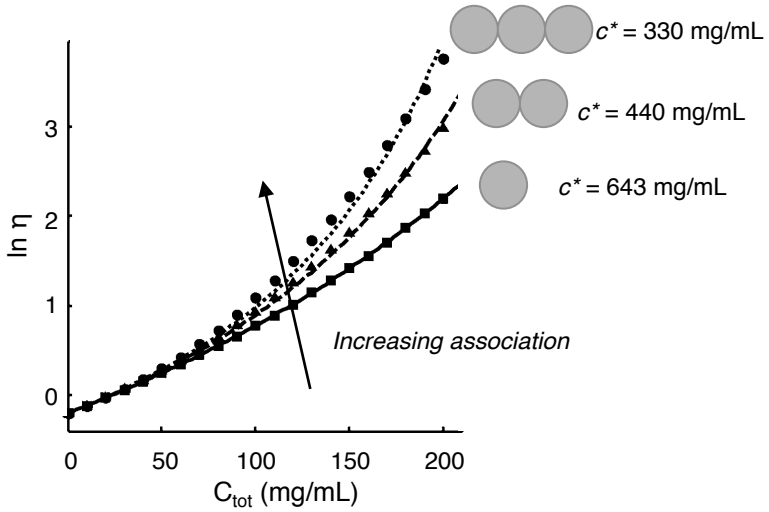

Figure 6.5: Semi-logarithmic plot of the solution viscosity of a model self-associating protein, simulated as described by Minton [88]. Self-association causes a rise in solution viscosity, and fitting the model solution viscosity of Eq. 6.10 gives decreasing values of c^* for increasing degrees of self-association.

volume v_h (Eq. 6.9).

The viscosity results from the microrheology experiments are shown in a semi-log plot in Fig. 6.6. The fit to the single species Ross–Minton equation (Eq. 6.8) via non-linear least squares, is applied to mAb-A (♦), mAb-B (•), and BsAb-A/B (▲) and shown in Fig. 6.6A with solid lines. The fits to mAb-C (▼), and BsAb-A/C (•) are shown separately in Fig. 6.6B. The best-fit values are reported in Table 6.2 at 95% confidence. Eq. 6.8 qualitatively describes all of the single species protein solutions. The best-fit values of the intrinsic viscosities $[\eta]$ of each monospecific antibody (A, B, C) range between 8 and 10 cm^3/g, which agree well with values previously reported for "normal" IgG antibodies in similar solution conditions [69, 85]. The bispecific antibodies BsAb-A/B and BsAb-A/C, on the other hand, have higher $[\eta]$ than the monospecific antibodies. Since all the protein solutions are formulated in the same medium, such observations may indicate that both bispecific antibodies have distinctly different conformations and protein-protein interactions, and hence different values of

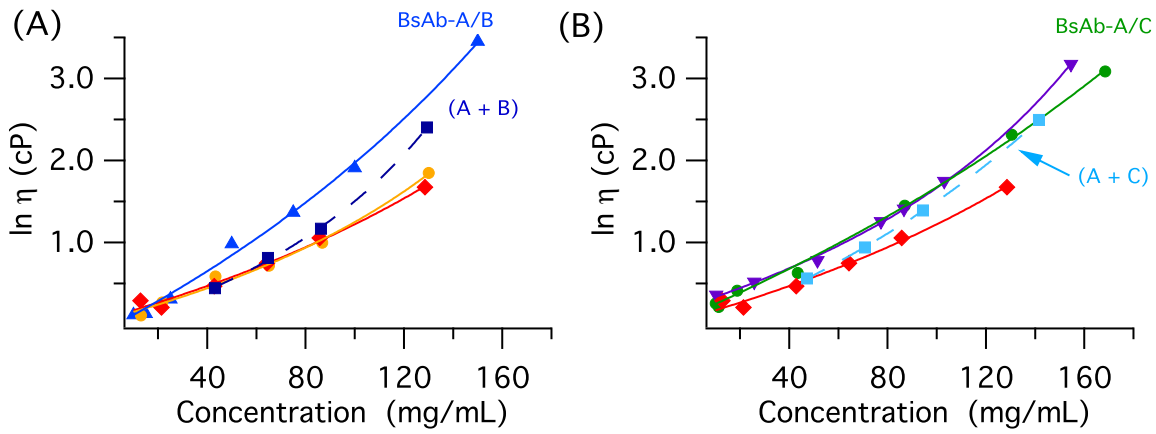

Figure 6.6: Semi-logarithmic plot of the viscosity data in Fig. 6.4 and Fig. 6.2. The smooth solid lines represent the fit to Ross-Minton equation (Eq. 6.8) and the dash lines represent the fit to the Minton mixture equation (Eq. 6.10).

ν and v_h in determining the intrinsic viscosity of a protein using Eq. 6.9. Interestingly, all of the antibodies except BsAb-A/C have a c^* value that is much less than the hard sphere jamming limit at 640 mg/mL, which may be an indicator of concentration-dependent self-association [88].

The concentration-dependent viscosities of the 1:1 mixtures of (mAb-A + mAb-B) and (mAb-A + mAb-C) are fitted to the Minton mixture equation (Eq. 6.10) and presented in Fig. 6.6A-B as dashed lines. The best-fit parameters are reported in Table

Table 6.2: Best-fit parameter values obtained by fitting Ross–Minton equation (Eq. 6.8) to the microrheology measurements of the five antibody solutions shown in Fig. 6.6A-B.

Molecule	η_0 (cP)	$[\eta]$ (cm^3/g)	c^* (mg/mL)
mAb-A	0.96 ± 0.04	8.17 ± 1.08	322 ± 62
mAb-B	0.95 ± 0.05	9.45 ± 1.54	505 ± 138
mAb-C	1.06 ± 0.12	9.86 ± 0.49	320 ± 16
BsAb-A/B	0.95 ± 0.05	16.0 ± 1.55	480 ± 100
BsAb-A/C	1.02 ± 0.04	13.2 ± 0.13	637 ± 191

Table 6.3: Best-fit parameter values obtained by fitting Minton mixture equation (Eq. 6.10) to the microrheology measurements of the binary protein mixtures shown in Fig. 6.6A-B.

Constraining parameters in the equation fit ([a]values obtained from Table 6.2)

Mixture	η_0 (cP)	$[\eta]_1$ (cm^3/g)	$[\eta]_2$ (cm^3/g)	c^*_{tot} (mg/mL)
mAb-A + mAb-B	0.95[a]	8.17[a]	9.45[a]	242 ± 2.7
mAb-A + mAb-C	1.01[a]	8.17[a]	9.86[a]	326 ± 13

6.3 with constrained parameters. The jamming limit c^*_{tot} for the mixture (mAb-A + mAb-B) is the lowest of all the fits (242 ± 2.7 mg/mL) that have been performed, showing that in the physical mixture mAb-A and mAb-B molecules are strongly interacting with each other and the Arrhenius mixture equation (Eq. 6.4) cannot sufficiently predict the mixture's viscosity, as observed in Fig. 6.4. For (mAb-A + mAb-C), the estimated c^*_{tot} is equal to the c^* for both single protein molecules; the jamming limit for mAb-A, mAb-C and the mixture (mAb-A + mAb-C) are all approximately 320 mg/mL (interestingly, at half the hard sphere packing limit). This observation supports the hypothesis mAb-A and mAb-C do not have heterogeneous protein-protein interactions that are fundamentally different from their own intermolecular interactions, similar to the 3 mAbs that were reported by Galush et al. [75], and in agreement with the conclusion drawn from fitting the mixture viscosity behavior to the Arrhenius mixing rule.

6.3.4 Size exclusion chromatography of cross-interacting antibodies

We hypothesized that, if mAb-A and mAb-B have strong cross-interactions, then BsAb-A/B would have strong self-association and may be forming reversible aggregates. Patapoff et al. [89] established a method using a very short SEC guard column (∼ cm) to study the thermodynamics and kinetics of such dissociable reversible protein aggregates, with half-lives of the dissociation on the order of seconds ($t_{1/2} \approx 5$ s for the human growth hormones in the study). The primary advantage of this technique

lies in the low retention volume (< 1 mL) and short retention time (< 1 min), which allow for partial spatial separation of the dimer from the monomer on the order of seconds, before the equilibrium is reached, whereas typical analytical SEC columns are inadequate to study reversible protein aggregates that rapidly dissociate (with half-lives $t_{1/2}$ < 30 s), due to the extended column transit time (5–6 min for IgGs in a standard 30 cm column). Though the separation is incomplete, the method is rapid and the molecular species can be adequately resolved for analysis, given a descriptive enough kinetic model (along with computer simulations on how the chromatograms would combine). The method as developed by Patapoff et al. [89] would allow us to observe the dissociation of the BsAb-A/B aggregates, as opposed to BsAb-A/C, for which we do not expect strong self-association, according to the c^* analysis from Eq. 6.8.

Fig. 6.7 and Fig. 6.8 show a series of chromatograms of the elution of BsAb-A/C and BsAb-A/B, respectively, at 6 flow rates. The retention volume, calculated as (retention time · flow rate), of the main molecular species remains constant as a function of flow rate and injection concentration (shown in dashed lines in both figures). The two bispecific antibodies have similar molecular weight and intrinsic viscosity $[\eta]$ (Table 6.2); thus the main peak at the same retention volume for both bispecific antibodies is considered to be the monomer species at ∼150 kDa. The arrows in Fig. 6.7 and Fig. 6.8 indicate the trailing, longer retention time peaks that are not well-separated from the main peak. The presence of these convoluted distributions of lower weight species indicates there might be fragments of the bispecific antibody in solution (1-2% fragments may be present in a fresh stock solution [90]). Interestingly, for BsAb-A/B, the approximate peak location of the lower weight species shifts as flow rate changes (Fig. 6.8). We did not observe the presence of dimers or higher-order structures as expected. If transient dimers of BsAb-A/B exist, the rates of their reversible dissociation are not on a time scale detectable with this method ($t_{1/2} < 1-10$ s).

Based on the chromatograms, we conclude that the experimental conditions for

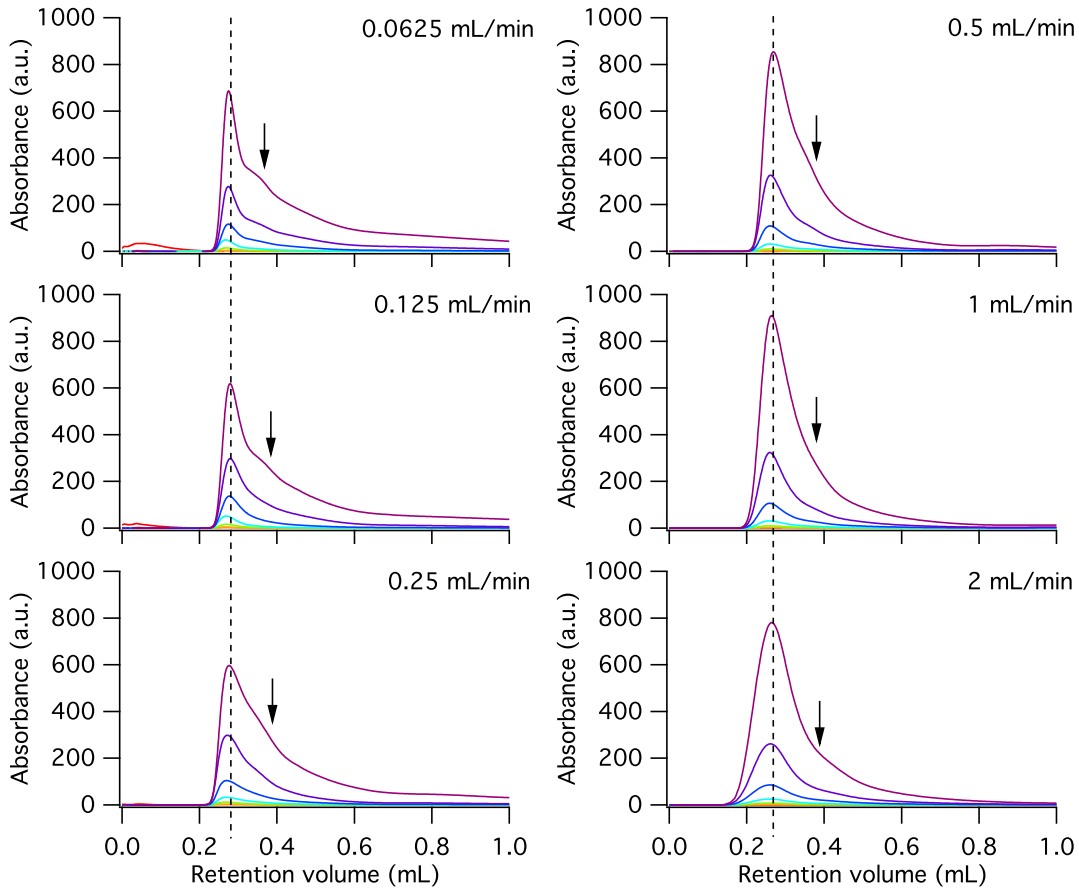

Figure 6.7: Chromatograms obtained by injecting 5 μL of BsAb-A/C from 0.01 to 20 mg/mL and eluting at 6 different flow rates. Mobile phase is 0.1 M K_3PO_4/0.125 M KCl, pH 6.2. The dashed lines indicate the peak of the major species; the dash arrows at the lower flow rates (left column) indicate the presence of a higher molecular weight species, and the solid arrows show the shoulder of the convoluted distribution of the lower weight species.

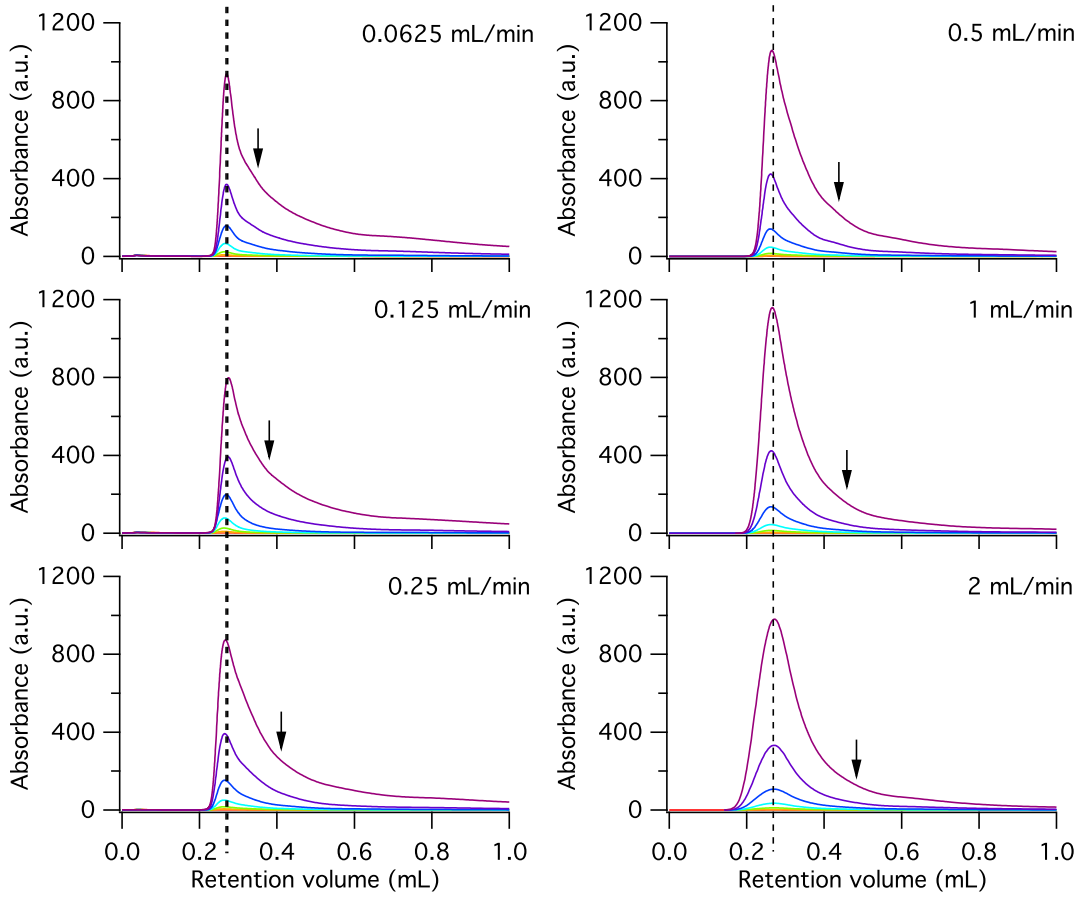

Figure 6.8: Chromatograms obtained by injecting 5 μL of BsAb-A/B from 0.01 to 20 mg/mL and eluting at 6 different flow rates. Mobile phase is 0.1 M K_3PO_4/0.125 M KCl, pH 6.2. The dashed lines indicate the peak of the major species. The dash arrows at flow rate of 0.0625 and 0.125 mL/min indicate the peak of higher molecular species. The solid arrows show the shoulder of the convoluted distribution of the lower weight species and its shift in retention volume.

the short guard column SEC are not optimized and thus our results are inconclusive. The mobile phase conditions, flow rates, and initial injection concentration/amount all need to be tuned so the (partial) separation between the reversible dissociating dimers, monomers, and fragments can be sufficiently discerned and analyzed. However, it is difficult to determine the peak characteristics (position, width, and shape) of the short-lived molecular species *a priori* or without simulations. To better analyze the experiments, comparison chromatograms of the nondissociable dimers of these bispecific antibodies under the same experimental condition should be made [89] (though that would then invoke a new study to identify conditions that form such dimers).

6.3.5 Light scattering of cross-interacting antibodies

Static light scattering and dynamic light scattering are used to determine the excess Rayleigh scattering and collective diffusion coefficient, respectively, for mAb-A, mAb-B, and BsAb-A/B as a function of low protein concentrations at pH 6. The analysis for low protein concentration samples is shown in Fig. 6.9. The excess Rayleigh scattering at the 90° scattering angle R_{90}^{ex}/K is determined as a function of concentration for the three antibodies and is illustrated in Fig. 6.9A with experimental data shown with symbols and lines corresponding to the model fits of the data to Eq. 6.6. Fig. 6.9A illustrates that the antibodies have different Rayleigh scattering profiles at the same pH. For instance, the upward curvature in excess Rayleigh scattering of BsAb-A/B suggests attractive interactions, while mAb-B exhibits a slight downward curvature suggesting repulsive interactions.

In order to quantify the apparent molecular weight and protein-protein interactions (PPI), Eq. 6.6 is used to fit the experimental data. Fig. 6.9B demonstrates the normalized apparent molecular weight, $M_{\text{w,app}}^{*} = M_{\text{w,app}}/M_w$, of the antibodies. The apparent molecular weights of mAb-A and mAb-B are statistically equivalent to the true molecular weight, indicating no significant monomer loss and/or buffer-protein interactions [31]. However, the bispecific had a higher apparent molecular weight (∼175 kDa) than the true molecular weight (∼145 kDa), which may suggest the presence of

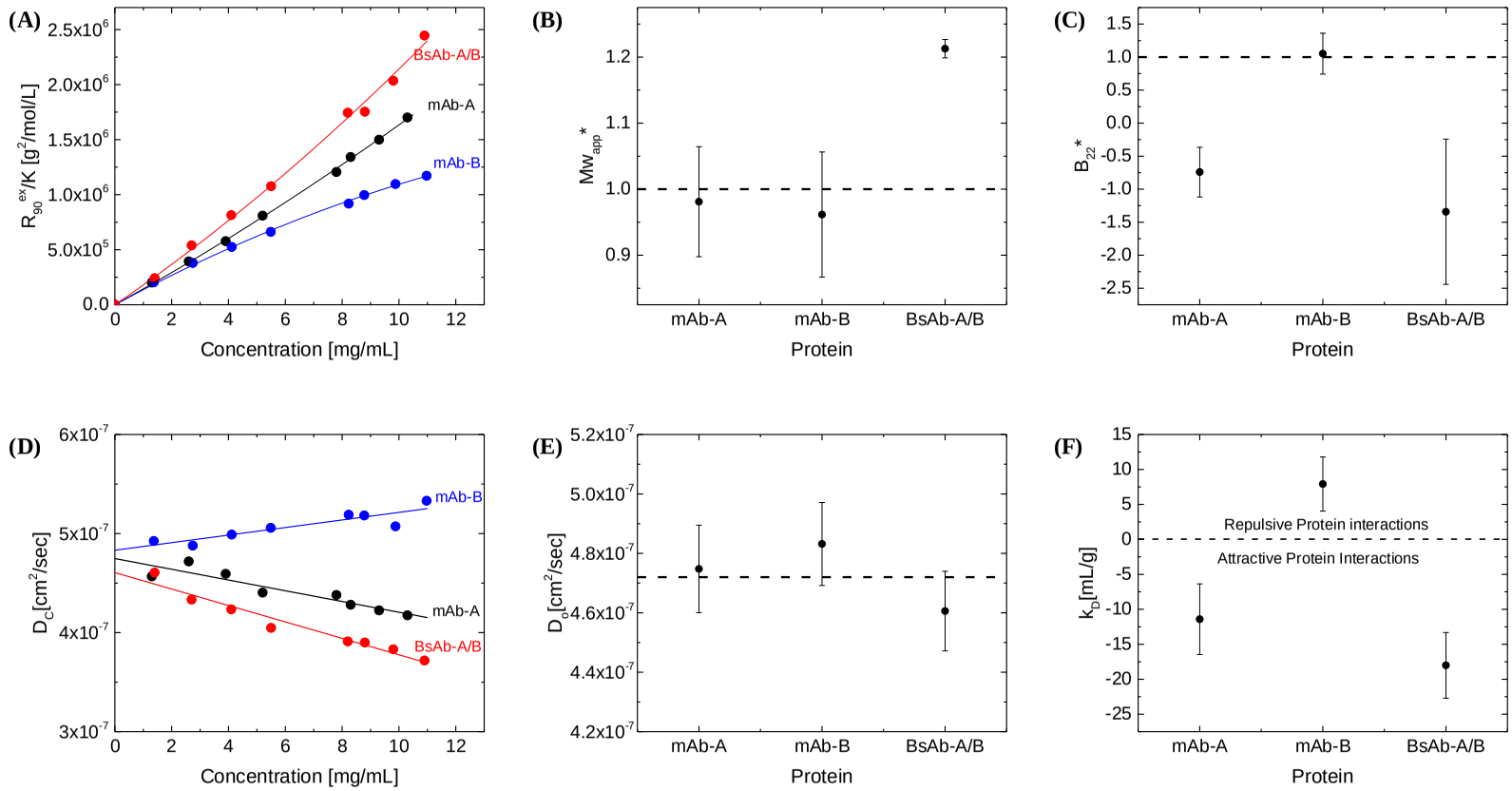

Figure 6.9: Low protein concentrations SLS (A-C) and DLS (D-F) results. (A) Excess Rayleigh scattering (B) Normalized apparent molecular weight (C) Normalized osmotic second virial coefficient ($B_{22}*$) (D) Collective diffusion coefficient (E) infinite dilutions diffusion coefficient (F) protein interaction parameter (kD) for mAb-A, mAb-B and BsAb-A/B at pH 6.

larger species and/or protein-co-solute interactions. Since $[\eta]$ is a function of M_w based on Eq. 6.9, the high $M_{\mathrm{w,app}}$ of BsAb-A/B correlates with the higher intrinsic viscosity $[\eta]$ of BsAb-A/B (Table 6.2) fitted from the Ross–Minton model (Eq. 6.8).

The second parameter from Eq. 6.6, B_{22}, is normalized by the B_{22}-steric value attained from all-atom Monte Carlo molecular simulations [91]. In this normalized scale, $B_{22}^* > 1$ indicates a net repulsive interaction beyond steric repulsion, while $B_{22}^* < 1$ indicates net-attractive protein interactions. As seen in Fig. 6.9C, mAb-B results in positive B_{22} (and $B_{22}^* \approx 1$), which suggests repulsive protein-protein interactions that are not significantly different from steric repulsion. On the other hand, both mAb-A and BsAb-A/B demonstrate moderately attractive PPI relative to steric repulsion.

In Fig. 6.9D, the collective diffusion coefficients from low concentration protein samples are shown along with the model fit to Eq. 6.7. Similar to the results from SLS, the DLS data illustrate differences in the collective diffusion coefficient for the three antibodies. The increase in D_c with an increase in concentration observed for mAb-B suggests repulsive protein interactions, while a decrease in D_c suggests attractive protein interactions for mAb-A and the bispecific antibody. Even though a decrease in D_c is observed for both mAb-A and BsAb-A/B, it is interesting to note that the D_c for BsAb-A/B is slightly lower than that for mAb-A, which might indicate that the species in the bispecific solution are slightly larger than those in the mAb-A solution (again, corroborating the Ross–Minton fit and the higher apparent molecular weight extracted from SLS). Eq. 6.7 is used to fit the D_c data in Fig. 6.9D. The resulting infinite-dilution diffusion coefficient D_0, as well as the expected diffusion coefficient calculated from a hydrodynamic radius of 5.2 nm (dashed line), is shown in Fig. 6.9E; the results show that all three antibodies have statistically equivalent hydrodynamic radii. Fig. 6.9F shows the extracted protein interaction parameter (k_D) from Eq. 6.7, and the DLS results support the conclusions from SLS (Fig. 6.9C), where repulsive interactions are found in mAb-B, and the other two antibodies demonstrate attractive protein interactions.

Light scattering experiments are also conducted at high protein concentrations

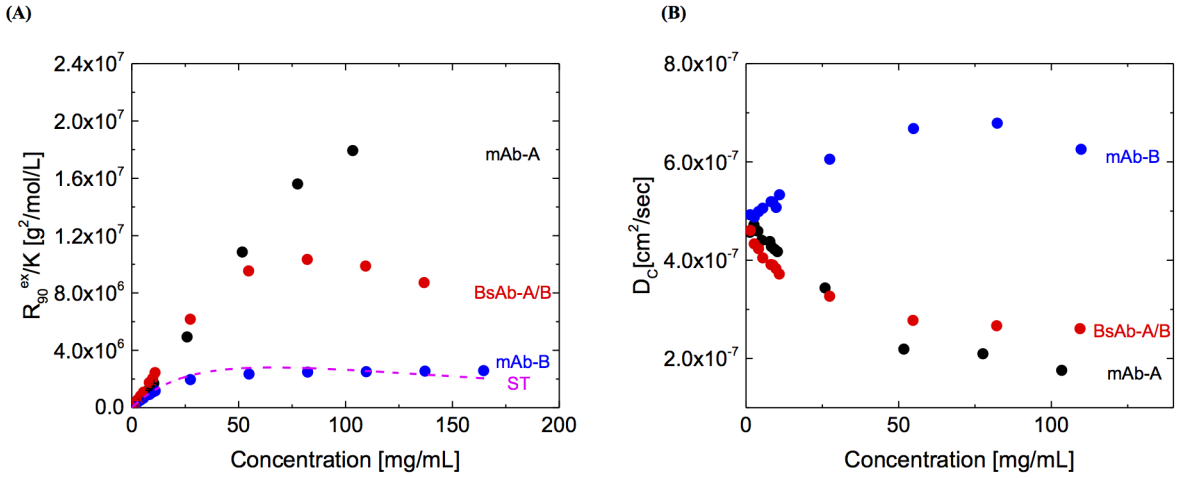

Figure 6.10: (A) Excess Rayleigh scattering as a function of high protein concentration (B) Collective diffusion coefficient D_c as a function of high protein concentration for mAb-A, mAb-B and BsAb-A/B at pH 6.

(Fig. 6.10). The excess Rayleigh scattering profile for the three antibodies, along with the dashed curve corresponding to the Rayleigh scattering profile of a steric-only coarse-grained model MC-simulation [91], is shown in Fig. 6.10A. Similar to the low concentration light scattering experiments, mAb-B demonstrates repulsive PPI that is comparable to steric repulsion, and mAb-A and BsAb-A/B display net-attractive PPI. However, at a concentration around 30 mg/ml, a switch in scattering pattern between mAb-A and the bispecific is observed, i.e. at concentrations greater than 30 mg/ml, mAb-A has higher excess Rayleigh scattering than BsAb-A/B.

In Fig. 6.10B the collective diffusion coefficient D_c measured from DLS is given as a function of high protein concentrations. D_c increases with increasing mAb-B concentrations, suggesting repulsive protein-interactions;,whereas the D_c decrease in mAb-A and BsAb-A/B shows attractive protein-interactions. As in Fig. 6.10A, the cross-over behavior between mAb-A and BsAb-A/B around 30 mg/ml is again observed with the DLS results in Fig. 6.10B. The origin of this crossover is not well-understood yet; however, one can speculate that it is a result of the nature of the interactions

and/or structural rearrangements in these antibodies as protein concentration is increased. Additionally, the DLS analysis of the hydrodynamic radius reveals a 4-10% polydispersity in molecular weight distribution. The variation in the molecular weight comes from lower molecular weight species, supporting the observations in the short column SEC that there are antibody fragments present in solution (as detailed in Sec. 6.3.4).

Based on the light scattering experiments, the correlation between viscosity and interactions is not clear. At low concentration, both mAb-A and BsAb-A/B show moderately attractive PPI, but the bispecific antibody shows a much larger change in viscosity (Fig. 6.4), whereas mAb-A and mAb-B have similar viscosity profiles but different protein-interactions (Fig. 6.10). It would be interesting to observe the protein-protein interactions on mAb-C, which has a very similar pI yet different viscosity behavior compared to mAb-A.

6.3.6 Possible solution microstructure and their impact on viscosity

Microrheology measurements are sensitive to the formation of microstructure in solution [65, 81, 92, 93]. The unusual trends in the viscosity profiles of (mAb-A + mAb-B) and BsAb-A/B as compared to the monospecific antibodies, while not explained by the B_{22} interaction parameter, are detected by microrheology; such observations indicate a change the microstructure in the antibody solutions as the protein concentration increases. The physics may have arisen from the different sequences in the complementarity determining region (CDR), which is indicated by the difference in the isoelectric point (pI) between the molecules. Asymmetry in charge distribution in the antibody could lead to a molecular alignment leading to reversible dimerization or cluster formation [28], a transient "daisy-chained" network in solution [57], or intermediate- to long-range order. Previously Yadav et al. [41] showed that an increase in charge asymmetry (done by swapping charge mutants on a monoclonal antibody) leads to an increase in self-associating behavior and a higher viscosity than the original mAb.

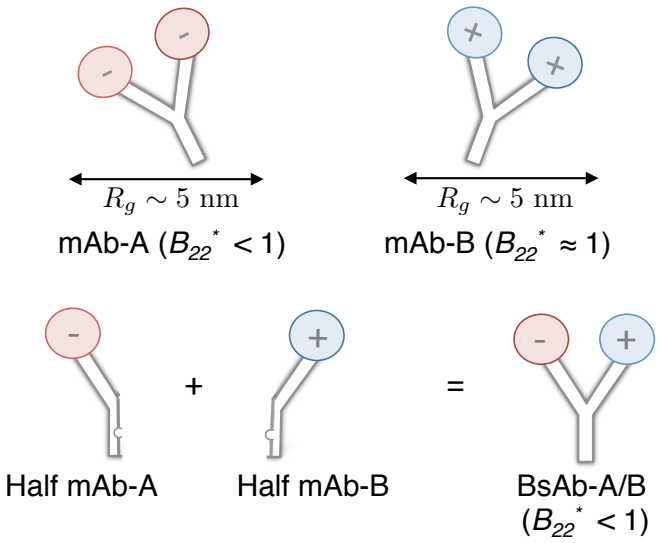

Figure 6.11: A simplified schematic of the structures of mAb-A, mAb-B, as well as the synthesis and structure of BsAb-A/B based on the knob-in-hole bispecific format developed by Spiess et al. [70].

Based on the knowledge that mAb-A has a theoretical pI of 6.25 (indication of negative patches in CDR), and mAb-B has a theoretical pI of 9.25 (indication of positive patches in its CDR), we propose that the asymmetric charge distribution on the BsAb-A/B gives rise to the transient microstructures in solution, which in turn affects the viscosity of the solution. In a simplified scheme (Fig. 6.11), we show the structure of mAb-A and mAb-B (with an expected radius of gyration $R_g \approx 5$ nm), as well as the combination of the half antibodies of mAb-A and mAb-B to make the knob-in-hole bispecific format [70]; thus BsAb-A/B would have one arm with a positive charge, and the other arm with a negative charge.

At concentrations below 20 mg/mL, the viscosity profiles of the monospecific antibodies and BsAb-A/B are very similar (Fig. 6.4); thus the solution behavior of BsAb-A/B is expected to be comparable to mAb-A and mAb-B, moving freely on the monomer length scale. As concentration increases, the deviation and increase in viscosity become more apparent for BsAb-A/B. We propose that transient dimers of the bispecific antibody begin forming as the solution becomes more packed (Fig. 6.12).

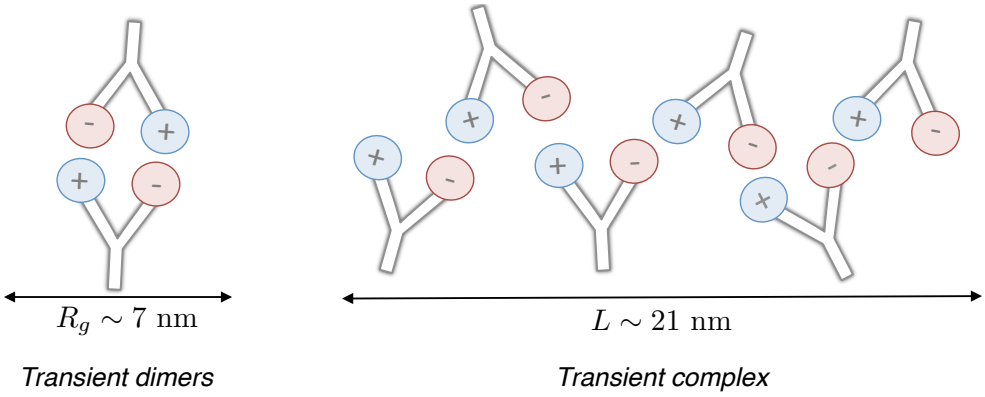

Figure 6.12: Schematic of proposed solution microstructures of BsAb-A/B as concentration increases. Due to the asymmetric charge distribution, the bispecific antibody has higher association interaction and begins forming dimers. At higher concentration, transient complexes of BsAb-A/B are formed with a characteristic length scale L.

Such transient dimers have been characterized to have a radius of gyration slightly greater than the monomer case, $R_g \approx 7$ nm [94]. Godfrin et al. [27] observed a strong correlation between the zero-shear viscosity (i.e. the viscosity measured in microrheology) and the characteristic length scale L of the microstructures in solution, by $\eta \sim L^3$. This scaling is as expected for semi-dilute polymer solutions [28] and particulate suspensions [95]. At the highest concentration of BsAb-A/B, we estimate a characteristic length scale of $L \approx 21$ nm using this scaling relationship and show a proposed scheme of a transient complex in Fig. 6.12. The time scale (∼10 ns) and length scale (∼10 nm) of these transient structures [27, 94] are outside the capabilities of the techniques we have employed to study these antibodies. Nevertheless, microrheology and its analysis with the Ross–Minton model are capable of detecting the rise in the bispecific antibody's viscosity at high concentrations, as well as its increased $[\eta]$, which may be explained by our theory.

6.4 Conclusions

We have investigated the viscosity behavior of 3 monospecific monoclonal antibodies (mAb-A, B, C), their mixtures, and 2 bispecific antibodies that are made from the combination of the monospecific half-mAbs, using multiple particle tracking microrheoology. Using the Arrhenius mixing rule and the Ross–Minton model to analyze the viscosity results, we discovered that mAb-A and mAb-C have similar cross-interactions as their self-interactions, whereas mAb-A and mAb-B are strongly cross-interacting, leading to a rise in the concentration-dependent viscosity not observed in the former case. The short guard column size exclusion chromatography and light scattering experiments on the antibodies do not show a clear picture on the interaction mechanism, nor do the measured B_{22} interaction parameters predict the viscosity behavior.

Based on our experimental observations from microrheology and light scattering with an increased $[\eta]$ and $M_{\mathrm{w,app}}$ in the bispecific antibody solution, we propose that transient, larger microstructures are forming in solution compared to the monospecific antibodies alone. Short time dynamics studies with neutron scattering [27] should provide more molecular insights on the protein-protein interactions and the origin of the viscosity increase for the cross-interacting mixture and the bispecific antibody made from mAb-A and mAb-B. Higher ionic strength experiments for the proteins can also provide more insights into the short range interactions of the proteins, and can be used as an input to Monte Carlo simulations [91]. Although these in-depth studies might not be suited for a protein molecule with a rapid timeline, the capability to screen for and discover unusual viscosity behavior using small samples is crucial in early development efforts.

REFERENCES

[1] A. Beck, T. Wurch, C. Bailly, and N. Corvaia. Strategies and challenges for the next generation of therapeutic antibodies. *Nature Reviews Immunology*, 10(5): 345–352, 2010.

[2] S. R. Aggarwal. What's fueling the biotech engine 2012 to 2013. *Nature Biotechnology*, 32(1):32–39, 2014.

[3] D. M. Ecker, S. D. Jones, and H. L. Levine. The therapeutic monoclonal antibody market. *mAbs*, 7(1):9–14, 2014.

[4] D. R. Mould and B. Meibohm. Drug Development of Therapeutic Monoclonal Antibodies. *BioDrugs*, 30(4):275–293, 2016.

[5] J. M. Reichert. Antibodies to watch in 2016. *mAbs*, 8(2):197–204, 2016.

[6] A. Thakur and L. G. Lum. Cancer therapy with bispecific antibodies: Clinical experience. *Current opinion in molecular therapeutics*, 12(3):340–349, 2010.

[7] R. Kontermann. Dual targeting strategies with bispecific antibodies. *mAbs*, 4(2): 182–197, 2012.

[8] R. E. Kontermann and U. Brinkmann. Bispecific antibodies. *Drug Discovery Today*, 20(7):838–847, 2015.

[9] C. Spiess, Q. Zhai, and P. J. Carter. Alternative molecular formats and therapeutic applications for bispecific antibodies. *Molecular Immunology*, 67(2):95–106, 2015.

[10] G. Fan, Z. Wang, M. Hao, and J. Li. Bispecific antibodies and their applications. *Journal of Hematology & Oncology*, 8(1):130, 2015.

[11] B. Cochlovius, S. M. Kipriyanov, M. J. J. G. Stassar, J. Schuhmacher, A. Benner, G. Moldenhauer, and M. Little. Cure of Burkitt's Lymphoma in Severe Combined Immunodeficiency Mice by T Cells, Tetravalent CD3 × CD19 Tandem Diabody, and CD28 Costimulation. *Cancer research*, 60(16):4336–4341, 2000.

[12] K. Els Conrath, M. Lauwereys, L. Wyns, and S. Muyldermans. Camel single-domain antibodies as modular building units in bispecific and bivalent antibody constructs. *Journal of Biological Chemistry*, 276(10):7346–7350, 2001.

[13] E. A. Rossi, D. M. Goldenberg, T. M. Cardillo, W. J. McBride, R. M. Sharkey, and C.-H. Chang. Stably tethered multifunctional structures of defined composition made by the dock and lock method for use in cancer targeting. *Proceedings of the National Academy of Sciences*, 103(18):6841–6846, 2006.

[14] D. Müller, A. Karle, B. Meißburger, I. Höfig, R. Stork, and R. E. Kontermann. Improved pharmacokinetics of recombinant bispecific antibody molecules by fusion to human serum albumin. *Journal of Biological Chemistry*, 282(17):12650–12660, 2007.

[15] C. Wu, H. Ying, C. Grinnell, S. Bryant, R. Miller, A. Clabbers, S. Bose, D. McCarthy, R.-R. Zhu, L. Santora, R. Davis-Taber, Y. Kunes, E. Fung, A. Schwartz, P. Sakorafas, J. Gu, E. Tarcsa, A. Murtaza, and T. Ghayur. Simultaneous targeting of multiple disease mediators by a dual-variable-domain immunoglobulin. *Nature Biotechnology*, 25(11):1290–1297, 2007.

[16] J. Bostrom, S.-F. Yu, D. Kan, B. A. Appleton, C. V. Lee, K. Billeci, W. Man, F. Peale, S. Ross, C. Wiesmann, and G. Fuh. Variants of the Antibody Herceptin That Interact with HER2 and VEGF at the Antigen Binding Site. *Science*, 323 (5921):1610–1614, 2009.

[17] D. Chelius, P. Ruf, P. Gruber, M. Plöscher, R. Liedtke, E. Gansberger, J. Hess, M. Wasiliu, and H. Lindhofer. Structural and functional characterization of the trifunctional antibody catumaxomab. *mAbs*, 2(3):309–319, 2010.

[18] K. D. Orcutt, M. E. Ackerman, M. Cieslewicz, E. Quiroz, A. L. Slusarczyk, J. V. Frangioni, and K. D. Wittrup. A modular IgG-scFv bispecific antibody topology. *Protein engineering, design & selection : PEDS*, 23(4):221–228, 2010.

[19] W. Schaefer, J. T. Regula, M. Bähner, J. Schanzer, R. Croasdale, H. Dürr, C. Gassner, G. Georges, H. Kettenberger, S. Imhof-Jung, M. Schwaiger, K. G. Stubenrauch, C. Sustmann, M. Thomas, W. Scheuer, and C. Klein. Immunoglobulin domain crossover as a generic approach for the production of bispecific IgG antibodies. *Proceedings of the National Academy of Sciences of the United States of America*, 108(27):11187–11192, 2011.

[20] J. Oates and B. K. Jakobsen. ImmTACs. *Oncoimmunology*, 2(2):e22891, 2013.

[21] S. R. Frankel and P. A. Baeuerle. Targeting T cells to tumor cells using bispecific antibodies. *Current opinion in chemical biology*, 17(3):385–392, 2013.

[22] S. Amin, G. V. Barnett, J. A. Pathak, C. J. Roberts, and P. S. Sarangapani. Protein aggregation, particle formation, characterization & rheology. *Current Opinion in Colloid & Interface Science*, 19(5):438–449, 2014.

[23] S. Yadav, S. J. Shire, and D. S. Kalonia. Factors Affecting the Viscosity in High Concentration Solutions of Different Monoclonal Antibodies. *Journal of Pharmaceutical Sciences*, 99(12):4812–4829, 2010.

[24] G. V. Barnett, V. I. Razinkov, B. A. Kerwin, T. M. Laue, A. H. Woodka, P. D. Butler, T. Perevozchikova, and C. J. Roberts. Specific-Ion Effects on the Aggregation Mechanisms and Protein–Protein Interactions for Anti-streptavidin Immunoglobulin Gamma-1. *Journal of Physical Chemistry B*, 119(18):5793–5804, 2015.

[25] M. S. Neergaard, D. S. Kalonia, H. Parshad, A. D. Nielsen, E. H. Møller, and M. van de Weert. Viscosity of high concentration protein formulations of monoclonal antibodies of the IgG1 and IgG4 subclass - prediction of viscosity through protein-protein interaction measurements. *European journal of pharmaceutical sciences : official journal of the European Federation for Pharmaceutical Sciences*, 49(3):400–410, 2013.

[26] J. A. Pathak, R. R. Sologuren, and R. Narwal. Do clustering monoclonal antibody solutions really have a concentration dependence of viscosity? *Biophysical Journal*, 104(4):913–923, 2013.

[27] P. D. Godfrin, I. E. Zarraga, J. Zarzar, L. Porcar, P. Falus, N. J. Wagner, and Y. Liu. Effect of Hierarchical Cluster Formation on the Viscosity of Concentrated Monoclonal Antibody Formulations Studied by Neutron Scattering. *Journal of Physical Chemistry B*, 120(2):278–291, 2016.

[28] E. J. Yearley, P. D. Godfrin, T. Perevozchikova, H. Zhang, P. Falus, L. Porcar, M. Nagao, J. E. Curtis, P. Gawande, R. Taing, I. E. Zarraga, N. J. Wagner, and Y. Liu. Observation of Small Cluster Formation in Concentrated Monoclonal Antibody Solutions and Its Implications to Solution Viscosity. *Biophysical Journal*, 106(8):1763–1770, 2014.

[29] M. R. Stoner, N. Fischer, L. Nixon, S. Buckel, M. Benke, F. Austin, T. W. Randolph, and B. S. Kendrick. Protein-solute interactions affect the outcome of ultrafiltration/diafiltration operations. *Journal of Pharmaceutical Sciences*, 93(9): 2332–2342, 2004.

[30] N. Prabhu and K. Sharp. Protein−Solvent Interactions. *Chemical Reviews*, 106 (5):1616–1623, 2006.

[31] M. A. Blanco, E. Sahin, Y. Li, and C. J. Roberts. Reexamining protein-protein and protein-solvent interactions from Kirkwood-Buff analysis of light scattering

in multi-component solutions. *The Journal of Chemical Physics*, 134(22):225103, 2011.

[32] V. Hlady and J. Buijs. Protein adsorption on solid surfaces. *Current Opinion in Biotechnology*, 7(1):72–77, 1996.

[33] J. S. Bee, D. Chiu, S. Sawicki, J. L. Stevenson, K. Chatterjee, E. Freund, J. F. Carpenter, and T. W. Randolph. Monoclonal antibody interactions with micro- and nanoparticles: Adsorption, aggregation, and accelerated stress studies. *Journal of Pharmaceutical Sciences*, 98(9):3218–3238, 2009.

[34] A. Nayak, J. Colandene, V. Bradford, and M. Perkins. Characterization of Subvisible Particle Formation During the Filling Pump Operation of a Monoclonal Antibody Solution. *Journal of Pharmaceutical Sciences*, 100(10):4198–4204, 2011.

[35] V. Sharma, A. Jaishankar, Y.-C. Wang, and G. H. McKinley. Rheology of globular proteins: apparent yield stress, high shear rate viscosity and interfacial viscoelasticity of bovine serum albumin solutions. *Soft Matter*, 7(11):5150–5160, 2011.

[36] M. M. Castellanos, J. A. Pathak, and R. H. Colby. Both protein adsorption and aggregation contribute to shear yielding and viscosity increase in protein solutions. *Soft Matter*, 10(1):122–131, 2014.

[37] J. L. Burns, Y.-d. Yan, G. J. Jameson, and S. Biggs. A Light Scattering Study of the Fractal Aggregation Behavior of a Model Colloidal System. *Langmuir*, 13 (24):6413–6420, 1997.

[38] V. Kumar, N. Dixit, L. L. Zhou, and W. Fraunhofer. Impact of short range hydrophobic interactions and long range electrostatic forces on the aggregation kinetics of a monoclonal antibody and a dual-variable domain immunoglobulin at low and high concentrations. *International Journal of Pharmaceutics*, 421(1): 82–93, 2011.

[39] S. J. Shire. Formulation and manufacturability of biologics. *Current Opinion in Biotechnology*, 20(6):708–714, 2009.

[40] J. Jezek, M. Rides, B. Derham, J. Moore, E. Cerasoli, R. Simler, and B. Perez-Ramirez. Viscosity of concentrated therapeutic protein compositions. *Advanced Drug Delivery Reviews*, 63(13):1107–1117, 2011.

[41] S. Yadav, T. M. Laue, D. S. Kalonia, S. N. Singh, and S. J. Shire. The influence of charge distribution on self-association and viscosity behavior of monoclonal antibody solutions. *Molecular Pharmaceutics*, 9(4):791–802, 2012.

[42] S. N. Singh, S. Yadav, S. J. Shire, and D. S. Kalonia. Dipole-Dipole Interaction in Antibody Solutions: Correlation with Viscosity Behavior at High Concentration. *Pharmaceutical Research*, 31(9):2549–2558, 2014.

[43] P. M. Buck, A. Chaudhri, S. Kumar, and S. K. Singh. Highly Viscous Antibody Solutions Are a Consequence of Network Formation Caused by Domain–Domain Electrostatic Complementarities: Insights from Coarse-Grained Simulations. *Molecular Pharmaceutics*, 12(1):127–139, 2014.

[44] S. Yadav, A. Sreedhara, S. Kanai, J. Liu, S. Lien, H. Lowman, D. S. Kalonia, and S. J. Shire. Establishing a Link Between Amino Acid Sequences and Self-Associating and Viscoelastic Behavior of Two Closely Related Monoclonal Antibodies. *Pharmaceutical Research*, 28(7):1750–1764, 2011.

[45] S. Saito, J. Hasegawa, N. Kobayashi, N. Kishi, S. Uchiyama, and K. Fukui. Behavior of Monoclonal Antibodies: Relation Between the Second Virial Coefficient (B 2) at Low Concentrations and Aggregation Propensity and Viscosity at High Concentrations. *Pharmaceutical Research*, 29(2):397–410, 2011.

[46] J. D. Schmit, F. He, S. Mishra, R. R. Ketchem, C. E. Woods, and B. A. Kerwin. Entanglement Model of Antibody Viscosity. *Journal of Physical Chemistry B*, 118 (19):5044–5049, 2014.

[47] I. E. Zarraga, R. Taing, J. Zarzar, J. Luoma, J. Hsiung, A. Patel, and F. J. Lim. High Shear Rheology and Anisotropy in Concentrated Solutions of Monoclonal Antibodies. *Journal of Pharmaceutical Sciences*, 102(8):2538–2549, 2013.

[48] W. Du and A. M. Klibanov. Hydrophobic salts markedly diminish viscosity of concentrated protein solutions. *Biotechnology and Bioengineering*, 108(3):632–636, 2010.

[49] L. Nicoud, M. Lattuada, A. Yates, and M. Morbidelli. Impact of aggregate formation on the viscosity of protein solutions. *Soft Matter*, 11(27):5513–5522, 2015.

[50] W. Cheng, S. B. Joshi, N. K. Jain, F. He, B. A. Kerwin, D. B. Volkin, and C. R. Middaugh. Linking the Solution Viscosity of an IgG2 Monoclonal Antibody to Its Structure as a Function of pH and Temperature. *Journal of Pharmaceutical Sciences*, 102:4291–4304, 2013.

[51] D. S. Tomar, S. Kumar, S. K. Singh, S. Goswami, and L. Li. Molecular basis of high viscosity in concentrated antibody solutions: Strategies for high concentration drug product development. *mAbs*, 8(2):216–228, 2016.

[52] W. G. Lilyestrom, S. Yadav, S. J. Shire, and T. M. Scherer. Monoclonal Antibody Self-Association, Cluster Formation, and Rheology at High Concentrations. *Journal of Physical Chemistry B*, 117(21):6373–6384, 2013.

[53] J. Liu, M. D. H. Nguyen, J. D. Andya, and S. J. Shire. Reversible Self-Association Increases the Viscosity of a Concentrated Monoclonal Antibody in Aqueous Solution. *Journal of Pharmaceutical Sciences*, 94(9):1928–1940, 2005.

[54] V. L. Dharmaraj, P. D. Godfrin, Y. Liu, and S. D. Hudson. Rheology of clustering protein solutions. *Biomicrofluidics*, 10(4):043509, 2016.

[55] S. Yadav, J. Liu, S. J. Shire, and D. S. Kalonia. Specific interactions in high concentration antibody solutions resulting in high viscosity. *Journal of Pharmaceutical Sciences*, 99(3):1152–1168, 2010.

[56] B. A. Salinas, H. A. Sathish, S. M. Bishop, N. Harn, J. F. Carpenter, and T. W. Randolph. Understanding and modulating opalescence and viscosity in a monoclonal antibody formulation. *Journal of Pharmaceutical Sciences*, 99(1):82–93, 2010.

[57] S. Yadav, S. J. Shire, and D. S. Kalonia. Viscosity Behavior of High-Concentration Monoclonal Antibody Solutions: Correlation with Interaction Parameter and Electroviscous Effects. *Journal of Pharmaceutical Sciences*, 101(3):998–1011, 2012.

[58] L. Li, S. Kumar, P. M. Buck, C. Burns, J. Lavoie, S. K. Singh, N. W. Warne, P. Nichols, N. Luksha, and D. Boardman. Concentration Dependent Viscosity of Monoclonal Antibody Solutions: Explaining Experimental Behavior in Terms of Molecular Properties. *Pharmaceutical Research*, 31(11):3161–3178, 2014.

[59] A. Saluja and D. S. Kalonia. Nature and consequences of protein–protein interactions in high protein concentration solutions. *International Journal of Pharmaceutics*, 358(1-2):1–15, 2008.

[60] A. S. Raut and D. S. Kalonia. Viscosity Analysis of Dual Variable Domain Immunoglobulin Protein Solutions: Role of Size, Electroviscous Effect and Protein-Protein Interactions. *Pharmaceutical Research*, 33(1):155–166, 2016.

[61] A. Goodman, Y. Tseng, and D. Wirtz. Effect of Length, Topology, and Concentration on the Microviscosity and Microheterogeneity of DNA Solutions. *Journal of Molecular Biology*, 323(2):199–215, 2002.

[62] T. G. Mason, A. Dhople, and D. Wirtz. Concentrated DNA Rheology and Microrheology. *MRS Proceedings*, 463:153, 1996.

[63] R. S. Tu and V. Breedveld. Microrheological detection of protein unfolding. *Physical review. E, Statistical, nonlinear, and soft matter physics*, 72(4), 2005.

[64] A. M. Corrigan and A. M. Donald. Particle tracking microrheology of gel-forming amyloid fibril networks. *The European Physical Journal E*, 28(4):457–462, 2009.

[65] G. Balakrishnan, D. Durand, and T. Nicolai. Particle Diffusion in Globular Protein Gels in Relation to the Gel Structure. *Biomacromolecules*, 12(2):450–456, 2011.

[66] M. H. Lee, D. H. Reich, K. J. Stebe, and R. L. Leheny. Combined Passive and Active Microrheology Study of Protein-Layer Formation at an Air−Water Interface. *Langmuir*, 26(4):2650–2658, 2010.

[67] K. M. Schultz and E. M. Furst. High-throughput rheology in a microfluidic device. *Lab on a Chip*, 11(22):3802–3809, 2011.

[68] L. L. Josephson, W. J. Galush, and E. M. Furst. Parallel temperature-dependent microrheological measurements in a microfluidic chip. *Biomicrofluidics*, 10(4): 043503, 2016.

[69] L. L. Josephson, E. M. Furst, and W. J. Galush. Particle tracking microrheology of protein solutions. *Journal of Rheology*, 60(4):531–540, 2016.

[70] C. Spiess, M. Merchant, A. Huang, Z. Zheng, N.-Y. Yang, J. Peng, D. Ellerman, W. Shatz, D. Reilly, D. G. Yansura, and J. M. Scheer. Bispecific antibodies with natural architecture produced by co-culture of bacteria expressing two distinct half-antibodies. *Nature Biotechnology*, 31(8):753–758, 2013.

[71] T. Savin and P. S. Doyle. Static and Dynamic Errors in Particle Tracking Microrheology. *Biophysical Journal*, 88(1):623–638, 2005.

[72] J. C. Crocker and D. G. Grier. Methods of digital video microscopy for colloidal studies. *Journal of Colloid and Interface Science*, 179(1):298–310, 1996.

[73] L. Van Hove. Correlations in Space and Time and Born Approximation Scattering in Systems of Interacting Particles. *Physical Review*, 95(1):249–262, 1954.

[74] L. T. DeCarlo. On the meaning and use of kurtosis. *Psychological Methods*, 2(3): 292, 1997.

[75] W. J. Galush, L. N. Le, and J. M. R. Moore. Viscosity Behavior of High-Concentration Protein Mixtures. *Journal of Pharmaceutical Sciences*, 101(3): 1012–1020, 2012.

[76] P. R. Naidu and V. R. Krishnan. Viscosities of binary liquid mixtures. In *Proceedings of the Indian Academy of Sciences- ...*, 1966.

[77] R. J. Fort and W. R. Moore. Viscosities of binary liquid mixtures. *Transactions of the Faraday Society*, 62(0):1112–1119, 1966.

[78] Q. F. Lei and Y. C. Hou. Correlation of viscosity of binary liquid mixtures. *Fluid Phase Equilibria*, 154(1):153–163, 1999.

[79] M. A. Blanco, T. Perevozchikova, V. Martorana, M. Manno, and C. J. Roberts. Protein-protein interactions in dilute to concentrated solutions: α-chymotrypsinogen in acidic conditions. *Journal of Physical Chemistry B*, 118 (22):5817–5831, 2014.

[80] R. Ghosh, C. Calero-Rubio, A. Saluja, and C. J. Roberts. Relating Protein-Protein Interactions and Aggregation Rates From Low to High Concentrations. *Journal of Pharmaceutical Sciences*, 105(3):1086–1096, 2016.

[81] T. H. Larsen and E. M. Furst. Microrheology of the Liquid-Solid Transition during Gelation. *Physical Review Letters*, 100(14):146001, 2008.

[82] K. M. Schultz and E. M. Furst. Microrheology of biomaterial hydrogelators. *Soft Matter*, 8(23):6198, 2012.

[83] P. D. Ross and A. P. Minton. Hard quasispherical model for the viscosity of hemoglobin solutions. *Biochemical and Biophysical Research Communications*, 76 (4):971–976, 1977.

[84] A. P. Minton. The effective hard particle model provides a simple, robust, and broadly applicable description of nonideal behavior in concentrated solutions of

bovine serum albumin and other nonassociating proteins. *Journal of Pharmaceutical Sciences*, 96(12):3466–3469, 2007.

[85] S. Kanai, J. Liu, T. W. Patapoff, and S. J. Shire. Reversible Self-Association of a Concentrated Monoclonal Antibody Solution Mediated by Fab–Fab Interaction That Impacts Solution Viscosity. *Journal of Pharmaceutical Sciences*, 97(10): 4219–4227, 2008.

[86] M. Mooney. The viscosity of a concentrated suspension of spherical particles. *Journal of Colloid Science*, 6(2):162–170, 1951.

[87] J. W. Mehl, J. L. Oncley, and R. Simha. Viscosity and the Shape of Protein Molecules. *Science*, 92(2380):132–133, 1940.

[88] A. P. Minton. Hard quasispherical particle models for the viscosity of solutions of protein mixtures. *Journal of Physical Chemistry B*, 116(31):9310–9315, 2012.

[89] T. W. Patapoff, R. J. Mrsny, and W. A. Lee. The Application of Size Exclusion Chromatography and Computer Simulation to Study the Thermodynamic and Kinetic Parameters for Short-Lived Dissociable Protein Aggregates. *Analytical Biochemistry*, 212(1):71–78, 1993.

[90] D. L. Leiske and J. Yan. Personal communication. 2015.

[91] C. Calero-Rubio, A. Saluja, and C. J. Roberts. Coarse-Grained Antibody Models for "Weak" Protein-Protein Interactions from Low to High Concentrations. *Journal of Physical Chemistry B*, 120(27):6592–6605, 2016.

[92] A. Aufderhorst-Roberts, W. J. Frith, M. Kirkland, and A. M. Donald. Microrheology and Microstructure of Fmoc-Derivative Hydrogels. *Langmuir*, 30(15):4483–4492, 2014.

[93] J. Apgar, Y. Tseng, E. Fedorov, M. B. Herwig, S. C. Almo, and D. Wirtz. Multiple-Particle Tracking Measurements of Heterogeneities in Solutions of Actin Filaments and Actin Bundles. *Biophysical Journal*, 79(2):1095–1106, 2000.

[94] E. J. Yearley, I. E. Zarraga, S. J. Shire, T. M. Scherer, Y. Gokarn, N. J. Wagner, and Y. Liu. Small-Angle Neutron Scattering Characterization of Monoclonal Antibody Conformations and Interactions at High Concentrations. *Biophysical Journal*, 105(3):720–731, 2013.

[95] J. Mewis and N. J. Wagner. *Colloidal Suspension Rheology*. Cambridge University Press, Cambridge, 2011.

Chapter 7

DIFFERENTIAL DYNAMIC MICROSCOPY (DDM) FOR MICRORHEOLOGY

7.1 Introduction

Differential dynamic microscopy (DDM) is an emerging method to measure the dynamics of complex colloidal or soft matter samples that have been measured with multiple particle tracking microrheology (MPT). DDM works by examining the temporal fluctuations of the local number density of particles via Fourier image analysis [1]. DDM has been used to characterize the dynamics of several complex fluids, including suspensions of motile bacteria [2, 3], anisotropic colloidal particles [4], and thermoreversible colloidal gels [5, 6]. It has also been used in both linear space-invariant imaging modes (i.e. bright-field, fluorescence, polarized, phase-contrast microscopy) [7] and a linear space-variant mode (i.e. dark-field microscopy) [8].

Here, we focus on the application and comparison of DDM to passive microrheology, as part of an effort to translate microrheology to an industrial workflow environment by providing a comprehensive and easy-to-implement software package. DDM has the advantage of less user involvement than standard particle tracking methods. In essence, DDM captures the function of dynamic light scattering, while retaining small sample sizes and the ability to directly observe the sample under test. However, a thorough error analysis for DDM as it is applied to microrheology is currently lacking. In this work, we apply DDM to fluorescence microscopy images of tracer probes dispersed in sucrose and PEO solutions. The DDM viscosity measurements are evaluated and compared to viscosity measured using particle tracking microrheology.

Ian Heffner, an undergraduate researcher working under my supervision, conducted the polymer experiments and performed an analysis using a nonlinear fitting

procedure I have developed. The images for DDM were co-processed by Ian Heffner and Alexandra V. Bayles (advised by Matthew E. Helgeson at University of California, Santa Barbara). The image processing was done using the software DDMCalc v1.0, developed by A V. Bayles and M. E. Helgeson, under the UCSB–DDMCalc License Terms.

7.2 Materials

Sucrose (ACS reagents grade, #84100, Sigma-Aldrich) is used as received. The sugar crystals are dissolved in ultra-pure Milli-Q water (resistivity ≤ 18.2 M Ω cm) at 0, 10, 25, 40, 55 wt% in 20 mL vials. The Milli-Q water and sucrose solutions are filtered using a centrifuge tube-top filter unit (EMD Millipore Steriflip-GP, 0.22 μm pore size, polyethersulfone, #SCGP00525) to prevent mold and bacteria growth. Poly(ethylene oxide) (PEO) solutions are prepared from 2.0 MDa PEO (Aldrich Chemistry, Lot No. MKBQ3351V). An amount of PEO for a given weight percent (0.2, 0.5, 1, 2, and 5 wt%) is added to 10 mL of ultra-pure water in a 20 mL scintillation vial at room temperature ($\sim$23°C). Samples will appear to have separate layers as the PEO slowly dissolves. The sample vials are placed on a stir plate at a medium speed for 30 minutes, until the solutions look visibly uniform; the vials then are incubated at 60°C overnight. The cross-over concentration c^* for 2MDa PEO is 0.25 wt%, and the entangled concentration c_e is 1.44 wt% [9].

Fluorescently-labeled polystyrene particles ($2a = 1.063 \pm 0.01$ μm, Fluoresbrite® Yellow Green Microspheres, Polysciences, Wallingford, PA) are chosen as scatterers; the particles are prepared by first washing them to remove excess fluorescent dye and possible contaminants from their manufacturing and storage. The polystyrene (PS) probes are taken from stock solution (2.5% w/v) and are centrifuged for 6 minutes at 5000 g. The centrifugation time depends on probe size and colloidal stability, and the washing procedures should be monitored carefully to prevent aggregation (see Ch. 2 Eq. 2.1). The supernatant is discarded and particles are redispersed in the same volume of ultra-pure Milli-Q water. This washing procedure is repeated three times.

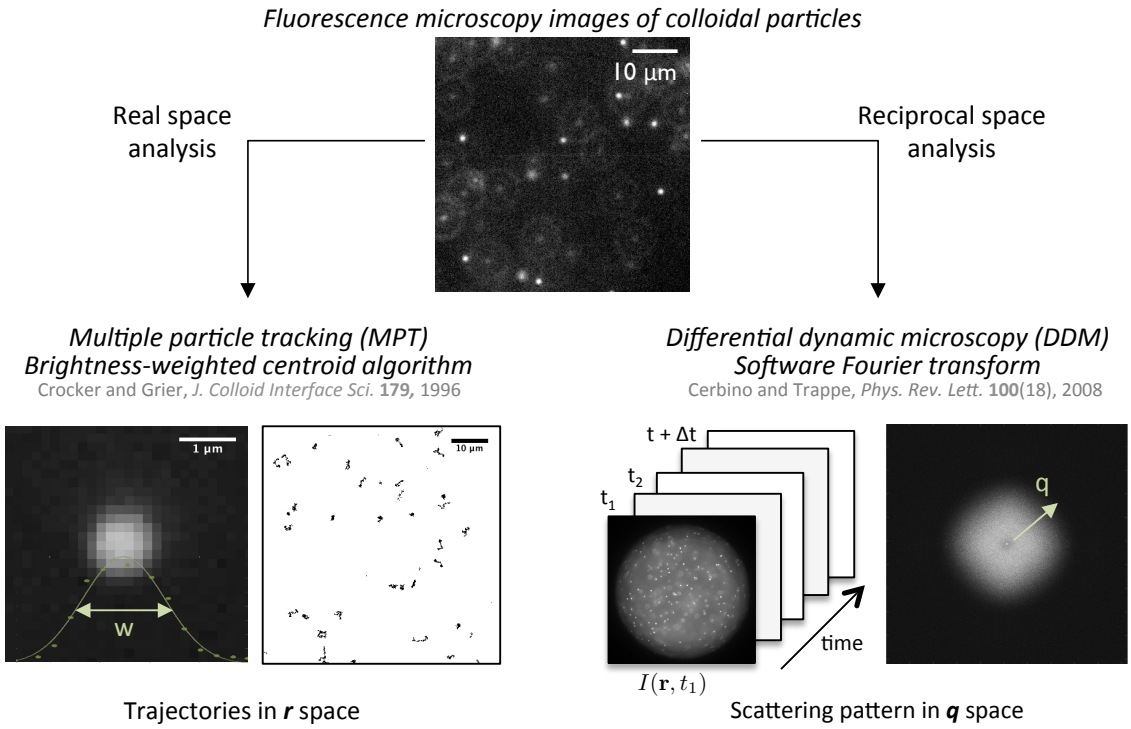

Figure 7.1: Two image analysis routes for processing the stack of micrographs of colloidal particles.

7.3 Experimental methods

Samples are loaded into the microcapillary channels (inside dimensions = 2.0 x 0.2 x 50 mm, glass thickness = 0.14 mm, part #3520, Vitrocom, Mountain Lakes, NJ) and sealed with NOA81 (Norland Products, Cranbury, NJ). Probe particles are imaged with a 40× objective (EC Plan-Neofluar, NA 0.75, Carl Zeiss) with a 1.6× tube-lens (Carl Zeiss) on an Axiovert 200 inverted microscope (Carl Zeiss). The pixel size is 0.252 μm/px and the image size is $L = 1024$ px. A CMOS high-speed camera (Phantom v5.1, Vision Research, Wayne, NJ) is used to record videos of the particles in the two dimensional focal plane at a shutter time σ at 2 ms or 5 ms and at acquisition rate $f = 30$ or 50 frames per second, respectively.

7.3.1 Image analysis in real space – Multiple particle tracking (MPT)

The algorithms behind multiple particle tracking microrheology (MPT) and the image analysis are described in detail in Ch. 2. In short, the particle positions are tracked using a brightness-weighted centroid algorithm [10, 11] to generate individual particle trajectories. The ensemble-averaged mean squared displacement is calculated at each time difference, and $\langle \Delta x^2 \rangle_{2D} = 4D\Delta t$. The Stokes-Einstein relation (SER) relates the diffusion coefficient D to the solution viscosity η by

$$D = kT/6\pi a\eta \tag{7.1}$$

where kT is the thermal energy and a is the particle radius.

7.3.2 Image analysis in reciprocal space – Differential dynamic microscopy (DDM)

DDM analyzes time-lapse images through the statistics of the image intensity $I(r,t)$, where r is the pixel position and t is time. The differential image correlation function $g(\mathbf{q}, \Delta t)$ is defined as

$$g(\mathbf{q}, \Delta t) = \langle |F_D(\mathbf{q}, \Delta t)|^2 \rangle_t = \langle |I(\mathbf{q}, t + \Delta t) - I(\mathbf{q}, t)|^2 \rangle_t \tag{7.2}$$

where $I(\mathbf{q}, t)$ is the Fourier transform of $I(\mathbf{r}, t)$. In a Newtonian fluid Eq. 7.2 describes of the motion of the particles. For isotropic diffusion, $g(\mathbf{q}, \Delta t)$ can be azimuthally averaged to give $g(q, \Delta t)$. Thus, the differential image correlation function (DICF) is related to the self-intermediate scattering function $f(q, \Delta t)$ [1] by

$$g(q, \Delta t) = A(q)[1 - f(q, \Delta t)] + B(q) \tag{7.3}$$

where $B(q)$ is related to camera noise that can be estimated as two times the power spectrum of the camera noise [3] and $A(q)$ is related to the light source coherence,

microscope objective properties, and particle scattering properties. For point-like scatterers, $A(\mathbf{q})$ is given by [12]

$$A(\mathbf{q}) = \frac{2a_p^2}{\sqrt{\pi}} \frac{C^2(\mathbf{q})}{\Delta q} [1 - e^{-(\bar{q}_z/\Delta q)^2}] \tag{7.4}$$

where a_p is the radius of the particles, $\Delta q^2(\mathbf{q}) = q^2\sigma_c^2/[1 + 2(\sigma_c/\sigma_o)^2]$ where σ_c gives an estimate of the numerical aperture of the condenser and σ_o of the objective, and their ratio $M = \sigma_\mathrm{c}/\sigma_\mathrm{o}$ gives the degree of incoherence, $C(\mathbf{q})$ is a decreasing function of the wave vector q that describes the overall frequency modulation introduced by the imaging process, defined as $C(\mathbf{q}) = \exp[-q^2/4q_\mathrm{ro}^2]/[1 + 2M^2]$. At the limit of low q, $A(q) \sim q^4$; at large q, the behavior of $A(q)$ is set by C^2/q that resulted from the progressive loss of coherence ($M \to \infty$) and with the limited numerical aperture of the collection optics. In their work detailing the above relations, Giavazzi et al. [12] used 73 nm particles to model as point-like scatterers and phase objects; if the size and the form factor of the scatterer are not negligible (e.g. 1 μm particles in this work), the right side of Eq. 7.4 should be multiplied by the form factor of the particles [13]. For the remainder of the discussion, we focus on the analysis of $g(q, \Delta t)$ and $f(q, \Delta t)$ for the materials of interest, and we leave to future work the mathematical analysis and determination of microscope and light source properties.

The image processing and fitting are based on Martinez et al. [3] and automated in MATLAB (code available in Appendix). Fig. 7.2 illustrates the steps used to process the images and arrive at the differential image correlation function. For a given lag time Δt, the difference images $D(\mathbf{r}, \Delta t) = I(\mathbf{r}, t + \Delta t) - I(\mathbf{r}, t)$ are calculated for a set of initial times t_i (typically logarithmically spaced). Each difference image is Fourier-transformed to become $F_D(\mathbf{q}, \Delta t) = \int D(\mathbf{r}, \Delta t) e^{i\mathbf{q}\cdot\mathbf{r}} d\mathbf{r}$, and the power spectrum of $F_D(\mathbf{q}, \Delta t)$ is calculated and averaged over the initial times t_i to yield $g(\mathbf{q}, \Delta t)$. The averaged scattering pattern improves the signal-to-noise ratio and appears less grainy. For isotropically diffusing particles, $g(\mathbf{q}, \Delta t)$ is azimuthally averaged to give $g(q, \Delta t)$. To create the azimuthal average in a discrete q-matrix, four adjacent points are linearly

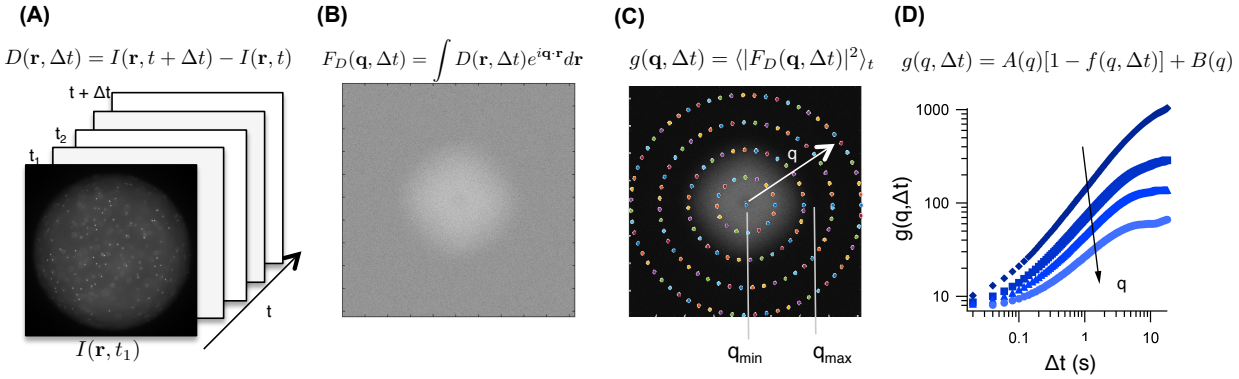

Figure 7.2: Schematic of image processing to obtain the differential image correlation function (DICF) from image stack collected in experiment (A), to the non-averaged Fourier-transformed difference image (B), to the ensemble-averaged scattering pattern with azimuthal rings (C), and to sample DICFs at different q vectors (D).

interpolated [3] to find values for $g(q, \Delta t)$ along a circle with radius q (depicted with the rings in Fig. 7.2C). The intermediate scattering function (ISF) for identical and independently diffusing particles is given by

$$f(q, \Delta t) = e^{-q^2 D \Delta t} = e^{-q^2 \langle \Delta r^2(\Delta t)/6 \rangle} \tag{7.5}$$

where $\langle \Delta r^2(\Delta t) \rangle$ is the ensemble mean squared displacement of the particles in 3 dimensions, and the viscosity of the material can be calculated from the diffusion coefficient D through the Stokes–Einstein relation (Eq. 7.1). Thus, each $g(q, \Delta t)$ curve is independently fitted to

$$g(q, \Delta t) = A(q)[1 - \exp(-\Delta t/\tau)] + B(q) \tag{7.6}$$

at each q vector using non-linear least squares fit with A, B and $\tau = 1/Dq^2$ as fitting parameters. Note that $f(q, \Delta t)$ is the Fourier transform of the Van Hove space-time correlation function (see Eq. 5.2).

Table 7.1: Summary of advantages of MPT and DDM

Multiple particle tracking	**Differential dynamic microscopy**
Small sample size	
Fast acquisition	
Simple microscopy setup	
Sub-pixel resolution	No user-selected parameter
Fast image analysis	Full system dynamics through FFT
Well-known errors and operating regime	Operating regime not well-established
Need well-controlled imaging conditions	Good for optically dense, blurry samples

7.3.3 Advantages and challenges of each method

Multiple particle tracking (MPT) and differential dynamic microscopy (DDM) share a number of advantages when used for microrheology; both only require a small sample and have fast acquisition times. The optical setup is also simple, requiring only a stable light source on an otherwise unmodified microscope. All of the experiments analyzed using the two methods in this chapter use the same samples and same image stack (with the same optical resolution) for each sample.

MPT can achieve subpixel resolution with the brightness-weighted centroid algorithm [10], whereas DDM operates in a discrete matrix of size L, and thus can only achieve the resolution of two pixels (based on Nyquist frequency, defined as the spatial frequency at which a signal can be sampled without introducing aliasing errors). Reduced spatial resolution effectively narrows the operating regime, as particles move less in a higher viscosity environment, and thus we do not expect DDM to be able to probe highly viscous materials (as is discussed on pg. 181). However, MPT's algorithm requires a significant degree of user involvement determining the tracking parameter w (the approximate width of particles in the image plane) and validating the tracking results against artifacts like pixel-biasing [11]. The brightness of the images also needs to be controlled in the MPT experimental setup to avoid overexposure of the particles, for the centroid algorithm can only accurately detect a Gaussian intensity profile with

one bright pixel in the center and more than 4 pixels wide. The MPT tracking algorithm constrains the density of the probe particles in the system as well as the choice of objective magnification that can be used to perform the experiment. On the other hand, DDM does not require the user to select any parameters (just sensible initial guesses for the fitting procedures). It also does not require perfect imaging conditions, as prior studies have shown that DDM works well in optically dense [8] and blurry samples [12]. However, such ability to capture the full dynamics in the images comes with a tradeoff in computational time. The fast Fourier transform (FFT) used in the DDM algorithm is much more computationally intensive than the centroid algorithm in MPT. In a computer with 8 Gb memory and 2.5 GHz quad core processor, the brightness-weighted centroid algorithm takes 353 seconds to analyze 1000 frames of images (1024×1024 px), but the FFT algorithm requires close to 12 hours to complete the analysis with a logarithmically-spaced vector of time steps. Recognizing the FFT is memory-intensive, we tested the DDM algorithm on the same set of images in a computer with 32 Gb RAM; the analysis time for log-spaced time steps is cut down to 36 minutes, and the full analysis takes 6.8 hours. There is no difference in processing time between 8 bit and 16 bit images, because when the images are read in as numerical arrays using the "double" command, they are converted to 64 bit precision.

MPT has well-characterized errors [14, 15] and is an established method in characterizing complex fluids [10, 16–19] through the generalized Stokes–Einstein relation. DDM, along with other digital Fourier microscopy methods [20], is relatively new compared to MPT; part of the goal of this work is to show how non-Newtonian material rheology and sample drifts and oscillations, whose effects are understood in MPT, manifest themselves in the differential image correlation functions obtained from DDM.

7.4 Results and Discussion

7.4.1 Comparison of MPT to DDM for Newtonian fluids

To compare the performance of MPT and DDM, we start with Newtonian fluids, 0 to 55 wt% sucrose solutions with 1μm PS particles used previously as calibration standards to characterize the precision of MPT. Fig. 7.3A shows the mean squared displacements (MSD) $\langle \Delta x^2(\Delta t) \rangle$ in the sucrose solutions. The MSDs are well above the noise floor (indicated as the horizontal data line in the plot), and all have a logarithmic slope of 1. The viscosity of the sucrose samples is calculated at the optimal lag time Δt as determined by the excess kurtosis of the Van Hove correlation (see Ch. 3 for details on the analysis method) and is shown in the x-axis of the parity plot (Fig. 7.3B). The same image stacks are also analyzed using DDM, and the resulting differential image correlation functions (DICFs) are shown in 3 different q vectors for all time steps for the 55 wt% sucrose solution (Fig. 7.4A). Each of the DICF is fitted to Eq. 7.6 and the resulting fitting parameters, $A(q)$, $B(q)$, and the material relaxation time $\tau = (q^2 D)^{-1}$, are plotted as a function of q (Fig. 7.4B-C). The diffusion coefficient of the particles in the sucrose solutions is calculated from $\tau(q)$ in the region ($q \sim$ 1–4 μm^{-1}) with a logarithmic slope of -2, and the calculated viscosity (through the Stokes–Einstein relation) is plotted in the y-axis in Fig. 7.4B. We have previously demonstrated that particle tracking microrheology is consistently capable of measuring the viscosity with less than 2% error for all of the sucrose samples [21]; thus we have not repeated the bulk rheology experiments here. The parity plot shows the MPT and DDM viscosity are in very good agreement (as well as tabulated data [22]). Both methods are robust techniques for Newtonian fluids that are well within the operating regime of passive microrheology [23].

The DDM results plotted in Fig. 7.4C can be better understood and compared to MPT by examining the corresponding MSD curves and particle displacement distributions from particle tracking experiments. Fig. 7.5 shows τ as a function of q marked with three different q regions. Corresponding Van Hove self-correlations for 10 wt% and 55 wt% sucrose solutions at various Δt are also depicted.

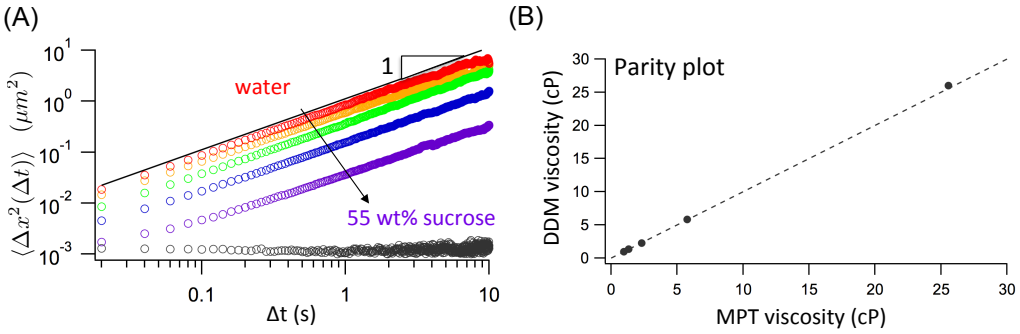

Figure 7.3: Comparison of the two methods, MPT and DDM, in measuring the viscosity of Newtonian fluids. (A) The mean-squared displacements of 1μm particles diffusing in sucrose solutions. The noise floor is indicated as the horizontal line of points. (B) Parity plot comparing the calculated viscosity of sucrose solutions from MPT to DDM.

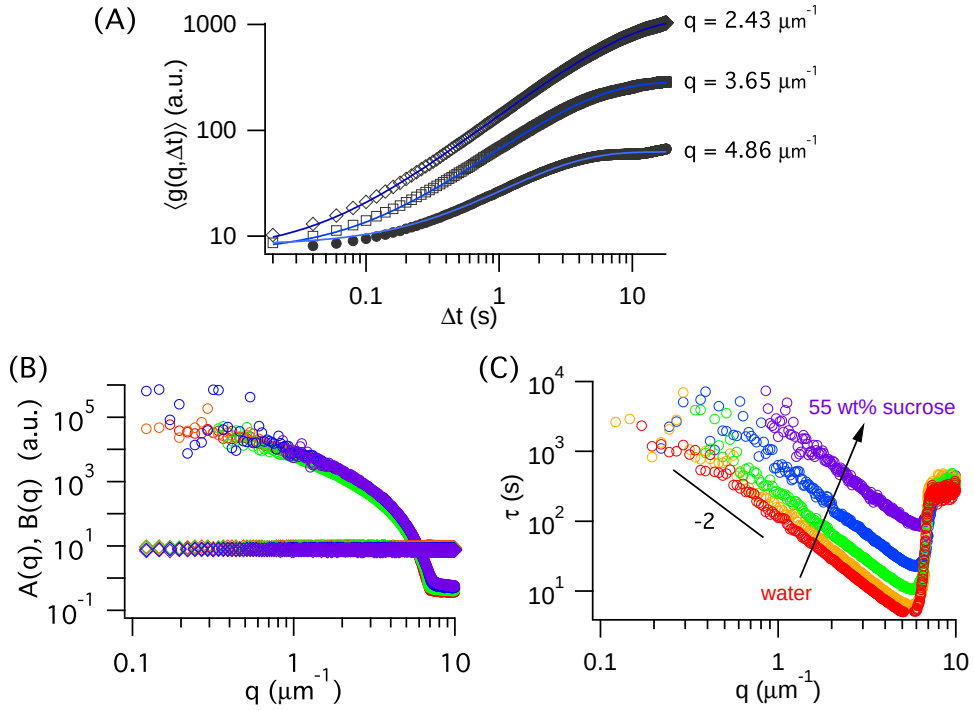

Figure 7.4: (A) Sample DICFs and their fits to Eq. 7.6 of 55 wt% sucrose at $q = 2.43$, 3.65, and 4.86 μm^{-1}. (B) The fitted $A(q)$ and $B(q)$ parameter from DICF as a function of q for all sucrose solutions. (C) The fitted τ parameter from DICF as a function of q for all sucrose solutions.

In the intermediate q region (Region 2 in Fig. 7.5), the log slope of $\tau(q)$ is -2. Similar to MPT (for $\langle \Delta x^2(\Delta t) \rangle \sim 1$), this is the region where precise and accurate viscosities can be extracted. At $q \sim 4$–5 μm^{-1}, $\langle \Delta x^2(\Delta t) \rangle \approx 0.04$–$0.0625$ μm^2; this MSD corresponds to displacement distributions with N $\gg$ 1000, typically at short time steps. The Van Hove functions for 10 wt% and 55 wt% with $\sigma^2 \approx 0.04$ μm^2 both show a good fit to a normal distribution.

However, at small q (or large displacements Δx), we see that τ fluctuates in all of the curves (Region 1 in Fig. 7.5). Observations of large particle displacements are rare; the corresponding values of $\langle \Delta x^2(\Delta t) \rangle$ have a low number of observations ($N \leq 1000$). At $q \sim 1.5$ μm^{-1}, the corresponding MSD is $\langle \Delta x^2(\Delta t) \rangle \approx 0.3$–$0.4$ μm^2. There are still enough observations ($N = 6396$) in the 10 wt% sucrose sample's Van Hove function at $\Delta t = 0.74$ s and $\sigma^2 = 0.44$ μm^2. However, in the more viscous 55 wt% sucrose solution, the total number of observations is $N = 165$; this Van Hove function is clearly not a normal distribution, and would not be useful for calculating the viscosity in MPT analysis. At these conditions, the probe particles are diffusing in and out of the focal plane, leading to low particle statistics and data that should not be included in a viscosity calculation.

Finally, as q increases beyond 5 μm^{-1} (Region 3 in Fig. 7.5), we see an abrupt change in τ between $q = 5$–6 μm^{-1}. This corresponds to $\Delta x < 0.2$ μm, which is smaller than the pixel size at 0.252 μm/px. Since there is no user-input, the fitting procedures do not take into account the pixel size, which is the reason why the fitting parameter τ suddenly approaches the same values at $q > 5$ μm^{-1}. Since DDM is performed in a discrete matrix, this method cannot achieve subpixel resolution as contrasted to MPT. The maximum limit of viscosity that can be probed by particles with diameter $2a$ can be estimated as

$$\eta_{\text{max}} = kT\Delta t / 3\pi a (\Delta x_{\text{min}})^2 \tag{7.7}$$

where Δx_{min} represents the minimum spatial resolution. For MPT, Δx_{min} is the noise floor, which is typically $\epsilon \sim 10$ nm. For DDM, the Nyquist sampling frequency is 2

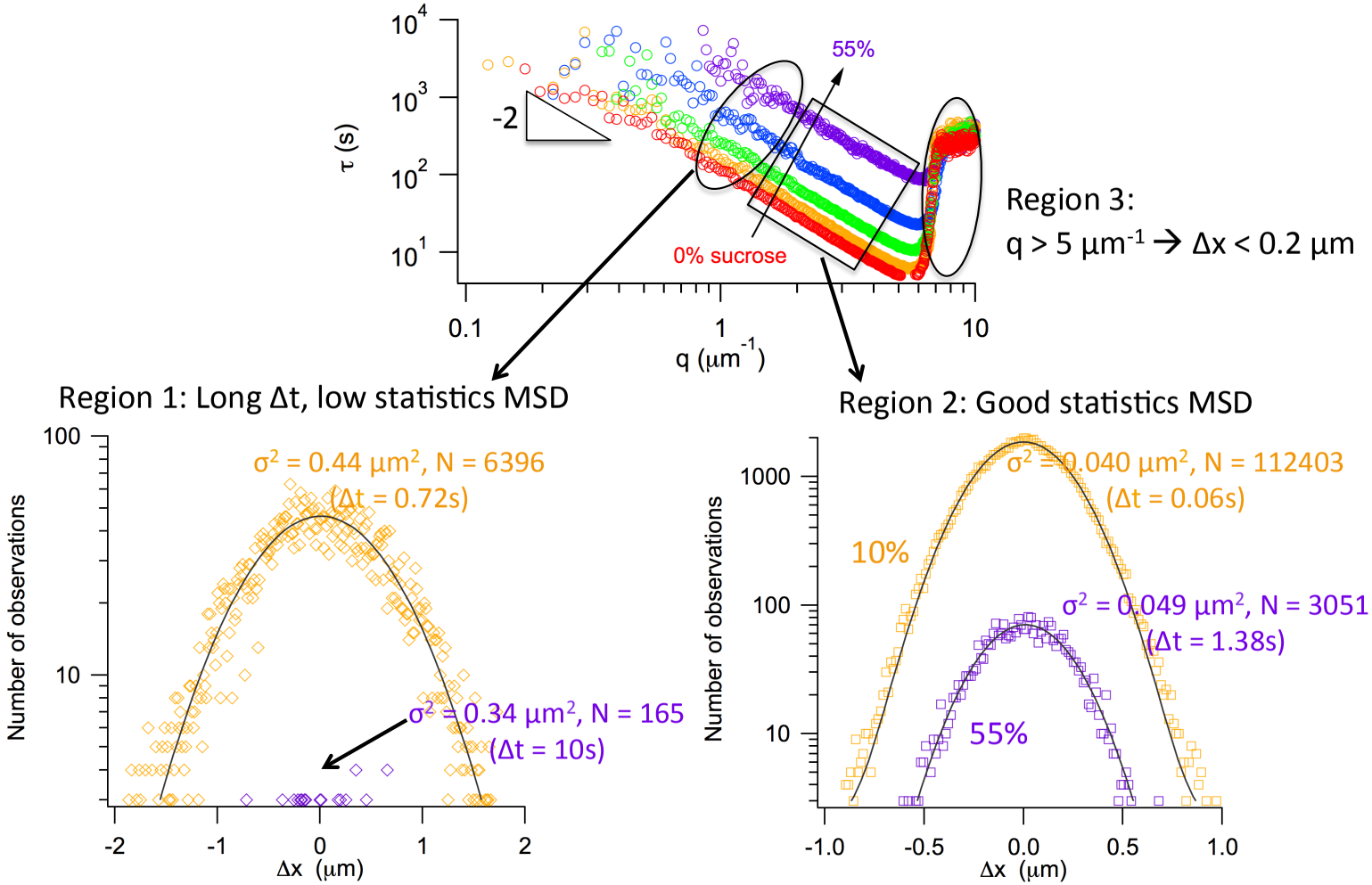

Figure 7.5: DDM in relation to Van Hove self-correlation. To better understand τ as a function of q, the plot is separated into 3 regions: small q limit (Region 1), intermediate q (where $\tau \sim 1/q^2$, Region 2), and large q limit (Region 3). The corresponding particle displacement distributions (or Van Hove self-correlation) are from MSD show the statistics in a particular q region.

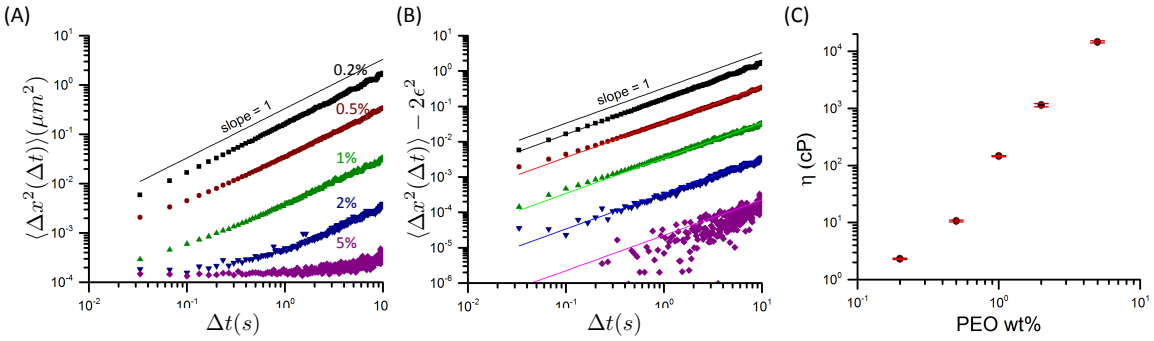

Figure 7.6: MPT results for 2MDa PEO solutions. (A) Apparent MSD of PEO solutions from 0.2 wt% to 5 wt%. (B) Corrected MSD with an estimated noise floor of $\epsilon \approx 12$ nm. (C) Viscosity of PEO solutions as a function of wt%.

pixels, which corresponds to $\Delta x_{\min} = 500$ nm in this microscopy setup. Therefore, the theoretical maximum viscosity that can be measured by DDM is 2500 times less than that by MPT.

7.4.2 Comparison of MPT to DDM for non-Newtonian fluids

The utility of differential dynamic microscopy has been demonstrated in characterization of the dynamics of many complex systems, including anisotropic magnetic particles [4], active swimmers [2, 3, 24], and fractal aggregation of nanoparticles [25, 26].

Both MPT and DDM are robust techniques for Newtonian fluids so long as the fluid dynamics are within the operating regime of passive microrheology. Here, we explore the applicability of DDM for non-Newtonian fluids by examining PEO solutions.

Fig. 7.6A shows the apparent MSD for 2 MDa PEO solutions from 0.2 wt% to 5 wt%. The low concentration solutions have linear behavior with logarithmic slopes of 1, while the slope is markedly less at low Δt for higher concentration solutions. The PEO solutions are expected to cross from non-Newtonian to viscous behavior beyond the polymer longest relaxation time τ_s. Nghe et al. [27] measured that 0.8 wt% 2MDa PEO has a $\tau_s = 43$ ms, and Arnolds et al. [9] estimated the longest shear

relaxation time of the 2MDa PEO to be τ_s ~1 ms at 0.2 wt%, τ_s ~50 ms at 1 wt% (which corroborate Nghe's measurement), and increases to τ_s ~1 s at 2 wt%. With our MPT measurements starting at $\Delta t = 1/30$ s or 33 ms, we are unable to observe non-Newtonian behavior in the low concentration samples. The apparent MSDs at short-time scales ($\Delta t < 0.1$ s) could be exhibiting slight curvature that increases with PEO concentration up to 1 wt%, but because we must be careful in particle tracking analysis to subtract out the static error, this apparent curvature disappears, and the 1 wt% PEO solution appears Newtonian with a logarithmic slope of 1 (Fig. 7.6B). When the apparent MSD is corrected for an estimated static error of $\epsilon \approx 12$ nm[1] with $\langle \Delta x^2 \rangle_{\text{apparent}} = \langle \Delta x^2 \rangle_{\text{true}} + 2\epsilon^2$ [14], the severe effect of the noise floor on the 2 wt% and 5 wt% PEO solutions is clear (Fig. 7.6B). The zero-shear viscosities of the solutions are calculated at the appropriate Δt with enough statistics in the Van Hove correlation and the results are shown in Fig. 7.6C. Our MPT calculated viscosity η for PEO solutions < 5 wt% matches the zero-shear viscosity reported in Arnolds et al. [9] and Nghe et al. [27] within experimental error. For the 5 wt% PEO sample, the viscosity is calculated at large Δt = 10 s, where the logarithmic slope recovers to 1; the maximum limit of viscosity that can be probed using particles with $2a = 1$ μm in a microscopy system with a noise floor $\epsilon \approx 12$ nm is estimated at $\eta_{\text{max}} \sim 30 \times 10^3$ cP using Eq. 7.7. With the calculated viscosity at $\eta \approx 14.5 \times 10^3$ cP, the 5 wt% PEO solution is at the limit of MPT (see calculated operating diagram Fig. 1.5 in Sec. 1.5.1).

Fig. 7.7A and Fig. 7.7B show sample DICFs from 0.2 wt% and 2 wt% PEO. The DICF should reach a plateau at long Δt, when the particle motions are decorrelated, and at short Δt, when they are completely correlated. For 0.2 wt% PEO solution, this is clearly seen (Fig. 7.7A), so when fitting these curves, we expect to find well-defined values of A, B, and τ, except for $q = 0.48 \mu\text{m}^{-1}$, in which the long time behavior has not yet reached a plateau. However, the 2 wt% solution is much more viscous, and the probes do not have enough time to decorrelate enough for the DICF to reach a

[1] See Chapter 4 for details on the *it situ* estimation of ϵ.

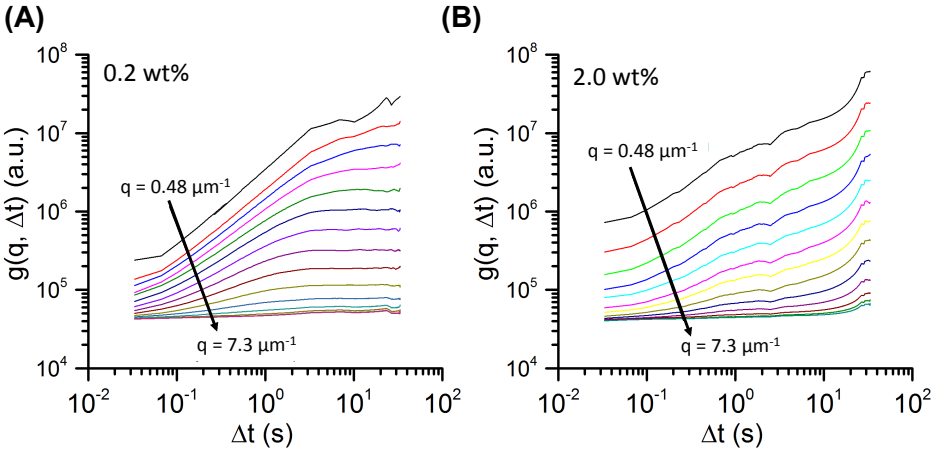

Figure 7.7: Sample differential image correlation functions from 0.2 wt% (A) and 2 wt% (B) 2MDa PEO samples, with $0.48 \leq q \leq 7.3\ \mu\text{m}^{-1}$.

plateau, even at high q.

Fitting the DICF to Eq. 7.6 gives the functions for $A(q)$ and $B(q)$ in Fig. 7.8A and τ(s) in Fig. 7.8B. For all solutions, the prefactor $A(q)$ takes the expected shape calculated by Giavazzi et al. [12], and the $B(q)$ baseline term, representing the camera noise, gives a consistent value across all solutions, as expected. The behavior of τ as a function of q is described in Fig. 7.8B. For values of $q > 5\ \mu m^{-1}$, the Nyquist frequency, no more useful data is available, and $A(q)$ flattens out while τ deviates from the logarithmic slope of -2, indicating the operating regime for this setup. The low concentration solutions exhibit the logarithmic slope of -2 in the intermediate q range, permitting the extraction of a diffusion coefficient D, and hence, the viscosity η (Fig. 7.8C). The viscosity according to DDM is a close match to that from MPT (Fig. 7.8D), though 1 wt% is beginning to deviate, which is likely due to the slope of τ deviating from -2 in Fig. 7.8B. However, the 2 wt% and 5 wt% solutions, which had significant static error in the MSD, did not return well-behaved functions of $g(q, \Delta t)$ and thus τ, so calculating D and η is not possible. Static error is well-characterized in MPT, enabling the extraction of viscosity even when the static error is dominating

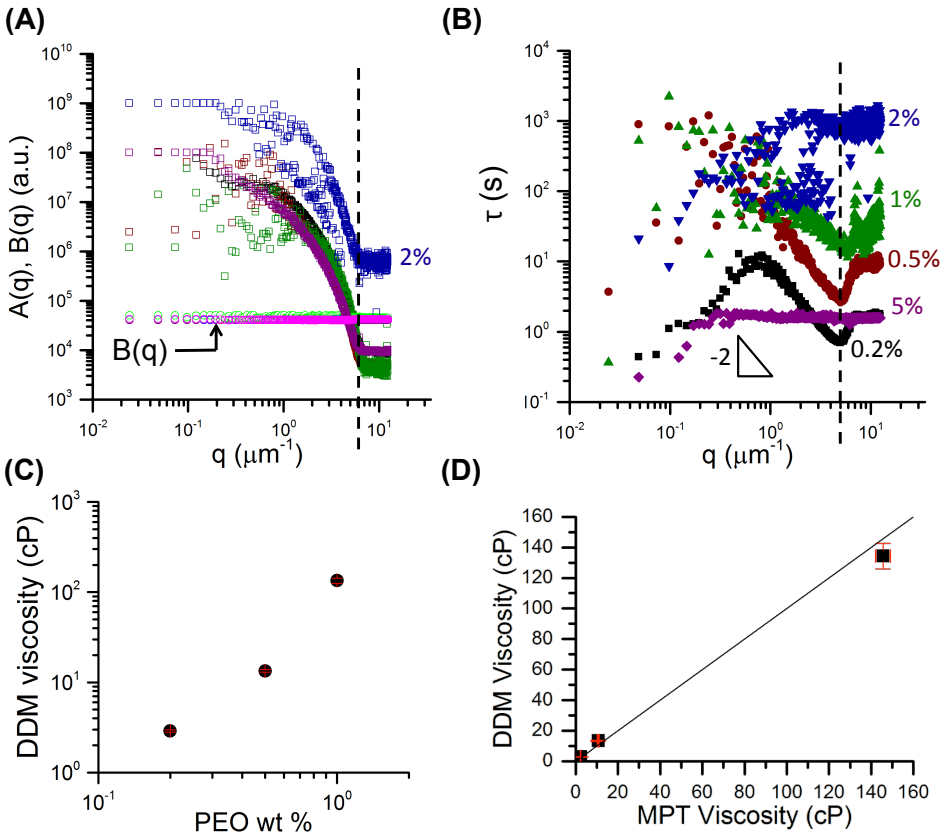

Figure 7.8: DDM results for 2MDa PEO solutions. (A-B) Fitted parameters from DICF as a function of q for all PEO solutions. The vertical dash lines indicate $q = 5\ \mu\text{m}^{-1}$, the Nyquist sampling frequency. (C) The calculated viscosity of the PEO solutions from 0.2 wt% to 1 wt%. (D) Parity plot comparing the calculated viscosity of PEO solutions from MPT to DDM.

the measurement. Even under difficult or extremely high viscosity conditions, some information can be extracted using MPT (refer to detail discussions in Sec. 1.5.1 and Chapter 4). However, the noise floor baseline in DDM is not well-explored, so no method currently available can account for this source of error, leaving the operating regime for DDM smaller than that of MPT.

These experiments did not measure the non-Newtonian behavior of these PEO solutions, as evidenced by the log slope of 1 in the corrected MSDs. A better material for examining non-Newtonian behavior in MPT would exhibit relaxation times $\tau_s \gg 0.03$ s. Even though the non-Newtonian behavior of these solutions was not detected, the experiment demonstrates the capabilities and limits of MPT and DDM in measuring high viscosities.

7.4.3 Samples with vibration or drift

To investigate the effects of oscillations on DDM analysis, we analyzed results from a 55 wt% sucrose solution at room temperature with vibrations from a water pump. The oscillations are visually apparent in Fig. 7.9A, where the MSD fluctuates with a period of 0.18 s. However, these oscillations don't interfere with the DDM analysis, as can be seen in Fig. 7.9B-D, where the DICF, $A(q)$, $B(q)$ and $\tau(q)$ are unaffected. The DDM-calculated viscosity of the sample, $\eta = 25$ cP, matches that expected for a 55 wt% sucrose solution.

The oscillations are observed in the MSD because their magnitude, calculated to be ∼19 nm, is greater than the noise floor of ∼12 nm. Nevertheless, these oscillations are outside the q range of the experiment (52 μm^{-1}), so they do not affect the analysis. Even if the oscillation were in the intermediate q range, the Fourier transform would render the oscillation as a single point, which could be removed as an outlier prior to analyzing the sample as usual. This would not be possible with MPT, and so illustrates an advantage of DDM.

To investigate the effects of drift on DDM analysis, we analyzed results from a 0.2 wt% PEO solution at room temperature with drift due to an improperly sealed

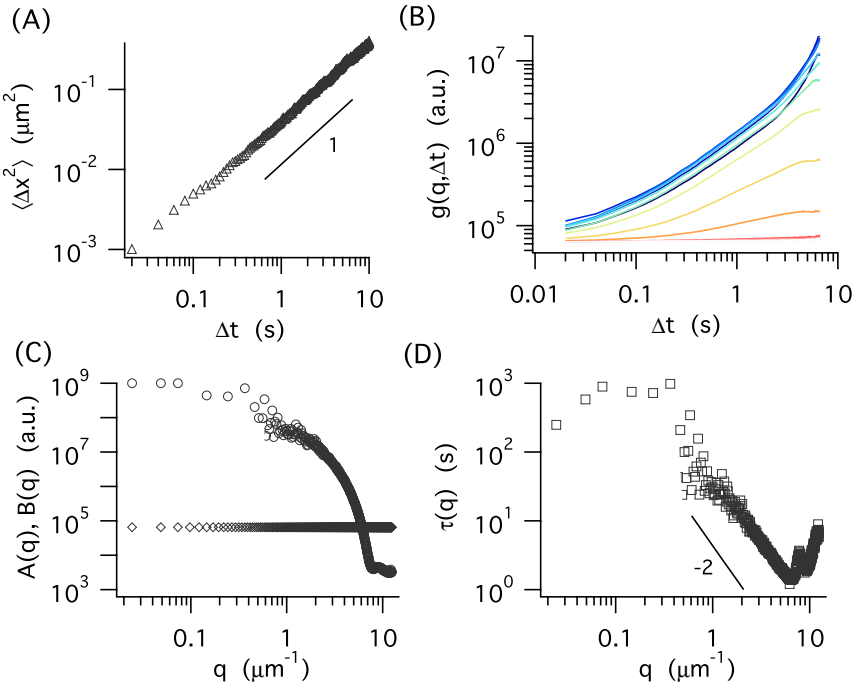

Figure 7.9: Oscillation in a sample and its effect on MPT and DDM analysis. (A) Apparent MSD of 55 wt% sucrose sample with an estimated vibration of 19 nm with a frequency of 1/0.18 s. (B) Sample DICFs of the oscillating sample, with $0.024 \leq q \leq 12$ μm^{-1}. (C-D) Fitted parameters from DICF as a function of q for the oscillating sample.

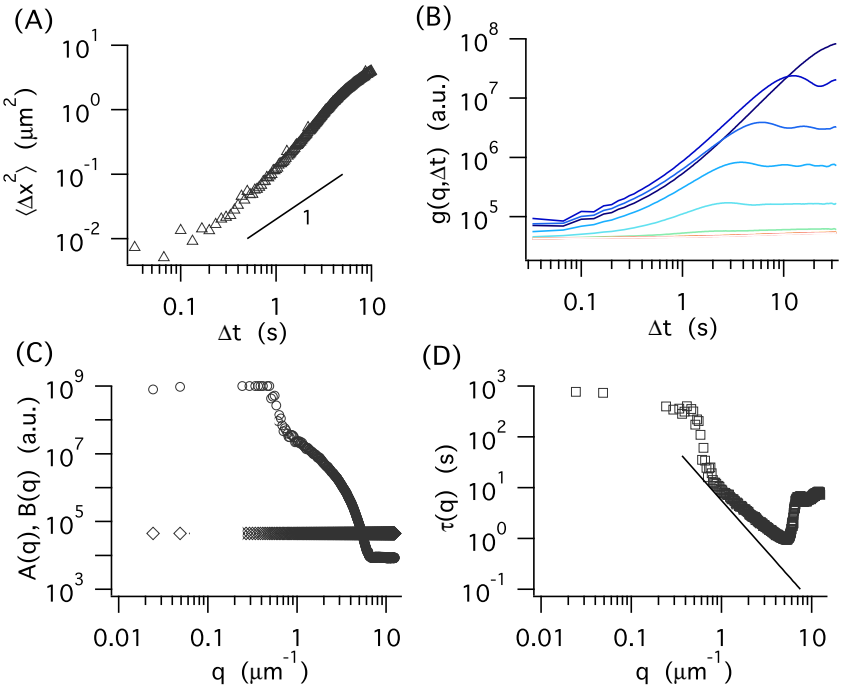

Figure 7.10: Drift in a sample and its effect on MPT and DDM analysis. (A) Apparent MSD of 0.2 wt% PEO sample with a drift induced by an incomplete seal. (B) Sample DICFs of the drifting sample, with $0.024 \leq q \leq 12$ μm^{-1}. (C-D) Fitted parameters from DICF as a function of q for the drifting sample.

sample. The MSD has a slope > 1 (Fig. 7.10A), so the solution appears to be super-diffusive, when it should be Newtonian. Even though the sample is drifting, the particle dynamics are unchanged, as evidenced by the plateaus in the DICF (Fig. 7.10B) and the expected behavior of $A(q)$ and $B(q)$ (Fig. 7.10C). Observing a $\tau(q)$ without a logarithmic slope of -2 is also indicative of drift in the sample. While MPT can correct for small drifts using a detrending algorithm [11, 28], this is not applicable for DDM because individual particles are not being tracked.

7.5 Conclusions and Outlook

With the advantages of fast acquisition, fewer user-selected parameters than particle tracking, the ability to examine optically dense, blurry, and oscillating systems, DDM could become a versatile method for characterizing the microrheology of complex fluids. The utility of microrheology with DDM has been illustrated for Newtonian solutions, for which viscosities calculated through DDM exhibit good agreement with those calculated through MPT, as well as with tabulated values for sucrose viscosity. In the next steps, the precision and accuracy of DDM could be evaluated by examining the particle statistics and error propagation in the Fourier analysis of DDM, to select an optimal wave vector q for calculating the viscosity, similar to work done for microrheology [21]. DDM could also be extended to examine non-Newtonian and non-ergodic samples [4] similar to what has been done in passive microrheology [29–32].

REFERENCES

[1] R. Cerbino and V. Trappe. Differential Dynamic Microscopy: Probing Wave Vector Dependent Dynamics with a Microscope. *Physical Review Letters*, 100 (18):188102, 2008.

[2] L. G. Wilson, V. A. Martinez, J. Schwarz-Linek, J. Tailleur, G. Bryant, P. N. Pusey, and W. C. K. Poon. Differential Dynamic Microscopy of Bacterial Motility. *Physical Review Letters*, 106(1):018101, 2011.

[3] V. A. Martinez, R. Besseling, O. A. Croze, J. Tailleur, M. Reufer, J. Schwarz-Linek, L. G. Wilson, M. A. Bees, and W. C. K. Poon. Differential Dynamic Microscopy: A High-Throughput Method for Characterizing the Motility of Microorganisms. *Biophysical Journal*, 103(8):1637–1647, 2012.

[4] M. Reufer, V. A. Martinez, P. Schurtenberger, and W. C. K. Poon. Differential dynamic microscopy for anisotropic colloidal dynamics. *Langmuir*, 28(10):4618–4624, 2012.

[5] Y. Gao, J. Kim, and M. E. Helgeson. Microdynamics and arrest of coarsening during spinodal decomposition in thermoreversible colloidal gels. *Soft Matter*, 11 (32):6360–6370, 2015.

[6] S. Buzzaccaro, M. D. Alaimo, E. Secchi, and R. Piazza. Spatially-resolved heterogeneous dynamics in a strong colloidal gel. *Journal of Physics Condensed Matter*, 27(19):194120, 2015.

[7] K. He, M. Spannuth, J. C. Conrad, and R. Krishnamoorti. Diffusive dynamics of nanoparticles in aqueous dispersions. *Soft Matter*, 8(47):11933–11938, 2012.

[8] A. V. Bayles, T. M. Squires, and M. E. Helgeson. Dark-field differential dynamic microscopy. *Soft Matter*, 12(8):2440–2452, 2016.

[9] O. Arnolds, H. Buggisch, D. Sachsenheimer, and N. Willenbacher. Capillary breakup extensional rheometry (CaBER) on semi-dilute and concentrated polyethyleneoxide (PEO) solutions. *Rheologica Acta*, 49(11-12):1207–1217, 2010.

[10] J. C. Crocker and D. G. Grier. Methods of digital video microscopy for colloidal studies. *Journal of Colloid and Interface Science*, 179(1):298–310, 1996.

[11] J. C. Crocker and E. R. Weeks. Particle tracking using IDL, 2007. URL http://www.physics.emory.edu/faculty/weeks//idl/tracking.html.

[12] F. Giavazzi, D. Brogioli, V. Trappe, T. Bellini, and R. Cerbino. Scattering information obtained by optical microscopy: Differential dynamic microscopy and beyond. *Physical review. E, Statistical, nonlinear, and soft matter physics*, 80(3): 031403, 2009.

[13] H. C. Van de Hulst. *Light Scattering by Small Particles*. Dover Publications, New York, 1957.

[14] T. Savin and P. S. Doyle. Static and Dynamic Errors in Particle Tracking Microrheology. *Biophysical Journal*, 88(1):623–638, 2005.

[15] T. Savin and P. S. Doyle. Statistical and sampling issues when using multiple particle tracking. *Physical review. E, Statistical, nonlinear, and soft matter physics*, 76(2):021501, 2007.

[16] J. C. Crocker, M. T. Valentine, E. R. Weeks, T. Gisler, P. D. Kaplan, A. G. Yodh, and D. A. Weitz. Two-Point Microrheology of Inhomogeneous Soft Materials. *Physical Review Letters*, 85(4):888–891, 2000.

[17] D. T. N. Chen, Q. Wen, P. A. Janmey, J. C. Crocker, and A. G. Yodh. Rheology of Soft Materials. *Annual Review of Condensed Matter Physics*, 1(1):301–322, 2010.

[18] T. H. Larsen and E. M. Furst. Microrheology of the Liquid-Solid Transition during Gelation. *Physical Review Letters*, 100(14):146001, 2008.

[19] Q. Xu, N. J. Boylan, J. S. Suk, Y.-Y. Wang, E. A. Nance, J.-C. Yang, P. J. McDonnell, R. A. Cone, E. J. Duh, and J. Hanes. Nanoparticle diffusion in, and microrheology of, the bovine vitreous ex vivo. *Journal of Controlled Release*, 167 (1):76–84, 2013.

[20] F. Giavazzi and R. Cerbino. Digital Fourier microscopy for soft matter dynamics. *Journal of Optics*, 16(8):083001, 2014.

[21] L. L. Josephson, E. M. Furst, and W. J. Galush. Particle tracking microrheology of protein solutions. *Journal of Rheology*, 60(4):531–540, 2016.

[22] J. F. Swindells, C. F. Snyder, R. C. Hardy, and P. E. Golden. Viscosities of sucrose solutions at various temperatures: Tables of recalculated values. Technical report, National Bureau of Standards, 1958.

[23] K. M. Schultz and E. M. Furst. Microrheology of biomaterial hydrogelators. *Soft Matter*, 8(23):6198, 2012.

[24] I. D. Vladescu, E. J. Marsden, J. Schwarz-Linek, V. A. Martinez, J. Arlt, A. N. Morozov, D. Marenduzzo, M. E. Cates, and W. C. K. Poon. Filling an Emulsion Drop with Motile Bacteria. *Physical Review Letters*, 113(26):268101, 2014.

[25] J. L. Burns, Y.-d. Yan, G. J. Jameson, and S. Biggs. A Light Scattering Study of the Fractal Aggregation Behavior of a Model Colloidal System. *Langmuir*, 13 (24):6413–6420, 1997.

[26] F. Ferri, A. D'Angelo, M. Lee, A. Lotti, M. C. Pigazzini, K. Singh, and R. Cerbino. Kinetics of colloidal fractal aggregation by differential dynamic microscopy. *The European Physical Journal Special Topics*, 199(1):139–148, 2011.

[27] P. Nghe, P. Tabeling, and A. Ajdari. Flow-induced polymer degradation probed by a high throughput microfluidic set-up. *Journal of Non-Newtonian Fluid Mechanics*, 165(7-8):313–322, 2010.

[28] M. Kilfoil. Microrheology Dedrifting Tools. URL http://people.umass.edu/kilfoil/downloads.html.

[29] P. N. Pusey and W. Van Megen. Dynamic light scattering by non-ergodic media. *Physica A: Statistical Mechanics and its Applications*, 157(2):705–741, 1989.

[30] F. Scheffold, S. E. Skipetrov, S. Romer, and P. Schurtenberger. Diffusing-wave spectroscopy of nonergodic media. *Physical Review E*, 63(6):061404, 2001.

[31] F. Scheffold and P. Schurtenberger. Light Scattering Probes of Viscoelastic Fluids and Solids. *Soft Materials*, 1(2):139–165, 2003.

[32] V. Tejedor, O. Bénichou, R. Voituriez, R. Jungmann, F. Simmel, C. Selhuber-Unkel, L. B. Oddershede, and R. Metzler. Quantitative Analysis of Single Particle Trajectories: Mean Maximal Excursion Method. *Biophysical Journal*, 98(7):1364–1372, 2010.

Chapter 8

CONCLUSIONS & FUTURE WORK

The goal of this thesis is to develop multiple particle tracking (MPT) methods to improve their accuracy and precision, and to apply these in a microrheology device to support pharmaceutical development of protein therapeutics. The viscosity of protein solutions is a critical formulation parameter affecting downstream manufacturing and drug properties. Characterizing the viscosity of protein solutions across a broad composition space is necessary in the early stages of pharmaceutical development, and in these stages, protein materials are scarce and all formulation tests must be completed on a rapid timeline. This thesis (1) documents the development of new statistical analysis of particle tracking data, as well as new experimental method of estimating the noise floor in microscopy system, (2) details the design of a microfluidic device for microrheology, and (3) demonstrates that MPT microrheology is applicable to protein therapeutic development, with its high-throughput screening capability by using μL sample sizes for measuring protein formulation viscosities.

8.1 Method development for particle tracking microrheology

Chapter 3 gives an overview of the accuracy and precision of the MPT microrheology technique. During an experiment, the mean-squared displacement of the probe particles is measured as a function of lag time τ. Traditionally, the viscosity is calculated using the logarithmic intercept of the mean-squared displacement. However, this overweighs the longest lag times, which are also those with the poorest statistics. Instead, the Van Hove self-correlation can be used to calculate the solution viscosity at a particular lag time. Any τ may be chosen; however, the sources of error at various lag times are unequal. To identify the optimum τ for maximizing measurement precision,

excess kurtosis α_2 and its test statistic Z_{α_2} are used as measures of the non-Gaussian behavior at each τ. The lag time that minimizes the excess kurtosis will provide the most accurate and precise measurements. The accuracy of this technique for measuring viscosity of protein solutions is also demonstrated by benchmarking with bulk rheology measurements, finding MPT microrheology to agree with bulk rheology and tabulated data within 2% relative error, and achieving better accuracy at low protein concentrations.

Chapter 4 describes a new method of measuring static error in MPT experiments. Static error ϵ arises from limited spatial resolution in the camera setup, and is especially pronounced for solutions with high viscosity. Traditionally, static error for a particular experimental setup is estimated by tracking particles confined in a gel. However, the conditions of the gel are not identical to those of the solution of interest, thus limiting the applicability of this estimation. A new theory based on the excess kurtosis is derived to estimate the static error in a sample from the same data measured in a typical multiple particle tracking experiment. This *in situ* estimate of ϵ is measured under the same conditions of the sample of interest, and without any additional experiments. Corrected MSDs calculated using the estimation from the gel and the *in situ* static error measurement show that the gel method overestimates ϵ, while the *in situ* method restores the MSD of the sucrose solutions to a logarithmic slope of 1. This method is also tested on highly viscous PEO solutions to examine its limits, and is shown to be valid as long as *some* measurable displacements are recorded for the sample.

Chapter 7 introduces differential dynamic microscopy (DDM), a new analysis method for gathering additional information from a microrheology experiment. DDM analyzes the evolution of the sample in Fourier-transformed frequency space, using the same image stack collected during an MPT experiment. DDM analysis gathers similar information to light scattering experiments, yet can also be performed on μL-sized samples and with a simple microscopy setup. DDM analysis is applied to sucrose and PEO solutions, and compared to MPT analysis. Viscosities calculated with DDM and

with MPT are in good agreement for the Newtonian fluids tested. DDM requires less user input compared to MPT. However, DDM does not benefit from the sub-pixel resolution of MPT, so its operating regime is 20 $\times$ smaller than that of MPT. Future opportunities to analyze sources of error in DDM are discussed.

8.2 Device development for pharmaceutical applications

To take advantage of the rapid acquisition time and small sample size of MPT microrheology, a microfluidic device is built for high-throughput microrheology experiments. Microfluidic stickers are fabricated with multiple 2 μL channels on a single microscope slide, and mounted on a Peltier thermoelectric module to control the temperature within 0.5°C. The design of the microfluidic sticker, as well as the material choice for fabrication, is discussed in detail in Chapter 5. The microfluidic sticker design ensures simultaneous and rapid temperature equilibration of all the samples, enabling high-throughput experiments on multiple formulations without waiting for separate samples to reach a set temperature. Heat transfer effects may cause deviations between the sample temperature and the set point temperature. Therefore, a calibration fluid is introduced in a channel on the same device to provide an *in situ* measurement of temperature by comparing the measured viscosity to tabulated viscosity data; this provides a more accurate temperature measurement *on chip* than attaching a second thermocouple to the slide. This high-throughput device is used to execute 72 temperature-concentration viscosity measurements of mAb solutions using 2 μL samples in $\sim$6 hours.

8.3 Application of microrheology for pharmaceutical development

Using the high-throughput device developed in this work, viscosity profiles of several mAb solutions are investigated. Solutions of mAb1 and mAb2 are validated against macrorheology to verify the accuracy of this technique with protein solutions in Chapter 3. Temperature profiles of mAb1 and mAb2 exhibited Arrhenius temperature

behavior. Although only 2% of the protein sequences are different in mAb-1 and mAb-2 and their viscosity profiles are similar at low concentrations, their behavior diverged at high concentrations, with as much as a ten-fold difference in viscosity at 90 mg/mL and 0.9°C, as examined in Chapter 5.

Multiple particle tracking also enables discovery of unusual emergent phenomena in bispecific antibody solutions detailed in Chapter 6. Monospecific antibodies (mAb-A, mAb-B, and mAb-C), bispecific antibodies (BsAb-A/B and BsAb-A/C), and mixtures thereof are characterized across a range of concentrations. mAb-C has higher viscosity than mAb-A, and the viscosity of BsAb-A/C and the physical mixture of (mAb-A + mAb-C) can be interpolated using the Arrhenius mixing rule. Remarkably, while mAb-A and mAb-B have similar viscosity, their mixture and BsAb-A/B have significantly higher viscosity than either mAb alone. Light scattering and size-exclusion chromatography studies are performed to investigate protein-protein interactions and the possible formation of clusters, but there are still open questions regarding the mechanism of this unusual viscosity increase.

Measuring these viscosity profiles is only possible because of the small sample volume available to microrheology; larger sample volumes would render these experiments too costly and consume too much material to be worthwhile in early stages of development. By developing the microrheology technique, and building and benchmarking this new microfluidic device, high-throughput, small-volume rheological characterizations of protein formulations are available. The methods, procedures, instrument design, and example data are available for download at the Furst group wiki. Multiple particle tracking microrheology has been implemented in the labs at Genentech, and continues to be used to support early stage pharmaceutical development and drive scientific discovery in protein characterization.

8.4 Suggested Future Work

The aim of this thesis is to develop small-scale microrheological measurements for biopharmaceutical applications. The methods developed have focused on decreasing

sample size, increasing throughput, and improving accuracy and precision of microrheology measurements, which enable several extensions of this work.

The obvious extension of this work is to use microfluidics technology to generate libraries of microrheology samples (instead of pipetting into the rectangular channels in the microfluidic sticker). High-throughput multi-well plates can be combined with microrheological screening [1, 2]. Schultz and Furst [3] demonstrated the capability of a droplet-forming microfluidic T-junction to generate a library of samples with a linear composition gradient. These droplets can be stored on chip [4, 5], and through the incorporation of a thin, water-permeable membrane [6–8], protein solutions can be concentrated and dialyzed into different formulation buffers, requiring little human interaction.

Microrheology has discovered interesting physics in the viscosity of the bispecific antibody solutions; further examination of the protein-protein interactions of the bispecific antibodies, as well as experiments at higher ionic strength, should provide more insights into the emerging behavior. Other formats of protein therapeutics could also be studied using microrheology, such as antibody-drug conjugates, hydrogel formulations [9–11] or polymer-solvent depots for sustained drug release [12–14]. Particle tracking microrheology has also been used to study the microstructure of the fibrils network in bovine vitreous humor [15, 16] and brain extracellular space [17], whose properties cannot be measured *ex vivo* in a macrorheometer. Similar work to study nanoparticle diffusion and tissue mechanical properties for guiding drug design and delivery can be carried out in leporine, simian and human tissues.

Further investigations of probe stability and design of a "master" probe that can be stable in protein solutions will also improve the measurement technique. Kim et al. [18] demonstrated a method for grafting a dense layer of PEG to latex microspheres that enhances colloidal stability, even at high ionic strengths (up to 150 mM). This is accomplished by trapping a water-soluble triblock copolymer, poly(ethylene glycol)-*b*-poly(propylene glycol)-*b*-poly(ethylene glycol), on the surface of the polystyrene particles via swelling with toulene followed by deswelling. Work has already been begun

in our lab to synthesize stable, fluorescent microparticles for protein applications.

The application of differential dynamic microscopy for microrheology is explored in this thesis. The main advantage of DDM is its ability to measure blurry (or not perfectly resolved features), and can be executed, potentially, at the speed of spatially resolved image correlation spectroscopy method, which would greatly decrease the time of experimentation by measuring all samples on the same device at once. However, a detailed error analysis for DDM is needed to further its application in measuring soft materials.

Ultimately, we want to provide a microrheology device, along with a software package for viscosity analysis, that can be implemented easily in a research lab. The biggest start-up cost in implementing particle tracking microrheology falls on the acquisition of a microscope and a high speed camera. However, smart phones are now capable of 60–90 frames per second [19, 20], and a portable microscope camera has been made for smart phones capable of up to 400× magnification [21]. These advances could lower the implementation barrier even further, bringing rheology to citizen scientists[1] and students at home and in the classroom.

[1] A citizen scientist is a member of the general public who engages in scientific work; an amateur or non-professional scientist.

REFERENCES

[1] V. Breedveld and D. J. Pine. Microrheology as a tool for high-throughput screening. *Journal of Materials Science*, 38(22):4461–4470, 2003.

[2] F. He, C. E. Woods, E. Trilisky, K. M. Bower, J. R. Litowski, B. A. Kerwin, G. W. Becker, L. O. Narhi, and V. I. Razinkov. Screening of Monoclonal Antibody Formulations Based on High-Throughput Thermostability and Viscosity Measurements: Design of Experiment and Statistical Analysis. *Journal of Pharmaceutical Sciences*, 100(4):1330–1340, 2011.

[3] K. M. Schultz and E. M. Furst. High-throughput rheology in a microfluidic device. *Lab on a Chip*, 11(22):3802–3809, 2011.

[4] J.-u. Shim, G. Cristobal, D. R. Link, T. Thorsen, Y. Jia, K. Piattelli, and S. Fraden. Control and measurement of the phase behavior of aqueous solutions using microfluidics. *Journal of the American Chemical Society*, 129(28):8825–8835, 2007.

[5] H. Boukellal, Š. Selimović, Y. Jia, G. Cristobal, and S. Fraden. Simple, robust storage of drops and fluids in a microfluidic device. *Lab on a Chip*, 9(2):331–338, 2009.

[6] S. Song, A. K. Singh, T. J. Shepodd, and B. J. Kirby. Fabrication and characterization of photopatterned polymer membranes for protein concentration and dialysis in microchips. In *Solid-State Sensor, Actuator and Microsystems Workshop*, 2004.

[7] C. Kim, C. Ryu, L. W. Kim, S. J. Sim, and H. Chae. Microfluidic dialysis device fabrication for protein solution enrichment and its enrichment enhancement by

plasma surface treatment of a membrane. *Journal of the Korean Physical Society*, 51(3):993–999, 2007.

[8] Š. Selimović, F. Gobeaux, and S. Fraden. Mapping and manipulating temperature-concentration phase diagrams using microfluidics. *Lab on a Chip*, 10(13):1696–1699, 2010.

[9] N. Peppas. Hydrogels in pharmaceutical formulations. *European Journal of Pharmaceutics and Biopharmaceutics*, 50(1):27–46, 2000.

[10] S. Frokjaer and D. E. Otzen. Protein drug stability: a formulation challenge. *Nature Reviews Drug Discovery*, 4(4):298–306, 2005.

[11] A. A. Aimetti, A. J. Machen, and K. S. Anseth. Poly(ethylene glycol) hydrogels formed by thiol-ene photopolymerization for enzyme-responsive protein delivery. *Biomaterials*, 30(30):6048–6054, 2009.

[12] V. R. Sinha and A. Trehan. Biodegradable microspheres for protein delivery. *Journal of Controlled Release*, 90(3):261–280, 2003.

[13] S. Kempe and K. Mäder. In situ forming implants — an attractive formulation principle for parenteral depot formulations. *Journal of Controlled Release*, 161(2): 668–679, 2012.

[14] D. P. Chang, V. K. Garripelli, J. Rea, R. Kelley, and K. Rajagopal. Investigation of Fragment Antibody Stability and Its Release Mechanism from Poly(Lactide-co-Glycolide)-Triacetin Depots for Sustained-Release Applications. *Journal of Pharmaceutical Sciences*, 104(10):3404–3417, 2015.

[15] C. S. Nickerson, J. Park, J. A. Kornfield, and H. Karageozian. Rheological properties of the vitreous and the role of hyaluronic acid. *Journal of Biomechanics*, 41 (9):1840–1846, 2008.

[16] Q. Xu, N. J. Boylan, J. S. Suk, Y.-Y. Wang, E. A. Nance, J.-C. Yang, P. J. McDonnell, R. A. Cone, E. J. Duh, and J. Hanes. Nanoparticle diffusion in, and microrheology of, the bovine vitreous ex vivo. *Journal of Controlled Release*, 167 (1):76–84, 2013.

[17] E. A. Nance, G. F. Woodworth, K. A. Sailor, T.-Y. Shih, Q. Xu, G. Swaminathan, D. Xiang, C. Eberhart, and J. Hanes. A Dense Poly(Ethylene Glycol) Coating Improves Penetration of Large Polymeric Nanoparticles Within Brain Tissue. *Science Translational Medicine*, 4(149):149ra119–149ra119, 2012.

[18] A. J. Kim, V. N. Manoharan, and J. C. Crocker. Swelling-based method for preparing stable, functionalized polymer colloids. *Journal of the American Chemical Society*, 127(6):1592–1593, 2005.

[19] Samsung. Samsung Galaxy Camera, 2015. URL http://www.samsung.com/us/support/answer/ANS00026097/.

[20] Apple. iPhone 7 - Technical Specifications, 2016. URL http://www.apple.com/iphone-7/specs/.

[21] Nurugo. nurugo-micro, 2016. URL http://www.nurugo.com/product/nurugo-micro/.

Appendix A

MATLAB CODE FOR MICRORHEOLOGY

A.1 Automated particle tracking routine

This following code is used in conjunction with the brightness-weighted centroid algorithm in MATLAB by Blair & Dufresne and Kilfoil. The routine will (1) loop through all data folders, and (2) calculate the viscosity based on excess kurtosis calculations.

```
clear all
close all
%%%%%% Input main folder and parameters here %%%%%%
basepath = 'G:\Data\20151214 static error validation';
outpath = 'C:\Users\josephl6\Copy\Genentech co-op\Data\20151203 mixture and gel';
datafile = 'data_20151214.txt';
temp = 273.15 + 23;
framerate = 30; %fps
sigma = 10; %exposure time
conversion = 0.168; %um/px 60x = 0.112
probe = 0.5e-6; %probe radius in m
probepx = 13; %tracking parameter in px (odd numbers only)
%%%%%% Don't touch below if you don't have to! %%%%%%

subdirs = dir(basepath);
subdirs(~[subdirs.isdir]) = [];
%And this filters out the parent and current directory '.' and '..'
tf = ismember( {subdirs.name}, {'.', '..'});
subdirs(tf) = [];
```

```
numberOfFolders = length(subdirs);

fileID = fopen([outpath filesep datafile],'a');
fprintf(fileID,'%6s\t %6s\t %6s\r\n', 'T (K)','Frame rate',...
    'Exposure time (ms)');
fprintf(fileID,'%6.2f\t %12f\t %12f\r\n',temp,framerate,sigma);
fprintf(fileID,'%6s\t %12s\t %12s\t %12s\t %12s\t %12s\r\n',...
    'Sample','Viscosity (cP)','Visc uncertainty','Frame Number',...
    'SNR (1st frame)','SNR (dB)');
for k = 1 : numberOfFolders
    %Here i am creating the variables to iterate over the folders
    sample = subdirs(k).name;
    D = dir([[basepath filesep sample], '\*.tif']);
    Num = length(D(not([D.isdir])));
    fprintf(1, 'Now reading %s\n', sample);
    pos_list=Ftrack([basepath filesep sample filesep sample 't'],1,Num,probepx);
    pos = pos_list(:,[1:2,5]);
%     [n, xout] = hist([mod(pos(:,1),1);  %this is for checking if the
%     parameters are good
%         mod(pos(:,2),1)],50);
%     stairs(xout, n,'color',[0.5 0.5 0.5])
%     ylim([0 25000])
%     box off
    param = struct('mem',0,'good',5,'dim',2,'quiet',0);
    result = track(pos,5,param);
    save([outpath filesep 'track ' sample '.txt'],'result','-ascii');
    % dedrifting_and_conversions(outpath, T, 10);
    % dd = load([outpath 'ddtrack ' sample num2str(T) '.txt'],'-ascii');
    % ddmsd = MSD(dd);
    [msd,VH] = MSD(result,framerate,conversion);
    frameVH = find(msd(:,5)<1.96,1);
    VH(:,1) = VH(:,1)*conversion; %convert VH to real dimensions
    f = fit(VH(:,1),VH(:,2),'gauss1');
    VHcoeff = coeffvalues(f);
    bounds = confint(f);
```

```
    VHcoeffpm = VHcoeff - bounds(1,:);
    variance = (VHcoeff(3)/2)^2;
    visc = (1.3806488e-23*temp*(msd(frameVH,1))*1000/...
        (6*pi*probe*variance*0.000000000001));
    variancelow = (bounds(1,3)/2)^2;
    viscerr = (1.3806488e-23*temp*(msd(frameVH,1))*1000/...
        (6*pi*probe*variancelow*0.000000000001));
    viscpm = abs(visc - viscerr);
    % figure()
    % plot(VH(:,1),log(VH(:,2)),'ko')
    % xlim([-2.5 2.5])
    % figure()
    % loglog(msd(:,1),msd(:,2));
    save([outpath filesep 'MSD ' sample ' v' num2str(visc)...
        ' f' num2str(frameVH) '.txt'],'msd','-ascii');
    save([outpath filesep 'VH ' sample ' v' num2str(visc)...
        ' f' num2str(frameVH) '.txt'],'VH','-ascii');
    figure()
    I = double(imread([basepath filesep sample filesep sample 't0001.tif']));
    [signal, noise] = SNR(I,13);
    s_n_r = (mean(signal)-mean(noise))/std(noise);
    snrdb = 10*log10((mean(signal)-mean(noise))/std(noise));

    fprintf(fileID,'%6s\t %12.6f\t %12.6f\t %12f\t %12.4f\t %12.4f\r\n',...
        sample,visc,viscpm,frameVH,s_n_r,snrdb);

end
fclose(fileID);
```

A.2 Differential dynamic microscopy

```
close all
clear all

basepath = '/Volumes/Lilian03/Data/20141110 static error validation/';
outpath = '/Users/Lilian/Dropbox/Research/Data/20150415 DDM test/';
T = 5000; %or run number or seconds
sample = '55wt sucrose ';
L = 1024; % image size in pixel
first = 1;
last = 500; % total number of frames
video = zeros(L,L,last);
ensemble = 50; % minimum number to be averaged in the ensemble

for frame=first:last

    if mod(frame,10)==0
        disp(['Frame number: ' num2str(frame)]);
    end
    % read in file
    image = double(imread([basepath sample num2str(T) '/frame ', ...
        num2str(frame,'%04u'),'.tif']));
    video(:,:,frame) = image;
end

tic
g = zeros(L,L,last-ensemble);
qmax = L/2-1;
average = zeros(last-ensemble,qmax);

for tau = first:(last-ensemble) %lag time
    inittimes = floor(linspace(1,(last-tau),ensemble));
```

```
sum=zeros(L,L);

for k = 1:ensemble %initial times
i = inittimes(k);
D = video(:,:,i+tau) - video(:,:,i);
f = (abs(fftshift(fft2(D)))).^2;
sum = sum + f;
end
g(:,:,tau) = sum/ensemble;


if mod(tau,10)==0
    disp(['tau: ' num2str(tau) ' frame']);
end

totalnumcp = 0;
for q=1:1:qmax
    % increments are 1/L (length^-1) = 0.004 um^-1 = 1/1024 px^-1
   C = 2*pi()*q;
   numcp=round(C/2);

   theta = linspace(0,2*pi(),numcp); % even distribution of pts on circle
   inter = zeros(1,numcp); % interpolated value of g at every circle point
   totalnumcp = totalnumcp + numcp;
   for j=1:1:numcp-1
       x=q*cos(theta(j))+L/2+1e-9;
       y=q*sin(theta(j))+L/2+1e-9;
       x1 = floor(x);
       x2 = ceil(x);
       y1 = floor(y);
       y2 = ceil(y);
       inter(j) = 1/((x2-x1)*(y2-y1))*...
           (g(x1,y1,tau)*(x2-x)*(y2-y)+...
            g(x2,y1,tau)*(x-x1)*(y2-y)+...
            g(x1,y2,tau)*(x2-x)*(y-y1)+...
```

```
                g(x2,y2,tau)*(x-x1)*(y-y1));
        end
        average(tau,q) = nanmean(inter(:));
    end

end


save([outpath 'avg-fft ' sample num2str(T) '.txt'],'average','-ascii');

%plotting fft before q-averaged
tau = 1;
D1 = video(:,:,1+tau) - video(:,:,1);
figure()
imshow(D1); colormap(gray); axis image
print([outpath sample 'diff dt_' num2str(tau) '.png'],'-dpng')
f1 = (abs(fftshift(fft2(D1)))).^2;
figure()
imagesc(100*log(1+abs(f1))); colormap(gray);
axis image
print([outpath sample 'f dt_' num2str(tau) '.png'],'-dpng')

%plotting fft after q-averaged
figure()
imagesc(100*log(1+abs(g(:,:,100)))); colormap(gray);
axis image
print([outpath sample 'g dt_' num2str(tau) '.png'],'-dpng')

figure()
plot(1:taup,avgPEO(:,[20 50 100 150 200 250 400]))
legend('q=20','q=50','q=100','q=150','q=200','q=250','q=400')
xlabel('tau, frames')
ylabel('g')

figure
```

```
plot(1:qmax,average([20 40 60 80 100],:))
xlabel('q')
ylabel('g')
toc


%% Fitting to get A(q), B(q), and f(q)
y = zeros(1,last-ensemble);
beta0 = [200;6;32];
count=1;
for q=40:1:500 %qmax
    y(:) = average(:,q); % response
    y = y*1e-10;
    x = 1:1:(last-ensemble); % tau
    modelfun = @(c,x)(c(1)*(1-(exp(-x/c(3))))+c(2));

    % fit A, B, and f for func at this particular q
    c = ones(1,3);
    opts = statset('nlinfit');
    opts.RobustWgtFun = 'bisquare';
    % options = optimoptions(@lsqnonlin,'Algorithm','levenberg-marquardt')

    beta = nlinfit(x,y,modelfun,beta0,opts);

    fity = (beta(1)*(1-(exp(-x/beta(3))))+beta(2));
    %hold on
    %loglog(x,y,'.',x,fity)

    A(q) = beta(1);
    B(q) = beta(2);
    H(q) = beta(3);

    data(count,1) = q;
    data(count,2) = beta(1); %A(q)
    data(count,3) = beta(2); %B(q)
```

```
    data(count,4) = beta(3); %H(q)

    count=count+1;
    beta0 = beta;
end

loglog(1:1:500,H)

save(['avg_fft' outpath sample num2str(x) '.txt'],'average','-ascii');
save([outpath 'fit_params ' sample num2str(T) '.txt'],'data','-ascii');

% azimuthal plot
for q=1:1:511 % increments are 1/L (length^-1) = 0.004 um^-1 = 1/1024 px^-1
    C = 2*pi()*q;
    numcp=round(C/2);
    theta = linspace(0,2*pi(),numcp); % even distribution of points on circle
    for j=1:1:numcp-1
        x=q*cos(theta(j))+L/2+1e-9;
        y=q*sin(theta(j))+L/2+1e-9;
        storecirclex(q,j)=x;
        storecircley(q,j)=y;
    end
end

for i = 1:511
    for j = 1:1604
        if storecirclex(i,j)==0
            storecirclex(i,j)=NaN;
            storecircley(i,j)=NaN;
        end
    end
end
figure, plot(storecirclex(1:100:500,1:20:1600), ...
    storecircley(1:100:500,1:20:1600),'.','markers',12)
```

Appendix B

ESSENTIALS FOR MICRORHEOLOGY EXPERIMENT SETUP

B.1 Video microscopy

- Microscope with fluorescent capability (mercury bulb attachment)
- Temperature control microscope stage
- 40× objective (NA 0.75+)
- 63× or 100× objective – NOT immersion if temperature control is desired
- Objective cleaning kit
- Ruler slide
- High speed CMOS camera
- Lab computer connected to camera (storage 1TB+, memory 8 GB+)
- Workstation for analysis (if not the same as lab computer)
- License for Matlab or IDL
- Back-up external hard drive (2 TB+)

B.2 Sample preparation

- Vortex mixer
- Centrifuge
- Pipette and tips– p100, p20 or p10, p2
- Eppendorf tubes – 0.5 mL, 1.5 mL
- Microscope slides – 75x25 (#12-550D), 75x50 (#12-550C) – fisher scientific (or any general purpose glass slides will do)
- Capillary tubes (borosilicate) – 0.20 × 2.00 × 50 mm – vitrocom.com, #3520
- Norland Optical Adhesive 81 (thiolene resin glue) – norlandprod.com, part #8101 (12 bottles)
- UV lamp at 365 nm – norlandprod.com, splice lamp part #5200

B.3 Polyacrylamide gel

- Acrylamide monomer – #A8887-100g, Sigma Aldrich
- Bis-acrylamide – #146072-100g, Sigma Aldrich
- Ammonium persulfate – #248614-100g, Sigma Aldrich
- TEMED – #T22500-100mL, Sigma Aldrich

B.4 Probes

- 1 μm polystyrene fluospheres – lifetechnologies.com, catalog #F13081
- 1 μm amide-modified polystyrene fluospheres – lifetechnologies.com, catalog #F8765
- 1 μm carboxylate-modified polystyrene fluospheres – lifetechnologies.com, catalog #F8823
- mPEG-SCM (5000MW) – creativepegworks.com, #PLS-213
- mPEG-NH2 (5000MW) – creativepegworks.com, #PLS-268
- PolyLink coupling kit – polysciences.com, #24350-1

Appendix C

PERMISSION LETTERS

AIP PUBLISHING LLC LICENSE
TERMS AND CONDITIONS

Oct 09, 2016

This Agreement between Lilian Lam Josephson ("You") and AIP Publishing LLC ("AIP Publishing LLC") consists of your license details and the terms and conditions provided by AIP Publishing LLC and Copyright Clearance Center.

License Number	3964860226892
License date	Oct 09, 2016
Licensed Content Publisher	AIP Publishing LLC
Licensed Content Publication	Journal of Rheology
Licensed Content Title	Particle tracking microrheology of protein solutions
Licensed Content Author	Lilian Lam Josephson,Eric M. Furst,William J. Galush
Licensed Content Date	May 6, 2016
Licensed Content Volume Number	60
Licensed Content Issue Number	4
Type of Use	Thesis/Dissertation
Requestor type	Author (original article)
Format	Print and electronic
Portion	Excerpt (> 800 words)
Will you be translating?	No
Title of your thesis / dissertation	Microrheology for Protein Therapeutics Development
Expected completion date	Oct 2016
Estimated size (number of pages)	200
Requestor Location	Lilian Lam Josephson 13 Ethan Allen Ct NEWARK, DE 19711 United States Attn: Lilian Lam Josephson
Billing Type	Invoice
Billing Address	Lilian Lam Josephson 13 Ethan Allen Ct NEWARK, DE 19711 United States Attn: Lilian Lam Josephson
Total	0.00 USD

Terms and Conditions

The Society of Rheology -- Terms and Conditions: Permissions Uses

The Society of Rheology ("SOR") hereby grants to you the non-exclusive right and license to use and/or distribute the Material according to the use specified in your order, on a one-time basis, for the specified term, with a maximum distribution equal to the number that you have ordered. Any links or other content accompanying the Material are not the subject of this license.

1. You agree to include the following copyright and permission notice with the reproduction of the Material:"Reprinted with permission from [FULL CITATION]. Copyright [PUBLICATION YEAR], The Society of Rheology." For an article, the copyright and permission notice must be printed on the first page of the article or book chapter. For photographs, covers, or tables, the copyright and permission notice may appear with the Material, in a footnote, or in the reference list.
2. If you have licensed reuse of a figure, photograph, cover, or table, it is your responsibility to ensure that the material is original to SOR and does not contain the copyright of another entity, and that the copyright notice of the figure, photograph, cover, or table does not indicate that it was reprinted by SOR, with permission, from another source. Under no circumstances does SOR, purport or intend to grant permission to reuse material to which it does not hold copyright.
3. You may not alter or modify the Material in any manner. You may translate the Material into another language only if you have licensed translation rights. You may not use the Material for promotional purposes. SOR reserves all rights not specifically granted herein.
4. The foregoing license shall not take effect unless and until SOR or its agent, Copyright Clearance Center, receives the Payment in accordance with Copyright Clearance Center Billing and Payment Terms and Conditions, which are incorporated herein by reference.
5. SOR or the Copyright Clearance Center may, within two business days of granting this license, revoke the license for any reason whatsoever, with a full refund payable to you. Should you violate the terms of this license at any time, SOR, The Society of Rheology, or Copyright Clearance Center may revoke the license with no refund to you. Notice of such revocation will be made using the contact information provided by you. Failure to receive such notice will not nullify the revocation.
6. SOR makes no representations or warranties with respect to the Material. You agree to indemnify and hold harmless SOR, The Society of Rheology, and their officers, directors, employees or agents from and against any and all claims arising out of your use of the Material other than as specifically authorized herein.
7. The permission granted herein is personal to you and is not transferable or assignable without the prior written permission of SOR. This license may not be amended except in a writing signed by the party to be charged.
8. If purchase orders, acknowledgments or check endorsements are issued on any forms containing terms and conditions which are inconsistent with these provisions, such inconsistent terms and conditions shall be of no force and effect. This document, including the CCC Billing and Payment Terms and Conditions, shall be the entire agreement between the parties relating to the subject matter hereof.

This Agreement shall be governed by and construed in accordance with the laws of the State of New York. Both parties hereby submit to the jurisdiction of the courts of New York County for purposes of resolving any disputes that may arise hereunder.

Questions? customercare@copyright.com or +1-855-239-3415 (toll free in the US) or +1-978-646-2777.

AIP PUBLISHING LLC LICENSE
TERMS AND CONDITIONS

Oct 09, 2016

This Agreement between Lilian Lam Josephson ("You") and AIP Publishing LLC ("AIP Publishing LLC") consists of your license details and the terms and conditions provided by AIP Publishing LLC and Copyright Clearance Center.

License Number	3964860401093
License date	Oct 09, 2016
Licensed Content Publisher	AIP Publishing LLC
Licensed Content Publication	Biomicrofluidics
Licensed Content Title	Parallel temperature-dependent microrheological measurements in a microfluidic chip
Licensed Content Author	Lilian Lam Josephson,William J. Galush,Eric M. Furst
Licensed Content Date	Jun 14, 2016
Licensed Content Volume Number	10
Licensed Content Issue Number	4
Type of Use	Thesis/Dissertation
Requestor type	Author (original article)
Format	Print and electronic
Portion	Excerpt (> 800 words)
Will you be translating?	No
Title of your thesis / dissertation	Microrheology for Protein Therapeutics Development
Expected completion date	Oct 2016
Estimated size (number of pages)	200
Requestor Location	Lilian Lam Josephson 13 Ethan Allen Ct NEWARK, DE 19711 United States Attn: Lilian Lam Josephson
Billing Type	Invoice
Billing Address	Lilian Lam Josephson 13 Ethan Allen Ct NEWARK, DE 19711 United States Attn: Lilian Lam Josephson
Total	0.00 USD
Terms and Conditions	

AIP Publishing LLC -- Terms and Conditions: Permissions Uses

AIP Publishing hereby grants to you the non-exclusive right and license to use and/or distribute the Material according to the use specified in your order, on a one-time basis, for the specified term, with a maximum distribution equal to the number that you have ordered. Any links or other content accompanying the Material are not the subject of this license.

1. You agree to include the following copyright and permission notice with the reproduction of the Material:"Reprinted from [FULL CITATION], with the permission of AIP Publishing." For an article, the credit line and permission notice must be printed on the first page of the article or book chapter. For photographs, covers, or tables, the notice may appear with the Material, in a footnote, or in the reference list.
2. If you have licensed reuse of a figure, photograph, cover, or table, it is your responsibility to ensure that the material is original to AIP Publishing and does not contain the copyright of another entity, and that the copyright notice of the figure, photograph, cover, or table does not indicate that it was reprinted by AIP Publishing, with permission, from another source. Under no circumstances does AIP Publishing purport or intend to grant permission to reuse material to which it does not hold appropriate rights.
   You may not alter or modify the Material in any manner. You may translate the Material into another language only if you have licensed translation rights. You may not use the Material for promotional purposes.
3. The foregoing license shall not take effect unless and until AIP Publishing or its agent, Copyright Clearance Center, receives the Payment in accordance with Copyright Clearance Center Billing and Payment Terms and Conditions, which are incorporated herein by reference.
4. AIP Publishing or Copyright Clearance Center may, within two business days of granting this license, revoke the license for any reason whatsoever, with a full refund payable to you. Should you violate the terms of this license at any time, AIP Publishing, or Copyright Clearance Center may revoke the license with no refund to you. Notice of such revocation will be made using the contact information provided by you. Failure to receive such notice will not nullify the revocation.
5. AIP Publishing makes no representations or warranties with respect to the Material. You agree to indemnify and hold harmless AIP Publishing, and their officers, directors, employees or agents from and against any and all claims arising out of your use of the Material other than as specifically authorized herein.
6. The permission granted herein is personal to you and is not transferable or assignable without the prior written permission of AIP Publishing. This license may not be amended except in a writing signed by the party to be charged.
7. If purchase orders, acknowledgments or check endorsements are issued on any forms containing terms and conditions which are inconsistent with these provisions, such inconsistent terms and conditions shall be of no force and effect. This document, including the CCC Billing and Payment Terms and Conditions, shall be the entire agreement between the parties relating to the subject matter hereof.

This Agreement shall be governed by and construed in accordance with the laws of the State of New York. Both parties hereby submit to the jurisdiction of the courts of New York County for purposes of resolving any disputes that may arise hereunder.

V1.1

Questions? customercare@copyright.com or +1-855-239-3415 (toll free in the US) or +1-978-646-2777.